Catching Dark Photons in the Sky: Looking for light vector particles using satellites

Dissertation

zur Erlangung des Doktorgrades an der Fakultät für Mathematik, Informatik und Naturwissenschaften

Fachbereich Physik der Universität Hamburg

vorgelegt von

Jonas Frerick
aus
Rhade

Hamburg
2024

Gutachter der Dissertation:	Dr. Kai Schmidt-Hoberg Prof. Dr. Marcus Brüggen
Zusammensetzung der Prüfungskommission:	Dr. Kai Schmidt-Hoberg Prof. Dr. Marcus Brüggen Prof. Dr. Dieter Horns Prof. Dr. Konstantinos Nikolopoulos Dr. Hyungjin Kim
Vorsitzender der Prüfungskommission:	Prof. Dr. Dieter Horns
Datum der Disputation:	07.10.2024
Vorsitzender des Fach-Promotionsausschusses Physik:	Prof. Dr. Markus Drescher
Leiter des Fachbereichs Physik:	Prof. Dr. Wolfgang J. Parak
Dekan der Fakultät MIN:	Prof. Dr.-Ing. Norbert Ritter

Abstract

The lack of signals in traditional dark matter (DM) searches beyond gravitational interactions provide an excellent reason to investigate weakly coupled and/or light dark sectors (DS). These receive motivation both from the theoretical and the phenomenological side with rich physics across many different scales. Depending on the exact composition of the DS the signals can show up at colliders, in astrophysical searches, and in specialised direct detection experiments, which differ significantly from traditional nuclear recoil searches. Furthermore, the low mass of these new particles opens up new opportunities for producing new physics in the lab beyond the typical high-energy accelerators required for detecting new heavy states.

This thesis will focus specifically on a broad class of DSs, namely those containing a Dark Photon (DP) in the particle spectrum. The DP is a well-motivated candidate which can act as a mediator between the standard model (SM) and the DS but it is also known to provide a rich phenomenology by itself. This ranges from the oblique corrections to electroweak precision observables (EWPO) at high DP masses to the subtle impact of a light DP on electromagnetism (EM). This thesis will provide an introduction to the conventional coupling of the DP to the full electroweak theory via the so-called kinetic mixing. We will further discuss potential generalisations of this mixing, i.e. via the Z boson mass or the Stückelberg mechanism. We will show how a light DP decouples from observables at colliders and that the kinetic mixing to electromagnetism is the low-energy theory emerging from the mixing with the hypercharge boson.

This mixing with the photon enables non-trivial effects of the DP in an SM plasma. We will use the well-known plasma effects to calculate the solar DP flux emerging from the plasma of solar electrons. In contrast to the majority of the literature, we will focus on the angular distribution of the solar DP flux and point out the advantage of applying this additional information to helioscope searches for DPs. Using data from Hinode XRT, a solar x-ray telescope, we demonstrate that the sensitivity boost can be significant. This observation is interesting in light of future helioscopes, which is briefly discussed in this thesis as well.

The second part of this thesis will then be focussing on the dark matter puzzle and the potential role of the DP as a DM candidate. After providing a brief introduction to the topic, we consider the LISA Pathfinder (LPF) mission as a direct detection experiment for ultralight DPDM. In the spirit of a “no-go theorem”, we provide reasons why the direct detection of kinetically mixed DPs using LPF is impossible. This result is also valid for other direct detection setups with only a few caveats. However, we demonstrate that LPF is an interesting instrument for investigating the signal of “general DPs”, i.e. DPs gauged under global SM symmetries such as $B - L$. We point out that the auxiliary channels of LPF provide a powerful tool to look for the DM signal, emphasising why it is expected to be better than the main channel. In addition, potential follow-up projects are discussed.

Zusammenfassung

Das Fehlen von Signalen in traditionellen Suchen nach dunkler Materie (DM) jenseits von Gravitations-Wechselwirkung bietet einen exzellenten Grund, schwach gekoppelte und leichte “dunkle Sektoren” (DS) zu untersuchen. Motivation, diese zu studieren, erhalten wir sowohl von theoretischer als auch von phänomenologischer Seite mit reichhaltiger Physik über viele Größenordnungen hinweg. Abhängig von der genauen Zusammensetzung des DS sind Signale an Teilchenbeschleunigern, in astrophysikalischen Suchen und in spezialisierten Experimenten zur direkten Detektion möglich, welche von traditionellen Suchen nach Rückstößen von Atomkernen stark abweichen. Desweiteren ermöglicht die geringe Masse dieser Teilchen ihre direkte Produktion im Labor ohne die Hilfe von den typischen Hochenergie-Beschleunigern, die notwendig sind, um schwerere Teilchen zu entdecken.

Diese Dissertation wird sich mit einer breiten Klasse an DS-Teilchen detailliert beschäftigen, nämlich mit den DS, die ein Dunkles Photon (DP) in ihrem Teilchen-Spektrum enthalten. Das DP ist ein wohlmotivierter Kandidat für neue Physik, da es als Mediator zwischen dem Standard Modell (SM) und dem DS dienen kann, aber es darüber hinaus auch an sich eine reichhaltige Phänomenologie bereithält. Diese reicht von den indirekten (“oblique”) Korrekturen zu elektroschwachen Präzisionsobservablen (EWPO) für hohe DP-Massen hin zum subtilen Einfluss auf den Elektromagnetismus (EM). Diese Dissertation wird eine Einleitung zur konventionellen Kopplung des DP zur vollen, elektroschwachen Theorie durch die sogenannte kinetische Mischung bieten. Wir werden desweiteren mögliche Verallgemeinerungen dieser Mischung diskutieren, d.h. durch die Masse des Z-Bosons oder durch den Stückelberg-Mechanismus. Wir werden zeigen, wie ein leichtes DP von den Observablen an Teilchenbeschleunigern entkoppelt und, dass die kinetische Mischung mit dem Elektromagnetismus als Niedrig-Energie-Theorie aus der Mischung mit dem Hyperladungs-Boson hervorgeht.

Diese Mischung mit dem Photon ermöglicht nicht-triviale Effekte des DP in einem Plasma aus SM-Teilchen. Wir werden diese bekannten Plasma-Effekte nutzen, um den Fluss an solaren DP zu berechnen, der aus dem Plasma an Elektronen in der Sonne hervorgeht. Im Gegensatz zum Großteil der Fachliteratur werden wir uns die Winkelverteilung des solaren Flusses der DP genauer ansehen und die Vorteile aufzeigen, die die Anwendung dieser zusätzlichen Information auf Helioskop-Suchen nach DP bietet. Auf Grundlage von Hinode XRT-Daten, einem Teleskop zur Beobachtung der solaren Röntgenstrahlung, zeigen wir, dass die Verstärkung der Sensitivität signifikant sein kann. Diese Beobachtung ist von Interesse im Kontext zukünftiger Helioskop-Experimente, was auch in kurzen Zügen im Rahmen dieser Dissertation diskutiert wird.

Der zweite Teil dieser Dissertation wird sich dann auf das Rätsel der dunklen Materie konzentrieren und dabei die mögliche Rolle des DP as DM-Kandidaten herausstellen. Nach einer kurzen Einführung in dieses Thema, werden wir die LISA Pathfinder (LPF) Mission als Experiment zur direkten Detektion von ultra-leichter DPDM indentifizieren. Im Stile eines “No-go-Theorem” zeigen wir, dass LPF nicht in der Lage ist, kinetisch gemischte DP zu detektieren. Dieses Ergebnis ist zu einem gewissen Grad universal und damit anwendbar auf andere Experimente. Dennoch demonstrieren wir, dass LPF ein interessantes Instrument ist, um “verallgemeinerte DP” zu untersuchen, d.h. DP die unter globalen Symmetrien des SM geeicht sind mit $B-L$ als Beispiel. Wir zeigen auf, dass die Nebenkanäle von LPF ein mächtiges Werkzeug darstellen, ein Signal der dunklen Materie zu entdecken. Dabei betonen wir, warum diese Suche den Erwartungen nach besser als eine Suche mithilfe des Hauptkanals ist. Desweiteren wird diskutiert, wie man dieses Ergebnis in vertiefender Arbeit weiterführen kann.

List of publications

This thesis is based on the following publications:

[1] J. Frerick, F. Kahlhoefer, and K. Schmidt-Hoberg, *A' view of the sunrise: boosting helioscopes with angular information*, *JCAP* **03** (2023) 001, [`arXiv:2211.00022`]

[2] J. Frerick, J. Jaeckel, F. Kahlhoefer, and K. Schmidt-Hoberg, *Riding the dark matter wave: Novel limits on general dark photons from LISA Pathfinder*, *Phys. Lett. B* **848** (2024) 138328, [`arXiv:2310.06017`]

The following additional publication was completed during the time of this thesis but will not be discussed:

[3] T. Emken, J. Frerick, S. Heeba, and F. Kahlhoefer, *Electron recoils from terrestrial upscattering of inelastic dark matter*, *Phys. Rev. D* **105** (2022), no. 5 055023, [`arXiv:2112.06930`]

List of abbreviations

ALP	Axion-like particle
ASD	amplitude spectral density
BBN	Big Bang Nucleosynthesis
BSM	beyond the Standard Model of particle physics
C.L.	confidence level
CMB	cosmic microwave background
CR	control region
DESI	Dark Energy Spectroscopic Instrument
DM	dark matter
DN	data number
DOF	degree of freedom
DP	Dark Photon
DPDM	Dark Photon dark matter
DS	dark sector
EM	electromagnetic/electromagnetism
EOM	equation of motion
EOS	equation of state
EP	equivalence principle
ET	Einstein Telescope
EW	electroweak
EWPO	electroweak precision observables
EWSB	electroweak symmetry breaking
FOV	field of view
IGM	intergalactic medium
KAGRA	Kamioka Gravitational Wave Detector
LHS/RHS	left-hand side/right-hand side
LIGO	Laser Interferometer Gravitational-Wave Observatory
LISA	Laser Interferometer Space Antenna
l.o.s.	line of sight
LPF	LISA Pathfinder *(see LISA)*
LSW	light shining through the wall
LVK	LIGO/Virgo/KAGRA
MACHO	massive astrophysical compact halo object
PBH	primordial black hole
SC	space craft
SIDM	self-interacting dark matter
SM	Standard Model of particle physics
SNR	signal-to-noise ratio
SUSY	supersymmetry
TM	test mass
WIMP	weakly interacting massive particle
XRT	X-ray telescope

Contents

1 Introduction

> Steal the lights from our eyes
> Take my blood from my heart
> We're in all of this dark matter
> Take the breaths from my chest
> Take the thoughts from my mind
> We're losing time, dark matter
>
> *Dark Matter*
> PEARL JAM

The observationally confirmed existence of Dark Matter (DM) is a long-standing puzzle in modern physics [4]. Although we have convincing evidence from both cosmology and astronomy, we are still left with many fundamental questions:

- Is DM a new particle beyond the Standard Model (BSM) of particle physics?
- If it is a particle, how was it produced?
- Why haven't we seen it in direct detection?
- Why haven't we found any (non-gravitational) traces in astrophysical observations
- Why haven't we observed it at colliders?

This list is far from exhaustive and in fact, this thesis can focus only on some aspects of the DM puzzle. The arguments for particle DM are considered convincing by most of the community, and we will adhere to this paradigm. While there is broad consent on the particle nature of DM[1] the basic properties of this particle, let alone the question if it is just a single species, are essentially completely unknown. This invites us to speculate about this particle, motivated both by theoretical considerations and observational or experimental hints. For many years, the so-called Weakly Interacting Massive Particle (WIMP) has been the main paradigm for DM searches and theory work [6]. Indeed, the theoretical need to overcome the hierarchy problem which in some formulations predicts particles at or above the electroweak scale together with sizeable couplings delivered an almost perfect DM candidate. This “coincidence” was therefore labelled the WIMP miracle and motivated a still-lasting experimental programme to search for direct and indirect signals of DM, as well as for direct production at accelerators.

Despite their theoretical motivation, all these searches have not found convincing evidence to date, although several hints have appeared (and disappeared) over time [7, 8]. This has brought the community to broaden the scope of the searches for other DM candidates. While the WIMP was and maybe still is leading among the very well-motivated and most sought-after DM candidates, parts of this community have experienced a paradigm shift towards lighter and more feebly interacting particles. A big role in the motivation of such DM candidates is played by the axion which, similar to the WIMP, comes with a

---

[1] Note that primordial black holes (PBHs) [5] are a valid non-particle DM (sub-component) candidate.

strong theory motivation, this time solving the strong CP problem [9–11]. It has opened up the path for a plethora of light and ultra-light DM candidates.

Nowadays, the list of DM candidates is very long [12] and even a discovery of a non-gravitational signal of DM might not immediately give away the identity of the particle.[2] In this thesis, we will focus especially on a single yet broad class of BSM particles, the dark photon[3] (DP) [19, 21–23] or its generalisations [20, 24, 25]. This model receives intriguing motivations from string theory [26–28] which predicts weakly coupled and potentially extremely light new vector bosons. Beyond this deep theory motivation, it is, in general, an interesting particle as a mediator to an extended dark sector, which can range from simple setups such as millicharged particles [29, 30] to complex sectors such as a mirror dark sector [31, 32].

These arguments motivate a thorough investigation of the DP as a BSM candidate. Due to the broad applicability of the DP in dark sector setups, we will restrict the scope of this thesis to certain aspects of the DP model. Throughout this thesis, the main focus will lie mostly on lighter DPs, i.e. way below the electroweak (EW) scale. In general, heavier DPs are often also referred to as Z' since their phenomenology will resemble more the Z boson than the photon. With this concluding remark, we will now give a brief overview of the structure of this thesis.

We will first give an extensive discussion of the standard DP in chapter 2. We will introduce the so-called kinetic mixing of the DP with the standard model $U(1)_Y$ of the hypercharge and consider the consequences. Furthermore, we will discuss different mixing terms that are not as prevalent in the literature. These additional terms will be studied using electroweak physics to understand the similarities and differences with the DP literature standard. According to the general theme of this thesis, we will then investigate the low-energy behaviour in greater detail. Furthermore, we will have a brief discussion on millicharges. Applying our findings in chapter 3, we will then fully turn to this low-energy regime and discuss solar DP production in general and more specifically study in detail the angular distribution of solar DPs. We will show how this can boost the detection prospects using data from the space-based x-ray telescope Hinode XRT. This chapter will also contain a brief discussion of plasma effects that drastically change the phenomenology of the DP inside the Sun. Following up, chapter 4 will give a concise introduction to the most important aspects of Dark Matter, specifically ultra-light DM. We will begin with a historical overview of how we inferred the existence of DM. Then we will quickly glance at the WIMP miracle as the methodology is interesting for the thermal production of DPs from the SM bath of the early Universe, hinting for the first time at Dark Photon Dark Matter (DPDM). Finally, we will sketch the idea behind wave DM, having in mind ultra-light DPs as DM candidates, even though some aspects of the discussion are more general. Chapter 5 will follow up on this by focussing completely on the DP in the ultra-light regime; more specifically, we will scrutinise an interesting aspect of direct detection for DPDM using gravitational wave observatories. We will discuss the phenomenology of this concept, explaining the concept of a “general” DP and deriving different signals in the process. We will then describe a novel approach and show how this can improve previous analyses. The end of this thesis is marked with a conclusion in chapter 6 which summarises the findings of the research carried out during this thesis. Throughout this thesis, we work in natural units $\hbar = c = 1$ if not mentioned otherwise.

---

[2] While this statement can be considered speculative, the many explanations brought forward for the XENON1T excess indicate that a single signal will leave much room for different DM candidates [3, 13–18].

[3] Also referred to as paraphoton [19] or hidden photon [20].

2 The Dark Photon

> Karma Police, arrest this man
> He talks in maths
> He buzzes like a fridge
> He's like a detuned radio
>
> *Karma Police*
> RADIOHEAD

This chapter of the thesis will introduce and discuss the DP in-depth, beginning by introducing the basic Lagrangian and subsequent analysis of mass and interaction eigenstates. From there it is very natural to discuss electroweak precision observables (EWPO) and comment on the vast literature. We will then go to the usual low-energy regime, where all effects except for photon-mixing are irrelevant. While this leads to rather simple vacuum behaviour, the introduction of matter effects leads to a plethora of interesting phenomena like low mass decoupling and resonant production. This is the foundation of the later chapter 3 on solar production and angular distributions. Furthermore, it is of great importance for the understanding of the potential couplings of general DPs as ultralight DM in chapter 4 & 5. However, this chapter will mainly focus on heavier DPs, heavy here typically referring to masses above the electron-positron pair threshold at around 1 MeV.

2.1 From kinetic mixing to the mass eigenbasis

The dark photon is a new vector boson added to the particle content of the standard model of particle physics (SM). It is one of only three renormalisable portals between the SM and a potential dark sector (DS). These three portals are

1. The vector or DP portal: $-\frac{\epsilon}{2}F'_{\mu\nu}F^{\mu\nu}$ with new vector boson A'_μ
2. The Higgs portal: $\epsilon\phi^2|H|^2$ or $\epsilon|\phi|^2|H|^2$ with a new real/complex scalar ϕ (In case of a real singlet field ϕ one can also add terms linear in ϕ like $m_\epsilon\phi|H|^2$)
3. The neutrino portal: ϵLHN_R with a new fermion (right handed neutrino) N_R .

Furthermore, we have introduced a generic dimensionless coupling ϵ that connects the visible sector and dark sector, and we used the standard notation H, $F_{\mu\nu} = \partial_\mu A_\nu - \partial_\nu A_\mu$, and L for the SM Higgs boson, the electromagnetic (EM) field strength tensor of the photon A_μ, and L for the leptonic $SU(2)$ doublet. These are the only mass dimension 4 terms that allow the coupling of new particles to the SM without explicitly charging new particles under the SM $SU(3) \times SU(2) \times U(1)$ gauge group or charging the SM particles under a new dark gauge group.

During this thesis, we will completely focus on the vector portal even though there is a natural and close connection to the Higgs portal in case of a dark Higgs origin of the DP mass. We will discuss the differences of the mass terms later in this chapter. In the case of the DP portal, we call ϵ the kinetic mixing parameter. This name of course derives from the fact that the mixing term combines the kinetic terms of the pure/unmixed $U(1)$s. It is important to point out that this mixing term can only be gauge invariant for the mixing of two $U(1)$s because only in that setup, the field strength tensor in itself is already gauge invariant. Put simply, in non-abelian gauge groups the gauge bosons itself are charged and thus a mixed term of field strength tensors cannot be gauge invariant.[1]

Introduction of kinetic mixing

We will now start from a general Lagrangian including only kinetic mixing and we will gradually build up an intuition for the physical effect on SM observables while we increase the complexity of the mixing.

We start by writing down the most general gauge invariant dark photon Lagrangian before electroweak symmetry breaking (EWSB),

$$\begin{aligned}\mathcal{L} = &-\frac{1}{4}\left(B_{\mu\nu}, W^3_{\mu\nu}, X_{\mu\nu}\right)\begin{pmatrix}1 & 0 & \epsilon_B\\ 0 & 1 & 0\\ \epsilon_B & 0 & 1\end{pmatrix}\begin{pmatrix}B^{\mu\nu}\\ W^{3\mu\nu}\\ X^{\mu\nu}\end{pmatrix} + \frac{1}{2}\left(B_\mu, W^3_\mu, X_\mu\right)\mathbf{M}\begin{pmatrix}B^\mu\\ W^{3\mu}\\ X^\mu\end{pmatrix}\\ &-\left(g_1\, j^Y_\mu, g_2\, j^3_\mu, g_x\, j^x_\mu\right)\begin{pmatrix}B^\mu\\ W^{3\mu}\\ X^\mu\end{pmatrix}, \end{aligned} \tag{2.1}$$

where ϵ_B is the kinetic mixing parameters between the dark photon[2] X and the hypercharge mediator B. The neutral component of the SU(2) triplet W^3 retains its couplings and does not experience any mixing if we demand gauge invariance. For our analysis, we can ignore $W^\pm$ because neither their mass nor their couplings will be modified. Once we move to the phase after EWSB, the (tree-level) mass matrix is given by

$$\mathbf{M} = \frac{v^2}{4}\begin{pmatrix} g_1^2 & -g_1\, g_2 & 0\\ -g_1\, g_2 & g_2^2 & 0\\ 0 & 0 & \frac{4\, M_X^2}{v^2}\end{pmatrix}. \tag{2.2}$$

Assuming that the DP mass does not come from the SM Higgs, we can find $\mathbf{M}$ in the unbroken phase by sending $v \to 0$.

For now, we have neglected additional mass mixing terms that are sometimes introduced between W^3 and X which will be discussed later. Furthermore, we will comment on the so-called Stückelberg mixing in the next subsection, where we give a brief explanation of the Stückelberg mechanism and show that the mixing that can be induced from this source can be absorbed into the kinetic mixing parameter ϵ_B.

For interactions with fermions, we have added the hypercharge, weak isospin[3], and potential dark[4] currents j^Y_μ, j^3_μ, and j^x_μ, respectively, which come with their corresponding gauge couplings.

Towards a different basis

This basis is not well suited for the typical QFT toolkit as the mass and kinetic terms are non-canonical. Our aim will now be to move to another basis which provides more insights.

---

[1] If one goes beyond the renormalisable level non-abelian kinetic mixing can play a role [33, 34].

[2] We previously introduced the dark photon via the more standard notation A'. We will now opt for this new notation to avoid confusion and to make clear that the mixing is actually with the $U(1)$ of hypercharge and not of electromagnetism.

[3] Here we have singled out the current coupled to the neutral component of the triplet.

[4] Note that in principle this dark current can contain both SM and BSM particles.

Finally, we will from now on assume that the bare DP mass is below the bare SM vector boson masses, i.e. the W and Z masses.[5]

We can bring the kinetic terms of the bosons defined by the matrix $\mathcal{K}$, i.e. the first matrix in eq. (2.1), into canonical form via $G^T\mathcal{K}G = \mathbf{I}$ using the non-unitary field redefinition,

$$G = \begin{pmatrix} \dfrac{1}{\sqrt{1-\epsilon_B^2}} & 0 & 0 \\ 0 & 1 & 0 \\ -\dfrac{\epsilon_B}{\sqrt{1-\epsilon_B^2}} & 0 & 1 \end{pmatrix} . \tag{2.3}$$

The most elegant way to see this invokes the Cholesky decomposition of a real, symmetric, positive-definite matrix.[6] We see immediately that, by definition, we have the freedom to rotate $G \to GO$ where O is an orthogonal matrix. We will use this important property to diagonalise the mass matrix while keeping the kinetic term canonical.

Simply applying the same transformation that brings the kinetic term to canonical form has the following effect on the mass matrix

$$\tilde{\mathbf{M}} = G^T\mathbf{M}G = \frac{v^2}{4}\begin{pmatrix} \frac{g_1^2+4\epsilon_B^2\frac{M_X^2}{v^2}}{1-\epsilon_B^2} & -\frac{g_1\,g_2}{\sqrt{1-\epsilon_B^2}} & -\frac{\epsilon_B}{\sqrt{1-\epsilon_B^2}}\frac{4\,M_X^2}{v^2} \\ -\frac{g_1\,g_2}{\sqrt{1-\epsilon_B^2}} & g_2^2 & 0 \\ -\frac{\epsilon_B}{\sqrt{1-\epsilon_B^2}}\frac{4\,M_X^2}{v^2} & 0 & \frac{4\,M_X^2}{v^2} \end{pmatrix} \tag{2.4}$$

$$= \frac{v^2}{4}\begin{pmatrix} \tilde{g_1}^2+4\alpha^2\tilde{\mu}^2 & -\tilde{g_1}\,g_2 & -4\alpha\tilde{\mu}^2 \\ -\tilde{g_1}\,g_2 & g_2^2 & 0 \\ -4\alpha\tilde{\mu}^2 & 0 & 4\tilde{\mu}^2 \end{pmatrix} , \tag{2.5}$$

where we have defined $\tilde{\mu}^2 \equiv M_X^2/v^2$, $\tilde{g_1} \equiv g_1/\sqrt{1-\epsilon_B^2}$, and $\alpha \equiv \epsilon_B/\sqrt{1-\epsilon_B^2}$ for convenience. This basis makes one thing apparent: if the DP was massless, we see that, except for a simple rescaling of the couplings, there is no effect on the EW physics, i.e. $M_X \to 0$ and $g_1 \to g_1/\sqrt{1-\epsilon_B^2}$. Before we proceed, let us do another helpful rotation that will make the following steps more intuitive. It is based on using the upper instead of the lower triangle matrix for the non-unitary transformation. Using

$$O = \begin{pmatrix} \frac{1}{\sqrt{1+\alpha^2}} & 0 & -\frac{\alpha}{\sqrt{1+\alpha^2}} \\ 0 & 1 & 0 \\ \frac{\alpha}{\sqrt{1+\alpha^2}} & 0 & \frac{1}{\sqrt{1+\alpha^2}} \end{pmatrix} \tag{2.6}$$

$$\Rightarrow G' = GO = \frac{v^2}{4}\begin{pmatrix} 1 & 0 & -\frac{\epsilon_B}{\sqrt{1-\epsilon_B^2}} \\ 0 & 1 & 0 \\ 0 & 0 & \frac{1}{\sqrt{1-\epsilon_B^2}} \end{pmatrix} , \tag{2.7}$$

---

[5] For most of the following steps this is not strictly necessary but we will see that some of the expressions will not be well-defined otherwise.

[6] The last condition breaks down for $\epsilon_B \geq 1$. Furthermore, we could have chosen an upper triangle matrix which would technically be beneficial for notation but we will go with this setup as it allows us to connect more elegantly to our later consideration of Stückelberg mixing, c.f. subsection 2.1.1.

is the conventional approach for bringing the kinetic term into canonical form, c.f. the remark above. Applying this new transformation to the mass matrix yields

$$\tilde{\mathbf{M}}' = O^T \tilde{\mathbf{M}} O = \frac{v^2}{4} \begin{pmatrix} g_Y^2 & -g_Y\, g_2 & -\alpha g_Y^2 \\ -g_Y\, g_2 & g_2^2 & \alpha g_Y\, g_2 \\ -\alpha g_Y^2 & \alpha g_Y\, g_2 & \alpha^2 g_Y^2 + 4\mu'^2 \end{pmatrix} , \tag{2.8}$$

where we have rewritten[7] $g_Y \equiv \tilde{g}_1/\sqrt{1+\alpha^2} = g_1$ and $\mu' = \tilde{\mu}\sqrt{1+\alpha^2}$. We see now why it can be considered favourable to work in this basis. The EW 2-by-2 part is restored to canonical form and thus invites us to define a (pseudo-)Weinberg angle.[8]

We can now change to what is often called the "physical" basis[9], in which the gauge boson mass matrix is diagonal, by two consecutive rotations,

$$R_1(\theta_W) = \begin{pmatrix} \cos\theta_W & -\sin\theta_W & 0 \\ \sin\theta_W & \cos\theta_W & 0 \\ 0 & 0 & 1 \end{pmatrix} , \tag{2.9a}$$

$$R_2(\xi) = \begin{pmatrix} 1 & 0 & 0 \\ 0 & \cos\xi & -\sin\xi \\ 0 & \sin\xi & \cos\xi \end{pmatrix} , \tag{2.9b}$$

where the first rotation defines the (pseudo-)Weinberg angle θ_W and the second rotation diagonalises the $Z - X$ block of the mass matrix.

Due to our clever choice of $\tilde{\mathbf{M}}'$, the first rotation can diagonalise the upper left 2-by-2 (EW) matrix following the usual conventions, i.e. $\cos\theta_W = g_2/(g_Y^2 + g_2^2)^{1/2}$. The resulting mass matrix will now be

$$\mathbf{M}_{\mathrm{EW}} = R_1^T \tilde{\mathbf{M}}' R_1 = \frac{v^2}{4} \begin{pmatrix} 0 & 0 & 0 \\ 0 & g_Y^2 + g_2^2 & \alpha g_Y \sqrt{g_Y^2 + g_2^2} \\ 0 & \alpha g_Y \sqrt{g_Y^2 + g_2^2} & \alpha^2 g_Y^2 + 4\mu'^2 \end{pmatrix} \tag{2.10}$$

$$= \tilde{M}_Z^2 \begin{pmatrix} 0 & 0 & 0 \\ 0 & 1 & \alpha \sin\theta_W \\ 0 & \alpha\sin\theta_W & \alpha^2 \sin^2\theta_W + \mu^2 \end{pmatrix} , \tag{2.11}$$

where we have defined the usual Z mass $\tilde{M}_Z = \sqrt{g_Y^2 + g_2^2}\,v/2$ as well as $\mu = \mu' v/\tilde{M}_Z$. Due to the many redefinitions required to keep the matrix notation minimal, we present a table with all relevant definitions in table 2.1 based only on the fundamental parameters from eq. (2.1). This result demonstrates that indeed, two orthogonal transformations are enough as we are left with only the lower right 2-by-2 components being non-diagonal. This follows intuitively from the fact that we only introduced one new coupling to the EW sector ϵ_B initially, which can be fully described by a single rotation angle which, together with the Weinberg angle, makes two rotation angles in total. We make the additional observation that the vanishing diagonal component of $\mathbf{M}_{\mathrm{EW}}$ will not be altered by the final rotation. Thus, we will at least have one massless particle, which of course corresponds to the photon which we expect to not receive a mass since we do not break electromagnetism.

---

[7] This seemingly unnecessary complication arises due to "Stückelberg-friendly" rewriting of the mass matrix in eq. (2.4). In the case of Stückelberg mixing, the relation between α and ϵ_B is modified, thus $g_Y \neq g_1$. The details can be found in the following subsection 2.1.1.

[8] We will see later that this will not necessarily be the Weinberg angle that we know from the SM.

[9] Of course, different bases are equivalent to each other and labelling one as physical is technically not ideal but due to our intuitive understanding of particles with well-defined masses, this is a particularly useful parametrisation.

Parameter	Definition (KM)	Definition (MM)	Definition (StM)
$\tilde{\mu}$	$\frac{M_X}{v}$	$\frac{M_X}{v}$	$\frac{M_X}{v}$
δ_m	not defined	not defined	$\frac{m_Y}{M_X}$
$\tilde{g}_1$	$\frac{g_1}{\sqrt{1-\epsilon_B^2}}$	$\frac{g_1}{\sqrt{1-\epsilon_B^2}}$	$\frac{g_1}{\sqrt{1-\epsilon_B^2}}$
α	$\frac{\epsilon_B}{\sqrt{1-\epsilon_B^2}}$	$\frac{\epsilon_B}{\sqrt{1-\epsilon_B^2}}$	$\frac{\epsilon_B-\delta_m}{\sqrt{1-\epsilon_B^2}}$
g_Y	$\frac{\tilde{g}_1}{\sqrt{1+\alpha^2}} = g_1$	$\frac{\tilde{g}_1}{\sqrt{1+\alpha^2}} = g_1$	$\frac{\tilde{g}_1}{\sqrt{1+\alpha^2}} \neq g_1$
μ'	$\tilde{\mu}\sqrt{1+\alpha^2}$	$\tilde{\mu}\sqrt{1+\alpha^2}$	$\tilde{\mu}\sqrt{1+\alpha^2}$
$\cos\theta_W$	$\frac{g_2}{\sqrt{g_Y^2+g_2^2}}$	$\frac{g_2}{\sqrt{g_Y^2+g_2^2}}$	$\frac{g_2}{\sqrt{g_Y^2+g_2^2}}$
$\tilde{M}_Z$	$\frac{\sqrt{g_Y^2+g_2^2}v}{2}$	$\frac{\sqrt{g_Y^2+g_2^2}v}{2}$	$\frac{\sqrt{g_Y^2+g_2^2}v}{2}$
μ	$\mu'\frac{v}{\tilde{M}_Z}$	$\mu'\frac{v}{\tilde{M}_Z}$	$\mu'\frac{v}{\tilde{M}_Z}$
δM^2	not defined	$\delta\tilde{M}^2\sqrt{1+\alpha^2}$	not defined

Table 2.1: Definition of the auxiliary variables defined throughout this chapter. If necessary, we distinguish between setups with kinetic mixing (KM), Z-mass mixing (MM), and Stückelberg mixing (StM).

The mass eigenbasis

To bring us into the desired diagonal form, we need the following rotation angle ξ

$$\tan(2\xi) = \frac{2g_Y\sqrt{g_Y^2+g_2^2}\alpha}{g_Y^2+g_2^2-\alpha^2 g_Y^2-4\mu'^2} \tag{2.12}$$

$$= \frac{2\sin\theta_W\alpha}{1-\alpha^2\sin^2\theta_W-\mu^2}\,. \tag{2.13}$$

With this definition, we have all the tools to describe the entire physics of our model. Based on our initial parameters, i.e. the usual EW couplings and the vev as well as the DP mass and mixing, we can go to the mass eigenbasis and find the corresponding masses and couplings in this basis.

We can gain further insight by considering the ultralight and weakly coupled DP limit, i.e. $\mu \ll \alpha \ll 1$. We find the following expressions

$$\tan(2\xi) \approx 2\sin\theta_W\alpha \Rightarrow \xi \approx \sin\theta_W\alpha \tag{2.14}$$

These expressions are valid to quadratic order in α and neglect the DP mass completely. In this limit, we see that there is just a linear relation between the mixing parameter and the additional rotation angle. On the other hand, we might also be interested in the limit of small mixing and non-negligible (bare) DP mass

$$\tan(2\xi) \approx \frac{2\sin\theta_W \alpha}{1-\mu^2} \Rightarrow \xi \approx \frac{\sin\theta_W \alpha}{1-\mu^2} \, . \tag{2.15}$$

This shows that there is an impact on the physics by the DP mass and we realise that, in agreement with our intuition, a small mixing parameter still leads to a decoupling even for sizeable DP masses.

Finally, we should evaluate the mass eigenvalues. As argued above, one of the three masses will vanish. We will define the corresponding particle as the photon γ. Of the massive particle, the weakly coupled one will be the DP while the strongly coupled vector boson corresponds to the Z

$$m_1 = m_\gamma = 0 \tag{2.16a}$$

$$m_2 = m_Z = \tilde{M}_Z \sqrt{(\cos\xi + \alpha\sin\theta_W \sin\xi)^2 + \sin^2\xi\mu^2} \tag{2.16b}$$

$$m_3 = m_{\mathrm{DP}} = \tilde{M}_Z \sqrt{(\sin\xi - \alpha\sin\theta_W \cos\xi)^2 + \cos^2\xi\mu^2} \, . \tag{2.16c}$$

A brief look at the definitions shows that for vanishing mixing $\alpha \to 0$, we will restore the bare DP and Z masses as the physical masses. Let us also look at the expansion in small mixing parameters but keeping μ arbitrary[10]

$$m_Z \approx \tilde{M}_Z \left(1 + \frac{\alpha^2 \sin^2\theta_W}{2\,(1-\mu^2)}\right) \tag{2.17}$$

$$m_{\mathrm{DP}} \approx \tilde{M}_Z \mu \left(1 - \frac{\alpha^2 \sin^2\theta_W}{2\,(1-\mu^2)}\right) \, , \tag{2.18}$$

which makes the aforementioned conversion to bare masses more explicit. All corrections to the masses will be at least quadratic in the mixing parameter of choice (α or ϵ_B). As we usually consider small mixing, we see that it is favourable to consider observables linear in the mixing. However, we will see that also the electroweak precision observables treated in the next section suffer from the same quadratic suppression.

Finally, let us point out a seemingly confusing observation: eq. (2.16b) suggests that the mass of the Z boson is modified no matter how light the DP is. This seems naively in conflict with the observation that a massless DP decouples completely from the visible/EW sector. We will solve this apparent contradiction in the following sections.

2.1.1 A note on the Stückelberg mechanism and Stückelberg mixing

Before we begin, as promised, to look at the phenomenological consequences of more general mixing, we need to discuss a mass generation mechanism that is often invoked for DPs.

Mass generation via the Stückelberg mechanism [35, 36] is a simple and elegant way to circumvent the existence of a (potentially) light scalar in the particle spectrum that emerges from the $U(1)$ breaking that generates the DP mass via the Higgs mechanism [37]. In general, these scalars have been shown to dominate the phenomenology in most of the parameter space due to various effects [38–40].

Therefore, it is desirable to have a setup in which one can confidently focus on just the effect of DPs. This can also be considered to be a more model-independent approach as one can always consider limits both from purely vectorial or purely scalar effects for a chosen model and focus on just the leading limit.

---

[10] It is extremely important to note that the region of equal/similar DP and Z masses is more tricky to handle and the formulae are in general only valid for light DPs (w.r.t. the Z boson). Nevertheless, it is in principle possible to cover heavy DPs as well.

Sketch of the mechanism

The Stückelberg mechanism provides such a "scalar-free" setup. Thus, focussing solely on the DP without any additional dark Higgs is not a simplification, since there exists a mechanism that naturally provides us with such a scenario. Let us start with the simplest possible DP-only Lagrangian[11]

$$\mathcal{L} = -\frac{1}{4}F_{\mu\nu}F^{\mu\nu} - g_{\mathrm{DP}}A_\mu j^\mu + \frac{1}{2}m^2 A^\mu A_\mu \ . \tag{2.19}$$

This Lagrangian seems to violate our notion of gauge invariance, which requires a transformation of the type $A_\mu \to A_\mu + \partial_\mu \alpha$ to leave the Lagrangian unchanged. As a first step towards seeing that our Lagrangian can be made explicitly gauge-invariant without changing the physics, we observe that $A_\mu + \frac{1}{m}\partial_\mu\phi$ is invariant under the aforementioned gauge transformation if the new field simultaneously obeys a shift symmetry $\phi \to \phi - m\alpha$.

We will now make use of our freedom to redefine the dark photon field in the way suggested above. As a brief remark, we note that this redefinition leaves the kinetic term invariant due to the commutativity of the derivatives, i.e. $F_{\mu\nu} \to F_{\mu\nu} + \frac{1}{m}\left(\partial_\mu\partial_\nu - \partial_\nu\partial_\mu\right)\phi = F_{\mu\nu}$. Furthermore, we will add a gauge-fixing term $\mathcal{L}_{\mathrm{gf}} = -(2\xi)^{-1}\left(\partial^\mu A_\mu + \xi m\phi\right)^2$ which also is invariant under the gauge transformation assuming that the gauge field obeys $\left(\partial_\mu\partial^\mu - \xi m^2\right)\alpha = 0$.[12] This produces a Lagrangian of the form[13]

$$\begin{aligned}
\mathcal{L} &= -\frac{1}{4}F_{\mu\nu}F^{\mu\nu} - g_{\mathrm{DP}}A_\mu j^\mu + \frac{1}{2}m^2\left(A^\mu + \frac{1}{m}\partial^\mu\phi\right)^2 - \frac{1}{2\xi}\left(\partial^\mu A_\mu + \xi m\phi\right)^2 && (2.20)\\
&= -\frac{1}{4}F_{\mu\nu}F^{\mu\nu} - g_{\mathrm{DP}}A_\mu j^\mu + \frac{1}{2}m^2 A^\mu A_\mu - \frac{1}{2\xi}(\partial_\mu A^\mu)^2 + \frac{1}{2}\partial_\mu\phi\partial^\mu\phi - \frac{1}{2}\xi m^2\phi^2 && (2.21)\\
&= \mathcal{L}_{\mathrm{vector}} + \mathcal{L}_{\mathrm{scalar}} \ , && (2.22)
\end{aligned}$$

where we have used partial integration to eliminate the $\phi - A$ cross term. We observe that this is the sum of the Lagrangian for a gauge-fixed, massive, and interacting gauge boson ($\mathcal{L}_{\mathrm{vector}}$) and the Lagrangian of a massive free scalar ($\mathcal{L}_{\mathrm{scalar}}$). This already indicates that the scalar will not influence the DP physics. Additionally, we get a gauge-dependent mass for the scalar which further provides evidence for the decoupling of the scalar from DP physics. As an important note, we have to mention that this mechanism is only valid for abelian symmetries even though there have been attempts to generalise the concept [41]. Let us conclude this brief explanation of the Stückelberg mechanism with the analogy to the Higgs mechanism with infinitely heavy Higgs mass/vev but infinitesimally small gauge coupling which also gives an interacting DP without any scalar in the spectrum. This can be achieved via the tuning of the vev of the (dark) Higgs field, the quartic term in its potential and the gauge coupling between scalar and vector boson. Let us discuss this idea more explicitly by looking at a Higgsed $U(1)$

$$\mathcal{L}_{\mathrm{Higgs}} = -\frac{1}{4}F_{\mu\nu}F^{\mu\nu} - g_{\mathrm{DP}}A_\mu j^\mu + |D_\mu\phi|^2 - V(\phi) \ . \tag{2.23}$$

We use the usual covariant derivative $D_\mu = \partial_\mu - ig_{\mathrm{DP}}A_\mu$ and the potential is chosen to be $V(\phi) = -\mu^2|\phi|^2 + \lambda|\phi|^4$. For $\mu^2 > 0$, the symmetry is spontaneously broken so that we get

---

[11] As there is no danger of confusion in this argument, we will drop the " $'$ " for the DP fields. We will reinstate it again as soon as we deal with multiple gauge bosons.

[12] For conventional gauge-fixing, the gauge field/phase has to obey $\partial_\mu\partial^\mu\alpha = 0$.

[13] We assume that the current coupling to the DP ensures gauge invariance by charging the particles under the $U(1)$ and we further note that $-g_{\mathrm{DP}}j^\mu\partial_\mu\phi = 0$ using partial integration and current conservation $\partial_\mu j^\mu = 0$.

$\phi = (h+v)e^{i\alpha/v}/\sqrt{2}$ in unitary gauge with $v = \sqrt{\mu^2/\lambda}$ being the vev of the field.[14] This amounts to a change in the Lagrangian of the form

$$\mathcal{L}_{\text{broken}} = -\frac{1}{4}F_{\mu\nu}F^{\mu\nu} - g_{\text{DP}}A_\mu j^\mu + \frac{1}{2}(\partial_\mu h)^2 + \frac{g_{\text{DP}}^2}{2}(v+h)^2(A_\mu - \frac{1}{g_{\text{DP}}v}\partial_\mu\alpha)^2 - \tilde{V}(h) \tag{2.24}$$

$$= -\frac{1}{4}\tilde{F}_{\mu\nu}\tilde{F}^{\mu\nu} - g_{\text{DP}}\tilde{A}_\mu j^\mu + \frac{1}{2}(\partial_\mu h)^2 + \frac{g_{\text{DP}}^2}{2}(v+h)^2\tilde{A}_\mu\tilde{A}^\mu - \tilde{V}(h)\ . \tag{2.25}$$

We see that we have once again reproduced the typical DP Lagrangian via a redefinition in the second step in complete analogy to the discussion above. This is the well-known case of the would-be Goldstone boson being eaten by the vector boson which then becomes the longitudinal component of the gauge boson. We further note that the DP mass is $m_{\text{DP}} = g_{\text{DP}}v$ and the potential becomes $\tilde{V}(h) = -\frac{\lambda}{4}V^4 + \frac{2\lambda v^2}{2}h^2 + \lambda v h^3 + \frac{\lambda}{4}h^4$ where the first term is just a constant that never impacts the physics of the Lagrangian[15] and the Higgs mass is given as $m_h = \sqrt{2\lambda}v$. We can now clearly observe that we can, in principle, arrange the free parameters to have the Higgs decoupled by increasing its mass. As an example, we could assume that the charges Q inside $j^\mu \propto Q$ are very large while we send the gauge coupling to 0, i.e. $g_{\text{DP}} \to 0$ and $Q \to \infty$ with $g_{\text{DP}}Q = \text{const.} = \tilde{g}$ which means that the DP does not decouple from potential additional particles in the DS. To not make the DP arbitrarily light in this scenario, we also increase the vev so that $v \to \infty$ with $g_{\text{DP}}v = \text{const.} \equiv m_{\text{DP}}$, a choice that automatically sends $m_h \to \infty$ as long as $\lambda \lesssim \mathcal{O}(1)$. With this choice, we end up with a Lagrangian that is effectively equivalent to eq. (2.19)

$$\mathcal{L} = -\frac{1}{4}\tilde{F}_{\mu\nu}\tilde{F}^{\mu\nu} - \tilde{g}\tilde{A}_\mu\tilde{j}^\mu + \frac{1}{2}m_{\text{DP}}^2 A^\mu A_\mu\ , \tag{2.26}$$

where we have integrated out the heavy scalar so that this result is correct up to corrections that roughly go like powers of m_{DP}/m_h. In conclusion, we have shown that indeed, the Higgs mechanism is equivalent to the Stückelberg mechanism in this specific limit. Therefore, we have found additional justification to consider a DS with a massive gauge boson that is not accompanied by an additional scalar of similar mass.

No Stückelberg mass in the SM

Now that we have a sufficient understanding of the underlying mechanism, let us investigate how this mechanism can also lead to gauge-invariant and renormalisable mixing like the well-known kinetic mixing. In terms of purely theoretical aspects, i.e. respecting gauge invariance, nothing restricts us from adding a Stückelberg mass for the hypercharge boson, as it would not explicitly break the $U(1)_Y$. We will now show that this is in sharp contrast with the well-measured fact of a massless (or at least extremely light[16]) photon.

Therefore, we will demonstrate that a direct Stückelberg mass term is problematic for the EW sector even without invoking the existence of an additional DP. Adding such a mass (m_Y) to the hypercharge gauge boson will result in the following mass matrix after

---

[14] Effectively, we have rewritten the two DOFs of the complex scalar into two real scalars.

[15] This is not the case for gravity, see the discussion on the cosmological constant in chapter 4.

[16] The photon mass limit is, depending on the confidence in astrophysical/cosmological limits, constrained to be $m_\gamma \leq m_{\gamma,\text{max}}$ with $10^{-18}\,\text{eV} \gtrsim m_{\gamma,\text{max}} \gtrsim 10^{-27}\,\text{eV}$. Therefore it is still desirable to have an exactly massless photon in the theory [42–46].

EW symmetry breaking (see also Ref. [47])

$$\mathbf{M}_{\mathrm{EW}} = \frac{1}{4}\begin{pmatrix} g_1^2 v^2 + 4m_Y^2 & -g_1\, g_2 v^2 \\ -g_1\, g_2 v^2 & g_2^2 v^2 \end{pmatrix} \tag{2.27}$$

$$\Rightarrow \det\left[\mathbf{M}_{\mathrm{EW}}\right] = m_\gamma^2\, m_Z^2 = \frac{1}{16} g_1^2\, g_2^2 v^4 + \frac{1}{4} g_2^2\, m_Y^2 v^2 - \frac{1}{16} g_1^2\, g_2^2 v^4 = \frac{1}{4} g_2^2\, m_Y^2 v^2 \neq 0\ , \tag{2.28}$$

using that the determinant is equal to the product of eigenvalues.[17] Based on this simple argument, we see that the additional hypercharge mass term will be inherited by the photon, rendering it massive as well. Assuming this mass to be a small perturbation, i.e. $m_Y \ll v$, we can infer that the photon mass will be proportional to the Stückelberg mass while the Z mass will only receive a minor correction, i.e. $m_\gamma = \mathcal{O}(m_Y)$ and $m_Z = \mathcal{O}(v)$.

Stückelberg mass mixing

Now, let us investigate how a mixed Stückelberg mass, i.e. adding a DP Stückelberg term next to the hypercharge mass term, can both save us from a photon mass and simultaneously lead to interesting phenomenological aspects. We begin by introducing the following term to the EW+DP Lagrangian following Refs. [48, 49]

$$\mathcal{L} \supset -\frac{1}{2}\left(m_X X_\mu + m_{\mathrm{Y}} B_\mu + \partial_\mu \tilde{\phi}\right)^2\ , \tag{2.29}$$

where we denote the Stückelberg scalar by $\tilde{\phi}$ and follow the gauge boson notation from eq. (2.1). This scalar now has two transformations to respect, $\phi \xrightarrow{i} \phi - m_i \alpha_i$ with $i \in [\mathrm{DP}, Y]$. This clearly shows that the expression above is gauge invariant. We will now ignore the scalar as argued above and consider the cross-term between the two gauge bosons induced by this term. This modifies the mass matrix in eq. (2.2) resulting in

$$\mathbf{M} = \frac{v^2}{4}\begin{pmatrix} g_1^2 + \frac{4m_{\mathrm{Y}}^2}{v^2} & -g_1\, g_2 & \frac{4m_{\mathrm{Y}} m_X}{v^2} \\ -g_1\, g_2 & g_2^2 & 0 \\ \frac{4m_{\mathrm{Y}} m_X}{v^2} & 0 & \frac{4\, m_X S^2}{v^2} \end{pmatrix} . \tag{2.30}$$

Applying now the transformation from eq. (2.3) and defining $m_{\mathrm{Y}} = \delta_m m_X$ we obtain

$$\mathbf{M} \rightarrow G^T \mathbf{M} G = \frac{v^2}{4}\begin{pmatrix} \frac{g_1^2 + 4(\delta - \epsilon_B)^2\, \frac{m_X^2}{v^2}}{1-\epsilon_B^2} & -\frac{g_1\, g_2}{\sqrt{1-\epsilon_B^2}} & \frac{(\delta_m - \epsilon_B)}{\sqrt{1-\epsilon_B^2}}\frac{4\, m_X^2}{v^2} \\ -\frac{g_1\, g_2}{\sqrt{1-\epsilon_B^2}} & g_2^2 & 0 \\ \frac{(\delta_m - \epsilon_B)}{\sqrt{1-\epsilon_B^2}}\frac{4\, m_X^2}{v^2} & 0 & \frac{4\, m_X^2}{v^2} \end{pmatrix} . \tag{2.31}$$

While many expressions here look rather convoluted, we realise that the definitions

$$\frac{\epsilon_B'}{\sqrt{1-\epsilon_B'^2}} = -\frac{\delta_m - \epsilon_B}{\sqrt{1-\epsilon_B^2}} \tag{2.32a}$$

$$\frac{g_1'}{\sqrt{1-\epsilon_B'^2}} = \frac{g_1}{\sqrt{1-\epsilon_B^2}}\ , \tag{2.32b}$$

---

[17] This is just based on the two facts that $\det[AB] = \det[BA]$ and that $\mathbf{M}_{\mathrm{EW,diag}} = O^T \mathbf{M}_{\mathrm{EW}} O$ with O being an orthogonal matrix and $\mathbf{M}_{\mathrm{EW,diag}}$ the diagonal matrix with eigenvalues on the diagonal.

restores exactly the form of eq. (2.4) with $\epsilon_B \to \epsilon'_B$ and $g_1 \to g'_1$. Furthermore, we see now why it is in principle helpful to distinguish between g_1 and g_Y as in the case of additional mass mixing they are not the same even though they will coincide for $\delta_m = 0$ (c.f. footnote 7). We therefore conclude that Stückelberg mixing does not introduce any new physics effect beyond a modification of the mixing parameter and thus a description in terms of an effective kinetic mixing will suffice to capture all effects on the masses. Later on, we will discuss possible further implications for the inclusion of Z mass mixing. We note in passing that this effective parameter was also found in Ref. [50]. For clarity, we point again to the summary of definitions contained in table 2.1.

Intriguingly, these findings imply that a potential cancellation between the two types of mixing can lead to a small effective mixing parameter which is especially interesting in the context of tight constraints on the kinetic mixing. However, to the best of our knowledge, there is no known mechanism which would introduce such a cancellation. Finally, let us point out that the sign of α is not fixed in this scenario and some of the steps should be treated with more care if $\alpha < 0$ as we assumed (and will assume throughout the following sections) that $\mathrm{sgn}(\alpha) = \mathrm{sgn}(\epsilon_B) = +1$.

2.1.2 Inclusion of Z mass mixing

Before we finally discuss the phenomenological consequences, let us also consider DP-Z mass mixing. As a hint towards UV completion, this could be attributed to a DP which couples very weakly to the SM Higgs. Such an additional coupling will lead to similar behaviour as in the classical EW sector, i.e. off-diagonal mass terms between W^3, Y and the DP. Naturally, a UV completion for this will come with additional observables and complications even without considering the effects of the DP. In the spirit of model independence, we should therefore take the mass mixing as a truly free parameter that is completely independent of the bare DP and Z mass, ignoring the potential presence of additional new particles or couplings.

A new source of mixing

In this idealised setup, the kinetic terms in eq. (2.1) remain the same and so does the auxiliary matrix G. It is not really well defined what Z mixing means in this context as we have performed several rotations before, obscuring our notion of a Z boson. We will focus on the would-be Z which means that we need to reweight the off-diagonal components so that after transforming the kinetic term to canonical form and rotating the EW 2-by-2 matrix, the would-be photon does not mix with the would-be DP. For this, we write in full generality

$$\mathbf{M}_Z = \frac{v^2}{4} \begin{pmatrix} g_1^2 & -g_1\,g_2 & -c_1 \frac{4\delta\tilde{M}^2}{v^2} \\ -g_1\,g_2 & g_2^2 & -c_2 \frac{4\delta\tilde{M}^2}{v^2} \\ -c_1 \frac{4\delta\tilde{M}^2}{v^2} & -c_2 \frac{4\delta\tilde{M}^2}{v^2} & \frac{4\,M_X^2}{v^2} \end{pmatrix} , \tag{2.33}$$

where we have included the new mixing parameter $\delta\tilde{M}^2$ together with two weighting factors $c_{1/2}$. Let us now follow closely our previous discussion and perform the same operation as before[18]

$$\tilde{\mathbf{M}}' = O^T G^T \tilde{\mathbf{M}}_Z G O \tag{2.34}$$

$$= \frac{v^2}{4} \begin{pmatrix} g_1^2 & -g_1\, g_2 & -\alpha g_1^2 - 4c_1\sqrt{1+\alpha^2}\frac{\delta\tilde{M}^2}{v^2} \\ -g_1\, g_2 & g_2^2 & \alpha g_1\, g_2 - 4c_2\sqrt{1+\alpha^2}\frac{\delta\tilde{M}^2}{v^2} \\ -\alpha c_1^2 - 4c_1\sqrt{1+\alpha^2}\frac{\delta\tilde{M}^2}{v^2} & \alpha g_1\, g_2 - 4g_2\sqrt{1+\alpha^2}\frac{\delta\tilde{M}^2}{v^2} & \alpha^2 g_Y^2 + 4\mu^2 \end{pmatrix}, \tag{2.35}$$

using also the same definitions as before. Once again, we can conclude that we can use the rotations R_1 and R_2 to diagonalise the mass matrix. Furthermore, R_1 can be parameterised by the same $\cos\theta_W$ as before because the upper left 2-by-2 matrix is unchanged

$$\mathbf{M}_{Z,\mathrm{EW}} = R_1^T \tilde{\mathbf{M}}' R_1 \tag{2.36}$$

$$= \tilde{M}_Z^2 \begin{pmatrix} 0 & 0 & 0 \\ 0 & 1 & \alpha\sin\theta_W + \frac{\delta M^2}{\tilde{M}_Z^2} \\ 0 & \alpha\sin\theta_W + \frac{\delta M^2}{\tilde{M}_Z^2} & \alpha^2\sin^2\theta_W + \frac{\mu^2}{\tilde{M}_Z^2} + 2\alpha\sin\theta_W\frac{\delta M^2}{\tilde{M}_Z^2} \end{pmatrix}. \tag{2.37}$$

To improve the notation, we redefined $\delta M^2 = \delta\tilde{M}^2\sqrt{1+\alpha^2}$ and we also defined $c_1 = \sin\theta_W$ and $c_2 = -\cos\theta_W$ to enforce strict Z-DP mass mixing.[19] It becomes clear that the additional mixing will at least require a change in ξ.

Modified mixing angles

Applying the second rotation R_2 we get a new expression for

$$\tan(2\xi) = \frac{2\left(\alpha\tilde{M}_Z^2\sin\theta_W + \delta M^2\right)}{\tilde{M}_Z^2\left(1-\alpha^2\sin^2\theta_W - \mu^2\right) - 2\alpha\sin\theta_W\delta M^2}. \tag{2.38}$$

Concluding this calculation, let us take a look at the expression for the mass terms

$$m_1 = m_\gamma = 0 \tag{2.39a}$$

$$m_2 = m_Z = \tilde{M}_Z\sqrt{(\cos\xi + \alpha\sin\theta_W\sin\xi)^2 + \sin^2\xi\mu^2 + 2\sin\xi\frac{\delta M^2}{\tilde{M}_Z^2}(\cos\xi + \alpha\sin\theta_W\sin\xi)} \tag{2.39b}$$

$$m_3 = m_{\mathrm{DP}} = \tilde{M}_Z\sqrt{(\sin\xi - \alpha\sin\theta_W\cos\xi)^2 + \cos^2\xi\mu^2 - 2\cos\xi\frac{\delta M^2}{\tilde{M}_Z^2}(\sin\xi - \alpha\sin\theta_W\cos\xi)}\,. \tag{2.39c}$$

It is clear from these expressions that we will recover the vanilla kinetic mixing scenario automatically if we send the mass mixing to zero, i.e. $\delta M \to 0$. We observe that the relevant (dimensionless) quantity is $\delta M/\tilde{M}_Z$ which clearly shows that mass mixing requires mixing terms not much smaller than the EW scale to have a large effect on EW physics.

---

[18] We immediately transform using GO because the transformation G was only relevant to demonstrate that Stückelberg mixing is effectively equivalent to kinetic mixing. Therefore, we will keep g_1 and refrain from using g_Y.

[19] This is equivalent to demanding that the photon remains massless as pointed out earlier, i.e. demanding that $\det[\mathbf{M}_Z] = 0$.

This thesis	Ref. [51]
ϵ_B	$\sin\chi$
α	$\tan\chi$
$\delta\tilde{M}$	$\delta\hat{M}$
δM	$\delta\hat{M}\cos^{-1/4}\chi$
$\tilde{M}_Z$	$\hat{M}_Z$
$\mu \ \left(=\sqrt{1+\alpha^2}\frac{M_X}{\tilde{M}_Z}\right)$	$\frac{\hat{M}_{Z'}}{\cos\chi\hat{M}_Z}$
$\sin\theta_W$	$\hat{s}_W$

Table 2.2: Dictionary between the present work and Ref. [51].

As we have already discussed the kinetic mixing effect on the masses in detail, let us also consider what happens for a dominant mass mixing, i.e. $\alpha \ll \delta M/\tilde{M}_Z \ll 1$

$$\tan(2\xi) \approx \frac{2\delta M^2}{\tilde{M}_Z^2\left(1-\mu^2\right)} \Rightarrow \xi \approx \frac{\delta M^2}{\tilde{M}_Z^2\left(1-\mu^2\right)}\ , \tag{2.40}$$

where we have neglected the cross term $\propto \alpha\delta M^2$. We realise that the structure is very similar to the kinetic mixing only case. For the masses instead, we find

$$m_Z \approx \tilde{M}_Z\left(1+\frac{\delta M^4}{2\tilde{M}_Z^4}\right) \tag{2.41a}$$

$$m_{\mathrm{DP}} \approx \tilde{M}_Z\mu\left(1-\frac{\delta M^4}{2\tilde{M}_Z^4\mu^2}\right)\ . \tag{2.41b}$$

Although Eq. (2.41b) is certainly valid for all values of $\mu < 1$ in our model-independent framework, we should be very careful with the interpretation of this result. Unless we invoke rather exotic physics, it seems only natural that the DP mass cannot be taken to be completely independent of the mass mixing term. As an intuitive example, we can take the EW mass mixing. If we send $g_1 \to 0$, we send the mixed mass term $g_1 g_2 \to 0$ as well. In our setup, if we now simply decrease μ, we will experience a breakdown of the perturbative expansion in $\delta M/\tilde{M}_Z$ due to problematic factors of μ^{-1}. Therefore, these results should be used only after ensuring that $\frac{\delta M}{2\tilde{M}_Z\mu} \ll 1$.

Comparison with the literature

Before concluding this section, let us reconcile our result with the well-known literature result from Ref. [51]. To be precise, we would like to prove that our eq. (2.38) is equivalent to their eq. (7). For this, we need to go back to our initial parameters and compare them to their initial Lagrangian. The translation between the different parametrisations can be found in table 2.2.

With these relations, we can write

$$\tan 2\xi = \frac{2\left(\tan\chi\hat{M}_Z^2\hat{s}_w + \frac{\delta\hat{M}^2}{\cos\chi}\right)}{\hat{M}_Z^2 - \hat{M}_Z^2\tan^2\chi\hat{s}_W^2 - \frac{\hat{M}_{Z'}^2}{\cos^2\chi} - 2\tan\chi\hat{s}_W\frac{\delta\hat{M}^2}{\cos\chi}} \tag{2.42}$$

$$= \frac{-2\cos\chi\left(\delta\hat{M}^2 + \sin\chi\hat{M}_Z^2\hat{s}_w\right)}{\hat{M}_{Z'}^2 - \hat{M}_Z^2\cos^2\chi + \hat{M}_Z^2\hat{s}_W^2\sin^2\chi + 2\sin\chi\hat{s}_W\delta\hat{M}^2}\ , \tag{2.43}$$

which exactly reproduces the literature result. At this point, we should point out that this is a remarkably simple result taking into account the plethora of parameters, including several redefinitions, and transformations that led us to this point. The fact that we required only two rotations to go from eq. (2.34) to the diagonal basis presented in eqs. (2.39a–2.39c) is a relic of enforcing one of the mass eigenstates, i.e. the photon, to be truly massless. If we allow ourselves to break the $U(1)_{\text{EM}}$ explicitly, we have to deal with the consequences of a more involved diagonalisation procedure. Thus, for theoretical and experimental reasons, we keep the photon mass strictly at zero and confine the DP phenomenology to this regime.

2.1.3 General mixing

In this brief interlude, we will generalise the previous results to the case of kinetic, Stückelberg and Z mixing. Therefore, we will merge eqs. (2.27&2.33)

$$\mathbf{M}_{\text{max}} = \frac{v^2}{4}\begin{pmatrix} g_1^2 + \frac{4m_Y^2}{v^2} & -g_1\, g_2 & -c_1\frac{4\delta\tilde{M}^2}{v^2} + \frac{4m_Y^2}{v^2} \\ -g_1\, g_2 & g_2^2 & -c_2\frac{4\delta\tilde{M}^2}{v^2} \\ -c_1\frac{4\delta\tilde{M}^2}{v^2} + \frac{4m_Y^2}{v^2} & -c_2\frac{4\delta\tilde{M}^2}{v^2} & \frac{4\,M_X^2}{v^2} \end{pmatrix} . \tag{2.44}$$

Unfortunately, we cannot simply proceed with the steps we have done before because the Z mixing makes a clever recombination of the parameters ϵ_B and δ_m impossible. This leads to the problem that we cannot just combine two parameters[20] into ξ implying that we need three separate rotations and therefore, we are required to introduce a third mixing angle beyond θ_W and ξ. The whole calculation becomes more complicated and no step in the calculation is very enlightening. We can already see this from taking the determinant of eq. (2.44) which will show that the simple previous conditions on $c_{1,2}$ to have a massless particle in the spectrum will be much more cumbersome and thus we will not discuss the maximum mixing in this thesis. However, this points to the interesting result that kinetic mixing and Stückelberg mixing, in general, are not equivalent for the mass matrix, although their impact thereon cannot be distinguished in the case of only kinetic and Stückelberg mixing. We will later come back to this result when we discuss millicharges.

2.2 From the mixing angles to observables

To summarise the results of the previous subsections, let us quote the total rotation matrix that diagonalises the mass matrix and the kinetic part in the case of kinetic and Z mixing[21]

$$\mathcal{D} = GOR_1R_2 = \begin{pmatrix} \cos\theta_W & -\left(\sin\theta_W\cos\xi + \alpha\sin\xi\right) & \sin\theta_W\sin\xi - \alpha\cos\xi \\ \sin\theta_W & \cos\theta_W\cos\xi & -\cos\theta_W\sin\xi \\ 0 & \sqrt{1+\alpha^2}\sin\xi & \sqrt{1+\alpha^2}\cos\xi \end{pmatrix} \tag{2.45}$$

$$\Rightarrow \mathcal{D}^T\mathcal{K}\mathcal{D} = \mathbf{I} \quad \& \quad \mathcal{D}^T\mathbf{M}\mathcal{D} = \text{Diag}\left[m_\gamma, m_Z, m_{\text{DP}}\right] . \tag{2.46}$$

It is important to realise that we also need to change the fields accordingly because only if we leave the Lagrangian unchanged we leave the physics invariant. Let us investigate this

---

[20] Note that before, either we redefined ϵ_B and δ_m into α and then into ξ or we redefined only ϵ_B into α and then α and $\delta\tilde{M}$ into ξ.

[21] In the case of kinetic and Stückelberg mixing, we can keep the appearance of ξ and θ_W changing only the definition of α since in this setup, α is a function of both ϵ_B and δ_m, see also table 2.1 for a summary of these definitions.

via the mass term

$$\mathcal{L}_{\mathbf{M}} = \begin{pmatrix} B_\mu & W_{3\mu} & X_\mu \end{pmatrix} \mathbf{M} \begin{pmatrix} B^\mu \\ W^{3\mu} \\ X^\mu \end{pmatrix} = \begin{pmatrix} A_\mu & Z_\mu & A'_\mu \end{pmatrix} \mathrm{Diag}\left[m_\gamma, m_Z, m_{\mathrm{DP}}\right] \begin{pmatrix} A^\mu \\ Z^\mu \\ A'^\mu \end{pmatrix} \tag{2.47}$$

$$= \begin{pmatrix} A_\mu & Z_\mu & A'_\mu \end{pmatrix} \mathcal{D}^T \mathbf{M} \, \mathcal{D} \begin{pmatrix} A^\mu \\ Z^\mu \\ A'^\mu \end{pmatrix} \tag{2.48}$$

$$\Rightarrow \begin{pmatrix} B^\mu \\ W^{3\mu} \\ X^\mu \end{pmatrix} = \mathcal{D} \begin{pmatrix} A^\mu \\ Z^\mu \\ A'^\mu \end{pmatrix} \, . \tag{2.49}$$

We therefore need to perform a $\mathcal{D}$ transformation to generate the interaction term for the mass eigenbasis Lagrangian.

Modification of the couplings

Following the analysis of Ref. [51], we will now work out the contribution to the oblique parameters S and T of the hidden photon through its mixing with the Z. For this purpose, we first work out the Lagrangian of the Z mass eigenstate following the above prescription, followed by a careful evaluation of the relation between theory parameters and the experimentally determined ones.[22] Using $Q = Y/2 + T_3$, defining $\tilde{e} = g_1 \cos\theta_W = g_2 \sin\theta_W$ for the interaction part of the Lagrangian, and ignoring potential dark currents $j^x = 0$ we find

$$\begin{aligned} \mathcal{L} \supset\ & \tilde{e} \bar{f}_i \gamma^\mu \, Q f_i \, A_\mu \\ & + \frac{\tilde{e}}{2 \sin\theta_W \cos\theta_W} \bar{f}_i \gamma^\mu \Big[\left(\left(\alpha \sin\xi \sin\theta_W + \cos\xi \right) T_3 - 2 \sin\theta_W \left(\alpha \sin\xi + \cos\xi \sin\theta_W \right) Q \right) \\ & \qquad + \left(\alpha \sin\xi \sin\theta_W + \cos\xi \right) T_3 \gamma_5 \Big] f_i Z_\mu \\ & + \frac{\tilde{e}}{2 \sin\theta_W \cos\theta_W} \bar{f}_i \gamma^\mu \Big[\left(\left(\alpha \cos\xi \sin\theta_W - \sin\xi \right) T_3 - 2 \sin\theta_W \left(\alpha \cos\xi - \sin\xi \sin\theta_W \right) Q \right) \\ & \qquad + \left(\alpha \cos\xi \sin\theta_W - \sin\xi \right) T_3 \gamma_5 \Big] f_i A'_\mu \, , \end{aligned} \tag{2.50}$$

where we have explicitly written all electroweak currents in terms of SM fermions f_i using the generic scheme $j_\mu = \bar{f} \left(a \gamma_\mu + b \gamma_\mu \gamma_5 \right) f$ as well as projecting out the left-handed component for the isospin via $P_L = (1 - \gamma_5)/2$. We make the following observations: if we send all mixings to zero, we restore the usual broken electroweak interactions, which is one of the key sanity checks for the calculation. Looking more carefully, we see that the interactions of the DP are always small if the mixing parameter (let's say ϵ_B) is small. Intriguingly, our parameter choices automatically restore the photon coupling to the EM current with the correct strength $\tilde{e}$. This invites us to define the fine-structure[23] constant accordingly

$$\tilde{\alpha} = \frac{\tilde{e}^2}{4\pi} \, , \tag{2.51}$$

---

[22] Of course, the parameters in the mass eigenbasis are not more physical than any other parametrisation but they are the ideal choice based on intuition and parameterising differences to the (DP-free) EW sector.

[23] The notation using $\tilde{\alpha}$ is due to the usage of α as a mixing parameter in the previous sections.

which could be measured e.g. from the anomalous electric moment of the electron. This will later confront us with a serious problem as this definition will lead to limits which do not decouple as $m_{\mathrm{DP}} \to 0$. We will dedicate parts of the following sections to this unpleasant effect of just defining the fine-structure constant following the suggestive notation. Indeed, we will realise the importance of distinguishing between an intuitive parametrisation and one based on carefully relating experimental results with the parameters. The core of this upcoming issue is the DP coupling to the SM charges as shown in the last line of eq. (2.50) which can mimic the photon in the low mass regime.

Electroweak precision observables

Before we conclude, let us quickly define the most relevant EWPO. In our setup, we are mostly interested in the Peskin-Takeuchi parameters S and T [51–55] defined via

$$\begin{aligned} \mathcal{L}_Z =& \frac{e'}{2\sin\tilde{\theta}_W\cos\tilde{\theta}_W}\left(1+\frac{\alpha' T}{2}\right)\bar{f}_i\gamma^\mu \\ &\times\left[\left(T_3 - 2Q\left(\sin^2\tilde{\theta}_W + \frac{\left(\frac{1}{4}\alpha' S - \cos^2\tilde{\theta}_W\sin^2\tilde{\theta}_W\alpha' T\right)}{\cos^2\tilde{\theta}_W - \sin^2\tilde{\theta}_W}\right)\right) - T_3\gamma_5\right] f_i Z_\mu \ , \end{aligned} \tag{2.52}$$

as well as the ρ parameter[24]

$$\rho = \frac{m_W^2}{m_Z^2\cos^2\tilde{\theta}_W} \ , \tag{2.53}$$

where we have introduced the W boson mass m_W. Note that we have explicitly taken into account that the “physical Weinberg angle” $\tilde{\theta}_W$ may not coincide with “Pseudo/parametrical Weinberg angle” θ_W. Furthermore, the same applies to the newly introduced electromagnetic coupling and fine-structure constant, which we denote with a “ $'$ ” and a “ $\tilde{}$ ”, respectively. In the following subsections, we investigate some specific limits of these universal expressions to gain more physical insight into the limits we can derive.

Before we begin, let us quickly state the values of these parameters according to the experimental results [46]

$$\rho = 1.00038 \pm 0.00020 \tag{2.54a}$$

$$S = \ -0.01 \pm 0.07 \tag{2.54b}$$

$$T = 0.04 \pm 0.06 \ , \tag{2.54c}$$

where we have assumed that $U = 0$ according to the SM prediction.[25] For a more robust analysis, one should consider the correlation coefficient 0.92 in the measurements of the S and T parameters.

---

[24] This definition of the parameter taken from the PDG book [46] deviates from the standard literature as claimed in the book itself which may lead to some confusion. In general, this subsection should be considered conceptual since a complete analysis would not align with the aim of this thesis which focusses on the direct detection of lighter DPs. This also implies that $\rho \neq T$.

[25] The U parameter is rather associated with modifications of the W bosons and thus will be less affected by our class of BSM physics [51]. Therefore we immediately plug in the SM value of 0.

2.2.1 Effects of kinetic mixing on electroweak (precision) observables

In this section, we will provide a rather simplified way to provide limits on the mixing parameters using precision information from EW physics. **Warning**: The discussion contains implicit assumptions about the definitions of several parameters. We will discuss the breakdown of these assumptions and their severe implications for understanding the low mass regime of the DP in the following subsections.

Evaluation of ρ

Let us begin with a thorough investigation of the ρ parameter in eq. (2.53). Since we have not changed anything about the W mass in this setup we can just take the measured value and use $m_W = \cos\theta_W \tilde{M}_Z$. For the Z mass which can also be directly measured, we can use eq. (2.39b). Finally, we get

$$\rho = \frac{\left(\frac{\cos\theta_W}{\cos\tilde{\theta}_W}\right)^2}{(\cos\xi + \alpha\sin\theta_W\sin\xi)^2 + \sin^2\xi\mu^2 + 2\sin\xi\frac{\delta M^2}{M_Z^2}(\cos\xi + \alpha\sin\theta_W\sin\xi)}\,, \tag{2.55}$$

which is a function[26] of μ, δM^2 and α. For simplicity, we will work with these parameters. In the previous sections, we can find formulae to translate these into other parametrisations, e.g. using the bare parameters or the physical DP mass. We will now set limits on the kinetic mixing and the Z mixing for every given value of μ. Before that, let us point out an important subtlety: the measured cosine of the Weinberg angle $\cos\tilde{\theta}_W$ in eq. (2.53) is usually determined by a global fit and thus will also have sensitivity to the mixing parameters. In conclusion, we have $\theta_W \neq \tilde{\theta}_W$ and we will therefore assume that we can determine $\sin\theta_W$ from the relation to the Fermi constant G_F, i.e.

$$G_F = \frac{\pi\tilde{\alpha}}{\sqrt{2}\sin^2\tilde{\theta}_W m_W^2}\,, \tag{2.56}$$

which can be inferred with high precision from the muon lifetime.[27] We see that within this expression, we have only quantities that are not altered by mixing, so we can conclude that $\theta_W \simeq \tilde{\theta}_W$ because we found a way to measure the Weinberg angle independently of the mixing parameters.

Alternatively, we can use the physical Z mass which is known with higher precision to fix the Weinberg angle. For this, we replace $m_W \to m_Z\cos\tilde{\theta}_W$. In conclusion, the Weinberg angle differs from the original definition. Due to the favourable error bars, this is the conventional way of defining the physical Weinberg angle. We have concentrated on the version presented above, as it is conceptually extremely helpful in understanding the decoupling of the DP in the following subsection. However, to keep in contact with the literature, we will from now on stick with the usual convention and define the new Weinberg angle via $\cos\tilde{\theta}_W\sin\tilde{\theta}_W m_Z = \cos\theta_W\sin\theta_W\tilde{M}_Z$.

Before we solve the given expression for the physical Weinberg angle, we will first consider the expression for the physical Z mass. Since it is quite tricky to fix $\tilde{M}_Z$ by the requirement

---

[26] This is under the assumption that $\tilde{M}_Z$ is fixed to give the measured physical Z mass.

[27] This also means that we need an independent determination of the W mass m_W. Although this is technically possible, there is some debate on the exact value since the CDF collaboration has released their new result at a stated $7\,\sigma$ discrepancy to the SM prediction in strong disagreement with the world average [56]. This greatly sparked the interest of the community [57–59], also in the context of DPs [60, 61], but the result could not be confirmed by the latest ATLAS result [62], which is in good agreement with the SM prediction and previous measurements.

given in footnote 26, we will now proceed by expanding all expressions from eq. (2.39a) to quadratic order in δM^2 and α. This should ensure that the final expression is self-consistently valid for small perturbations to the SM results, well-justified by the smallness of the deviation of the measured ρ parameter from 1

$$m_Z^2 \approx \tilde{M}_Z^2 \left(1 + \left(\frac{\left(\alpha \sin\theta_W + \frac{\delta M^2}{\tilde{M}_Z^2}\right)}{\sqrt{1-\mu^2}}\right)^2\right) \Leftrightarrow \tilde{M}_Z^2 \approx m_Z^2 \left(1 - \left(\frac{\left(\alpha \sin\theta_W + \frac{\delta M^2}{m_Z^2}\right)}{\sqrt{1-\mu^2}}\right)^2\right) . \tag{2.57}$$

Thus, we can fix $\tilde{M}_Z$ for every parameter point. Furthermore, since we expect $\sin\theta_W$ to only be affected at higher order in mixings, we are free to choose θ_W or $\tilde{\theta}_W$ in the expression. We could even use the same approach to fix μ to the correct physical DP mass we would like to investigate. We will refrain from this additional step because, as we have already pointed out in subsection 2.1.2, the behaviour of the physical DP mass in the small mixing limit becomes dubious for small μ once $\delta M^2 \gtrsim m_{\mathrm{DP}}^2$. This will be partially discussed in the next section. For a thorough analysis, it is of course advised to take the general expression without any approximations but Z mixing and a small DP mass should be handled with extra care anyways.

In our next step, we will extract the physical mixing angle from the aforementioned condition. To leading order, we find

$$\sin^2\theta_W \approx \sin^2\tilde{\theta}_W \left(1 + \frac{\cos^2\tilde{\theta}_W}{\cos^2\tilde{\theta}_W - \sin^2\tilde{\theta}_W}\left(\frac{m_Z^2}{\tilde{M}_Z^2} - 1\right)\right) \tag{2.58a}$$

$$\cos^2\theta_W \approx \cos^2\tilde{\theta}_W \left(1 - \frac{\sin^2\tilde{\theta}_W}{\cos^2\tilde{\theta}_W - \sin^2\tilde{\theta}_W}\left(\frac{m_Z^2}{\tilde{M}_Z^2} - 1\right)\right) \tag{2.58b}$$

$$\cos\theta_W \sin\theta_W \approx \cos\tilde{\theta}_W \sin\tilde{\theta}_W \left(1 + \frac{1}{2}\left(\frac{m_Z^2}{\tilde{M}_Z^2} - 1\right)\right) . \tag{2.58c}$$

Equipped with these relations, we are now in a position to evaluate the electroweak precision observables to leading order.

Let us now investigate the limits we can derive in this simplified setup. Expanding eq. (2.55) using our previous results, we find

$$\rho \approx \left(1 - \frac{\cos^2\tilde{\theta}_W}{\cos^2\tilde{\theta}_W - \sin^2\tilde{\theta}_W}\left(\frac{\alpha \sin\tilde{\theta}_W + \frac{\delta M^2}{m_Z^2}}{\sqrt{1-\mu^2}}\right)^2\right) , \tag{2.59}$$

which simply allows us to derive a first limit on the mixing parameters. For this, we observe two things: first, the way we have defined the mixing parameters, they are always positive. Secondly, the induced correction to the SM value of $\rho_{\mathrm{SM}} = 1$ is always negative. This should be contrasted with the measured result in eq. (2.54a) being larger than one by almost 2σ. We, therefore, present the 3σ exclusion limits over the measured result in fig. 2.1 (left) in the limit of small mixing, $1 \gg \alpha \approx \epsilon_B$ as shown on the x-axis. We see that this is self-consistently true for all our limits as the maximum reach always corresponds to small mixing.[28] We arrive at these limits simply by demanding that the deviation from the

---

[28] Of course, the ruled-out region also naively extends to arbitrarily large α and δM^2. While our assumptions break down in this region, there will most likely be other observables ruling out the scenario as large mixing implies strong couplings. However, only a complete analysis will be able to tell if the entire parameter space is truly ruled out.

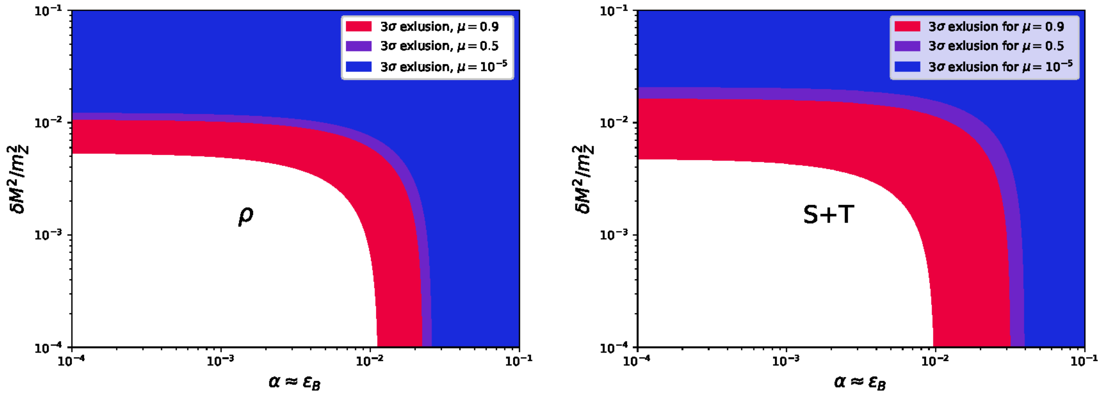

Figure 2.1: **Left**: 3σ exclusion limits of the kinetic mixing, parameterised by $\alpha \approx \epsilon_B$, and the mass mixing, expressed as $\delta M^2/m_Z^2$, for three different DP masses parameterised by $\mu = 10^{-5}$ (blue), 0.5 (purple), 0.9 (red). The limits are derived from the ρ parameter. **Right**: Analogous limits based on the S and T parameters.

measurement be contained within 3 standard deviations. We have taken three benchmark masses $\mu = 10^{-5}$ (blue), 0.5 (purple), 0.9 (red), and the coloured region is excluded by the aforementioned argument.

We make two interesting observations. On the one hand, we see that for $\mu \to 1$, we can exclude the entire parameter space. As mentioned above, this part of the parameter space should be handled with care. On the other side of the mass spectrum, the limits are the weakest but they are not arbitrarily weak as we would naively assume knowing that for a massless DP, we should not see any effects. This will be discussed in greater detail in the next section.

Evaluation of S and T

For now, let us turn to the parameters S and T. Comparing eq. (2.50) and eq. (2.52), we conclude in the small mixing expansion[29]

$$\alpha' T \approx \xi^2\left(\mu^2 - 2\right) + 2\alpha \sin\tilde{\theta}_W \xi = -\frac{\left(\frac{\delta M^2}{m_Z^2} + \alpha \sin\tilde{\theta}_W\right)\left(\frac{\delta M^2}{m_Z^2}(2-\mu^2) + \mu^2 \alpha \sin\tilde{\theta}_W\right)}{(1-\mu^2)^2} \tag{2.60a}$$

$$\begin{aligned}\alpha' S &\approx 4\cos^2\tilde{\theta}_W\left(\xi^2 \sin^2\tilde{\theta}_W + \alpha \sin\tilde{\theta}_W \xi\right)\\ &= 4\cos^2\tilde{\theta}_W \frac{\left(\frac{\delta M^2}{m_Z^2} + \alpha \sin\tilde{\theta}_W\right)\left(\sin^2\tilde{\theta}_W\left(\frac{\delta M^2}{m_Z^2} + \alpha \sin\tilde{\theta}_W\right) + \alpha \sin\tilde{\theta}_W\left(1-\mu^2\right)\right)}{(1-\mu^2)^2}\end{aligned} \tag{2.60b}$$

assuming as before $\theta_W = \tilde{\theta}_W$ and $\tilde{e} = e'$. Furthermore, we will use a correlation coefficient of 0.92 for S and T [46, 63]. We can exclude all values at 95% confidence level (C.L.) that are outside the ellipse defined by the above errors in eqs. (2.54b&2.54c), the correlation

---

[29] The slight deviation from Ref. [51] is due to their treatment of large DP masses. Our treatment should be more general and valid over a larger DP mass range, including smaller masses. However, on resonance, our treatment also breaks down.

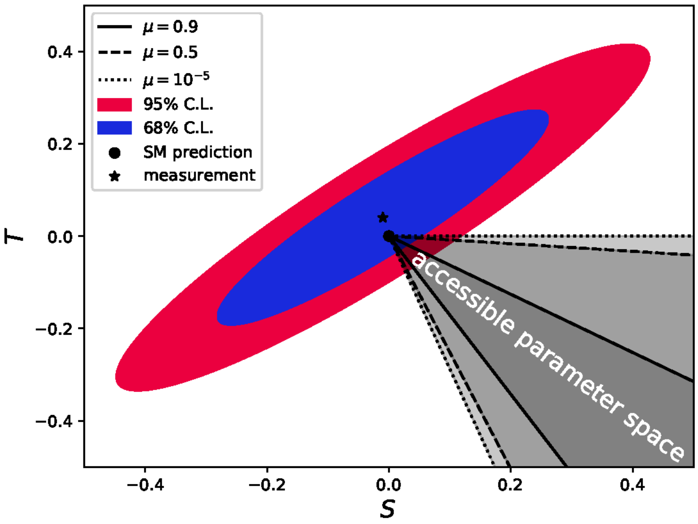

Figure 2.2: 95% C.L. on the measurement of the S and T parameter. We see that the SM prediction is already in mild tension with the measurement. We furthermore indicate the region in S-T-space which can be populated by DP corrections with black lines. Our benchmark DP masses are again $\mu = 10^{-5}$ (dotted), 0.5 (dashed), 0.9 (solid).

coefficient, and our choice of the confidence level. Once again, we see that $T \leq 0$ and $S \geq 0$ for $\mu < 1$ and thus the mild tension with the SM in fig. 2.2 will only be increased by the presence of a DP. The grey regions demonstrate that the accessible DP parameter space can only worsen the match between measurement and theory prediction, effectively independent of the DP mass as long as $\mu < 1$.

We can therefore also derive the 3σ exclusion bounds by demanding that the theory prediction for a given combination α and δM^2 does not deviate too far from the measurement [46]. These bounds are shown in fig. 2.1 (right). Unsurprisingly, their reach is very similar to the above discussion of the ρ parameter since both are quadratic in the mixing parameters with similar error bars.

2.2.2 Decoupling of the low mass DP

Let us consider the often studied case of a low mass DP without any additional mass mixing, neither Z nor Stückelberg. We expect a decoupling for small masses based on the additional symmetry gained when the DP becomes massless. Therefore, we will now explicitly decrease the (bare) DP mass. We aim to use a mass so small that we cannot observe it. In the most extreme case, this amounts to a Compton-wavelength exceeding the size of the observable Universe if we expect that the theorem stated in Ref. [42] also holds for photons mixed with massive DPs. It says effectively that experiments can only see the effect of a photon mass m_γ if the corresponding "experimental scale" is similar to the length scale m_γ^{-1}.[30] Following this logic, it is expected to be impossible to distinguish between massless and massive DP in this case. Therefore, we expect that there cannot be any effect

---

[30] We note in passing that this theorem has been challenged in Ref. [64]. The authors find that the boundary conditions that need to be imposed upon the EM fields inside a coaxial cable strongly rule out a photon mass. Although this paper has passed peer review and was published in PRD, this topic has not been picked up yet by the community despite their strong claims with potentially interesting implications.

on the EW precision observables as intuitively, they can only probe comparatively massive (i.e. around the EW scale) new physics.

An inconsistency

We will now prove this claim, but on the way there we will see that the decoupling is not trivial

$$\tan(2\xi) \xrightarrow{\delta M^2,\ \mu^2\to 0} \frac{2\sin\theta_W\alpha}{1-\sin^2\theta_W\alpha^2} \Rightarrow \tan\xi = \sin\theta_W\alpha\ , \tag{2.61}$$

where we have used the trigonometric identities relating $\tan(x)$ and $\tan(2x)$. This helpful simplification invites us to rewrite eq. (2.50)

$$\begin{aligned}\mathcal{L} \xrightarrow{\delta M^2,\ \mu^2\to 0}\ & \tilde{e}\bar{f}_i\gamma^\mu Q f_i\, A_\mu \\ & + \frac{\tilde{e}}{2\sin\theta_W\cos\theta_W}\bar{f}_i\gamma^\mu\left[\left(\sqrt{1+\sin^2\theta_W\alpha^2}T_3 - 2\sin^2\theta_W\frac{1+\alpha^2}{\sqrt{1+\sin^2\theta_W\alpha^2}}Q\right)\right. \\ & \qquad \left. + \sqrt{1+\sin^2\theta_W\alpha^2}T_3\gamma_5\right] f_i Z_\mu \\ & + \frac{\tilde{e}}{2\sin\theta_W\cos\theta_W}\bar{f}_i\gamma^\mu\left[-2\sin\theta_W\alpha\frac{\cos^2\theta_W}{\sqrt{1+\sin^2\theta_W\alpha^2}}Q\right] f_i A'_\mu\ .\end{aligned} \tag{2.62}$$

We note that the Z-like contribution to the dark photon vanishes as long as we can neglect the bare DP mass w.r.t. the bare Z mass, i.e. up to higher order in μ. In fact, the coupling to the $SU(2)$ isospin via T_3 is generically suppressed by $\mathcal{O}\left(\alpha\mu^2\right)$. Therefore, the new vector boson couples like a photon which can be interpreted as another sanity check: in the low mass limit (and without any mass mixing) we restore the photon-like A' coupling as the only interaction of the new particle.

As already pointed out, we have just encountered an interesting issue. Although we have considered a limit that should intuitively decouple the DP from EW physics, we still observe a non-vanishing contribution to the S and T parameter, as well as for the ρ parameter, c.f. eqs. (2.52&2.53). We will now single out the assumptions that lead us to this paradoxical behaviour.

Rethinking our definitions

The gravest mistake in the above chain of arguments is given by assuming that eq. (2.51) gives what we measure as fine-structure constant. Let us therefore investigate the measurement of the fine-structure constant via the anomalous magnetic dipole moment of the electron [46, 65, 66]. The fine-structure constant is the best-measured fundamental quantity in particle physics with an impressive precision of less than a part in a billion. In fact, at the moment the best determination comes from atomic interferometry and not the electron $g-2$ [67] but as this should only demonstrate that we can assume the fine-structure constant to be very well-known it will not influence the argument in any way.[31] In a setup with an ultralight DP, i.e. with a macroscopic Compton wavelength, the magnetic field will consist of a massless and a massive contribution, both of which will couple to the anomalous moment of the electron.

---

[31] In fact, some of the measurements are in slight tension with each other, see Ref. [68] for a brief discussion.

Nevertheless, there is a reason why we can ignore the external DP leg (see also fig. 2.3) following a very basic consideration in electrostatics. Let us assume for now that the Compton wavelength is much larger than any experimental scale that has ever been used to measure EM forces in the lab with high precision. Then, for example, as we have seen in eq. (2.74), all the charged particles in an object will source a strong, static photonic field and a weak, static dark photonic field. If we were to now measure the effect of this field on a test charge, we would assume, based on standard EM, that the field is sourced by a single (massless) field, the apparent photon which is just a superposition of photon (the truly massless field) and DP (the ultralight field). Therefore, a description in terms of a single massless particle with adjusted coupling strength is sufficient, and we encode the two different particles into a single effective vertex between field and charged particles. This effective interaction is described by the measured electric field via $E = F/q$ where F is given by a superposition of forces from the two mass eigenstates.

This means that in the case of a measurement of the anomalous magnetic moment, the external magnetic field is also a superposition as argued above. Thus, if we have a B-field of fixed strength and a sufficiently light DP, this automatically takes into account that there is a DP and a photon on the external leg. In a sense, it means that we use the interaction eigenbasis for the external leg, suppressing any mixing effects there but modifying the external field instead, while we keep the mass eigenbasis for the internal lines as demonstrated in fig. 2.3.

Furthermore, for dark photon masses too light to matter at typical modern accelerators, i.e. usually much lighter than the Z mass[32], but still heavy enough such that its Compton wavelength is microscopic, we expect that there is no “dark” external leg contribution to static magnetic fields. This consideration follows a simple Yukawa potential reasoning, assuming that the effect on a static field of a mediator with mass m is exponentially suppressed over distances larger than $1/m$. Taking, for example, $m = 1\,\mathrm{eV} \ll m_Z$, this would correspond to length scales of $\mathcal{O}(10^{-7}\,\mathrm{m})$ which we consider here to be shorter than the experimental scales.

Following the above argument closely, we see that the assumptions of well-separated scales will break down if the Compton wavelength roughly coincides with the experimental size or if we take and compare measurements of the EM interactions at different energy/spatial scales. The point here is that in this scenario the limits derived from this transition between only photonic and superposition of photon and DP will yield stronger results than any EWPO limit. This can be seen from the compilation of results shown in Ref. [72], especially using tests of the Coulomb law in macroscopic lab experiments [43, 73–75] but also tests on astrophysical [42, 76, 77] or microscopic [78] scales. The latter paper also provides a very illuminating discussion on how to handle the transition region between the ultraheavy and the ultralight DP. See also the discussion on limits on the photon mass in footnote 16.[33] Finally, let us emphasise that this is only a rather limited selection of DP limits based on the modified Maxwell's equations. We will discuss the very relevant astrophysical limits in later chapters as they require at least a small introduction to EM plasma effects.

---

[32] Of course, several accelerators/experiments are operating at lower energies [69–71] but they typically have at least energies on the GeV scale so this hardly changes the argument.

[33] As pointed out in Ref. [77], photon mass limits are not necessarily in one-to-one correspondence to DP limits.

Redefining the parameters

In conclusion, we can self-consistently assume that we just need to modify the internal line for the anomalous magnetic moment to account for the existence of a light DP. We get to leading order in the mixing[34] a contribution to $g-2$ like

$$\Delta a_e \equiv \frac{\alpha'}{2\pi} = \frac{e^2}{8\pi^2} = \frac{\tilde{e}^2}{8\pi^2}\Big(1+\frac{\cos^2\theta_W\alpha^2}{1+\sin^2\theta_W\alpha^2}\Big) = \frac{\tilde{e}^2}{8\pi^2}\Big(\frac{1+\alpha^2}{1+\sin^2\theta_W\alpha^2}\Big) \tag{2.63}$$

$$\Rightarrow e = \tilde{e}\sqrt{\frac{1+\alpha^2}{1+\sin^2\theta_W\alpha^2}}\,, \tag{2.64}$$

where we measure a_e directly and thus extract the effective coupling which we call e. As the DP is ultralight and couples photon-like, we have included it for the internal line in the triangle. This means, we sum up the usual triangle diagram and the one where we replace the internal photon with a dark photon as shown in fig. 2.3 which gives in sum exactly the result we have just seen as the impact of the mass vanishes at least like m_{DP}/m_e as the DP propagator will roughly be given by

$$\frac{-g^{\mu\nu}+\frac{p^\mu p^\nu}{m_{\mathrm{DP}}^2}}{p^2-m_{\mathrm{DP}}^2} \to -\frac{g^{\mu\nu}}{p^2}+\mathcal{O}\left(\frac{m_{\mathrm{DP}}^2}{p^2},\,\frac{m_{\mathrm{DP}}^2}{(\max[p^\mu])^2}\right)\,. \tag{2.65}$$

Assuming that the 4-momentum p is at least coming from a non-relativistic electron, we would conclude that $p^2 \sim (\max[p^\mu])^2 \sim m_e^2$ which is even stronger than the point made above. Of course, this is a rather weak argument as p^μ can be a loop momentum and therefore, it might take arbitrary values. Now, the point is that whatever structure we are integrating over with the loop integrals, the result can only depend on the external scales. For a_e, an essentially non-relativistic experiment, the only scale involved is the electron mass in usual QED and since a_e is dimensionless, there are only terms that depend on m_e/m_μ or m_e/m_τ which are typically small. With the addition of a massive DP, we can also write the combination m_{DP}/m_e. We might already guess that $(m_{\mathrm{DP}}/m_e)^2$ is the leading behaviour because only m_{DP}^2 appears in the propagators and to have a smooth limit for vanishing mass, we need to avoid $(m_{\mathrm{DP}}/m_e)^{-n}$ with $n>0$. The integration of the loop momenta might change this behaviour but in any case, the contribution will be suppressed by the electron mass, as it is the smallest additional scale in the calculation.[35]

In complete analogy to our previous discussion, we can use our new definition of e or respectively α', the "measured couplings", to fix the "measured" Weinberg angle by substituting this for $\tilde{\alpha}$ in eq. (2.56).[36] From this, we can get the following relation

$$\sin\tilde{\theta}_W = \sin\theta_W\frac{e}{\tilde{e}} = \sin\theta_W\sqrt{\frac{1+\alpha^2}{1+\sin^2\theta_W\alpha^2}}\,, \tag{2.66}$$

---

[34] For simplicity, we also stay at leading order in quantum electrodynamics (QED) for this calculation. In principle, of course, we should take into account the effect of the DP up to the required number of loops, i.e. it is up to α_{EM}^5 [68]. Fortunately, we can apply the rescaling found at leading order for all higher orders. This is simply because, for every internal photon, line we also need to put an internal DP line and add up the contributions.

[35] Indeed, a quick numerical analysis of the exact contribution of the DP to a_e shows that deviations from the leading DP term in eq. (2.63) have a behaviour $\propto \alpha^2 m_{\mathrm{DP}}/m_e$, and thus they do not follow the naive expectation. However, the decoupling still takes place as can be inferred from the expression eq. (4) in Ref. [79] or eq. (3) in Ref. [80].

[36] Since it is conceptionally simpler, we will use this definition instead of the usual convention from the literature. As we do not intend to make any quantitative statements in this section, this suffices to prove the point because the larger error bars from the W mass never play a role. Of course, the final result is independent of the choice but the resulting equation relating θ_W and $\tilde{\theta}_W$ are simpler in this setup.

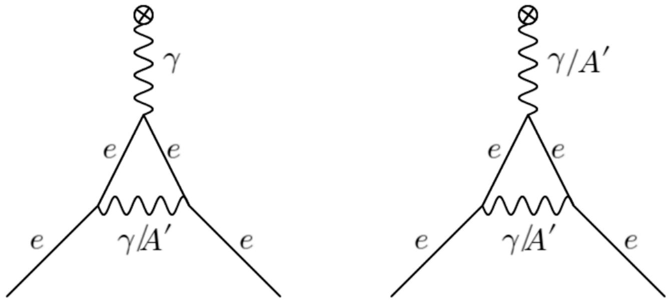

Figure 2.3: Left: Diagrams of the contribution to the electron $g-2$ from photon and DP in the scenario where the DP contribution to the magnetic field is Yukawa suppressed. For extremely low masses, macroscopic magnetic fields are partially composed of DPs. This is however already included in the measurement of the external magnetic field and thus for the effective description, the internal line is the most interesting contribution.

as the remaining quantities in eq. (2.56) are determined by measurement and do not change if we redefine $\tilde{e}$. This therefore provides us with a "clean" determination of the "physical" Weinberg angle assuming that we can measure the W mass independently.

Successful decoupling

With these observations, let us investigate the interactions of the Z boson and see how these new definitions change the S and T parameters. We begin from eq. (2.74) and then simplify the expressions further

$$\begin{aligned}
\mathcal{L} \supset\ & \frac{\tilde{e}}{2\sin\theta_W\cos\theta_W}\bar{f}_i\gamma^\mu\Bigg[\left(\sqrt{1+\sin^2\theta_W\alpha^2}T_3 - 2\sin^2\theta_W\frac{1+\alpha^2}{\sqrt{1+\sin^2\theta_W\alpha^2}}Q\right) \\
& \qquad + \sqrt{1+\sin^2\theta_W\alpha^2}T_3\gamma_5\Bigg]f_i Z_\mu \qquad (2.67a)\\
=\ & \frac{e\sqrt{1+\sin^2\theta_W\alpha^2}}{2\sin\tilde{\theta}_W\cos\theta_W}\bar{f}_i\gamma^\mu\left[\left(T_3 - 2\sin^2\tilde{\theta}_W Q\right) + T_3\gamma_5\right]f_i Z_\mu \qquad (2.67b)\\
=\ & \frac{e}{2\sin\tilde{\theta}_W\cos\tilde{\theta}_W}\bar{f}_i\gamma^\mu\left[\left(T_3 - 2\sin^2\tilde{\theta}_W Q\right) + T_3\gamma_5\right]f_i Z_\mu\ , \qquad (2.67c)
\end{aligned}$$

where we used the inversion of eq. (2.66) in the last step, i.e.

$$\begin{aligned}
\sin\theta_W &= \sin\tilde{\theta}_W\frac{1}{\sqrt{1+\cos^2\tilde{\theta}_W\alpha^2}} \qquad (2.68a)\\
\cos\theta_W &= \cos\tilde{\theta}_W\sqrt{\frac{1+\alpha^2}{1+\cos^2\tilde{\theta}_W\alpha^2}}\ . \qquad (2.68b)
\end{aligned}$$

We conclude that all seemingly non-vanishing contributions to S and T cancel due to our new definitions directly guided by measurement. We now just need to show that the ρ parameter (eq. (2.53)) decouples following the same arguments. For this, we take the Z

mass from eq. (2.16b) or equivalently eq. (2.39b) in the appropriate limit

$$m_Z \to \tilde{M}_Z \sqrt{(\cos\xi + \alpha \sin\theta_W \sin\xi)^2} = \tilde{M}_Z \sqrt{1 + \sin^2\theta_W \alpha^2} \tag{2.69}$$

$$\Rightarrow \rho = \frac{m_W^2}{m_Z^2 \cos^2\tilde{\theta}_W} = \frac{m_W^2}{\tilde{M}_Z^2 \cos^2\tilde{\theta}_W (1 + \sin^2\theta_W \alpha^2)} = \frac{\cos^2\theta_W}{\cos^2\tilde{\theta}_W (1 + \sin^2\theta_W \alpha^2)} = 1\,, \tag{2.70}$$

where we have made use of eq. (2.66) in the last step. In conclusion, we see that in fact, all the typical EWPOs are unaffected by the existence of a light DP which only couples via kinetic mixing, an observation known in the literature for a long time [54][37] even though it is rarely discussed explicitly.

Let us emphasise our findings once again before we conclude with this section. We have seen that going to the extremely low mass limit of the kinetically mixed DP we restore the usual EW Lagrangian, albeit with the modification that the original DP conspires with the would-be photon to mimic the presence of a single massless photon. This combination modifies the relationship between the theoretical parameters and the real measured values of the coupling constant[38] that lead to the same physical observables as a DP-free EW sector would provide. This relies on the effective restoration of the additional symmetry in the system for vanishing DP mass. See also Ref. [78] for a thorough discussion on this aspect of DP limits. In essence, this work provides a framework for connecting the two limiting behaviours where the DP is either too heavy to participate in typical processes or is sufficiently light that it needs to be taken into account.[39]

The proper low-energy Lagrangian

Before we end this subsection, let us quickly write down the standard Lagrangian for the low-energy theory of kinetic mixing (and only kinetic mixing). As we have seen just now, the Z boson can be completely ignored in this setup. Therefore, we write for the interacting part (referring back to eq. (2.74))

$$\begin{aligned}
\mathcal{L}_{\text{int}} &= \tilde{e}\bar{f}_i\gamma^\mu Q f_i A_\mu - \frac{\alpha\tilde{e}\cos\theta_W}{\sqrt{1+\sin^2\theta_W\alpha^2}} \bar{f}_i\gamma^\mu Q f_i A'_\mu && (2.71a)\\
&= \tilde{e}\bar{f}_i\gamma^\mu Q f_i \left(A_\mu - \frac{\epsilon_B \cos\theta_W}{\sqrt{1-\cos^2\theta_W \epsilon_B^2}} A'_\mu \right) && (2.71b)\\
\xrightarrow{\epsilon=\epsilon_B\cos\theta_W} &\ \tilde{e}\bar{f}_i\gamma^\mu Q f_i \left(A_\mu - \frac{\epsilon}{\sqrt{1-\epsilon^2}} A'_\mu \right) && (2.71c)\\
\Rightarrow m_{\text{DP}} &= \frac{M_X}{\sqrt{1-\epsilon^2}}\,, && (2.71d)
\end{aligned}$$

---

[37] The low mass limit is an “amusing” exercise according to the author.

[38] Of course, coupling constants are not considered physical quantities and thus it would be more precise to replace “measured coupling constant” with “coupling constant naively extracted from data”.

[39] We have mostly discussed this regime separately but the most interesting behaviour will exactly lie in this central region where DP effects cannot be fully explained by the previous simplified descriptions.

where we defined ϵ as the conventional kinetic mixing used in low-energy setups. To see that this indeed corresponds to the correctly mixed Lagrangian, let us start with

$$\mathcal{L} = -\frac{1}{4}F^{\mu\nu}F_{\mu\nu} - \frac{1}{4}F'^{\mu\nu}F'_{\mu\nu} - \frac{\epsilon}{2}F^{\mu\nu}F'_{\mu\nu} + j_\mu A^\mu + \frac{M_X^2}{2}A'^\mu A'_\mu \tag{2.72a}$$

$$\xrightarrow[A'\to 1/\sqrt{1-\epsilon^2}A']{A\to A-\epsilon/\sqrt{1-\epsilon^2}A'} -\frac{1}{4}F^{\mu\nu}F_{\mu\nu} - \frac{1}{4}F'^{\mu\nu}F'_{\mu\nu} + j_\mu\left(A^\mu - \frac{\epsilon}{\sqrt{1-\epsilon^2}}A'^\mu\right) + \frac{M_X^2}{2\left(1-\epsilon^2\right)}A'_\mu A'^\mu \tag{2.72b}$$

with a self-evident notation of the fields and parameters. A comparison between eqs. (2.71c), (2.71d) & (2.72b) shows self-consistently that we have indeed recovered the correct low-energy kinetic mixing from our “UV complete” Lagrangian taking the appropriate limits. However, we note that this does not automatically solve our issue with the rescaling of the masses. We need to perform the same renormalisation between the high and low mass cases that we have thoroughly discussed in this subsection. This is the case as there is an enormous hierarchy between the Z mass, i.e. the scale below which the simplified Lagrangian eq. (2.72b) is a good approximation and the electron mass which roughly marks the point below which virtual DP effects, e.g. in the calculation of a_e, become irrelevant. The correct decoupling behaviour should therefore always be investigated with care. In the next chapter, we will further investigate the decoupling but then taking into account plasma effects, which become especially interesting in the low mass regime.

With this remark, let us conclude the vanilla case of simple kinetic mixing. Today, the focus of DP studies, including this thesis, is on the light side of the mass spectrum. Therefore, kinetic mixing being gauge-invariant and not invoking new, potentially heavy scalars seems like a natural extension. Early works like [51] considered mass mixing as the usual term and studied kinetic mixing as a new effect. This also means that the above discussion should rather be seen as a simplified discussion since light DPs will not only contribute to the oblique parameters but will actively be produced. Therefore, only a generalised study can treat the scenario consistently.[40] In the next step, we will discuss the case beyond kinetic mixing in more detail.

Before we conclude with this subsection, we can consider the visualisation of the previous results in fig. 2.4 where we show the 3σ exclusion bounds for kinetic mixing only derived from the S and T parameters. On the right, we cut out the Z-resonance where our expansion breaks down since $|\mu - 1| \ll 1$ which makes the use of eq. (2.60a) and eq. (2.60b) inconsistent. In the regime of lower masses, the cutoff is slightly softer since the impact of the DP on the measurement of the finestructure context (at least for the determination via the electron magnetic moment) increases with decreasing DP mass roughly until the DP mass drops below the electron mass [79]. Therefore, in this regime, it is clear that the DP will be decoupled from the EWPO.

2.2.3 Pure mass mixing

Going back to our general expression in eq. (2.38), it is clear that the whole phenomenology is driven by three parameters, namely μ, α, and δM^2. We have already discussed kinetic mixing in great detail now so it seems only natural to focus on the case of pure Z mass mixing featuring again a very light DP. Our aim now is to investigate if the same decoupling

---

[40] This would among other things also include a discussion of the U parameter and a quantitative description of the decoupling discussed in this subsection.

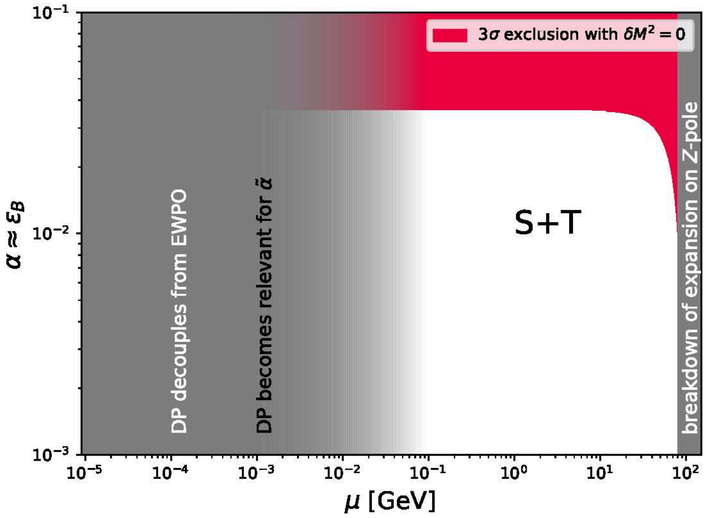

Figure 2.4: 3σ exclusion bounds derived from the S and T parameters without mass mixing. We indicate the breakdown of our expansions around the Z-mass and for low masses where the DP will be probed in measurements of the finestructure constant $\tilde{\alpha}$. This happens around the electron mass below which the DP is definitely decoupled from the EWPO.

takes place.[41] For this, let us also find an analogue of eq. (2.61)

$$\tan 2\xi \xrightarrow{\alpha\to 0} \frac{2\frac{\delta M^2}{\tilde{M}_Z^2}}{1-\mu^2} . \tag{2.73}$$

Unfortunately, this expression does not simplify the way it does for the case of kinetic mixing. Nevertheless, once again we can take a limit for the interaction term

$$\begin{aligned} \mathcal{L} \xrightarrow{\alpha\to 0} &\, \tilde{e}\bar{f}_i\gamma^\mu Q f_i A_\mu \\ &+ \frac{\tilde{e}\cos\xi}{2\sin\theta_W\cos\theta_W}\bar{f}_i\gamma^\mu\left[\left(T_3 - 2\sin^2\theta_W Q\right) + T_3\gamma_5\right] f_i Z_\mu \\ &+ \frac{-\tilde{e}\sin\xi}{2\sin\theta_W\cos\theta_W}\bar{f}_i\gamma^\mu\left[\left(T_3 - 2\sin^2\theta_W Q\right) + T_3\gamma_5\right] f_i A'_\mu , \end{aligned} \tag{2.74}$$

which clearly shows that the case of pure Z mixing leads to a particle that couples essentially like the Z boson. Therefore, we cannot expect a decoupling of the limits in the same sense as above. Nevertheless, as we need $\mu^2\tilde{M}|_Z^2 > \delta M^2$ for a consistent theory the limit $\mu \to 0$ automatically decouples the theory as $\xi \to 0$.

We conclude that as long as no exotic new physics is involved, Z mass mixing cannot generate new ultralow-energy phenomena. Still, should a mechanism exist that decouples δM^2 and μ we would expect strong signals from a low-energy particle with both axial and vectorial couplings [81–83]. In this case, there is no way of redefining the couplings in the style presented for the kinetic mixing since the photon cannot compensate for the axial part.

---

[41] We note from the discussion beforehand in subsection 2.1.2 that this is a rather unnatural limit if we take $\mu^2\tilde{M}|_Z^2 \ll \delta M^2$. Therefore, we also keep the terms containing μ.

2.2.4 Stückelberg and kinetic mixing

We have observed now that pure kinetic mixing leads to a photon-like DP while pure Z mass mixing results in a Z-like DP when it comes to the coupling structure. We have observed that in the case of no Z mixing, the Stückelberg mixing conspires with the kinetic mixing into a single parameter. While this is true for the masses of the DP and Z boson as becomes clear from eq. (2.30) the impact on the interacting part of the Lagrangian is more subtle as we need to perform all rotations on the interaction part, including eq. (2.3) which depends only on the kinetic mixing which makes a redefinition impossible.

For clarity, we will reiterate the most important definitions for the case of Stückelberg mixing here (see also table 2.1)

$$\alpha = \frac{\epsilon_B - \delta_m}{\sqrt{1-\epsilon_B^2}} \tag{2.75a}$$

$$g_Y = \frac{g_1}{\sqrt{1+\alpha^2}\sqrt{1-\epsilon_B^2}} \tag{2.75b}$$

$$\cos\theta_W = \frac{g_2}{\sqrt{g_Y^2 + g_2^2}} \tag{2.75c}$$

$$\tilde{M}_Z = \sqrt{g_Y^2 + g_2^2}\frac{v}{2} \tag{2.75d}$$

$$\mu = \frac{1}{\sqrt{1-\epsilon_B^2}}\frac{M_X}{\tilde{M}_Z} \tag{2.75e}$$

$$\tan(2\xi) = \frac{2\sin\theta_W\alpha}{1-\alpha^2\sin^2\theta_W - \mu^2} \tag{2.75f}$$

$$m_Z = \tilde{M}_Z\sqrt{(\cos\xi + \alpha\sin\theta_W\sin\xi)^2 + \sin^2\xi\mu^2} \tag{2.75g}$$

$$m_{\mathrm{DP}} = \tilde{M}_Z\sqrt{(\sin\xi - \alpha\sin\theta_W\cos\xi)^2 + \cos^2\xi\mu^2}\,. \tag{2.75h}$$

We observe some subtle changes here, especially $g_Y \neq g_1$ as noted earlier indirectly impacts the Weinberg angles and the Z mass. W.l.o.g. we assume that $\alpha > 0$. With this, we can express the analogue of eq. (2.45)

$$\mathcal{D}_{\mathrm{St}}^T = \begin{pmatrix} \frac{\cos\theta_W}{\sqrt{1+\alpha^2}\sqrt{1-\epsilon_B^2}} & \sin\theta_W & \cos\theta_W\frac{\alpha-\frac{\epsilon_B}{\sqrt{1-\epsilon_B^2}}}{\sqrt{1+\alpha^2}} \\ -\frac{\sin\theta_W\cos\xi+\alpha\sin\xi}{\sqrt{1+\alpha^2}\sqrt{1-\epsilon_B^2}} & \cos\theta_W\cos\xi & \frac{\left(1+\frac{\alpha\epsilon_B}{\sqrt{1-\epsilon_B^2}}\right)\sin\xi-\left(\alpha-\frac{\epsilon_B}{\sqrt{1-\epsilon_B^2}}\right)\sin\theta_W\cos\xi}{\sqrt{1+\alpha^2}} \\ \frac{\sin\theta_W\sin\xi-\alpha\cos\xi}{\sqrt{1+\alpha^2}\sqrt{1-\epsilon_B^2}} & -\cos\theta_W\sin\xi & \frac{\left(1+\frac{\alpha\epsilon_B}{\sqrt{1-\epsilon_B^2}}\right)\cos\xi+\left(\alpha-\frac{\epsilon_B}{\sqrt{1-\epsilon_B^2}}\right)\sin\theta_W\sin\xi}{\sqrt{1+\alpha^2}} \end{pmatrix} \tag{2.76}$$

$$= \begin{pmatrix} \frac{\cos\theta_W}{\sqrt{1-2\epsilon_B\delta_m+\delta_m^2}} & \sin\theta_W & -\cos\theta_W\frac{\delta_m}{\sqrt{1-2\epsilon_B\delta_m+\delta_m^2}} \\ \frac{-\left(\sin\theta_W\cos\xi+\frac{\epsilon_B-\delta_m}{\sqrt{1-\epsilon_B^2}}\sin\xi\right)}{\sqrt{1-2\epsilon_B\delta_m+\delta_m^2}} & \cos\theta_W\cos\xi & \frac{\frac{1-\epsilon_B\delta_m}{\sqrt{1-\epsilon_B^2}}\sin\xi+\delta_m\sin\theta_W\cos\xi}{\sqrt{1-2\epsilon_B\delta_m+\delta_m^2}} \\ \frac{\sin\theta_W\sin\xi-\frac{\epsilon_B-\delta_m}{\sqrt{1-\epsilon_B^2}}\cos\xi}{\sqrt{1-2\epsilon_B\delta_m+\delta_m^2}} & -\cos\theta_W\sin\xi & \frac{\frac{1-\epsilon_B\delta_m}{\sqrt{1-\epsilon_B^2}}\cos\xi-\delta_m\sin\theta_W\cos\xi}{\sqrt{1-2\epsilon_B\delta_m+\delta_m^2}} \end{pmatrix}, \tag{2.77}$$

where we have used the transpose in the first line to improve the readability and we have reintroduced the mass mixing parameter in the second line. Of course, we recover eq. (2.45) in the limit $\delta_m \to 0$.

With this result, we can write the interacting part of the Lagrangian. Interestingly, due to eq. (2.75b), we exactly recover the structure of eq. (2.50) as the factor of $(1 - 2\epsilon_B \delta_m + \delta_m^2)^{-1/2}$ always gets multiplied by the coupling constant g_1, again allowing a description using only the effective parameter α. Interestingly, our entire discussion in section 2.2.2 only depended on α which leads us to the conclusion that also arbitrary combinations of kinetic and Stückelberg mixing decouple in the low mass limit. Furthermore, this discussion once again emphasises the similarity between these two seemingly different types of mixing.

Nevertheless, eq. (2.76) makes clear that in the presence of an extended dark sector, i.e. $j_X \neq 0$, there will be observable and distinct effects due to the presence of terms directly proportional to δ_m which can never be reabsorbed into other couplings. To be specific, this corresponds to the third column in eq. (2.76) leading to "non-redefinable" couplings to the dark current which vanish only for $\delta_m = 0$. We will discuss this in the next subsection, where we briefly discuss the idea of induced millicharge.

2.2.5 (Induced) Millicharge

The idea of millicharge (sometimes also minicharge) is an intriguing concept. First, all charges that we observe are multiples of the elementary charge e (excluding quarks that have multiples of $e/3$) although this is not necessarily required by the SM symmetries [84]. Apart from these fundamental considerations, millicharged particles also offer intriguing phenomenology in lab experiments, astrophysics, and cosmology [29, 78, 85–90].

The massless case

In general, millicharged particles can generically be split into "true" and "effective/induced" millicharge [91]. The former consists of particles genuinely charged under electromagnetism and will not be of any concern in this section. The latter requires two $U(1)$s, one for electromagnetism and the other one in the dark sector, as well as charged particles in the dark sector. We will focus on the low-energy regime to simplify the procedure and reproduce a few results from Ref. [30], including a discussion about the impact of Stückelberg mixing on millicharged particles. We will begin with the simplest possible setup of only kinetic mixing of a *massless* DP and the SM photon and a dark current j_d^μ as well as the EM current j_EM^μ

$$\mathcal{L} = -\frac{1}{4} F^{\mu\nu} F_{\mu\nu} - \frac{1}{4} F'^{\mu\nu} F'_{\mu\nu} - \frac{\epsilon}{2} F^{\mu\nu} F'_{\mu\nu} + j_\mathrm{EM}^\mu A_\mu + j_\mathrm{d}^\mu A'_\mu \tag{2.78}$$

$$\xrightarrow[A \to 1/\sqrt{1-\epsilon^2} A]{A' \to A' - \epsilon/\sqrt{1-\epsilon^2} A} -\frac{1}{4} F^{\mu\nu} F_{\mu\nu} - \frac{1}{4} F'^{\mu\nu} F'_{\mu\nu} + \frac{1}{\sqrt{1-\epsilon^2}} j_\mathrm{EM}^\mu A_\mu - j_\mathrm{d}^\mu \left(A'_\mu - \frac{\epsilon}{\sqrt{1-\epsilon^2}} A_\mu \right) . \tag{2.79}$$

We observe that the dark current now couples weakly, and approximately proportional to ϵ, to the photon. However, we note that there is a hidden $SO(2)$ symmetry, i.e. we can rotate the states arbitrarily into each other without changing the kinetic term. While this basis makes the millicharge of the dark current apparent, it exists in any other basis as well. After all, since we live in a world dominated by EM interactions, we would call A in the above basis the photon, and this basis enormously simplifies all calculations.[42]

In the next step, we will allow for a mass term of the DP. This will break the $SO(2)$ symmetry and determine a preferred basis: the mass eigenbasis. Clearly, in this case, we would prefer to rotate the kinetic mixing away in the style of eq. (2.72b). Thus, the interacting part of the Lagrangian will be

$$\mathcal{L}_{\text{int}} = \frac{1}{\sqrt{1-\epsilon^2}} j_{\text{d}}^{\mu} A'_{\mu} - j_{\text{EM}}^{\mu} \left(A_{\mu} - \frac{\epsilon}{\sqrt{1-\epsilon^2}} A'_{\mu} \right) . \tag{2.80}$$

Ref. [30][43] claims (rightfully so) that this should not be called millicharge since the dark sector particles do not couple to the photon at all. In contrast, only the SM particles receive a dark millicharge.

The massive case

Before we comment on this in more detail, let us also include the case of Stückelberg mixing using the eq. (2.29) in our simplified case of just two $U(1)$s[44]

$$\mathcal{L} = -\frac{1}{4} F^{\mu\nu} F_{\mu\nu} - \frac{1}{4} F'^{\mu\nu} F'_{\mu\nu} - \frac{\epsilon}{2} F^{\mu\nu} F'_{\mu\nu} + j_{\text{EM}}^{\mu} A_{\mu} + j_{\text{d}}^{\mu} A'_{\mu} - \frac{m^2}{2} \left(A'_{\mu} + \delta A_{\mu} \right)^2 , \tag{2.81}$$

which we will transform exactly like eq. (2.80)

$$\begin{aligned} \mathcal{L} = &-\frac{1}{4} F^{\mu\nu} F_{\mu\nu} - \frac{1}{4} F'^{\mu\nu} F'_{\mu\nu} + \frac{1}{\sqrt{1-\epsilon^2}} j_{\text{d}}^{\mu} A'_{\mu} - j_{\text{EM}}^{\mu} \left(A_{\mu} - \frac{\epsilon}{\sqrt{1-\epsilon^2}} A'_{\mu} \right) \\ &- \frac{m^2}{2} \left(\frac{1-\epsilon\delta}{\sqrt{1-\epsilon^2}} A'_{\mu} + \delta A_{\mu} \right)^2 \end{aligned} \tag{2.82}$$

$$\mathcal{L}_{\text{int}} \to \frac{1}{\sqrt{1-2\epsilon\delta+\delta^2}} j_{\text{d}}^{\mu} \left(\frac{1-\epsilon\delta}{\sqrt{1-\epsilon^2}} A'_{\mu} - \delta A_{\mu} \right) + \frac{1}{\sqrt{1-2\epsilon\delta+\delta^2}} j_{\text{EM}}^{\mu} \left(A_{\mu} - \frac{\epsilon-\delta}{\sqrt{1-\epsilon^2}} A'_{\mu} \right) , \tag{2.83}$$

using the following redefinition to go to the mass eigenbasis

$$\begin{pmatrix} A' \\ A \end{pmatrix} \to \begin{pmatrix} c & -s \\ s & c \end{pmatrix} \begin{pmatrix} A' \\ A \end{pmatrix} \tag{2.84a}$$

$$c = \frac{1-\epsilon\delta}{\sqrt{1-2\epsilon\delta+\delta^2}} \tag{2.84b}$$

$$s = \sqrt{1-c^2} = \delta \sqrt{\frac{1-\epsilon^2}{1-2\epsilon\delta+\delta^2}} . \tag{2.84c}$$

We see that we cannot consistently recover the effective α parameter from eq. (2.75a) which would be sufficient to describe the DP physics if we did not have a non-empty dark sector. As noted at the end of the previous subsection 2.2.4 this is an additional effect which distinguishes kinetic and Stückelberg mixing. Since the dark sector is now directly connected to the photon, Ref. [30] concluded that only Stückelberg mixing yields millicharge. While

---

[42] At this point it is important to once again emphasise the basis-independence of the physics. The above basis is just convenient and in the most extreme case of a physicist (or another entity) living in the dark sector, they would of course prefer the opposite choice.

[43] Note that their convention of the labelling ϵ and δ is inverse to the one used throughout this thesis.

[44] We will neglect the Stückelberg field in the following expressions.

this statement is correct if taken at face value, the impact and implications of it are not exactly clear since, in a similar fashion, the SM sector gets a dark millicharge, and thus also the DP acts as a mediator between the two sectors. The exact interplay between the two mediators which interfere with each other depends on the mass of the DP. From some simple arguments, we can at least understand the limiting behaviour. In the high mass limit, we can effectively integrate out the DP and thus we realise that the photonic contribution drives the interactions and thus we indeed find what is usually considered as millicharge. For very light DPs, i.e. lighter than the scales involved in the processes, particularly the SM and dark sector masses, we effectively reintroduce the $SO(2)$ symmetry and we eliminate the Stückelberg mixing from our setup, since the mixing term decouples with $m \to 0$.

This simplified picture of mixing in vacuum is often insufficient in realistic setups as we will see in the following chapter where we will introduce plasma effects. In the case of a millicharged dark sector that accounts for (parts of) the DM relic density, it is possible or even required to investigate the interesting interplay between the DP and the background DM [92, 93] since millicharged particles can generate dark plasma effects for the DP. The existence of the dark sector is imperative for these searches since we have now seen good evidence that the massless DP decouples completely otherwise. We note however, that millicharged particles can also affect SM observables via virtual effects as demonstrated in Ref. [78].

3 Light Shining Through The Dark Side Of The Moon: Improving helioscope limits with angular information

> And if your head explodes with dark forbodings too
> I'll see you on the dark side of the moon
>
> *Brain Damage*
> PINK FLOYD

This chapter is based on the following publication:

[1] J. Frerick, F. Kahlhoefer, and K. Schmidt-Hoberg, *A' view of the sunrise: boosting helioscopes with angular information*, *JCAP* **03** (2023) 001, [`arXiv:2211.00022`]

We further introduce the following improvements:

- More exhaustive and pedagogical discussion of the plasma effects

In this chapter, we discuss the solar production of DPs. For this, we need to discuss the more general topic of plasma/matter effects on the kinetic mixing portal. We will make several interesting observations, including the different decoupling behaviours of the transverse and longitudinal components. We will concentrate on the low-energy kinetic mixing parameter $\epsilon = \epsilon_B \cos\theta_W$ and the DP mass m for simplified notation, in agreement with our discussion of the low-energy decoupling of the Z boson in the low-energy regime presented in the previous chapter, e.g. in eq. (2.71c).

With the ever-increasing evidence for DM in the Universe, we have an excellent motivation to look for BSM. Despite enormous experimental efforts, we are still lacking convincing direct or indirect signals from DM beyond its gravitational impact. These null results have prompted parts of the community to shift their attention towards lighter and feebly coupled new physics. With the heavy DP discussed, it is time to investigate the light and very weakly coupled DP now as an outstanding example for such a new physics candidate. Therefore, we will focus on kinetic mixing only and use that the light DP behaves more photon-like than Z-like in this regime. We will focus on the DM aspects of the DP later in this thesis, but it should be noted that the DP is a valid DM candidate over a wide range of parameter space, offering a rich phenomenology even if DPs are only a fraction of the observed DM abundance.

In the following, we will consider the simplest case from chapter 2. We introduce a DP which has no gauge interactions with any other particles, neither from the visible nor the dark sector, such that the setup is completely described by the mixing parameter ϵ and the DP mass m. As mentioned above, it is favourable to generate a mass for the DP via the Stückelberg mechanism since it circumvents the strong exclusion limits on the case of a spontaneously broken $U(1)$ via a dark Higgs boson [38–40].

In general, DP limits extend over a massive parameter space. Usually, there is a boundary between heavy and light DPs around the MeV to GeV scale, and these two parts of the parameter space are typically shown separately. In particular, the mass threshold for decay of the DP into an electron-positron pair distinguishes two phenomenologically distinct regions. Although far from exhaustive, we have achieved a good understanding of the heavy DP in the previous chapter. The interested reader can find more on collider and beam dump experiments in Refs. [20, 94, 95]. In most of the literature, the light regime extends from the MeV/GeV scale down to the fuzzy DM [96, 97] regime at around 10^{-21} eV. We will discuss these ultralight DPs more in chapters 4 & 5 and so we will now focus more on the intermediate regime. There is an important distinction between two classes of DP searches with the first being a pure DP search while the second type relies on the DP being (a major part of) DM. In the latter case, there is an interesting mass region down to $\sim 10^{-7}$ eV which can be probed directly using so-called haloscopes [98–101], i.e. experiments looking directly for the presence of DPDM in the solar neighbourhood. The former case is more general and yields more powerful bounds which are typically harder to achieve though. Typically, one has to rely on indirect effects (like the impact of virtual DPs) or a local production mechanism.

In the following, we will discuss a local DP source of particular importance in more detail: the Sun. The Sun may copiously produce DPs with mass smaller or around its (core) temperature [102–106].[1] A thorough description of the DP's behaviour in the Sun requires the rigorous treatment of plasma effects, which can either resonantly increase or massively suppress the DP production. These plasma effects, and with it the "dark" luminosity of the Sun, depend sensitively on the DP mass, and so do the resulting DP limits. Conservatively demanding that the dark luminosity stays below the visible luminosity, we can constrain the coupling strength, i.e. the kinetic mixing strength, through this so-called solar cooling argument. Indeed, this argument is not confined to the Sun, but can also be applied to different astrophysical environments, such as horizontal branch stars, red giants [106] or neutron stars [107]. Additionally, these plasma effects are crucial to understanding the effect of DPs on early Universe cosmology [108–113]. One notable example of these effects is the distortion of the CMB black body spectrum by resonant photon-DP conversions. Finally, plasma effects might also play a role in black hole superradiance of DPs [114] where electrons can quench the superradiant instability.

Most of these plasma-effect-driven probes of the existence of a DP are considered indirect searches. However, we might also be able to directly observe the flux of DPs emerging from the Sun. This idea is similar to earlier proposals of solar axion searches [115, 116], i.e. we are looking for DPs oscillating into SM photons over a finite distance (called oscillation length). These so-called helioscopes such as CAST [117] do not require any modifications to be repurposed as DP searches [102]. On the contrary, DPs do not require a magnetic field to oscillate into SM photons and therefore, their setup is less involved which allows for the construction of simpler, dedicated DP-only helioscopes like SHIPS [118]. These searches are sensitive from several keV down to the μeV scale. Finally, there are even stronger limits from considering the absorption of the longitudinal DP component in conventional direct detection experiments [104, 105, 119, 120].

In this chapter, we explicitly work out that DP constraints from helioscopes can be improved significantly once their spectral and angular distributions are taken into account. This aspect has previously been ignored in the literature even though it was studied for axion searches [121].[2] To underline this point, we will present an analysis of the publicly

---

[1] The precise quantity of interest is the Sun's plasma frequency as we will see in the following discussion.

[2] Axions are known to be dominantly produced in the solar core.

available data of the Hinode X-Ray Telescope (XRT) [122], offering outstanding angular resolution. Furthermore, we extract spectral information from the data even though the energy resolution is originally rather poor. Our analysis is based on long exposure "darks", i.e. calibration images of the Sun taken with the telescope closed, resulting in a clear improvement of the DP limits over the naive strategy of just counting events without any spectral or angular information, mimicking previous helioscope searches. Even though not built to be a helioscope, we show that the additional information allows Hinode XRT to compete with purpose-built helioscopes.

Furthermore, we will also have a look at Hinode XRT data taken during a solar eclipse. This data set combines the large solar DP flux available at helioscopes with the advantageously long oscillation length of so-called light-shining-through-the-wall (LSW) experiments [19, 123, 124]. This "light shining through the Moon" experiment offers an unparalleled oscillation length using the entire distance between the Earth and the Moon. Of course, this comes at the price of small exposure times but we will show that the long oscillation baseline can compensate for this, leading to increased sensitivity below meV scale DP masses when compared to conventional helioscope searches. Of course, there were/are many x-ray satellites beyond Hinode XRT constantly tracking the solar activity [122, 125, 126] which in principle allow for even stronger constraints by combining several data sets and observations of multiple eclipses. This can also help to reject unphysical features in the data.

This chapter is divided into several sections. First of all, in section 3.1 we will discuss the solar production of DPs, especially focussing on the angular distribution in different mass regimes. In section 3.2, we will identify Hinode XRT as a very useful instrument for our kind of analysis. We will then present our analysis strategy, stressing the impact of proper calibration, background subtraction, and robust theory predictions for the angular and spectral distribution. For the next step, we put our results into the larger context of DP searches, ending in a generalisation of our results on helioscope searches and their effect on future experiments. Finally, we present a brief discussion of the overall results in 3.3. [3]

3.1 Solar production of DPs and their detection

This section briefly reviews the key properties of DPs in vacuum and then generalises the framework to homogeneous plasma environments. Afterwards, we discuss how this knowledge can be used to calculate the flux of solar DPs and their angular dependence.

3.1.1 DP oscillations in vacuum and homogeneous plasmas

Let us begin with a brief discussion of the vacuum physics of a massive DP A'_μ in the low-energy limit, i.e. ignoring the mixing with the Z boson. In this specific case, we can simplify eq. (2.1) for A'_μ and the photon A_μ in vacuum to the following form

$$\mathcal{L}_{\text{vac}} = -\frac{1}{4}F^{\mu\nu}F_{\mu\nu} - \frac{1}{4}F'^{\mu\nu}F'_{\mu\nu} - \frac{\epsilon}{2}F^{\mu\nu}F'_{\mu\nu} + j_\mu A^\mu + \frac{m^2}{2}A'^\mu A'_\mu \,, \tag{3.1}$$

where, as before, the off-diagonal kinetic term allows for coupling the dark and SM sector, with $F^{\mu\nu}$ ($F'^{\mu\nu}$) being the electromagnetic (dark) field strength. Redefining the fields yields again the canonical kinetic term, leading to either off-diagonal mass or interaction

---

[3] For the clarity of text, we have moved appendices from Ref. [1] to the corresponding parts in the main text.

terms.[4] We should stress that there are only two new parameters, namely the DP mass m and the mixing angle ϵ. Let us quickly write the interaction eigenbasis

$$A_\mu \to \frac{1}{\sqrt{1-\epsilon^2}} A_\mu \tag{3.2}$$

$$A'_\mu \to A'_\mu - \frac{\epsilon}{\sqrt{1-\epsilon^2}} A_\mu \tag{3.3}$$

$$\begin{aligned}\mathcal{L}_{\text{vac,int}} &= -\frac{1}{4}F^{\mu\nu}F_{\mu\nu} - \frac{1}{4}F'^{\mu\nu}F'_{\mu\nu} + \frac{1}{\sqrt{1-\epsilon^2}} j_\mu A^\mu \\ &\quad + \frac{m^2}{2}A'^\mu A'_\mu - \frac{\epsilon m^2}{\sqrt{1-\epsilon^2}} A^\mu A'_\mu + \frac{\epsilon^2 m^2}{1-\epsilon^2} A^\mu A_\mu\,,\end{aligned} \tag{3.4}$$

and the mass eigenbasis[5]

$$A_\mu \to \sqrt{1-\epsilon^2} A_\mu - \epsilon A'_\mu \tag{3.5}$$

$$A'_\mu \to \sqrt{1-\epsilon^2} A'_\mu + \epsilon A_\mu \tag{3.6}$$

$$\mathcal{L}_{\text{vac,m}} = -\frac{1}{4}F^{\mu\nu}F_{\mu\nu} - \frac{1}{4}F'^{\mu\nu}F'_{\mu\nu} + j_\mu \left(A^\mu - \frac{\epsilon}{\sqrt{1-\epsilon^2}} A'^\mu\right) + \frac{m^2}{2(1-\epsilon^2)} A_\mu A'^\mu\,. \tag{3.7}$$

Oscillations in vacuum

Staying in the interaction eigenbasis for now, the kinetic mixing introduces DP-photon oscillation completely analogous to neutrinos [127, 128]. As a result, any SM process producing photons can also produce DPs. In the case of small kinetic mixing, we can derive the oscillation formula in a very simplified quantum mechanical framework. For this, let us denote an interaction state DP by $|A'\rangle$ and a photon state by $|A\rangle$. Furthermore, we denote the mass eigenstates by $|\gamma'\rangle$ and $|\gamma\rangle$, respectively. Then, assuming we can approximate all fields as plane waves propagating in x direction, we find the following for the wave functions

$$|A(t)\rangle = \left(\sqrt{1-\epsilon^2}|\gamma(t)\rangle - \epsilon|\gamma'(t)\rangle\right) = \left(\sqrt{1-\epsilon^2}|\gamma(0)\rangle e^{ikx} - \epsilon|\gamma'(0)\rangle e^{ik'x}\right) e^{-i\omega t} \tag{3.8a}$$

$$|A'(t)\rangle = \left(\sqrt{1-\epsilon^2}|\gamma'(t)\rangle + \epsilon|\gamma(t)\rangle\right) = \left(\sqrt{1-\epsilon^2}|\gamma'(0)\rangle e^{ik'x} + \epsilon|\gamma(0)\rangle e^{ikx}\right) e^{-i\omega t} \tag{3.8b}$$

where we have written the initial amplitude using $|\gamma^{(\prime)}(0)\rangle$ and assumed that the time evolution of this state is given by the usual plane wave notation with energy ω and momentum k. Note that the mass eigenstates have fixed energy, but different momenta. With this, we can determine the oscillation probability $P(A \to A') = |\langle A(0)|A'(t)\rangle|^2$

$$\langle A(0)|A'(t)\rangle = \epsilon\sqrt{1-\epsilon^2}\left(e^{ikx} - e^{-ik'x}\right) e^{i\omega t} \tag{3.9}$$

$$\Rightarrow P(A \to A') = 4\epsilon^2\left(1-\epsilon^2\right)\sin^2\left((k-k')x\right) \tag{3.10}$$

where we have used several trigonometric relations and $x = x(t)$ with $x(0) = 0$ as we are free to shift the origin. Furthermore, we assumed orthogonality $\langle\gamma(0)|\gamma'(0)\rangle = 0$, while

---

[4] We see that in eq. (2.74) the DP couples to the EM current as well. To make the DP completely sterile, we would need another orthogonal rotation that would induce off-diagonal mass terms between DP and SM photon. Of course, the physics is invariant under this redefinition, but the interaction eigenbasis is more useful for lighter DPs as they tend to have a larger oscillation length than the typical interaction length scale.

[5] In this step we go from the interaction eigenbasis to the mass eigenbasis, i.e. the kinetically mixed basis is not involved. Thus we can apply an orthogonal rotation leaving the kinetic term invariant as demonstrated in chapter 2.

equal states are normalised to 1 as the interaction eigenstates are independent of each other and just the propagation drives the mixing. Assuming small mixing, i.e. $\epsilon \ll 1$, and further going to the ultra-relativistic limit[6] $k' = \sqrt{\omega^2 - m^2} \approx \omega - m^2/(2\omega)$ we get to leading order

$$P(A \leftrightarrow A') = (2\epsilon)^2 \sin^2\left(\frac{m^2 L}{4\omega}\right) , \tag{3.11}$$

where we have used that the above argument is symmetric in $A \leftrightarrow A'$. L is the distance from the creation point of the initial DP/photon and ω denotes the particle's energy. It should be emphasised again that this formula is only valid in vacuum. This is identical to the literature results, e.g. Ref. [103].

In the limit of $m^2 L \gg \omega$, we find that the probability rapidly oscillates with L which implies that the sine averages out to $\frac{1}{2}$ and the macroscopic effects (i.e. inside the detector) do not depend exactly on the involved energy and length scales. In particular, we can argue that eq. (3.11) is valid even if the DPs are not fully relativistic. In the opposite limit, $m^2 L \ll \omega$, we can apply the small-angle approximation which shows that the oscillation probability decreases with mass for fixed length and energy scale. From an intuitive point of view, this is not surprising as the superposition of photon and DP mass eigenstate sent out in an EM interaction is very degenerate in momentum, and therefore it takes very long for the two propagating modes to decohere. We conclude that any experiment searching for DP oscillation within some experimental apparatus of typical size L rapidly loses sensitivity as soon as the DP mass drops below $m < \sqrt{\omega/L}$. In particular, terrestrial helioscopes suffer from this effect, as we will point out in section 3.2.4. See also table 3.2 for a compilation of helioscopes and sensitivity range.

A first glance at plasma oscillations

The above can be handled with relative ease since apart from the two fundamental parameters ϵ and m, there is only an additional length scale L and an additional energy scale ω. If we now consider processes embedded in an EM plasma, there will be more scales of relevance, leading to a more complicated oscillation probability. Nevertheless, the plasma also opens up the option of resonant conversions and it changes the decoupling behaviour, making a dedicated study not only important but also very interesting with the potential of probing deep into new parameter space on resonance. For a first hint at plasma physics at work, let us briefly review the simplified calculation from Ref. [129]. Due to its interactions, the photon receives an effective mass m_γ inside an EM plasma [130], essentially given by the plasma frequency ω_p

$$m_\gamma \approx \omega_p = \sqrt{\frac{4\pi\alpha n_e}{m_e}} \tag{3.12}$$

with the electron mass m_e and electron density n_e.[7] In principle, all charged particles inside a given plasma contribute but as we focus on the relatively cold solar plasma, electrons and ions are the only (relevant) species. Since $m_e \ll m_{\text{ion}}$, it is sufficient to consider electrons for this simplified treatment.

---

[6] With the photon being massless we of course have $\omega = k$.

[7] More correctly, this is a contribution to the self-energy of the photon. There are many contributions in a generic plasma as shown by the concise review in Ref. [103] with a focus on the solar plasma.

In the interaction eigenbasis, only the photonic field couples to the plasma, inducing an effective mass. Therefore, eq. (3.2) will be modified to

$$\begin{aligned}\mathcal{L}_{\text{vac,int}} = &-\frac{1}{4}F^{\mu\nu}F_{\mu\nu} - \frac{1}{4}F'^{\mu\nu}F'_{\mu\nu} + \frac{1}{\sqrt{1-\epsilon^2}}j_\mu A^\mu \\ &+ \frac{m^2}{2}A'^{\mu}A'_\mu - \frac{\epsilon m^2}{\sqrt{1-\epsilon^2}}A^\mu A'_\mu + \frac{\epsilon^2 m^2 + m_\gamma^2}{1-\epsilon^2}A^\mu A_\mu\end{aligned} \quad , \tag{3.13}$$

where we have used that the interaction term modifies the effective value of the finestructure constant α and thus also ω_p. Furthermore, we have suppressed the spatial dependence of the photon mass which depends on the local properties of the plasma. In fact, for the case of solar production, this results in a radial dependence $m_\gamma = m_\gamma(\mathbf{r}) = m_\gamma(r)$ invoking spherical symmetry. Introducing this additional mass scale now opens up two limiting cases. For comparatively heavy DPs, i.e. $m \gg m_\gamma$, we can safely neglect all plasma effects and just work with the vacuum physics of the DP. In the opposite case, $m \ll m_\gamma$, we will find the well-known case of the DP decoupling at low masses in an otherwise empty dark sector. In the literature, one can often find a discussion that the purely massive case and the massless case are not the same [23], i.e. “$m = 0$” $\neq$ “$m \to 0$”. This claim is well justified, as the third degree of freedom (DOF) of the massive DP cannot continuously go to 0 like other properties of the DP. This is true in an idealised setup of pure vacuum, but in more realistic environments, there will come the point where the energy scale of matter effects $\sim m_\gamma$ will become larger than the DP mass if one just decreases m arbitrarily. Thus, there will be a rather smooth decoupling of the kinetic mixing. In conclusion, the following considerations are not in contradiction with the conceptual difference between massless and massive DPs.

To explore this further, let us go to the mass eigenbasis by diagonalising

$$\mathbf{M} = \begin{pmatrix} m^2 & \frac{-\epsilon m^2}{\sqrt{1-\epsilon^2}} \\ \frac{-\epsilon m^2}{\sqrt{1-\epsilon^2}} & \frac{\epsilon^2 m^2 + m_\gamma^2}{1-\epsilon^2} \end{pmatrix} . \tag{3.14}$$

Diagonalising this matrix yields the following physical masses

$$M_\pm^2 = \frac{m^2 + m_\gamma^2 \pm \sqrt{\left(m^2+m_\gamma^2\right)^2 - 4\left(1-\epsilon^2\right)m^2 m_\gamma^2}}{2\left(1-\epsilon^2\right)} , \tag{3.15}$$

where the + denotes the solution for the heavier particle, based on m and m_γ, i.e. M_+ is the DP mass if the “bare” DP mass m is larger than the plasma mass. This already hints at a degeneracy for $m = m_\gamma$ as we will see very soon.[8] Let us further consider the interaction part of this new mass eigenbasis where we denote the plasma basis with a subscript $_p$

$$A_p = \frac{\sqrt{1-\epsilon^2}m^2 - M_+^2}{\sqrt{(1-\epsilon^2)(m^2-M_+^2)^2 + \epsilon^2 m^4}} A + \frac{\epsilon m^2}{\sqrt{(1-\epsilon^2)(m^2-M_+^2)^2 + \epsilon^2 m^4}} A' \tag{3.16a}$$

$$A'_p = \frac{\sqrt{1-\epsilon^2}m^2 - M_-^2}{\sqrt{(1-\epsilon^2)(m^2-M_-^2)^2 + \epsilon^2 m^4}} A + \frac{\epsilon m}{\sqrt{(1-\epsilon^2)(m^2-M_-^2)^2 + \epsilon^2 m^4}} A' , \tag{3.16b}$$

---

[8] In fact, an exact degeneracy can never be reached as the term under the square root is always larger than 0 for physical parameters. This is known as avoided crossing [131, 132].

for $m > m_\gamma$ and

$$A_p = \frac{\sqrt{1-\epsilon^2}m^2 - M_+^2}{\sqrt{(1-\epsilon^2)(m^2-M_+^2)^2+\epsilon^2 m^4}}\,A - \frac{\epsilon m}{\sqrt{(1-\epsilon^2)(m^2-M_+^2)^2+\epsilon^2 m^4}}\,A' \tag{3.17a}$$

$$A'_p = \frac{\sqrt{1-\epsilon^2}m^2 - M_-^2}{\sqrt{(1-\epsilon^2)(m^2-M_-^2)^2+\epsilon^2 m^4}}\,A - \frac{\epsilon m}{\sqrt{(1-\epsilon^2)(m^2-M_-^2)^2+\epsilon^2 m^4}}\,A' \,, \tag{3.17b}$$

for $m < m_\gamma$. Although these results are exact, they are not particularly enlightening. To connect with well-known literature results, we will now expand in small mixing, i.e. $\epsilon \ll 1$. Then, we find for the states to leading order

$$A_p = A - \frac{\epsilon m^2}{|m_\gamma^2 - m^2|}\,A' \tag{3.18a}$$

$$A'_p = \frac{\epsilon m^2}{|m^2 - m_\gamma^2|}\,A + A' \,, \tag{3.18b}$$

which is valid for $m < m_\gamma$. Making contact with our results from eq. (3.7), we observe that we can define an effective kinetic mixing parameter here ϵ_{eff}

$$\epsilon_{\text{eff}} = \epsilon \frac{m^2}{|m_\gamma^2 - m^2|} \approx \begin{cases} \epsilon \,, & m^2 \gg m_\gamma^2 \\ \epsilon \frac{m^2}{m_\gamma^2} \,, & m^2 \ll m_\gamma^2 \end{cases} . \tag{3.19}$$

In complete analogy to the previous derivation of the vacuum oscillation, we can then modify eq. (3.11) with this new mixing parameter $\epsilon \to \epsilon_{\text{eff}}$. While the resonant region, i.e. $m = m_\gamma$ needs more scrutiny, we can already observe the important fact of the decoupling of the (transverse) DP. In the resonant regime, we expect the production rate to be massively boosted and additionally, we will find the interesting property of a factorisation between the spectral and the angular part of the DP flux. This result substantially simplifies the calculation of the flux, especially when compared to the two non-resonant regimes above and below the resonance. In the next subsection, we will use a more careful treatment of plasma effects to study this case.

A closer look at plasma effects

We will derive the above result now in more detail from the plasma equations in the presence of a DP. For this, we will show a minimal computation of the plasma frequency in a non-relativistic plasma of electrons by combining Maxwell's equations extended by a massive dark photon and the equations of motion (EOMs) for an electron in a background field. For an analytical solution, this requires a linearisation of the equations. This calculation is inspired by the work in Ref. [133] and is originally based on classical plasma physics presented e.g. in Ref. [134]. We will, however, simplify to a scenario in which the electrons do not experience any scattering.

In such a plasma environment, the electron velocity follows the momentum conservation equation

$$m_e \frac{\partial \mathbf{v}_e}{\partial t} + m_e \left(\mathbf{v}_e \cdot \nabla\right) \mathbf{v}_e = -e\left(\mathbf{E} - \frac{\epsilon}{\sqrt{1-\epsilon^2}}\mathbf{E}' + \mathbf{v}_e \times \left(\mathbf{B} - \frac{\epsilon}{\sqrt{1-\epsilon^2}}\mathbf{B}'\right)\right) \,, \tag{3.20}$$

where we denote the electron velocity and mass by $\mathbf{v}_e$ and m_e, respectively. Furthermore, we have introduced the electric and magnetic fields in the above mass eigenbasis. This basis further provides us with the modified Maxwell's equations in the form of

$$\left(\Box - \begin{pmatrix} \frac{m^2}{1-\epsilon^2} & 0 \\ 0 & 0 \end{pmatrix}\right) \begin{pmatrix} A'_\mu \\ A_\mu \end{pmatrix} - \partial_\mu \partial^\nu \begin{pmatrix} A'_\nu \\ A_\nu \end{pmatrix} = \begin{pmatrix} \frac{-\epsilon}{\sqrt{1-\epsilon^2}} \\ 1 \end{pmatrix} j_\mu \,, \tag{3.21}$$

where we used that the photon and the DP couple to the same current but with different strengths. Our first observation is that the temporal component of the field is fully determined by the (pseudo-)Lorenz condition (see also Chapter 5)

$$\partial^\mu A^{(\prime)}_\mu = 0 \,. \tag{3.22}$$

Although this is a pure gauge choice for the photon, we can see that this is a required condition for the DP if we apply an additional partial derivative ∂^μ to eq. (3.21). Since the current is conserved, the RHS is eliminated by that operation. The d'Alembertian, on the other hand, cancels with the additional derivative term, and thus we see that the additional mass term truly enforces the above condition. We will therefore from now on drop the additional derivative term beyond the box operator in the eom. Furthermore, we will focus on the 3-vector component of the fields since we can always determine the temporal component via eq. (3.22).

For our next step, we will introduce the Fourier transformation for our quantities of interest. We will assume that there are no background fields and that the plasma is non-relativistic. We can therefore treat the fields and the electron velocity as perturbations. For a generic quantity, we then have

$$X(\mathbf{x}, t) = \frac{1}{4\pi^2} \int d\omega d^3k \, X(\mathbf{k}, \omega) e^{-i(\omega t - \mathbf{k}\cdot\mathbf{x})} \,. \tag{3.23}$$

We can then solve the EOM of the electron velocity in Fourier space

$$\mathbf{v}_e = -i \frac{e}{m_e \omega} \left(\mathbf{E} - \frac{\epsilon}{\sqrt{1-\epsilon^2}} \mathbf{E}' \right) \,, \tag{3.24}$$

where we have neglected all second-order quantities, i.e. the gradient and the magnetic field term. For Maxwell's equations, we will split the vector fields into transverse and longitudinal component

$$\mathbf{A} = A_L \frac{\mathbf{k}}{k^2} + \mathbf{A}_T \quad \text{with} \quad \mathbf{k} \cdot \mathbf{A}_T = 0 \,. \tag{3.25}$$

Deriving the electric field from this decomposition and the previous Lorenz condition, we find

$$\partial^\mu A^{(\prime)}_\mu = 0 \Leftrightarrow i\omega A^{(\prime)}_0 = i A_L \tag{3.26}$$

$$\Rightarrow \mathbf{E}^{(\prime)} = -\nabla A^{(\prime)}_0 - \partial_t \mathbf{A}^{(\prime)} = i\omega \left[\left(1 - \frac{k^2}{\omega^2} \right) A^{(\prime)}_L \frac{\mathbf{k}}{k^2} + \mathbf{A}^{(\prime)}_T \right] \,, \tag{3.27}$$

which means that longitudinal and transverse components will contribute differently to the non-relativistic current density

$$j_\mu = -(n_e, n_e \mathbf{v}_e) \tag{3.28}$$

$$\Rightarrow \mathbf{j} = \omega_p^2 \left[\left(\left(1 - \frac{k^2}{\omega^2} \right) A_L \frac{\mathbf{k}}{k^2} + \mathbf{A}_T \right) - \frac{\epsilon}{\sqrt{1-\epsilon^2}} \left(\left(1 - \frac{k^2}{\omega^2} \right) A'_L \frac{\mathbf{k}}{k^2} + \mathbf{A}'_T \right) \right] \,, \tag{3.29}$$

where we have introduced the electron density again from eq. (3.12). For a stationary electron density, current conservation dictates that the temporal component is not required to determine the EM and DP fields. This leads to two different sets of EOMs

$$\left(\omega^2 + \begin{pmatrix} \frac{m^2}{\left(1-\frac{k^2}{\omega^2}\right)(1-\epsilon^2)} + \frac{\epsilon^2\omega_p^2}{(1-\epsilon^2)} & -\frac{\epsilon\omega_p^2}{\sqrt{1-\epsilon^2}} \\ -\frac{\epsilon\omega_p^2}{\sqrt{1-\epsilon^2}} & \omega_p^2 \end{pmatrix}\right)\begin{pmatrix} A'_L \\ A_L \end{pmatrix} = 0 \ , \tag{3.30}$$

and

$$\left(\omega^2 - k^2 - \begin{pmatrix} \frac{m^2+\epsilon^2\omega_p^2}{(1-\epsilon^2)} & -\frac{\epsilon\omega_p^2}{\sqrt{1-\epsilon^2}} \\ -\frac{\epsilon\omega_p^2}{\sqrt{1-\epsilon^2}} & \omega_p^2 \end{pmatrix}\right)\begin{pmatrix} A'_T \\ A_T \end{pmatrix} = 0 \ . \tag{3.31}$$

This already hints at the fact that the longitudinal mode of the DP is non-propagating. This becomes apparent if we send $\epsilon \to 0$, in which case photon and DP decouple, and thus all the k dependence drops out of the EOM. This is an indicator that the longitudinal mode is just a so-called plasmon, i.e. an excitation of the plasma and not of the EM field. We see that we have re-derived eq. (3.14) from first principles, and we can now understand better the physical origin of this effect. We further realise that the above argument is only valid for transverse modes, but these will be the focus of this chapter anyway. However, we note that the longitudinal component requires greater care as the wave function renormalisation needs to be taken into account [106].

Now that we have derived the plasma frequency in this simplified framework, let us investigate the resonant regime under more realistic conditions. At the moment, it seems like the oscillation probability diverges, cf. eq. (3.11) plugging in eq. (3.19). This is an unphysical result. The reason for this behaviour is the lack of damping in the plasma EOMs above. One contribution to this damping would be the interactions of the electrons with the ions of the plasma. This Coulomb term was taken into account e.g. in Ref. [133]. With this choice, the above calculation essentially reproduces the Drude model of electrical conduction [135]. For the solar plasma, different contributions dominate the picture [102, 103]. The quantity to consider in general is the (transverse) photon self-energy in the plasma Π [102, 136] that yields the oscillation probability

$$\Pi = m_\gamma^2 + i\omega\Gamma \tag{3.32}$$

$$P(A_T \to A'_T) \simeq \frac{\epsilon^2 m^4}{\left(m_\gamma^2 - m^2\right)^2 + \omega^2\Gamma^2} \ , \tag{3.33}$$

which is valid for small ϵ and at distances from the point of photon production beyond an absorption length Γ^{-1} [102–104, 106]. Strictly speaking, this result is only valid for homogeneous plasmas, for a treatment of inhomogeneous plasmas we refer to Refs. [102, 103]. However, in a plasma that only mildly changes in time and/or position, this expression is still a robust approximation.[9] At leading order and with focus on electrons, we find $m_\gamma = \omega_p$ and

$$\Gamma = \frac{8\pi\alpha^2}{3m_e^2} n_e \ . \tag{3.34}$$

As mentioned above, for a more thorough discussion of the different contributions, we refer the interested reader to [103].

---

[9] The quantity of interest is given by ΓL where L denotes the length scale of the inhomogeneities of the plasma.

These ingredients are already sufficient for a discussion of solar DP production which we will do in the following subsection. In that context, we will learn that Γ also plays an important role in DP production beyond the damping of the resonance. In a thermodynamical context, Γ is known as the absorption coefficient.

3.1.2 Solar DP physics

In the following, we will specialise the previous discussion more towards solar DP production. We will reproduce parts of the exhaustive discussion from Refs. [102, 103] here. Additional literature [104, 106] focuses more on the longitudinal component of the DP which is, for most parts of this chapter, of secondary interest, as outlined above and discussed in further detail in section 3.1.3.

Our description of solar DP production is based on the solar standard model [137–139] that provides us with solid predictions of the plasma properties. Our original publication [1] was the first work to explicitly estimate the angular distribution of DPs over the entire mass spectrum. In the following, we will explain these estimates in detail.

General considerations

We now derive the total production rate of DPs. The first ingredient we need is the local production rate of photons Γ_{prod}. Assuming local thermodynamic equilibrium, we generally have the following

$$\Gamma_{\text{prod}} = e^{-\omega/T}\Gamma_{\text{abs}} \, , \tag{3.35}$$

where we have further introduced the absorption rate Γ_{abs} and the temperature of the plasma T. Of course, $T = T(r)$ carries a radial dependence inside the Sun. We now want to relate this quantity to the damping rate (or absorption coefficient) Γ encountered before. The relevant expression is $\Gamma = \Gamma_{\text{prod}} - \Gamma_{\text{abs}}$. We therefore conclude

$$\Gamma_{\text{prod}}(\omega, \mathbf{r}_0) = \frac{\Gamma(\omega, \mathbf{r}_0)}{e^{\omega/T(\mathbf{r}_0)} - 1} \, . \tag{3.36}$$

The production rate of DPs at one point $\mathbf{r}_0$ can be written as [102]

$$\frac{\mathrm{d}N}{\mathrm{d}V\mathrm{d}t}(\mathbf{r}_0) = 2\int \frac{\mathrm{d}^3k}{(2\pi)^3}\Gamma_{\text{prod}}(\omega, \mathbf{r}_0)P(\omega, \mathbf{r}(l)) \, , \tag{3.37}$$

where we have furthermore introduced the oscillation probability P which needs to be multiplied by the photon production rate to get the DP production rate. This, as we have seen, depends sensitively on the local plasma properties. Therefore, the correct argument for P is $\mathbf{r}(l) = \mathbf{r}_0 + l\hat{\mathbf{k}}$, the path from the point of creation to the point of observation in the direction of the produced DP $\hat{\mathbf{k}}$ at a distance l. The whole setup is sketched in 3.1. Finally, we integrate over all momenta to derive the total production of DPs at a given l away from a given point $\mathbf{r}_0$ which implicitly depends on the energy of the initial photon and the local plasma properties via the oscillation probability. Finally, it should be noted that we took into account a factor of two for the two transverse polarisations of the DP.

We can simplify this expression further via the on-shell relation $\omega^2 = k^2 + m^2$ and the rotational symmetry of the momentum in eq. (3.37) to find

$$\frac{\mathrm{d}N}{\mathrm{d}V\mathrm{d}t} = \frac{4\pi}{(2\pi)^3}\int \mathrm{d}\cos\theta_k k^2\mathrm{d}k\frac{\Gamma(\omega, \mathbf{r}_0)}{e^{\omega/T(\mathbf{r}_0)} - 1}P(\omega, \mathbf{r}(l)) \tag{3.38}$$

$$\Rightarrow \frac{1}{4\pi R_e^2}\frac{\mathrm{d}N}{\mathrm{d}V\mathrm{d}t\mathrm{d}\omega} = \frac{\mathrm{d}\Phi}{\mathrm{d}V\mathrm{d}\omega} = \frac{\omega\sqrt{\omega^2 - m^2}}{8\pi^3R_e^2}\int \mathrm{d}\cos\theta_k\frac{\Gamma(\omega, \mathbf{r}_0)}{e^{\omega/T(\mathbf{r}_0)} - 1}P(\omega, \mathbf{r}(l)) \, , \tag{3.39}$$

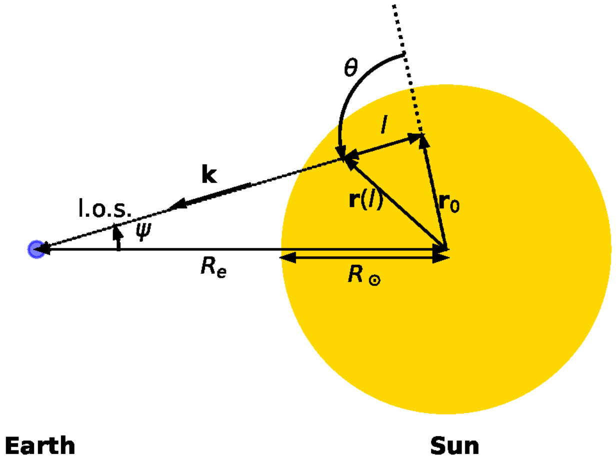

Figure 3.1: Sketch of the Sun-Earth system (adapted from Ref. [103]), where all geometric quantities necessary to calculate the solar DP flux are defined. Assuming that the Sun is to good approximation isotropic, the angular flux will only depend on the angle ψ under which the Sun is observed.

where we have defined the flux of DPs Φ at the position of Earth, i.e. at distance R_e from the Sun. Now in the next step, we integrate over the entire solar volume to compute the total spectral[10] DP flux of the Sun

$$\frac{\mathrm{d}\Phi}{\mathrm{d}\omega} = \frac{\omega\sqrt{\omega^2 - m^2}}{8\pi^3 R_e^2} \int_{\text{sun}} \mathrm{d}V \int \mathrm{d}\cos\theta_k \frac{\Gamma(\omega, r)}{e^{\omega/T(r)} - 1} P(\omega, \mathbf{r}(l)) \tag{3.40}$$

$$= \frac{\omega\sqrt{\omega^2 - m^2}}{2\pi^2 R_e^2} \int_0^{R_\odot} r^2 \mathrm{d}r \int_{-1}^{1} \mathrm{d}\cos\theta \frac{\Gamma(\omega, r)}{e^{\omega/T(r)} - 1} P(\omega, r, \theta) \tag{3.41}$$

with $R_\odot$ denoting the solar radius. Furthermore, we used that P can only depend on the radial coordinate r as well as the angle θ between $\mathbf{r}$, i.e. the position vector, and $\mathbf{k}$, i.e. the photon's/DP's momentum. Thus we have defined $\mathbf{r} \cdot \mathbf{k} = rk\cos\theta$ while we performed the remaining trivial angular integral.

The angular distribution

In the following, we will refine the previous calculation by adding also the angular dependence of the rate. As we assume the Sun to obey perfect spherical symmetry, the signal can only depend on ψ, the angle under which we observe the Sun as also shown in fig. 3.1. In other words, the 2D image of the Sun in DPs will have exact polar symmetry.

Let us now become more explicit with the calculation. For the angular flux, we must consider only the DP production along a given line of sight (l.o.s.) as shown in figure 3.1. The l.o.s. can be parametrised by its radius r (in solar centric coordinates) and the point

---

[10] In the previous and following paragraphs, we have made and will often make use of the terms “angular” and “spectral”. Let us therefore define them in a bit more detail here. Generically, this refers to the differential spectrum of DPs observed from the Earth. Angular here refers to the dependence of the flux on the radius of the 2D projection of the Sun that we observe while spectral is identified with the energy distribution of the flux.

of closest distance to the solar core $r_{\rm min}$. We find

$$\frac{\mathrm{d}\Phi}{\mathrm{d}\omega\mathrm{d}\Omega} = \frac{\omega\sqrt{\omega^2-m^2}}{4\pi^3}\int_{\rm l.o.s.} \mathrm{d}s \frac{\Gamma(\omega,r)}{e^{\omega/T(r)}-1} P(\omega,\mathbf{r}(l)) \tag{3.42}$$

$$= \frac{\omega\sqrt{\omega^2-m^2}}{4\pi^3}\int_{r_{\rm min}}^{R_\odot} \frac{2r\mathrm{d}r}{\sqrt{r^2-r_{\rm min}^2}} \frac{\Gamma(\omega,r)}{e^{\omega/T(r)}-1} P(\omega,r,\theta)\ , \tag{3.43}$$

which, following Ref. [103], can be further simplified under the assumption that the typical oscillation length of the photon into the DP is always much smaller than the scale of gradients in the plasma, i.e. the plasma is assumed to be locally homogeneous. We will now make good use of the general expression derived above. Doing so requires to plug in the oscillation probability from above, i.e. eq. (3.33) with $m_\gamma \to m_\gamma(r)$ and $\Gamma \to \Gamma(r)$.[11] The radial dependence of the plasma mass and the absorption coefficient are important for the position and the strength of the potential resonance of the conversion probability. We note in passing that this setup allows us to connect the microphysics of the oscillation to the macroscopic plasma properties, such as its electron density.

The resonant regime

Let us first investigate the arguably most interesting regime of $m \approx m_\gamma(r)$, i.e. the resonance condition is fulfilled. This equality is only valid for a finite mass window as the maximum plasma mass in the Sun is capped by the densities in the core while for the lowest mass, the resonance will be Boltzmann suppressed in the outer solar layers due to the low temperatures compared to our energies of interest, cf. eq. (3.36).[12] In this mass range, which will be defined later in more detail, there will be a radius $r = r_*$ where the resonance condition is met. A thin shell around that radius will dominate the total production of DPs. To understand this, let us evaluate the conversion probability in more detail, especially in the resonance region.

To derive the full distribution, we need to focus on the spectral part in eq. (3.41) first, plugging in explicitly the conversion probability. In the resonant regime, we can use the narrow resonance approximation

$$P(\omega,r,\theta) = \frac{\epsilon^2 m^4}{(m_\gamma^2(r)-m^2)^2+(\omega\Gamma(\omega,r))^2} \xrightarrow{\Delta r_* \ll R_\odot} \frac{\pi\epsilon^2 m^4 \delta(r-r_*)}{\omega\Gamma(\omega)\left|\frac{\mathrm{d}m_\gamma^2}{\mathrm{d}r}\right|} \tag{3.44}$$

with $\Delta r_* = \omega\Gamma(\omega,r_*)\left|\mathrm{d}m_\gamma^2/\mathrm{d}r\right|_{r_*}^{-1}$ defining the sharpness of the resonance. For this step we have first expanded the plasma mass of the photon around the radius of resonance, i.e. where $m_\gamma(r_*) = m$. This expansion yields

$$m_\gamma^2(r) \approx m_\gamma^2(r_*) + \left.\frac{dm_\gamma^2}{dr}\right|_{r_*}(r-r_*)\ , \tag{3.45}$$

which naturally explains the appearance of $(r-r_*)$ in eq. (3.44). In the next step, we follow the discussion of Ref. [103] where it was discussed that the previously introduced Δr_* resonance width is sufficiently narrow to allow for the approximation of the Breit-Wigner term as a $\delta-$distribution

$$\frac{1}{\pi}\frac{\epsilon}{x^2+\epsilon^2} \xrightarrow{\epsilon\to 0} \delta(x)\ . \tag{3.46}$$

---

[11] Note also the brief discussion on spatially varying plasmas in that context.

[12] See also Ref. [103] for a very thorough discussion of the more technical details of the oscillation probability and the outskirts of the solar plasma.

In passing, we note that with the previous discussion, we now have a hierarchy of length scales: we demand that the plasma changes slowly on scales of an oscillation length l_{plasma} and also, the resonance region is supposed to be much smaller than the radial extent of the Sun, i.e. $l_{\text{plasma}} \ll \Delta r_* \ll R_\odot$. Using the above approximation we find

$$\frac{\mathrm{d}\Phi}{\mathrm{d}\omega} \approx \frac{\omega\sqrt{\omega^2 - m^2}}{2\pi^2 R_e^2} \int_0^{R_\odot} r^2 \mathrm{d}r \int_{-1}^{1} \mathrm{d}\cos\theta \frac{\Gamma(\omega, r)}{e^{\omega/T(r)} - 1} \frac{\pi\epsilon^2 m^4 \delta(r - r_*)}{\omega\Gamma(\omega, r_*) \left|\frac{\mathrm{d}m_\gamma^2}{\mathrm{d}r}\right|_{r_*}} \tag{3.47}$$

$$= \epsilon^2 m^4 \frac{r_*^2}{R_e^2} \frac{\sqrt{\omega^2 - m^2}}{\pi\left(e^{\omega/T(r_*)} - 1\right)\left|\frac{\mathrm{d}m_\gamma^2}{\mathrm{d}r}\right|_{r_*}} , \tag{3.48}$$

which agrees with Ref. [102] except for a factor of $\pi/2$ which can be traced back to a slight normalisation error in the implementation of the narrow resonance in the original work.[13]

This result now allows us to evaluate eq. (3.43) explicitly

$$\frac{\mathrm{d}\Phi}{\mathrm{d}\omega\mathrm{d}\Omega} \approx \frac{\omega\sqrt{\omega^2 - m^2}}{4\pi^3} \int_{r_{\text{min}}}^{R_\odot} \frac{2r\mathrm{d}r}{\sqrt{r^2 - r_{\text{min}}^2}} \frac{\Gamma(\omega, r)}{e^{\omega/T} - 1} \frac{\pi\epsilon^2 m^4 \delta(r - r_*)}{\omega\Gamma(\omega)\left|\frac{\mathrm{d}m_\gamma^2}{\mathrm{d}r}\right|} \tag{3.49}$$

$$= \left(\epsilon^2 m^4 \frac{r_*^2}{R_e^2} \frac{\sqrt{\omega^2 - m^2}}{\pi(e^{\omega/T} - 1)\left|\frac{\mathrm{d}m_\gamma^2}{\mathrm{d}r}\right|}\right) \left(\frac{1}{2\pi} \frac{R_e}{r_*} \frac{1}{\sqrt{\psi_*^2 - \psi^2}} \Theta(r_* - r_{\text{min}})\right) , \tag{3.50}$$

which invites us to factorise the angular from the spectral part

$$\frac{\mathrm{d}\Phi_{\text{res}}}{\mathrm{d}\omega\mathrm{d}\Omega} \approx \frac{\mathrm{d}\Phi}{\mathrm{d}\omega} \frac{\mathrm{d}X_{\text{res}}}{\mathrm{d}\Omega} , \tag{3.51}$$

using $\mathrm{d}\Phi/\mathrm{d}\omega$ according to eq. (3.41) and

$$\frac{\mathrm{d}X_{\text{res}}}{\mathrm{d}\Omega} = \frac{1}{2\pi} \frac{R_e}{r_*} \frac{1}{\sqrt{\psi_*^2 - \psi^2}} \Theta(r_* - r_{\text{min}}) . \tag{3.52}$$

Notation-wise we follow Ref. [103] here, i.e. we define the angle $\psi = \frac{r_{\text{min}}}{R_e}$ (see figure 3.1) and the resonance angle $\psi_* = \psi\big|_{m=m_\gamma}$. However, our final result slightly deviates from the discussion found in Ref. [103], in particular in the normalisation factor. Let us therefore quickly demonstrate that our result is indeed correctly normalised in the sense of an angular distribution

$$\int \mathrm{d}\Omega \frac{\mathrm{d}X}{\mathrm{d}\Omega} \approx \frac{2\pi}{2\pi} \int_0^{\psi_*} \frac{R_e}{r_*} \frac{\sin\psi\mathrm{d}\psi}{\sqrt{\psi_*^2 - \psi^2}} = \frac{R_e}{r_*}\psi_* = 1 . \tag{3.53}$$

For this result, we used that $\psi \ll 1$ over the entire integration range, i.e. the Sun only covers a small part of the solid angle. In contrast, the corresponding formula in Ref. [103] does not fulfil this normalisation condition, although nevertheless, the approximate shape of the angular distribution is qualitatively similar. We will therefore use the expression derived above in the following analysis, disregarding the literature result.

We will now discuss the applicability of the narrow resonance approximation in more detail. Looking at the photon mass of the solar plasma, we can roughly see that the resonance condition can only be met for a small interval of DP masses [5, 300] eV. As already mentioned above, since the Sun more or less continuously goes over into the interplanetary medium, we would expect that for $m < 5\,\text{eV}$ there will be resonances in the outer

---

[13] While this error indeed makes the angular spectrum somewhat inconsistent, the $\mathcal{O}(1)$ differences will hardly affect the exclusion bounds.

solar region. Fortunately, the exponential suppression in eq. (3.36) will render any contribution from this region irrelevant anyway for the x-ray energies we are interested in.[14] Helioscopes can be sensitive in a much larger mass range of $[10^{-6}, 10^{3}]\,\mathrm{eV}$ which requires us to also investigate the non-resonant regimes above and below the mass window. With the breakdown of the narrow width resonance, the factorisation of the angular and energy dependence will not be available to us as a tool of simplification since the absorption term now depends inseparably on position *and* energy. With a full numerical calculation being computationally very expensive, an approximate expression for the angular distribution in these cases is still very desirable. Here, we recap these approximate formulae, which have been presented for the first time in Ref. [1] derived from basic arguments.

The non-resonant regimes

To begin with, we note that there are of course two distinct non-resonant regimes. On the one hand, we have the suppressed regime ($m < m_{\gamma,\mathrm{min}} \sim 5\,\mathrm{eV}$) where plasma effects start suppressing the impact of kinetic mixing, while on the other hand, we have the unsuppressed/vacuum-like regime ($m > m_{\gamma,\mathrm{max}} \sim 300\,\mathrm{eV}$) where the DP barely feels the presence of the plasma. Our approximate expressions rely on the weak energy dependence of the flux which we will use now for both cases. We will label the relevant quantities with the subscript $_{\mathrm{vac}}$ and $_{\mathrm{sup}}$, respectively. Thus, for fixed values of ϵ and m we find

$$P_{\mathrm{vac}}(\omega, r, \theta) \approx \frac{\epsilon^2 m^4}{\left(m_\gamma^2(r) - m^2\right)^2 + \left(\omega\Gamma(\omega, r)\right)^2} \xrightarrow{m \gg m_\gamma} \mathrm{const} \tag{3.54}$$

$$\Rightarrow \frac{\mathrm{d}\Phi_{\mathrm{vac}}}{\mathrm{d}\omega\mathrm{d}\Omega} \propto \int_{r_{\mathrm{min}}}^{\infty} \frac{2r\mathrm{d}r}{\sqrt{r^2 - r_{\mathrm{min}}^2}} \frac{n_e(r)}{e^{\omega/T(r)} - 1}\,, \tag{3.55}$$

and analogously for the suppressed case

$$P_{\mathrm{sup}}(\omega, r, \theta) \xrightarrow{m \ll m_\gamma} \frac{\mathrm{const}}{m_\gamma^4(r)} \tag{3.56}$$

$$\Rightarrow \frac{\mathrm{d}\Phi_{\mathrm{sup}}}{\mathrm{d}\omega\mathrm{d}\Omega} \propto \int_{r_{\mathrm{min}}}^{\infty} \frac{2r\mathrm{d}r}{\sqrt{r^2 - r_{\mathrm{min}}^2}} \frac{n_e(r)}{e^{\omega/T(r)} - 1} m_\gamma^{-4}(r)\,. \tag{3.57}$$

For both expressions, we made the crucial assumption that the absorption coefficient Γ is dominated by the contribution from the solar electron density.[15] In general, the electron density should qualitatively track the general behaviour of the absorption coefficient. This approximation should be seen as a first attempt to calculate the angular spectrum explicitly and not as a high-precision prediction for the solar DP flux. The angular dependence of the flux arises directly from the integration limit r_{min}.

Now in the next step, we obtain the angular distribution of DPs for a telescope/helioscope of our choice.[16] For that we convolute the flux of DPs with the energy-dependent efficiency $Q(\omega)$ of the given instrument, which yields

$$\frac{\mathrm{d}X_{\mathrm{vac/sup}}}{\mathrm{d}\Omega} \propto \int_{E_{\mathrm{min}}}^{E_{\mathrm{max}}} \mathrm{d}\omega\; Q(\omega) \frac{\mathrm{d}\Phi_{\mathrm{vac/sup}}}{\mathrm{d}\omega\mathrm{d}\Omega}\,. \tag{3.58}$$

---

[14] This is fortunate as the breakdown of spherical symmetry in the outer solar layers makes the calculation much harder if not impossible.

[15] See Ref. [103] for a detailed discussion of all contributions.

[16] For consistency, we also need to introduce the binning which becomes important later in our analysis. We do this by dividing the signal region into 50 annuli $[r_j, r_{j+1}]$ of equal width, allowing for radial binning of the events. We further divide the energy spectrum into 10 bins $[E_i, E_{i+1}]$ of equal size.

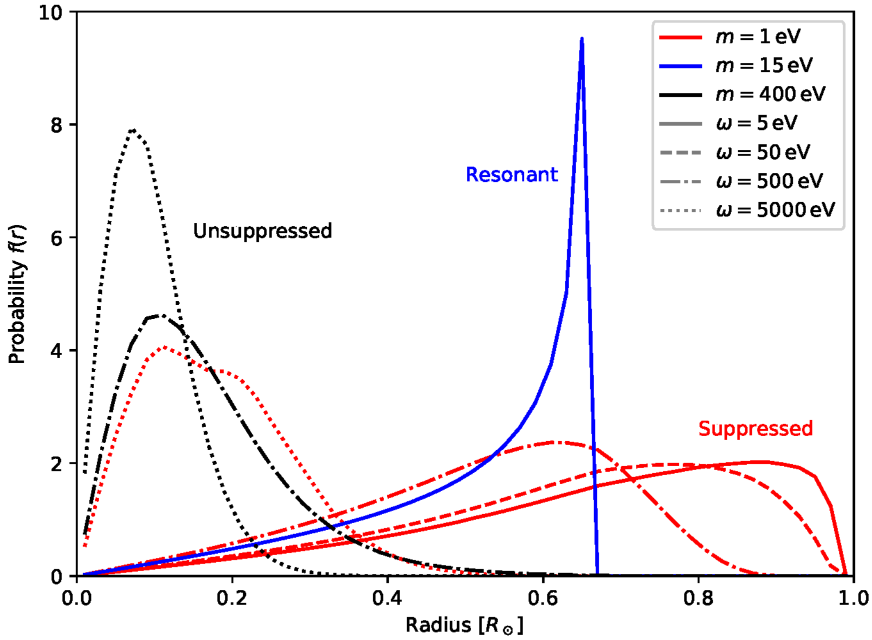

Figure 3.2: Examples of different angular shapes of the DP distribution in the suppressed (red), resonant (blue), and unsuppressed (black) regimes. $f(r)$ is the probability density of these distributions normalised such integration over the dimensionless radius $r/R_\odot$ yields 1. It should be noted that the resonant case is *not* energy-dependent except for the obvious kinematic threshold of $m < \omega$ while the other two are directly dependent on the energy.

This approximation is reasonable as long as the range of integration $[E_{\mathrm{min}}, E_{\mathrm{max}}]$ is smaller than the scale of significant changes in the DP production rate.[17] Setting appropriate values of $E_{\mathrm{min/max}}$, eq. (3.58) can either be used for the entire spectrum or individual bins.

Now in the final step, we use the temperature, density and plasma mass in dependence on the radius shown in Ref. [102] which were originally published in Ref. [137]. The only issue left for us is the normalisation which we need to fix by hand. Therefore, we can write an effectively factorised angular DP flux using the tools used above

$$\frac{\mathrm{d}\Phi_{\mathrm{res/vac/sup}}}{\mathrm{d}\omega \mathrm{d}\Omega} \approx \frac{\mathrm{d}\Phi}{\mathrm{d}\omega} \frac{\mathrm{d}X_{\mathrm{res/vac/sup}}}{\mathrm{d}\Omega}\,, \tag{3.59}$$

which explicitly depends on the detector properties.[18] This approximation can of course be applied to both non-resonant regions. With the steps shown above, we have demonstrated that within reasonable precision we can factorise the spectrum for all masses and energies as made explicit in eq. (3.59), i.e. we can use the prediction of $\frac{\mathrm{d}\Phi}{\mathrm{d}\omega}$ from Ref. [103] for all regimes.[19]

While we will consider specific instruments and their explicit efficiency functions later in section 3.2 we should briefly consider the predictions without weighted averaging, i.e. specifying a DP energy. In this context, we define

$$f(r) \equiv 2\pi \frac{r}{R_e} \frac{\mathrm{d}X}{\mathrm{d}\Omega} \frac{\mathrm{d}\psi}{\mathrm{d}r} = \frac{r}{R_e} \frac{\mathrm{d}X}{\mathrm{d}r}\,, \tag{3.60}$$

---

[17] This specifies the rather vague requirement of “weak energy dependence” from above.

[18] In particular, the approximation technically becomes better if the energy range of the detector is narrow.

[19] Thanks to Javier Redondo for providing the tabulated dark photon predictions!

which yields the probability of finding a DP coming from a solar ring of radius r with width $\mathrm{d}r$ given by $f(r)\mathrm{d}r$. This probability distribution is displayed in figure 3.2 where, as expected, the resonant regime shows a strong peak where $r = r_*$, i.e. $m_\gamma(r_*) = m$. The position of this peak is independent of the DP energy as long as the resonant production is kinematically allowed. In contrast to that, the radial distribution of the suppressed and vacuum-like regimes is both broader and energy-dependent. The vacuum-like case in particular has a distinct peak close to the solar centre as it massively benefits from the high densities which allow for larger production rates. Interestingly, these high densities suppress the production in the suppressed case[20] which pushes the maximum of the distribution towards larger radii, especially for the lowest energies. In other words, there is a competition between the enhanced production of photons and the suppressed conversion into DPs in this case. For the highest energies available, the main contribution will nevertheless come from the solar centre due to the exponential/Boltzmann suppression in the solar outer, i.e. colder, regions according to eq. (3.36).

3.1.3 DP oscillation and detection

After its production, a transversely polarised DP inside the Sun will propagate through the solar plasma and may oscillate back into a visible, i.e. (mostly) interacting, photon. However, the solar plasma will constantly project the DP onto its local propagation eigenstate since the interacting component quickly gets absorbed. Therefore, using the rather slow change of the plasma density on typical oscillation scales and the efficient absorption processes even far in the outer regions of the Sun the DP will approach its *vacuum propagation eigenstate* when leaving the Sun [102].[21] Thus, the DP will propagate through the vacuum without oscillating back into the vacuum photon state irrespective of the travelled distance.

Nevertheless, as soon as this DP state passes through dense matter (like the shutter of a telescope or the Moon), the interacting component of the DP will be absorbed by EM interactions. Then, the DP will leave the medium in the *sterile interaction eigenstate* instead of the propagation eigenstate.[22] Now with the DP in an interaction eigenstate, the two different mass eigenstates will start to decohere and an oscillation probability will build up.

Before beginning our analysis in more detail, let us quickly discuss the case of longitudinal DPs. Unfortunately, longitudinal DPs can effectively only show up due to matter effects as the vacuum state of the photon is purely transverse. This results in an issue for helioscope detection: the propagating DP mode cannot oscillate as there is no photonic counterpart. However, inside a dense medium, absorption of the longitudinal mode is still possible, which allows for direct detection experiments to search for solar DPs.

For masses below 1 eV, the longitudinal component even gives the dominant contribution of the total solar DP flux, which enables leading limits from DM direct detection experiments [119] (see also section 3.2.4). The following discussion and the presented methods are, in principle, also applicable to these kinds of experiments, provided they can be made sufficiently precise in their angular resolution. There is enormous interest in directional detection [140–143] which is very interesting in the context of the DM substructure and

---

[20] Hence the name.

[21] In this context, vacuum refers to the mean free path of photons being large compared to the oscillation length $\lambda_{\mathrm{osc}} = \omega/m^2$.

[22] This is possible due to the rapid change of the medium when compared to the slow/adiabatic change in the solar plasma. This issue is discussed in greater detail in Ref. [102] where this whole process is also described in a helpful sketch (fig. (5)).

neutrino fog [144–146]. However, the angular resolution will not reach the one of telescopes in the foreseeable future, which gives us motivation to focus on helioscope setups which already provide data sets with excellent angular resolution.

3.2 Analysis

Having completed the detailed discussion of the solar DP production, it is now time to discuss the question of detection in more detail. The most important question now is which data set we should use to investigate the impact of the angular resolution. This is tightly linked to the question of which telescope is best suited for detecting the predicted signal using both our angular and energy dependence of the spectrum. In the following, we will demonstrate that Hinode XRT is the best option to obtain data sets with excellent angular resolution. We will focus on two types of data sets: on the one hand, we want to maximise the exposure and thus consider calibration images taken with the telescope closed (so-called darks with an oscillation baseline of around 1 m) and on the other hand, we prioritise a large oscillation baseline, i.e. around 380000 km from observing a solar eclipse, which effectively shuts the helioscope.

3.2.1 The Hinode solar X-Ray Telescope

As we want to set the most stringent constraints possible, it is clear that the exposure of the solar observation should be maximised. For our case in particular, there are two reasons for this: first of all, long observation times lead to the telescope witnessing more solar eclipses and secondly, it increases the statistics for the analysis of the darks. Indeed, there are several telescopes dedicated to observing the Sun over different wavelengths and time scales. Of these, we are mainly interested in x-ray telescopes, since the lunar and terrestrial x-ray albedos, and with them, the probability of observing x-rays from various sources, are very low [147]. This fact ensures that the background is minimal, especially in the case of analysing a solar eclipse. Furthermore, the sensitivity to higher energies allows us to probe up to higher DP masses when compared to telescopes operating at lower frequencies, making them more attractive for our purposes, as they can easily cover all three production regimes. For example, a telescope in the optical regime never fulfils $m > m_\gamma$ except for regions where $m \sim \omega \gg T$. But this can only happen in the exponential tail of the production rate, which leads to a massive penalty for this parameter regime from the Boltzmann suppression of this process, c.f. eq. (3.36). A resonance will still be hit but only in the outer regions of the Sun. However, in this region, the description of the plasma requires more sophisticated modelling than in the inner regions. For details, we refer to Ref. [103], especially subsection (4.3).

With this list of requirements in mind, we are set to choose from a small list of telescopes, including YOHKOH [125], Hinode [122] and the GOES series (see e.g. Ref. [126]). All of these satellites carried/carry an x-ray telescope on board, and the collaborations made the relevant data publicly available. The height of the orbit is another important factor in choosing the instrument, as it determines the dominant background sources (see below for a more detailed discussion). Hinode is on a Sun-synchronous orbit of only a few hundred kilometres while GOES-12 was on a geostationary orbit at around 36000 km.

Due to the long exposure times and good data availability with helpful documentation, we will focus on Hinode XRT [122, 148–152].[23] Figure 3.3 presents two representative

---

[23] We acknowledge the use of the complete data sets which are available at `http://sdc.uio.no/search/form` also offering very helpful search criteria. Hinode is a Japanese mission developed and launched by

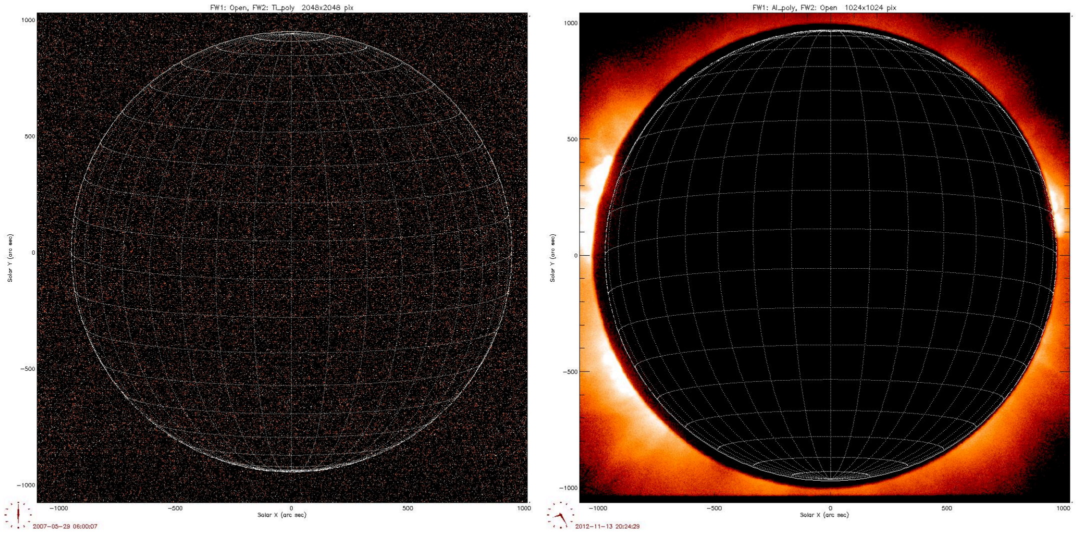

Figure 3.3: Representatives for our two data sets from `http://sdc.uio.no/search/form`. Left: Calibration image (dark) with 2048 × 2048 pixels. Right: Solar eclipse from 2012 with 1024 × 1024 pixels.

images for the two types of data sets of interest: on the left a calibration image and a solar eclipse on the right. Originally, the main purpose of these calibration images was to collect statistics for background subtraction, which included looking for time-varying effects. However, even though the backgrounds are expected to be large for space-based telescopes, we can in principle analyse them just like terrestrial helioscopes of oscillation baseline L on the scale of a few metres. For obvious reasons, images of a solar eclipse are much rarer, but their strength lies in the enormous boost for the oscillation baseline, increasing the length scale by 8 orders of magnitude. For the remainder of this section, we will consider the details for the analyses of the two different types of data.

3.2.2 Analysing the darks

Our analysis begins by selecting all full-resolution images, i.e. 2048 × 2048 pixels on a $35 \times 35\ \mathrm{arcmin}^2$ field of view (FOV). We discard the lower resolution darks as the zero-point subtraction method of the calibration routine is optimised for the full-resolution images [153]. This data set is then calibrated using the "empiric" version of the XRT standard routine [153] of SolarSoft [154] available at `https://www.lmsal.com/solarsoft/`. The zero point calibration is found to be precise with an uncertainty of around 1 data number (DN), i.e. the telescope's measure for energy. We can translate using the factor 208.05 eV/DN which demonstrates that the calibration results in much better resolution compared to the uncalibrated images with zero points scattered around 42 DN. As a last step, we choose a set of quality requirements which removes damaged, incomplete, or unsuitable images.

Discussion of image selection and choice of cuts

In the following, we will discuss the aforementioned quality cuts in more detail. For this, we will automatically set criteria to exclude damaged pictures.

ISAS/JAXA, with NAOJ as domestic partner and NASA and STFC (UK) as international partners. It is operated by these agencies in co-operation with ESA and NSC (Norway).

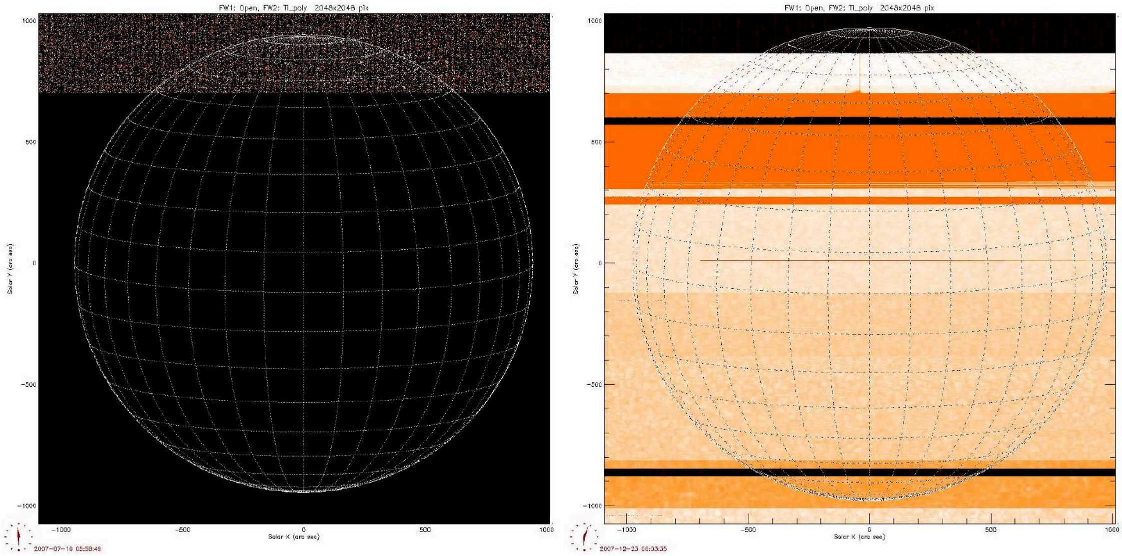

Figure 3.5: Images from `http://sdc.uio.no/search/form`. Left: Image with mostly empty pixels. Right: Image with obvious damage which does not however have necessarily empty pixels. The quality selection cuts eliminate both images from the candidate list for the final analysis.

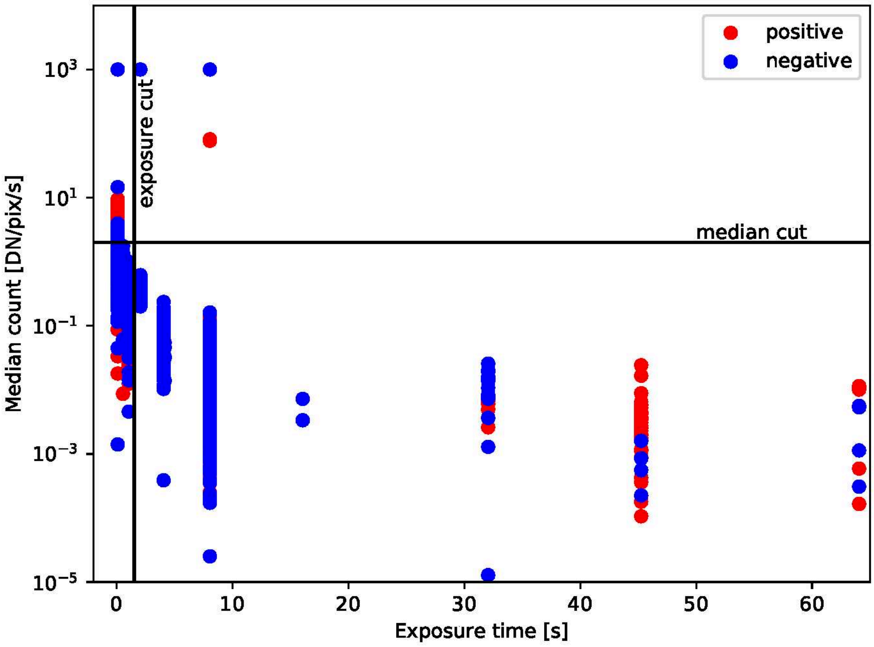

Figure 3.4: Exposure time versus median count rate for all darks. To allow for a logarithmic plot, we show the sign of the median in red/blue. We choose to focus on the high-quality images outside the two cuts represented by the horizontal and vertical black lines.

Initially, we require a way to identify (potentially) damaged images. The software represents damaged or oversaturated pixels with DN value −999 during calibration which enables a simple way to discard images with extreme damage. We just require that the absolute value of the median for a given image is smaller than 1 DN/pix/s for a usable

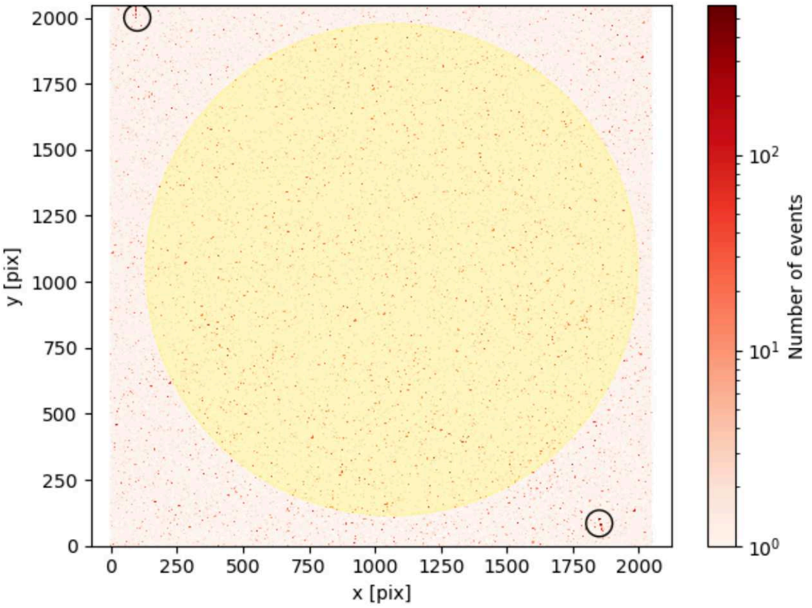

Figure 3.6: Image of all viable events stacked into a 2D histogram which demonstrates that two clear streaks (encircled) will systematically lead to larger event rates in the background (light red shading) region than in the signal region light yellow shading).

Table 3.1: Specifications of different DP searches

Analysis	image size	# of images	combined exposure
Darks	2048×2048pix	960	$\sim$ 9500s
Eclipse ´07	512×512pix	few	$\sim$ 1s
Eclipse ´12	1024×1024pix	few	$\sim$ 1s

image which already offers a good hint toward finding intact data sets. Additionally, we ignore data sets with exposure < 1.5 s since these show larger fluctuation than long exposure images. The reason for these cuts lies in the observation that only for images with exposure longer than 1.5 s the median is consistently and robustly lower than the median cutoff as long as we ignore the obvious outliers (see figure 3.4). Furthermore, removing the low-exposure images only mildly affects the total statistics, as it decreases the total exposure by only a few per cent. Figure 3.3 presents an image chosen for analysis (left) and figure 3.5 (left) shows an image that was rejected due to empty pixels.

Even with these strict cuts, there are still some damaged images such as the right image in figure 3.5. It is possible to limit the number of allowed events per image, which provides a simple but relatively secure method of identifying strongly damaged images. The cut we impose removes images with at most 9900 counts outside the solar region and at most 990 counts in each radial bin inside the solar region.[24] This leaves us with 960 (potentially) valid images with a combined exposure of $t_{\text{exp}} = 9463\,\text{s}$. A concise summary of our results can be found in table 3.1.

---

[24] Adding to the 50 radial bins mentioned before, we have also introduced a 51st bin which contains everything outside the 2D projection of the solar disk in the images. See also the later discussion of the analysis methods to learn more about the bin size.

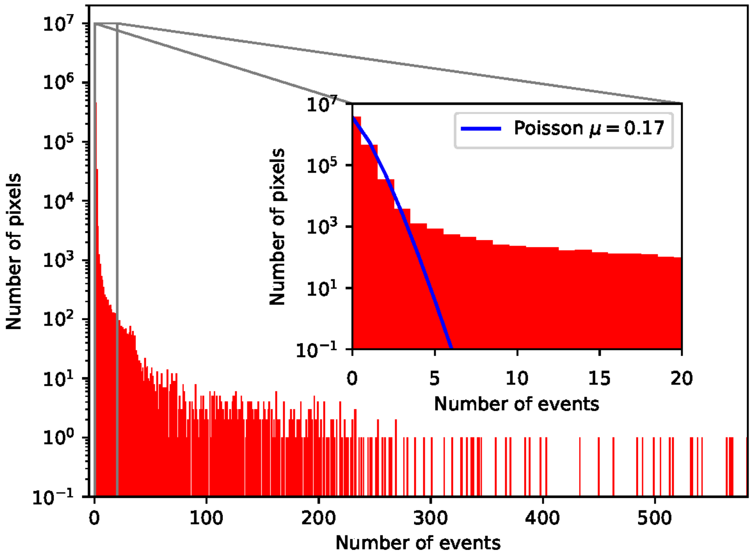

Figure 3.7: Number of events detected in each pixel after stacking all images into a histogram. The resulting distribution is very broad with up to 600 events per pixel. The (expected) Poisson distribution deviates significantly from the data as shown in the inset.

After all these extensive measures, there are still some clear systematic trends inside these images. As one example, the inner radial bins contain (on average) significantly fewer events per pixel when compared to the outer radial or the background bins. In part, this is due to a small subset of pixels showing an anomalously high count number which is visible in the 2D histogram of figure 3.6. This effect is hard to detect in a single image, but stacking up all 960 viable images makes this systematic effect clear. Especially in the upper left and lower right corner, we observe two streaks which show several hundred events in only a few pixels compared to an average of 0.17 events per pixel. Apart from these two striking features, several smaller substructures can be observed all over the histogram.

We can easily sort out many of these anomalously populated pixels by investigating the 1D histogram of event counts in figure 3.7. We expect a Poisson distribution with $\mu = 0.17$ but observe a significantly longer tail of events up to an extremely high event number. Effectively, the Poisson distribution predicts that the number count per pixel should not exceed 5 which leads us to the simple method of removing all pixels from the stacked image which violate this condition. This cut is very efficient as it reduces the total number of observed events by 23% while removing only 0.1% of all pixels.

With the help of this removal of anomalous pixels, we can reduce the systematic trend in the data set but we cannot fully eliminate it. Indeed, even with a now almost Poissonian distribution, we still note that outer bins contain typically a larger number of events. This may hint at a physical effect that requires a more refined background model. Unfortunately, such a detailed analysis of the issue at hand is beyond the scope of this thesis.

We confirm the interesting observation of Ref. [153] where it was noted that the number of counts in the darks is to good approximation independent of the exposure time, i.e. the active time of the detector hardly impacts the calibration data. Similarly, we do not have any hints for significant variations in the counts over the several years of data taking. We can interpret this as a sign of a dominant internal noise source as external backgrounds

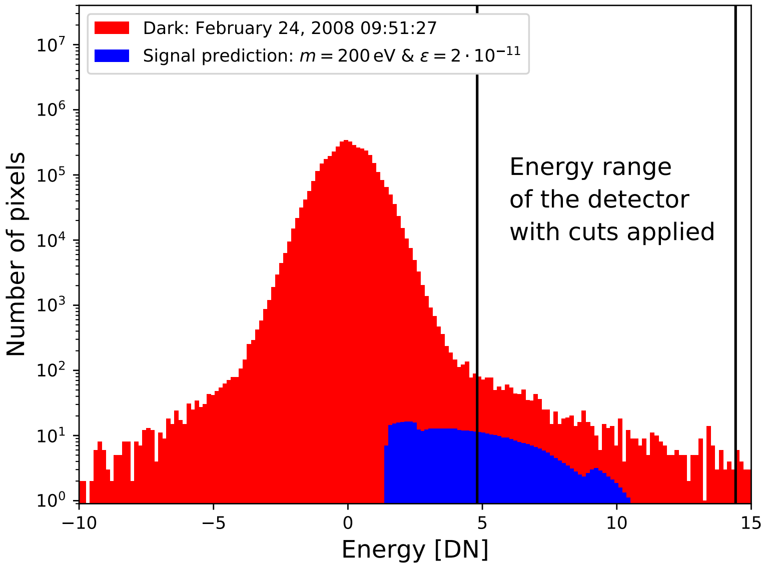

Figure 3.8: Demonstration of the noise domination by a histogram of the darks in red. In blue we show the expected signal for a DP with $m = 200\,\mathrm{eV}$ and $\epsilon = 2 \cdot 10^{-11}$. Black lines indicate cuts on the energy range aiming to suppress the noise further.

such as cosmic-ray hits should increase with exposure and fluctuate in time. This result is advantageous for us as such a noise source is well handled by the calibration routine.

Since Hinode XRT was built to sustain the intense stress of near-constant exposure to the solar x-ray flux, the instrument needed to be rather robust than ultra-sensitive. Therefore, its energy resolution cannot compete with more sensitive telescopes like XMM-Newton [155] or Chandra [156] which were constructed to detect even faint x-ray signals. Among the most striking consequences of this technical decision, the instrument was not designed to resolve individual photons. Instead, the focus was on the measurement of the large flux of solar x-rays, which allows us to only access the total energy deposited per pixel over the entire exposure of an image. This prevents us from distinguishing individual photon hits.[25] However, we can recover limited sensitivity to the spectral distribution under the assumption that the exposure time of each image is small enough to expect at most one event per pixel for a given signal hypothesis. This assumption was verified a posteriori to be consistent with the sensitivity reached within the analysis.

Based on the above discussion of the calibration routine and its zero-point adjustment, we can now identify potential hits lying in the correct energy range.[26] The fundamental idea is illustrated in figure 3.8, showing a histogram with the energy deposition across all pixels for a single representative dark. Due to the calibration routine, the distribution is rather narrowly peaked around a data number of zero, indicating that physical detector hits, i.e. external backgrounds and DP events, will become visible as an excess of events in the regions marked by the two black lines. This choice of the upper bound ($E_{\mathrm{max}} = 3\,\mathrm{keV} \approx 15\,\mathrm{DN}$) is motivated by the Hinode XRT sensitivity limit, while the lower bound ($E_{\mathrm{min}} = 1\,\mathrm{keV} \approx 5\,\mathrm{DN}$) is given by a compromise between the nominal threshold of 200 eV and our aim of suppressing the background noise and maintaining ideal sensitivity to a potential DP signal.

---

[25] Note also the comment on photon counting in the data analysis guide `https://xrt.cfa.harvard.edu/resources/documents/XAG/XAG.pdf`.

[26] See Ref. [157] for another approach to extracting energy-resolved information from Hinode XRT data.

Also shown in figure 3.8 is the signal prediction for a 200 eV DP with $\epsilon = 2 \cdot 10^{-11}$. The signal is below the background noise level, indicating that exclusion of this parameter point is impossible unless additional information on spectral and/or angular distribution is included in the analysis. In the following, we will discuss and demonstrate the method of including this additional information with emphasis on the significant improvement of sensitivity to the DP signal. Finally, we will from now on denote pixels with DN in the above range as an "event".

Increasingly complex analyses

A first step towards these improved limits is to sum up the observed events for all pixels pointing at the Sun as indicated by the white circle in the left panel of figure 3.3. We call this number S and we aim to compare this number with the full solar signal prediction for the number of events

$$R = t_{\mathrm{exp}} \int_0^{R_\odot} \mathrm{d}r \int_{E_{\mathrm{min}}}^{E_{\mathrm{max}}} \mathrm{d}\omega \frac{\mathrm{d}\Phi}{\mathrm{d}\omega} \frac{\mathrm{d}X}{\mathrm{d}r} P(\mathrm{DP} \to \gamma) Q(\omega) \; , \tag{3.61}$$

where $\mathrm{d}X/\mathrm{d}r$ is computed from eq. (3.59) via $\mathrm{d}\Omega \approx 2\pi\psi\mathrm{d}\psi$ and $\psi \approx r/R_e$. We denote the combined detector efficiency by $Q(\omega)$. This total efficiency is made up of the effective area, the quantum efficiency, and the transmittivity of the filter [122] of the telescope. The prediction depends solely on the two parameters of the DP model, i.e. the DP mass m and the mixing parameter ϵ.

Collecting the above arguments, we expect that the entirety of the observed events follow a Poisson distribution. With only this information, we can already immediately set an exclusion limit on the signal at 90% confidence level. For this, we simply use $R - 1.28\sqrt{R} > S$ which can be approximately solved for sufficient statistics, i.e. $R, S \gg 1$, by $R > S + 1.28\sqrt{S}$. This simple exclusion limit is shown by the dotted purple line in figure 3.9. We label this analysis method as SHIPS/CAST-like since it does not take into account any radial or spectral information of the signal as it is integrated out in eq. (3.61).

Now that we handled the more technical details of the calibration, let us remember that to improve upon the first analysis, we divided the signal region into 50 annuli $[r_j, r_{j+1}]$ of equal width, allowing for radial binning of the events. We further divide the energy spectrum into 10 bins $[E_i, E_{i+1}]$ of equal size. Therefore, we can categorise all events by two parameters, i.e. $S(E_i, r_j)$, whereas we find the signal prediction as

$$R(E_i, r_j) = t_{\mathrm{exp}} \int_{r_j}^{r_{j+1}} \mathrm{d}r \int_{E_i}^{E_{i+1}} \mathrm{d}\omega \, \frac{\mathrm{d}\Phi}{\mathrm{d}\omega} \frac{\mathrm{d}X}{\mathrm{d}r} P(\mathrm{DP} \to \gamma) Q(\omega) \; . \tag{3.62}$$

This binning choice provides us with further means to exclude any signal hypothesis which predicts a number of events significantly exceeding the background noise in any bin. With sufficient events in each bin, i.e. $S(E_i, r_j) \gg 1$ for all i, j, we are able to define the test statistic

$$\chi^2(m, \epsilon) = \sum_{i,j} \frac{\max\left(R(E_i, r_j) - S(E_i, r_j), 0\right)^2}{S(E_i, r_j)} \; , \tag{3.63}$$

using the maximum to ensure only bins with $R(E_i, r_j) > S(E_i, r_j)$ give contributions to the sum. This choice is important to guarantee that the "background-only" hypothesis $\chi^2(\epsilon = 0)$ does not give an artificially large value as would be the case without taking the maximum. This provides us with an upper bound on the mixing parameter by solving for

$$\Delta\chi^2 \equiv \chi^2(\epsilon) - \chi^2(\epsilon = 0) = 1.64 \; , \tag{3.64}$$

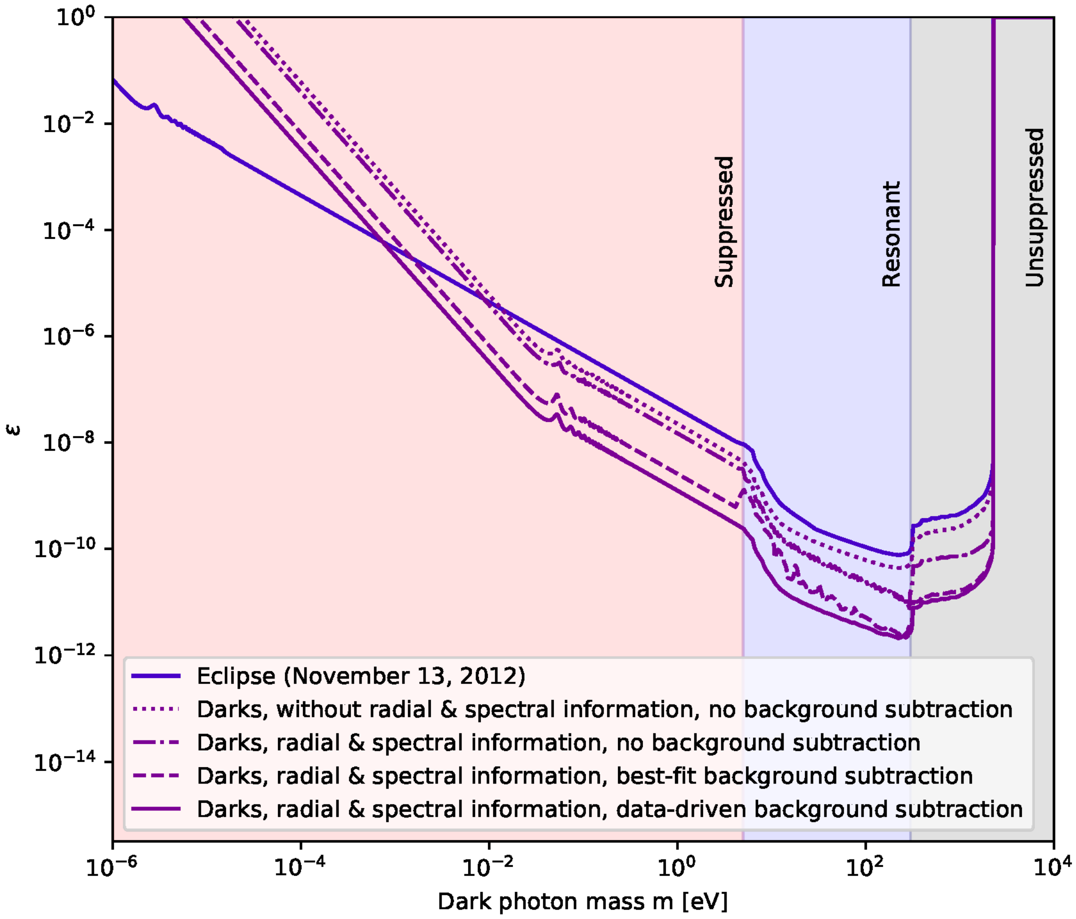

Figure 3.9: Sensitivity plot to DPs in the m–ϵ plane. The focus of the plot lies on the different constraints derived in the previous paragraphs emphasising the improvements of the full analysis over the more naive initial analysis.

at 90% confidence level according to Chernoff's theorem [158].

Following this method, we obtain the exclusion limit shown as the dash-dotted purple line in figure 3.9 which indicates a significant improvement over the previous analysis ignoring angular and radial information. Of course, this results from the substantial differences between the shape of the signal and of the background as is visible in figure 3.10. The top-left panel displays the simple distribution of the actual data in units of events per pixel per second over all selected signal bins. There is a clear tendency of a decrease in the event rate towards lower energies but the rate is rather constant in the angular/radial direction. This needs to be contrasted with the signal prediction for three representative DP masses (1 eV (suppressed), 15 eV (resonant), 400 eV (unsuppressed)) in the other three panels of figure 3.10. We have adjusted the values of the kinetic mixing parameter ϵ so that they are close to the exclusion bound discussed above to emphasise that the shape of the signal strongly impacts the limits. To follow up on the above-discussed problem that the total signal is hidden beneath the background noise level, we now realise that the inclusion of additional differential information allows us to even investigate much smaller signal hypotheses.

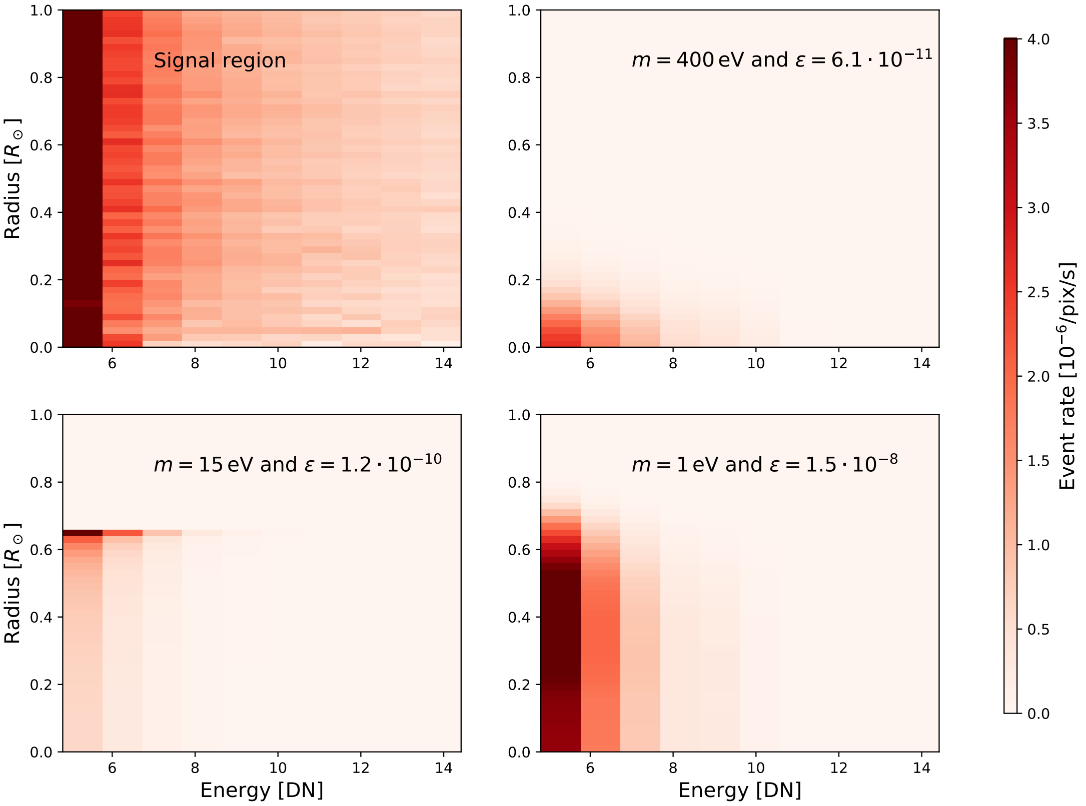

Figure 3.10: 2D plot of the actual data in the selected signal region in the top left as well as the signal predictions for 400 eV (top right), 15 eV (bottom left), and 1 eV (bottom right) DP masses.

Yet another important realisation from figure 3.10 is the fact that the background shape is flat in its radial extent even up to large radii, while the signal tends to peak at lower radii. This additional feature invites us to perform background subtraction aiming at even more stringent limits. In the next step, we will investigate two potential methods for the subtraction of the background noise: fitting the data with a simple constant or relying on a data-driven approach by considering the event rate in a control region, i.e. a region not used for the analysis.

It is apparent from figure 3.3 that there is a large “reservoir” of pixels not pointing at the Sun which we have not used yet. In the next step, we will incorporate this additional information. As we do not expect any (significant) DP signal to originate from that region, we can consider this part of the images as a control region (CR), allowing us to determine the background rate. Introducing $B(E_i)$, the number of events in the control region for a given energy bin, it is straightforward to predict the background for all radial bins by a simple rescaling relation with the number of pixels

$$B_S(E_i, r_j) = B(E_i)\frac{N_{\mathrm{pix}}(E_i, r_j)}{N_{\mathrm{pix,CR}}}\,. \tag{3.65}$$

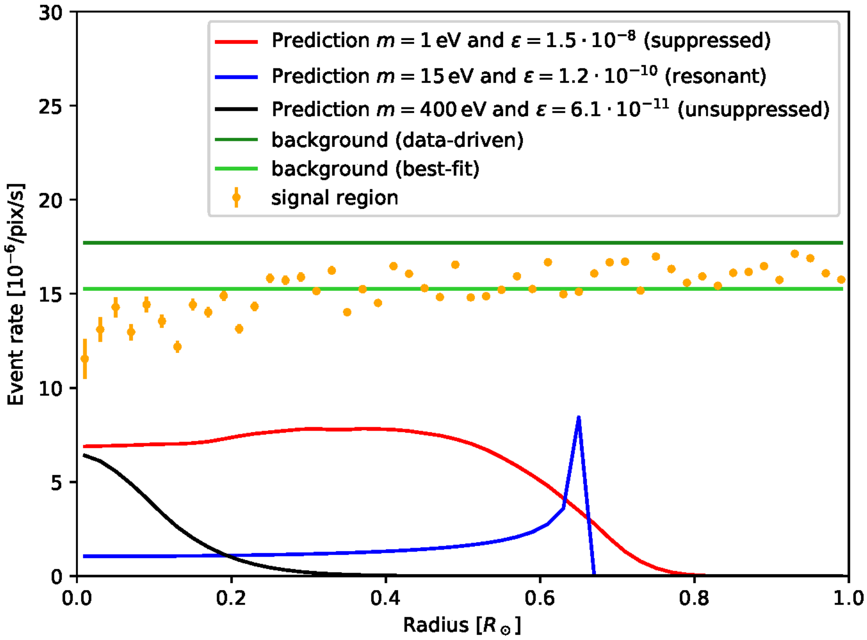

Figure 3.11: Comparison of data from signal and control region as well as the prediction for the three benchmark masses introduced above. The values for ϵ are, as discussed above close to the exclusion bounds.

Relying on the massive number of pixels in the control region compared to any signal region bin, we will from now on neglect the systematic uncertainty of the background rate arising from Poisson fluctuations as it will always be subdominant to the uncertainty of the signal region bins due to the generic $1/\sqrt{B}$ scaling.

Figure 3.11 shows a comparison between the background prediction obtained from the CR and the actual radial dependence, obtained by summation over all energy bins, and the three benchmark DP parameter points introduced before. As we have noted before, the signals have a substantially different radial dependence than both the predicted and observed event rates. The most striking feature of course is the very distinct peak of the resonance similar to figure 3.2 while both the suppressed and unsuppressed signal predictions are fairly smooth.[27] Nevertheless, we still get rather distinct predictions with the vacuum-like regime producing a strong signal at small radii due to the local high temperatures and densities, whereas the suppressed regime leads to a more stretched-out signal.

Furthermore, figure 3.11 also makes it obvious that the background prediction based on the evaluation of the CR is flawed since there is a mild decrease of the observed event rate towards the centre of the solar disk, such that the data-driven method of background subtraction fails in this region and overpredicts the observational event rate. It is of extreme importance to make sure that this issue does not bias our analysis and therefore, we will now discuss an alternative method for the estimation of the background. For this, we simply fit the observed event rate individually for each energy bin and then multiply

---

[27] The careful observer may note that the signal predictions seem to disagree with the ones shown in figure 3.2. This is simply explained by the different observables shown here. Figure 3.11 shows the event rate per pixel, whereas figure 3.2 gives it per radial bin. Also, as noted in the discussions of section 3.1.2, the predictions for the non-resonant production regimes here are based on the Hinode XRT instrument specific-sensitivity according to the prescription in eq. (3.58).

with t_{exp} and $N_{\mathrm{pix}}(E_i, r_j)$ to rescale this result to the predicted number of background events which we denote by $B_S^{\mathrm{fit}}(E_i, r_j)$.[28] Once more, the systematic uncertainties from this method can be neglected against the statistical uncertainty for any signal region bin.

Now that we have access to fairly robust estimates for each signal bin, we can define an improved test statistic

$$\chi^2(m, \epsilon) = \sum_{i,j} \frac{\left(R(E_i, r_j) + B_S^{(\mathrm{fit})}(E_i, r_j) - S(E_i, r_j)\right)^2}{S(E_i, r_j)} \,. \tag{3.66}$$

The additional background model inside our test statistic enables us to perform a search for constellations of DP parameters preferred over the background-only hypothesis, i.e. $\epsilon = 0$. Thus, we obtain improved exclusion limits from eq. (3.64) by a simple replacement $\chi^2(\epsilon = 0) \to \chi^2(\epsilon = \epsilon_{\mathrm{bf}})$ with ϵ_{bf} as the best-fit point [159]. Once we have determined the best-fit point, we can even solve eq. (3.64) analytically for fixed DP mass because the signal is just proportional to ϵ^4.

These new bounds are shown in figure 3.9 as a solid (dashed) purple line for the data-driven (best-fit) background subtraction method. As became clear from our previous discussions, both approaches lead to substantially stronger exclusion bounds, outperforming our earlier naive analysis by more than an order of magnitude in ϵ, i.e. by more than four orders of magnitude in terms of the signal strength. Furthermore, the two distinct methods give similar results confirming the robustness of our analysis.[29] From this chapter we can conclude that it is necessary to use the full angular and spectral information to distinguish signal from background, thus maximising the sensitivity of Hinode XRT.

3.2.3 Analysing the eclipse

With the analysis of the darks being completed now, we turn our attention towards the analysis of images of solar eclipses, i.e. changing long exposure times for a large oscillation baseline to probe smaller DM masses. Ideally, we would try to stack as many images of eclipses on top of each other to increase the exposure, but as these events are very rare, we are left only with a very limited data set. The only way to produce a usable data set is to manually search for all solar eclipses in Hinode's lifetime. This leaves us with two good candidates, the eclipses on March 19, 2007, and November 13, 2012, as indicated in table 3.1. For our analysis, we will focus on the latter as these images have a higher resolution, 1024 × 1024 vs. 512 × 512 pixels to be specific. As both the Moon and the Sun cover very similar solid angles, only very few images show an actual total eclipse for the telescope. The image closest to such a total eclipse is shown in figure 3.3 on the right.[30]

The right image of figure 3.3 makes it clear that both the control region and even parts of the signal region are “polluted” by solar activity. As an obvious conclusion, the control region becomes effectively useless for background subtraction. Furthermore, we notice a

---

[28] Of course, it is possible and, depending on the scope of the analysis, even preferable to fit a more complicated function than just a constant to account for the observed slight radial dependence. For this specific analysis, we have made sure that a more complex fitting function has no significant impact on our results.

[29] We note in passing that the data-driven method never yields a preference for a DP signal as the background prediction is always larger than the actual observed event rate. Nevertheless, the best-fit method finds a few points with small excesses (see figure 3.11) in the resonant regime, which tends to weaken the exclusion limits. As the parameter space under scrutiny is already excluded and the hints for DPs are very weak, we will not further investigate these points.

[30] The entire eclipse is nicely displayed in this short movie: `https://www.youtube.com/watch?v=XNzleYZL6u8`.

tendency towards increasing event rates in the outer regions of the image, both for the raw and the calibrated data. This is in agreement with the observations in Ref. [160], where this systematic was studied in the context of calibrating the telescope's point spread function. To enable a robust analysis, the outermost parts of the signal region should therefore be excluded from our analysis.

In the following, we quickly discuss how to prepare the eclipse data in a way that makes the same statistical methods as for the darks from section 3.2.2 applicable.

We observe that the image of the eclipse did not get properly calibrated, which is expressed as a massive deviation from the expected scattering around zero signal as is visible in red in figure 3.12. Unfortunately, we cannot even use a dark from the same day and with the same resolution to correct the zero-point since for these images, the zero-point calibration yields another badly calibrated result as apparent from the blue histogram in figure 3.12.[31]

However, the inner regions of the solar disk and the corresponding bins still allow us to fix the true zero-point of the data number. To visualise the idea we can see as the blue histogram of the dark in figure 3.12 that the distribution looks Gaussian to good approximation while the distribution of the eclipse (red histogram) exhibits a substantial non-Gaussian tail due to pixels with large energy deposition from solar x-rays originating from parts of the Sun not covered by the Moon. Nevertheless, the central parts of the image the x-rays are fully blocked and we see in the approximately Gaussian shape of the main peak that the dominant contribution in this region is due to internal noise.

Focussing for now solely on the pixels contained within the inner 50% of the solar radius, the distribution indeed resembles a Gaussian to good approximation. This invites us to use these pixels for the determination of the zero point which we find to be at $-5.16\,\mathrm{DN/s}$. Similar to the darks there is a tendency of increased event rates towards larger radii after the (manual) zero-point calibration which we demonstrate in figure 3.13. This trend is more pronounced for eclipse images than for darks, and when compared to figure 3.11 we also realise that due to the contamination of solar x-rays and limited statistics, the overall event rate and the error bars are orders of magnitude larger.

As a final step in this dedicated calibration, we scrutinise the efficiency of our cuts with a small consistency check: even with the identification of pixels with deposited energy of more than 3000 eV as a double (or even multiple) hit of background photons of any energy within the sensitivity range, we find that the fraction of pixels with this potential background pollution stays below 5% even in the most outer radial bin. However, as we know that such large energy depositions are unlikely to arise from internal noise, we conclude that these physical background events from the solar corona are the most likely explanation. As we suppress this pollution below 5% with our cuts, we can confidently conclude that the cuts efficiently remove the problematic regions, leaving us with a data set effectively free of external backgrounds.

After this small detour into the more technical details of the calibration, we can now go ahead and perform a darks-like analysis for the eclipse as well. Theoretically, we can perform the same energy and angular binning as before, but because of the very limited exposure time, this procedure would result in a large number of empty bins, indicating an unnecessarily fine binning. Thus, we restrict ourselves to a single bin taking up to half the solar radius, minimising the pollution of physical background hits in the process. Especially in the suppressed and unsuppressed regime, we additionally expect that these

---

[31] Furthermore, a straightforward subtraction of a dark will also subtract any trace of a potential DP signal, at least in the mass range where the closed telescope can already be considered a good helioscope, i.e. when the DP oscillation length is low.

cuts still retain very good signal efficiency, but there will be a stronger loss in sensitivity in the parameter space that produces peaks at large solar radii, as these will be cut out of the analysis. We have made sure that this sensitivity decrease has only a mild impact on the strength of the actual limits.

We find a total of 389 events in the signal region, a number that may still be background-dominated due to additional physical backgrounds originating from outside the Sun and of course internal noise. An interesting example for this class of non-solar x-ray sources would be solar wind charge transfer [161] which in principle can produce x-rays in the entire signal region.[32] For simplicity, we will not attempt to design a background model and instead, we will perform a SHIPS/CAST-like analysis without background subtraction as initially discussed for the darks. While this naively seems to imply that the additional differential information is unnecessary for this analysis, we have to realise that the cuts require us to know at least the angular distribution, as we cannot rely on the total signal of the solar disk.

We show these final limits as the blue solid line in figure 3.9. Following our expectations, these eclipse bounds are much weaker for the more massive region of the DP parameter space, as the oscillation length is tiny compared to the size of the telescope. Still, these limits are only mildly subdominant to the darks exclusion bounds obtained ignoring the additional radial and spectral information as well as any form of background subtraction. This once more emphasises the point that the refinements imposed upon our analysis in section 3.2.2 are of extreme importance to profit from the large exposure of the darks.

Only once the mass drops below the threshold value where the oscillation length exceeds the telescope scale, we truly benefit from the enormous oscillation baseline. The transition where the eclipse becomes the dominant bound occurs for DP masses below around 1 meV as is visible in figure 3.9.

3.2.4 Our limits in the context of the DP literature

To clarify the broader context of these limits, we make a comparison with different limits from the literature in figure 3.14. The two limits labelled “Hinode XRT” reflect the most optimistic reach of our analysis. The solid purple region is based on the data-driven background subtraction and the blue region stems from the eclipse analysis. For the plot, we have consulted the excellent database and design available via Ref. [162] which was, at least for DPs, initially introduced in Ref. [72] which also acts as a brief review on many of the limits shown.[33] As already briefly discussed initially in section 3.1.3, the solar limits, and any other limit in this mass range, are mostly dominated by the longitudinal production of DPs. These can be split into applying the solar cooling argument which leads to the limit label “solar” or the search for absorption of DPs in DM direct detection experiments, labeled “XENON1T longitudinal absorption”) [120]. Although these search channels are dominant, we still conclude that Hinode XRT is setting significantly more stringent limits than lab experiments such as spectroscopy searches [78].

Additionally, we observe that LSW searches, here mainly in the form of ALPS [163], become important for small DP masses as the design of these experiments is not required to be able to track the Sun which allows for the construction of larger oscillation baselines. The next generation of LSW experiments, especially ALPS II [164], will probe much deeper

---

[32] Here “non-solar” of course refers to being produced in a way that is not blocked by the eclipse which covers the direct line of sight.

[33] This plot can be considered somewhat historic as the most up-to-date version already includes our Hinode XRT limits as well as further updated results. To keep the internal logic of this chapter intact, we nevertheless focus on the original plot from Ref. [1].

Experiment	CAST	SHIPS	Darks	Eclipse
Typical energy in eV	5000	3	1000	1000
Length in m	9.26	5	~ 1	$\sim 3.8 \cdot 10^8$
Kink mass in eV	$7 \cdot 10^{-3}$	$2 \cdot 10^{-3}$	$3 \cdot 10^{-2}$	$2 \cdot 10^{-6}$
Exposure times in s	709200	1188000	9500	1
Sensitivity to ϵ at $m = 1\,\text{eV}$	$6 \cdot 10^{-10}$	$3 \cdot 10^{-10}$	$1 \cdot 10^{-9}$	$4 \cdot 10^{-8}$

Table 3.2: Specifications of different solar DP searches.

into this parameter space. The clear advantage of these experiments is the extremely precise control over the entire setup which eliminates the astrophysical uncertainty of the solar production that affects helioscope searches. The price to pay for the higher quality of initial state control is the immense reduction of the dark luminosity of the experiment, i.e. a laser versus the entire Sun.

Even when compared to dedicated helioscope experiments like CAST and SHIPS, the Hinode XRT limits are only slightly weaker. This emphasises the potential reach available for helioscope searches using the additional information and analysis approaches supplied above as these dedicated instruments are very precise and have extremely long exposure times as shown in table 3.2. In conclusion, we have seen that the angular and spectral resolutions are on a similar footing as exposure for running a helioscope most efficiently.

Let us now investigate the advantages and disadvantages of the different instruments in more detail. As the large DP mass cutoff is only driven by the maximum energy accessible to a given experiment, we realise that CAST with its sensitivity up to 15 keV, is the best instrument in that regard, especially when compared to SHIPS, which focused on the optical energy range, suffering from insensitivity for masses beyond the eV scale. Furthermore, we observe a distinct bump structure in the spectra for the two x-ray-sensitive experiments in the range of $\sim$ 5–300 eV originating in the resonant DP production regime of the solar plasma. However, the low DP mass sensitivity loss is less directly affected by the energy scale of the experiment. It corresponds to the oscillation length becoming equal to the telescope length. Therefore, the position of the kink can be obtained from setting the argument of the sine in eq. (3.11) to an $\mathcal{O}(1)$ number

$$\frac{m^2 L}{4\omega} \sim 1 \Leftrightarrow m \sim \sqrt{\frac{4\omega}{L}}. \tag{3.67}$$

All relevant scales for the experiments discussed above are compiled in table 3.2. Finally, the eclipse data offers unparalleled reach in terms of small DP masses due to the enormous oscillation length.

3.3 Discussion

The solar plasma is an intriguing laboratory for light and weakly coupled BSM physics and has received much attention [165, 166]. The DP in particular is known to be a candidate for potential solar production with many of the most stringent constraints derived from this source in the eV to keV mass range. In this chapter, we investigated if the exploitation of all the available information from the DP angular and spectral distribution can be used to maximise the reach of helioscopes. To this end, we have found a new approach to approximating the angular distribution of solar DPs outside the resonant production window. To demonstrate the potential sensitivity increase we have used the publicly available data from Hinode XRT, a solar x-ray telescope with outstanding angular resolution, for a thorough analysis.

Initially, we have investigated so-called darks. These are calibration images taken with the shutter closed, effectively transforming the telescope into a space-based helioscope. Based on the very low count rates, we generated additional spectral information from the darks with the help of the standard calibration procedure of Hinode XRT. After a detailed study of the calibrated data, we have introduced quality cuts identifying and removing damaged images and pixels with intrinsically large backgrounds. This further enabled us to perform an additional background subtraction, which we have done in two different approaches, i.e. data-driven or fitting. Combining the inclusion of additional differential information and background subtraction yields a sensitivity improvement of more than an order of magnitude in terms of the kinetic mixing parameter over the naive bounds from "event counting".

In addition to this analysis, we also investigated the amusing idea of interpreting Hinode XRT during a solar eclipse as a giant helioscope. This approach provides an impressive sensitivity boost in the low DP mass region of the parameter space while it suffers substantially from the decrease in exposure time for heavier DPs. Based on a single image of a total eclipse in 2012, we were able to bound the parameter space of DPs more stringently than existing dedicated helioscopes below 1 meV. However, this parameter space is also covered by LSW experiments like ALPS since the production of very light DPs becomes increasingly suppressed for particle masses below the solar plasma frequency.

At this point, we need to point out that the analysis above is thought to be a proof-of-principle, based on very simplified background modelling. These simplifications ignore several features in the data sets, an issue that could easily be refined, especially for the data from the solar eclipse. Further improvements in the analysis and the inclusion of partial eclipses are a pathway to a simple boost of sensitivity due to the exposure potentially increasing by more than an order of magnitude. Unfortunately, an effectively indefinite increase in exposure time is impossible for the eclipse data due to the rarity of such events.[34] This issue could be partially solved by a telescope in a lunar-centric orbit, an exciting possibility that trades some of the oscillation baseline for potentially much longer exposure.

To conclude this chapter, let us emphasise that the entire analysis routine above which was developed in the context of Hinode XRT is also applicable to studying the angular distribution of solar DPs in the most recent version of the CAST experiment and the future helioscopes BabyIAXO and IAXO [167, 168]. To guarantee the robustness of the limits from these high precision observations, it is imperative to improve the calculation of the DP angular distribution, including an update of the solar model [169, 170], and to estimate the corresponding uncertainties. Another interesting direction is to consider additional specific observables beyond the total DP flux such as the polarisation of solar DPs which might become an interesting new avenue towards DP searches with upcoming plans to measure the polarisation of solar x-rays with the CUSP project [171]. This would constitute an entirely new lever on solar DP detection. Of course, combining the maximal information will lead in the long run to the strongest bounds and allow for the detection of potentially new physics hidden in the vast amount of open parameter space.

---

[34] For helioscope-like observations, increasing the run time is more a question of costs or usefulness for the analysis since the permanent observation of the Sun requires tracking of the relative motion between the Earth and the Sun. Long oscillation baselines are highly favourable for good limits but they are counterproductive to extensive tracking manoeuvres. For an interesting example, see this video of the tracking mechanism of CAST on the CERN website.

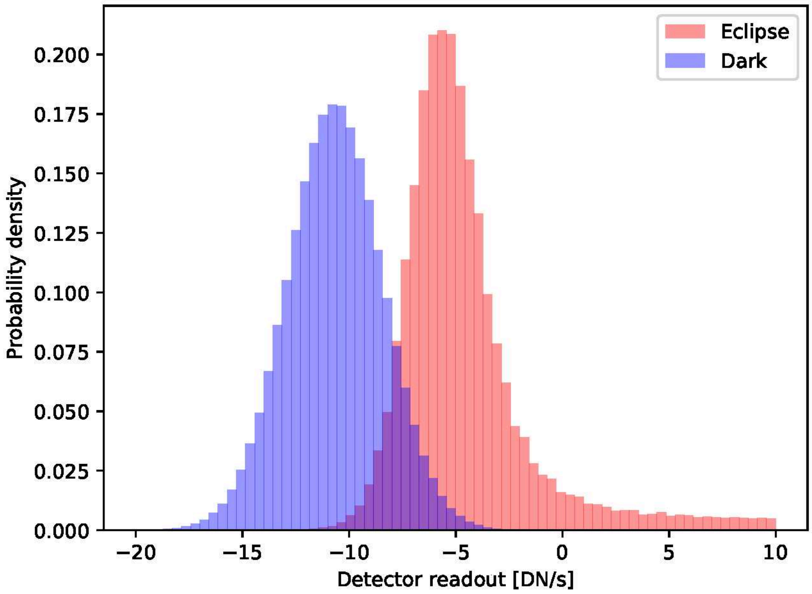

Figure 3.12: Normalised histogram of the DN/s for the eclipse (red) and a dark with the same resolution taken on the same day (blue). The zero-point calibration did not work as efficiently as for the darks analysed above and both images give rather different results. The image of the eclipse has a clear non-Gaussian tail from the physical x-ray hits that sits on top of the mostly Gaussian internal noise.

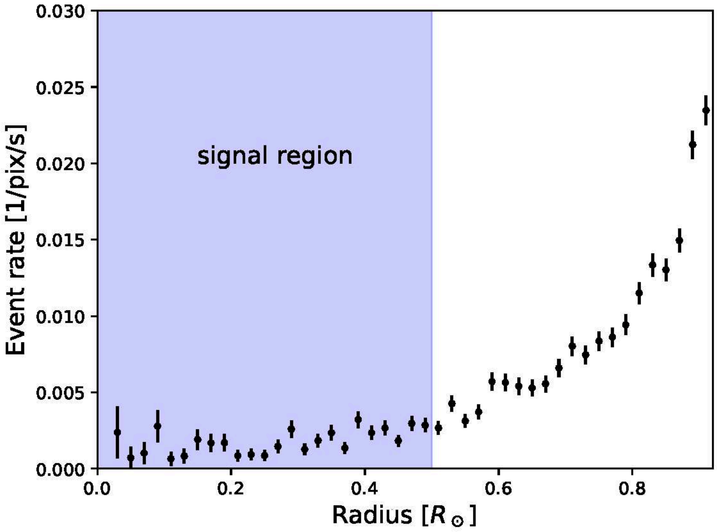

Figure 3.13: Plot of the event rate as a function of radius for the eclipse image. The zero-point determination is fully driven by the inner region.

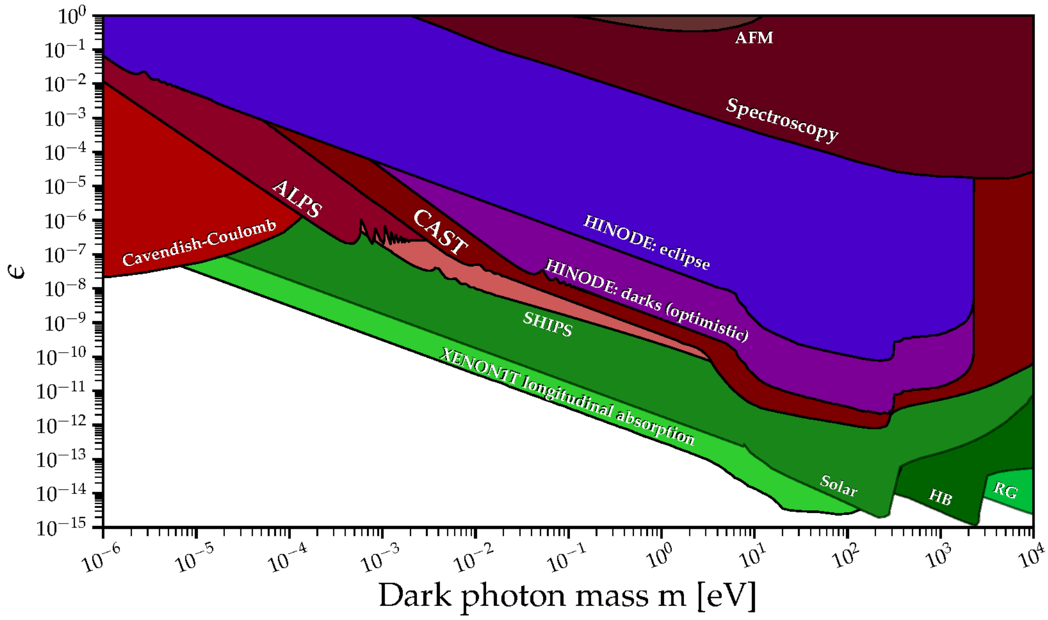

Figure 3.14: Same limits as in figure 3.9, but focusing only on the strongest and thus most optimistic limits obtained in this work, i.e. using the data-driven background subtraction, in comparison to other competing DP bounds. The plot design is taken from the outstanding repository for DP and axion-like particle (ALP) bounds by Ciaran O'Hare Ref. [162], see also Ref. [72] for a compilation of many of these limits. Generically, green contours are driven by the astrophysical production of DPs, whereas red bounds are often based on various lab-based experiments.

4 The Dark Photon as a Dark Matter candidate

> I guess you have a point
> Modified gravity
> Seems like a perfectly legitimate alternative
> There's almost no evidence against it
> Except the CMB
> Large scale structure
> Galaxy clusters
> The light element abundances
> The diversity of galaxy halos
> And common fucking sense
>
> *Stop Emailing Dan (About MOND)*
> THE SPECTRAL DISTORTIONS

In this chapter, we will apply our previous results on the DP to the DM problem to allow for a smooth transition into the results from Ref. [2], i.e. the core of Ch. 5. We will first give a minimalistic review of the idea behind and the state of the Dark Matter paradigm. Once we have collected the most important facts and the relevant observations that DM has to explain, we will turn towards the DP as a DM candidate. In particular, we will sketch the central aspects of producing Dark Photon Dark Matter (DPDM). Finally, we will summarise a selection of important works on the bounds limiting the DM parameter space. This chapter acts as a preparation for the following chapter 5 in which we will perform and discuss general[1] DPDM search in detail.

4.1 Evidence for Dark Matter

The existence of Dark Matter is a well-established observational fact. We will now quickly trace the main steps towards our modern understanding of the DM problem. For a dedicated history of DM, we refer the interested reader to Ref. [4]. For a very complete review, we refer to recent work in Ref. [12] and a textbook on particle DM is provided in Ref. [172].

Both the SM of particle physics and the ΛCDM model of cosmology are in remarkable agreement with observations. It is fascinating that our understanding of the most fundamental processes at the energies available on Earth allowed us to tell a consistent story of cosmology. However, just relying on the SM clashes with our cosmological observations in three important points: first of all, the observed dark energy is much lower than the naive expectation from the SM of particle physics, the so-called cosmological constant problem which has spawned an enormous number of ideas providing potential solutions [173–180].[2]

---

[1] We will discuss the concept of general DPs in chapter 5 as well. For now, it suffices to know that most of the following points are applicable for both standard DPs as discussed so far and general DPs.

[2] The observations yield an approximate energy density of $\rho_\Lambda \sim 10^{-47}\,\mathrm{GeV}^4$ [46, 181]. The naive expectation of the SM is that the energy density is dominated by the EW scale, leading to $\rho_\Lambda \sim (100\,\mathrm{GeV})^4 \sim 10^8\mathrm{GeV}^4$ [182], which leads to the unexpected hierarchy of many decades in orders of magnitude between

On the other hand, the SM cannot explain the amount of matter-antimattwer asymmetry in our Universe [183, 184]. Finally, and in the focus of this chapter, there is cosmological and astrophysical evidence on a variety of scales that the visible/baryonic matter around us is not the entire story. In contrast, it seems to make up only around 20 % of the total matter in the universe [46, 181]. We will now collect the major observational evidence and discuss the implications. Before we do that, we should note, however, that both standard models also have more theoretical issues, both internal and in their interplay. Among the most prominent ones are the hierarchy problem [185–187] and the strong CP problem [188–190][3] on the side of the SM whereas the so-called Hubble tension between late- and early-time probes of the expansion of the Universe [194–196] represents one of the most urgent questions in cosmology. Furthermore, the lack of a consistent theory of quantum gravity is one of the most urgent questions in modern theoretical physics [197, 198].

Rotation curves

After this short detour through a very brief (and biased) selection of pressing questions in particle physics and cosmology, let us return to the problem of DM. The common lore is that the Swiss astronomer Zwicky was the first to introduce the term “Dark Matter” (“dunkle Materie”) to explain the anomalously large velocity dispersion in the Coma cluster [199]. Over the coming decades, the question of missing mass remained unclear until 1970, when Rubin and Ford published the rotation curve of M31 [200], which is flat out to large radii, a telltale sign of an extended distribution of DM. By now we even have access to the local DM density using a mixture of simulations and observations [201].

The CMB

Now that we have reviewed the early, astrophysical evidence for DM, let us turn towards cosmological data. With the detection of the cosmic microwave background (CMB) by Penzias and Wilson [202], cosmology was able to turn, over the decades, into precision physics whereas before it was often considered to be barely predictive [4]. Subsequent missions increased the precision of the CMB measurements [203–205] and today, with the results from the Planck mission, we have convincing evidence for non-baryonic, long-lived DM at the time of CMB decoupling [46, 181]

$$\Omega_{\mathrm{CDM}} h^2 = 0.1200 \pm 0.0012 \tag{4.1a}$$

$$\Omega_{\mathrm{baryon}} h^2 = 0.02237 \pm 0.00015 \tag{4.1b}$$

$$h = \frac{H_0}{100\,\mathrm{km/s/Mpc}} = \ 0.674 \pm 0.005\ , \tag{4.1c}$$

where he have introduced the fractional abundances Ω_i and the Hubble constant H_0 (see also section 4.2). This implies, together with the Universe being flat within observational uncertainty, i.e. $\sum_i \Omega_i = 1$, that the energy budget of the Universe today has a substantial, but not dominant matter contribution. The most significant observation here is nevertheless that the baryonic contribution to the total matter budget is small, at the level of $(18.64 \pm 0.22)\,\%$. This is a fascinating observation, as it makes for a very consistent

---

observation and prediction. If instead of the EW scale we consider the Planck scale ($m_{\mathrm{p}} \sim 10^{19}$ GeV), this even gives around 120 orders of magnitude difference.

[3] Recent developments question the physical relevance of the θ term in quantum chromodynamics (QCD) which is responsible for the strong CP problem [191, 192] but they require further scrutiny as there are robust arguments for the physicality of the θ term [193].

story together with the astrophysical DM evidence. Furthermore, it rules out conventional baryonic DM candidates like massive astrophysical compact halo objects (MACHOs) [206, 207].[4]

On top of these observations, we have an ever-improving set of large-scale N-body simulations at our disposal which we can use to study DM properties by comparing simulations of differently modelled DM particles with the observations in our Universe. One central aspect is that DM cannot be fully relativistic if it is supposed to account for the formation of structure from an otherwise hot and very homogeneous Universe [209], a fact that was also derived analytically [210].

The Bullet cluster

The probably most famous piece of evidence for the existence of DM is the so-called Bullet cluster [211]. This is the observation of the remnant of a merger between two galaxy clusters which has a set of outstanding properties giving us insight into the nature of DM, albeit only superficially. The visible component of the cluster is dominated by hot gas with a subdominant fraction of stellar mass. Compact objects such as stars survive the merger virtually unaffected because of their small, practically geometric cross section. The two respective plasma clouds, however, interact more strongly since they get slowed down and heated up in the centre of the merger, as visible in the x-ray emission of the gas. A galaxy dominated by visible matter, and thus by the plasma, would necessarily have a gravitational potential that is especially deep in the central region. On the contrary, the bullet cluster has two potential minima offset significantly from the peak of the plasma density. This is demonstrated in fig. 4.1 where the green contours track the gravitational well and the yellow to blue regions show the plasma distribution. On top of this unique hint towards particle DM, we can immediately conclude that DM has limited self-interactions, as these would change the post-collision distribution significantly. These limits are, however, rather weak and allow still for interesting effects [212] which often require large simulations [213–215] to be fully understood. The upper limit on the self-interaction strength is found to be around $\sigma/m \lesssim 1\,\mathrm{cm}^2\,\mathrm{g}^{-1}$ [216].[5] Should the cross section be velocity-dependent, this result is not necessarily true for probes of self-interactions on smaller, i.e. galactic, scales [217] where slightly larger cross sections are allowed. This result is especially interesting as light mediators in DM self-interactions naturally imply a velocity-dependent cross section. Ref. [218] discusses this issue and presents an interesting discussion of the impact of SIDM on the small-scale structure and with it the possible resolution of the so-called small-scale crisis, a collection of (long-standing) mismatches between observations and collisionless DM simulations [219, 220].

DM lifetime

Additionally, we can also constrain the lifetime of DM with further observations. While the CMB tells us about the DM density at the time of photon decoupling, the story is of course more complicated. First of all, we know from local observations that there is a non-zero DM density in the larger solar neighbourhood [201]. Furthermore, the observation of the DM-dominated rotation curves implies that, at the time of the photon emission, DM was

---

[4] Furthermore, gravitational lensing robustly rules out MACHOs [208] as primary DM component.

[5] This is the standard quantity for self-interacting DM (SIDM) since most probes are sensitive to the interaction rate $\Gamma = \sigma n v$ and we only have experimental/observational access to the energy density ρ and the relative DM velocity v. Thus, replacing the number density n with the relation $\rho = mn$, we get that σ/m is what can be determined from observation [216].

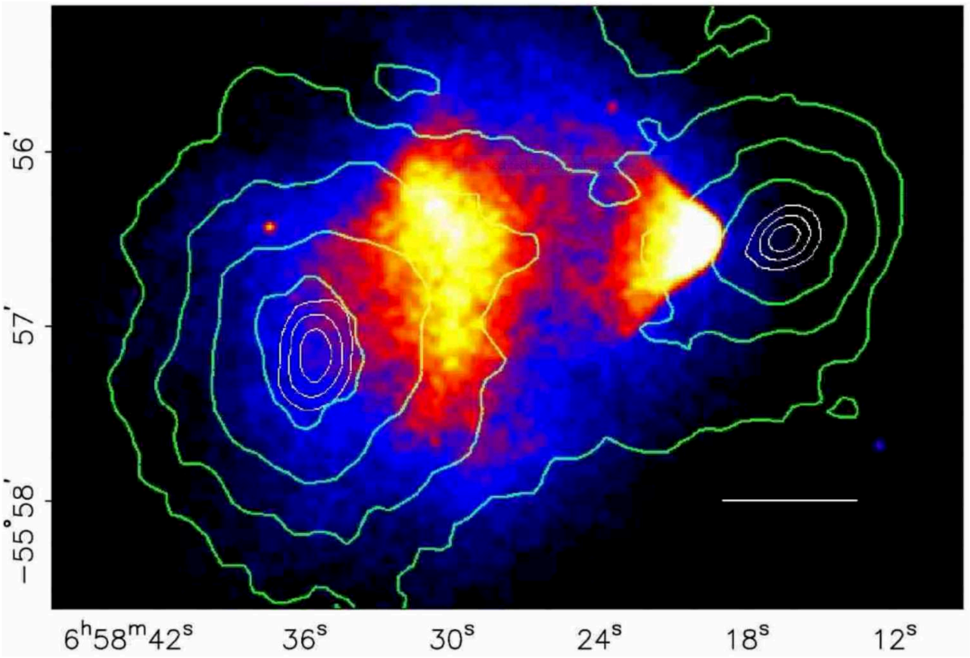

Figure 4.1: Image of the bullet cluster from the original publication [211]. The deviation between SM mass distribution (blue-red-yellow) and total mass distribution (green and white contours) becomes immediately clear.

present in those galaxies. On cosmological time scales, this time of emission is of course a very recent event. From all that we have discussed before, we know that DM has to be more long-lived than the Universe $\tau_{\text{DM}} > \tau_{\text{uni}} = (13.801 \pm 0.024)\,\text{Gyr}$. For rather heavy DM, which in the context of this thesis means above the GeV scale, this simple constraint from the consistency of the early Universe and late Universe data can be improved by many orders of magnitude. Looking for ultra-high energy neutrinos or gamma-rays, especially from a directed search in a region with high expected DM density, a broad variety of visible DM decay channels can be covered over an enormous spectrum of DM masses [221–223]. For lighter particles, Ref. [224] showed that these limits can still be extended but now rather from an overproduction of the Isotropic Diffuse Photon Background, covering parameter space down to almost keV scales while still excluding lifetimes of $\tau_{\text{DM}} \sim 10^{22}\,\text{s} \gg 10^{17}\,\text{s} \sim \tau_{\text{uni}}$. In this mass regime, the only visible decay channels are neutrinos and photons and for even lighter DM, neutrinos will become kinematically unavailable (unless one neutrino turns out to be massless). Following a very basic argument, we can estimate that the lighter the DM candidate, the easier it is to stabilise it due to kinematic suppression. In fact, with only (effectively) massless particles remaining for the decay channels, the decay width will typically be given by

$$\frac{1}{\tau_{\text{DM}}} = \Gamma_{\text{DM}} \simeq \kappa m_{\text{DM}} \,, \tag{4.2}$$

where κ is some constant. This means generically that the lighter the particle is, the less the coupling is constrained by demanding that the DM lifetime obeys the observations. The prefactor κ can furthermore be very small, especially in the case of light DPs [225]. But no matter how sophisticated the decay channels, there are model-independent, and thus unavoidable, bounds for any kind of DM which arise from purely gravitational interactions.[6] These gravitational probes include, but are not limited to, the Lyman-α forest [226, 227] and late-time effects on the CMB [228, 229]. While these limiting frameworks are generically unavoidable the exact results still have some remnant model dependence like the number and mass distribution of the decaying particles. Nevertheless, in most of the parameter space, this approach can improve the naive lifetime limits by about an order of magnitude.

Direct detection

Having now discussed the history of the DM paradigm and a handful of the most powerful observations on the DM properties, we can turn to perhaps the most urgent question: *Why isn't the DM showing up in our direct detection experiments? Why don't we see its annihilation signals in our astrophysical observation? Why didn't we produce it directly at one of our colliders?* Although it is possible to formulate a more unified framework for the three questions within a single thesis [230], the focus of this work will remain on the DP. In the following, in preparation for chapter 5, we will therefore focus on the direct detection aspect of the DM puzzle with a strong emphasis on the ultralight regime.

As we will discuss the detection of ultralight DM candidates in more detail later, let us for now consider the heavier side of the DM mass spectrum. Particle DM masses are usually considered up to the Planck scale for two reasons. The pragmatic reason is that, to have the correct local DM energy density, the number density necessarily has to be low for ultra-heavy DM. Indeed, the Planck mass roughly corresponds to fluxes, which can yield event rates of at most a few per year. Additionally, our usual QFT description will begin to break down around this scale as quantum effects of general relativity become no longer negligible close to the Planck scale. Although this does not necessarily forbid particle DM in this regime, the description requires tools that do not exist at this moment. Therefore, even heavier DM is often not expected to be a fundamental particle but instead a composite state [231]. In this extremely heavy regime, there is even hope for direct gravitational detection using mechanical sensors [232, 233]. Let us now again turn to more conventional direct detection, i.e. via the recoil of a nucleus induced by a DM scattering event [234]. This technology is well-established and gives the dominant limits over a large mass range between the GeV scale [235–238] and the Planck scale [239, 240]. These instruments are typically placed in a well-shielded underground lab to avoid any SM backgrounds like cosmic rays. Infamously, the reach of these detectors is fundamentally limited by the so-called neutrino fog (or floor) [241], the unshieldable background of ambient neutrinos which coherently scatter on nuclei and thus mimic a recoil from a much heavier but non-relativistic DM particle. This is shown in fig. 4.2 for a sample of experiments from the year 2021. One way to distinguish the signals is directional detection [140–142, 242] since we have robust predictions for the velocity distribution of the DM particles [243].[7]

Going to even lighter DM masses makes conventional direct detection looking for nuclear recoils increasingly insensitive. Simply applying energy conservation to the kinematics of the process tells us that the recoil energy cannot be higher than the incoming kinetic energy of the DM particle.[8] Once the DM is significantly lighter than the nucleus, the

---

[6] Especially decays into other lighter particles within a secluded dark sector will erase the aforementioned limits from indirect detection as they do not provide any SM signature.

[7] During the writing process of this thesis, first hints for the detection of solar neutrinos were presented by the XENON collaboration [244, 245] and the PandaX collaboration [246] at the level of 2.7 and 2.6σ, respectively.

[8] A simple workaround here is the concept of inelastic DM [3, 247, 248].

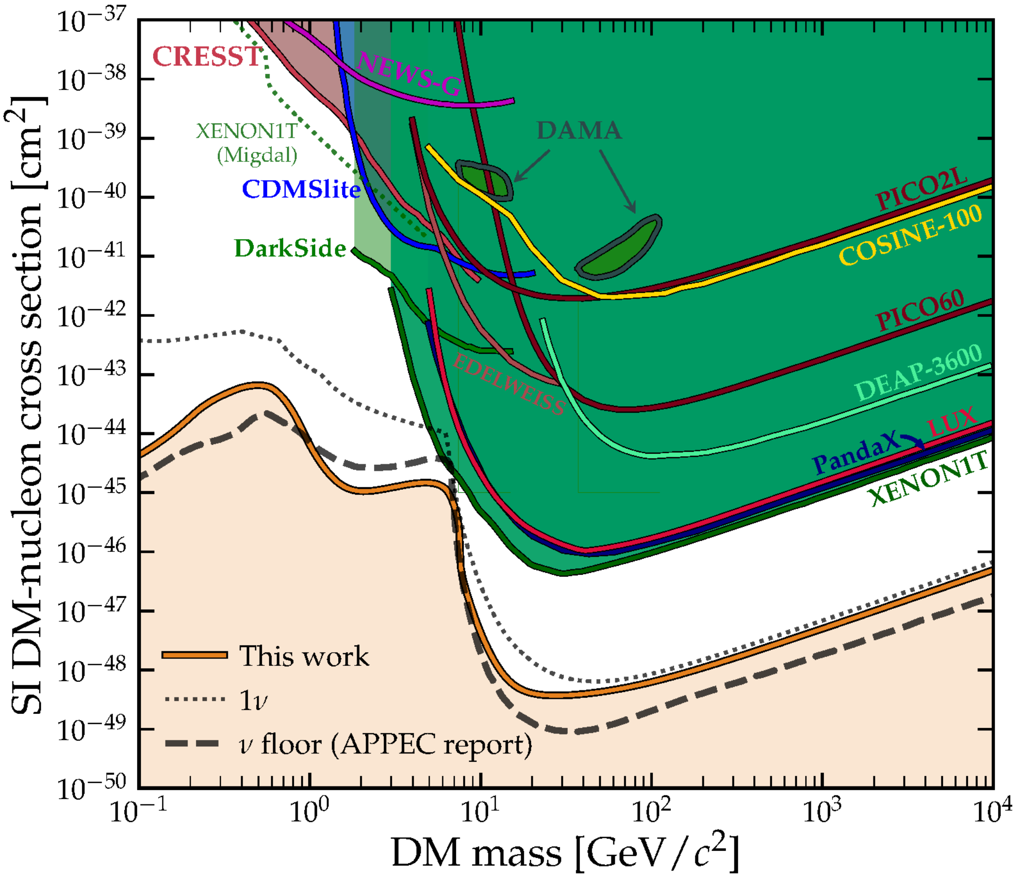

Figure 4.2: Exclusion limit of several direct detection experiments around the GeV scale from [144]. The plot also shows the neutrino fog. See the same publication for more details on this challenging but fascinating aspect of direct detection.

recoil energy of a nucleus quickly becomes too small for detection as we know that the (bulk of the) local DM particles should not exceed velocities of $v \sim 10^{-3}$ since they are gravitationally bound to the Milky Way [243]. The options are typically to consider signatures different from conventional nuclear recoils, e.g. the Migdal effect [249, 250] which corresponds to the ionisation of an atom due to the electronic cloud lagging behind after a nuclear scattering event.[9] Another option is to look for the ionisation of an atom directly induced by a DM particle scattering on an electron. While the nucleus can usually be treated as a free (but composite [6]) particle, the electrons are clearly in a bound state. This changes the description significantly since bound particles do not have fixed momentum but rather follow a distribution which needs to be predicted from their wave function. This complication has spawned several solutions and nowadays these effects are well-known [252–254]. Similarly, more “exotic” materials receive increasingly more attention as they open up the opportunity to probe the parameter space deep within the sub-GeV range [255]. See also Ref. [256] for a recent review on the status of sub-GeV DM.

We will later discuss the options we have for the detection of even lighter DM but as these are typically less model-independent, we will then focus mostly on the DP as the DM candidate.

---

[9] We note in passing that, although the Migdal effect is a robust prediction of atomic physics, it has never been observed despite dedicated searches [251].

Table 4.1: Brief recap of the most important DM properties

DM needs to be...	Constraint (if applicable)	Source
weakly interacting	no single figure of merit	[235–238, 261]
globally abundant	$\Omega_{\mathrm{CDM}} \simeq 0.12$	[46, 181]
non-baryonic	$\Omega_{\mathrm{CDM}} \simeq 5\Omega_{\mathrm{b}}$	[46, 181]
locally abundant	$\rho_{\mathrm{DM,loc}} \simeq 0.4\,\mathrm{GeV/cm^3}$	[201, 262–265]
stable	$\tau_{\mathrm{DM}} \gtrsim 14\,\mathrm{Gyr}$ or even $\gg 14\,\mathrm{Gyr}$	[226–229] or [221–224]
restricted self-interactions	$\sigma/m \lesssim 1\,\mathrm{cm^2\,g^{-1}}$	[216–218]

As a minimalistic recap of all the aforementioned DM properties, we present a collection of the most significant features in table 4.1. Basically, any viable DM candidate must meet all of these requirements[10] as they are derived from purely gravitational observations or null results in searches for interactions with the SM.

Without going into too many details, it is still imperative to discuss the potential mechanism of production for DM in general (to fulfil the condition of the correct global relic abundance) and more specifically for DPDM. First of all, we will review the most famous generic production process, the so-called freeze-out mechanism. We will then demonstrate that this mechanism cannot be valid for DPs. Therefore, we will discuss aspects of how to produce lighter DPs from the thermal bath but finally, we will realise that, especially for ultralight DPs, the production can only proceed non-thermally.

Due to its historical importance and still lasting impact on the way we think about DM, we will now sketch the fundamental idea of the so-called WIMP (weakly interacting massive particle) miracle. This describes the curious incident that a weak-scale particle with an electroweak-like interaction strength yields the correct DM abundance via the freeze-out process. As the interactions are, despite their name, relatively strong, the WIMP will be in thermal equilibrium early on in the primordial plasma as long as the temperature is sufficiently above the mass of the WIMP. As soon as the temperature drops below the DM mass, the process drops out of equilibrium and the remaining WIMPs survive until today, acting as a potentially detectable DM candidate.

4.2 A little bit of cosmology and the WIMP miracle

We will now review a minimal amount of cosmology required to understand the freeze-out mechanism in particular and DM production in general following mostly Ref. [182]. As a proper introduction to the Friedmann-Lemaître-Robertson-Walker (FLRW) metric and ΛCDM is not necessary for a good understanding of thermal DM production, we will state only the most basic facts relevant to the computation.

Cosmological basics

For this, let us quickly emphasise the assumption of (statistical[11]) isotropy and homogeneity. This simplifies our calculations enormously: The metric, which describes the geometry

---

[10] For DM with strong interactions (strong referring to interaction strength, *not* QCD), we refer to Refs. [257, 258] for strong interactions with the SM and to Ref. [259, 260] for strong interactions within the dark sector.

[11] In cosmological perturbation theory the geometry and matter content of the Universe is only homogeneous and isotropic on the background level while small perturbations are allowed on top. These, of course, then seed the structure formation which leads to the enormous small-scale anisotropies/inhomogeneities we observe today.

of the Universe and therefore controls all general relativistic effects, will be confined to the following form[12]

$$g_{\mu\nu} = \begin{pmatrix} -1 & 0 & 0 & 0 \\ 0 & a(t) & 0 & 0 \\ 0 & 0 & a(t) & 0 \\ 0 & 0 & 0 & a(t) \end{pmatrix} \tag{4.3}$$

with the so-called scale factor $a(t)$ (see below).[13] Similar considerations also drive the description of the matter content of the universe, i.e. assuming a perfect fluid, the stress-energy tensor of the matter distribution in the cosmic comoving frame must take the form

$$T^{\mu}_{\nu} = \begin{pmatrix} \rho(t) & 0 & 0 & 0 \\ 0 & p(t) & 0 & 0 \\ 0 & 0 & p(t) & 0 \\ 0 & 0 & 0 & p(t) \end{pmatrix} , \tag{4.4}$$

where ρ and p denote the energy density and pressure, respectively. For now, these two results are unrelated, and thus we need additional equations to connect them. These are of course the celebrated Einstein equations[14]

$$R_{\mu\nu} - \frac{1}{2} R g_{\mu\nu} = 8\pi G T_{\mu\nu} , \tag{4.5}$$

where G is Newton's constant and $R_{\mu\nu}$ and R are the Ricci tensor and scalar respectively which involve derivatives of the metric g and thus amount to a system of partial differential equations. In general, an analytical solution is impossible to find. Still, in our specific setup the high degree of symmetry allows for an exact solution, the aforementioned Friedmann-Lemaître-Robertson-Walker metric which is only determined by the time-dependent scale factor of an expanding Universe. The evolution of $a(t)$ is driven by the content of the Universe backreacting on the changes in the metric. From a simplified point of view, all particles in the Universe can be divided into relativistic/hot and non-relativistic/cold species at a given time. In the equations, this difference is given by the equation of state (EOS) w of a given species

$$w(t) = \frac{p(t)}{\rho(t)} = \begin{cases} 0 \quad , & \text{non-rel.} \\ \frac{1}{3} \quad , & \text{ultra-rel.} \\ -1 \quad , & \Lambda \end{cases} , \tag{4.6}$$

where we have also added the cosmological constant Λ for completeness. In a more realistic setup, the EOS is of course time-dependent as indicated in the equation. This is naturally the case for a massive particle red-shifting down from relativistic to non-relativistic energies, but the same is valid for models of evolving dark energy [267], which became especially interesting recently in the context of observations from the Dark Energy Spectroscopic Instrument (DESI) which shows a preference for an evolving EOS for dark energy [268]. As one expample, there exist models where the cosmological constant is mimicked by the evolution of a scalar field [269].

---

[12] To simplify our results further, we also assume that the Universe has vanishing curvature which of course is well in agreement with observations [181].

[13] We will follow the metric conventions according to Refs. [182, 266]).

[14] Once again for simplicity, we disregard the (in)famous cosmological constant term $\Lambda g_{\mu\nu}$ which can in principle also be absorbed into the stress-energy tensor and is also negligible for early cosmology.

With these considerations, we can now go ahead and evaluate the Einstein equations for a generic matter content

$$H(t)^2 \equiv \left(\frac{\dot{a}(t)}{a(t)}\right)^2 = \frac{8\pi G}{3}\rho(t) \tag{4.7a}$$

$$\dot{H}(t) = -4\pi G(\rho(t) + p(t)) = -4\pi G\rho(t)(1 + w(t)) \, , \tag{4.7b}$$

where we have now defined the Hubble parameter mentioned earlier.[15] It is now instructive to solve these equations separately for different EOSs. We can simply solve the continuity equation $\nabla_\mu T^{\mu\nu} = 0$ to find (suppressing the time dependence for conciseness from now on)

$$\dot{\rho} = -3H(\rho + P) = -3H\rho(1 + w) \, . \tag{4.8}$$

We will now make a simple power law ansatz for $\rho \propto a^k$ and assume that w is either constant or only mildly time-dependent which in turn implies

$$k = -3(1 + w) = \begin{cases} -3 \quad , & \text{non-rel.} \\ -4 \quad , & \text{ultra-rel.} \\ 0 \quad , & \Lambda \end{cases} \, . \tag{4.9}$$

This result can also be derived on more intuitive grounds. For that, we realise that the number density of particles dilutes proportionally to the change in the overall volume[16], that is, it must be proportional to a^{-3} in our setup. As for non-rel. particles the energy is dominated by the mass of the particles, the scaling of ρ with a will follow the number density. For the relativistic case, we simply note that on top of the dilution, there is also the redshifting of the energy of the particles, adding another factor of a^{-1}. Finally, for a cosmological constant, it is almost self-evident that the energy density is not impacted by the expansion.

In addition, we also derive the relation between the scale factor and time. Having the scaling derived above this is a fairly simple exercise

$$a \propto \begin{cases} t^{2/3} \quad , & \text{non-rel.} \\ t^{1/2} \quad , & \text{ultra-rel.} \\ e^{\Lambda t} \quad , & \Lambda \end{cases} \, , \tag{4.10}$$

where we, in an abuse of notation, have defined $\Lambda = (8\pi G\rho/3)^{1/2}$ as the cosmological constant which, as expected, has units of energy. This essentially concludes the gravitational part of our mini-review of particle cosmology.

Particle cosmology

Let us therefore now turn to the particle side. If we want to track the evolution of the particle distribution for species x, we need to use the Boltzmann equation[17]

$$\frac{\partial f_x(t,p)}{\partial t} - Hp\frac{\partial f_x(t,p)}{\partial p} = \frac{C[f_x, f_i](t,p)}{E_x} \, . \tag{4.11}$$

---

[15] Before we used H_0, i.e. the Hubble parameter today.

[16] If the total number of particles is conserved.

[17] The Boltzmann equation is technically classical and the inclusion of the QFT matrix elements makes it therefore semi-classical. A full quantum field theoretical generalisation can be found in the so-called Kadanoff-Baym equations [270].

For a more pedagogical and stringent derivation, the interested reader can find more material in Refs. [271, 272] which also mainly use the same notation. The distribution function contains all the information about the bulk of particles, but due to the imposed homogeneity and isotropy, it can only depend on time and the absolute value of the momentum, which of course is related to the particle's energy via the usual on-shell relation $E_x^2 = p^2 + m_x^2$. We see that the second term on the left-hand side (LHS) is driven by the expansion of the Universe since in Minkowski space (where $\dot{a} = 0 \Rightarrow H = 0$) the second term vanishes. The RHS on the other hand describes the collision between the particles of species x and others (i) as well as self-interactions. We will not discuss this further as for our description of the particles' time evolution, it is sufficient to look at the leading moments of the distribution function

$$n_x(t) = g_x \int \frac{\mathrm{d}^3p}{(2\pi)^3} f_x(t,p) \tag{4.12a}$$

$$\rho_x(t) = g_x \int \frac{\mathrm{d}^3p}{(2\pi)^3} E_x f_x(t,p) \tag{4.12b}$$

$$p_x(t) = g_x \int \frac{\mathrm{d}^3p}{(2\pi)^3} \frac{p^2}{3E_x} f_x(t,p) \ , \tag{4.12c}$$

i.e. the number density n_x and energy density ρ_x, as well as the pressure p_x, respectively. We see immediately that the definition of the pressure is consistent with eq. (4.6) in the non- and ultra-relativistic case. Additionally, we have introduced the internal degrees of freedom (DOFs) g_x.

Before we specify the setup to the case of freeze-out, let us quickly discuss the Boltzmann equation in equilibrium. A simple consideration of demanding that processes containing x are equilibrated (with rates faster than the Hubble expansion) yields the famous thermal equilibrium distributions

$$f_x(t,p) = \frac{1}{\exp[(E_x - \mu_x(t))/T_x(t)] \mp 1} \ , \tag{4.13}$$

where T_x denotes the temperature of the species x. The $-$ is for the bosonic solution (Bose-Einstein) and the $+$ is for fermions (Fermi-Dirac), and μ_x denotes the chemical potential of the species x which we will however set to 0 from now on. At least for the SM, this is a reasonable assumption for the early cosmic history [273, 274], i.e. before big bang nucleosynthesis (BBN). It should also be noted that all the particles participating in these equilibrium processes share the same temperature.

Unfortunately, it is impossible to find a closed form for the Boltzmann moments for all regimes. We will nevertheless give the results for the non- and ultra-relativistic regimes

$$n_x(t) \simeq g_x \begin{cases} \left(\frac{m_x T_x}{2\pi}\right)^{3/2} e^{-m_x/T_x} \ , & \text{non-rel.} \\ \frac{\zeta(3)}{\pi^2} T_x^3 \begin{cases} 1 \ , & \text{bosonic} \\ 3/4 \ , & \text{fermionic} \end{cases} \ , & \text{ultra-rel.} \end{cases} \tag{4.14a}$$

$$\rho_x(t) \simeq g_x \begin{cases} \left(m_x + \frac{3}{2} T_x\right) n_x(t) \ , & \text{non-rel.} \\ \frac{\pi^2}{30} T_x^4 \begin{cases} 1 \ , & \text{bosonic} \\ 7/8 \ , & \text{fermionic} \end{cases} \ , & \text{ultra-rel.} \end{cases} \tag{4.14b}$$

$$p_x(t) \simeq g_x \begin{cases} T_x n_x(t) \ , & \text{non-rel.} \\ \frac{\pi^2}{90} T_x^4 \begin{cases} 1 \ , & \text{bosonic} \\ 7/8 \ , & \text{fermionic} \end{cases} \ , & \text{ultra-rel.} \end{cases} \ , \tag{4.14c}$$

with ζ being the Riemann zeta function. The immediate conclusion is that non-relativistic particles in equilibrium will be exponentially suppressed in number (and thus energy) density. However, our Universe famously carries an asymmetry in the baryon number which allows for a late Universe as we know it [183] which makes the non-relativistic formulae inappropriate for low enough temperatures. In other words, there is a chemical potential that becomes non-negligible at some point in time.

With that knowledge, let us further investigate the Boltzmann equation. The moments of the Boltzmann distribution come with their own version of eq. (4.11). For the following, it is sufficient to consider only the Boltzmann equation for the number density. We will further simplify the setup by considering a toy model DM candidate in contact with the SM. Before we can discuss this setup, we should quickly explain the thermal history of the SM. Under the assumption that the thermal bath of SM particles drives the expansion of the Universe, we note that the heavy particles in the SM become non-relativistic first. They could potentially start an era of matter domination, but since they are both short-lived and strongly interacting, they annihilate and decay away before the a^{-3} scaling can take over. It is thus fair to assume that species in chemical equilibrium become irrelevant once the temperature drops below their mass. We can therefore relate the total number density of the Universe with the temperature via

$$n_{\mathrm{SM}} \equiv g_{*,n} \frac{\zeta(3)}{\pi^2} T_{\mathrm{SM}}^3 \,, \tag{4.15}$$

and analogously for the other moments. These variables $g_{*,n/\rho/p}(T)$ are known as effective DOFs and are functions of temperature. They can either be inferred from the literature [275] or alternatively, the system can be solved by taking into account all SM particles and using effective masses for the light quarks to account for the QCD phase transition [272]. Since we are not interested in a separate dark sector, we will from now on use $T_{\mathrm{SM}} = T$. For us, it suffices to know that the relation for the energy density allows us to relate the time with the temperature immediately. To this end, we write

$$H = \frac{\frac{\mathrm{d}a}{\mathrm{d}t}}{a} = \frac{\frac{\mathrm{d}a}{\mathrm{d}T}}{a} \frac{\mathrm{d}T}{\mathrm{d}t} \Rightarrow \frac{\mathrm{d}T}{\mathrm{d}t} = -HT \,, \tag{4.16}$$

where we have used that $\rho \propto a^{-4} \propto T^4$ from eqs. (4.9) and (4.14a), respectively. We note that the second proportionality is only valid using the observation that the $g_{*,\rho}$ is only slightly time-dependent in the SM.

The freeze-out mechanism

Equipped with these relations, let us now finally consider the behaviour of a DM candidate interacting with the SM. In addition, assume that this particle is stable and only coupled to the SM via 2-by-2 annihilation processes DM + DM ↔ SM + SM. For the number density, we find the following expression after integrating over momentum space as defined in eq. (4.12a)

$$\dot{n}_{\mathrm{DM}} + 3Hn_{\mathrm{DM}} = \langle \sigma_{\mathrm{prod}} v \rangle n_{\mathrm{SM}}^2 - \langle \sigma_{\mathrm{ann}} v \rangle n_{\mathrm{DM}}^2 \tag{4.17}$$

$$\Leftrightarrow \frac{\mathrm{d}n_{\mathrm{DM}}}{\mathrm{d}x} + \frac{3}{x} n_{\mathrm{DM}} = \frac{\langle \sigma_{\mathrm{ann}} v \rangle}{Hx} \left(\frac{\langle \sigma_{\mathrm{prod}} v \rangle}{\langle \sigma_{\mathrm{ann}} v \rangle} n_{\mathrm{SM}}^2 - n_{\mathrm{DM}}^2 \right) \,, \tag{4.18}$$

where $\langle \sigma v \rangle$ denotes the thermally averaged cross section. The first term on the RHS of the first line can be understood intuitively by the following consideration: the number density changes at the rate of DM production from SM annihilations. Parametrically, nv

is a current of particles and $n\sigma$ is essentially an inverse mean free path. In combination, this yields the number of annihilations per time and volume, exactly what we need for the evolution of the number density. In analogy, the second term describes the annihilation of DM particles into the SM. In the second step, we have replaced time with the inverse temperature via eq. (4.16). To be precise, we choose $x = m/T$ since the DM mass is the only additional scale in the problem, and thus we have a dimensionless quantity at hand. For this choice, the relation in eq. (4.16) transforms into $\mathrm{d}x/\mathrm{d}t = Hx$.

Noting that the RHS must vanish in chemical equilibrium, we can invoke detailed balance, which says

$$\langle\sigma_{\mathrm{prod}} v\rangle n_{\mathrm{SM,eq}}^2 = \langle\sigma_{\mathrm{ann}} v\rangle n_{\mathrm{DM,eq}}^2 \,. \tag{4.19}$$

To further simplify the Boltzmann equation we need to introduce the total[18] entropy density s_{tot} (see e.g. Ref. [182] for details). The central observation is that this quantity is comovingly conserved in thermal equilibrium, i.e. $s_{\mathrm{tot}} \propto a^{-3}$. With the help of this quantity, we can define the (dimensionless) yield $Y_{\mathrm{DM/SM}} = n_{\mathrm{DM/SM}}/s_{\mathrm{tot}}$ and further write

$$\frac{\mathrm{d}Y_{\mathrm{DM}}}{\mathrm{d}x} = \frac{\langle\sigma_{\mathrm{ann}} v\rangle s_{\mathrm{tot}}}{Hx}\left(\left(\frac{Y_{\mathrm{DM,eq}}}{Y_{\mathrm{SM,eq}}}\right)^2 Y_{\mathrm{SM}}^2 - Y_{\mathrm{DM}}^2\right) \,. \tag{4.20}$$

Our next step towards a more illuminating equation requires us to realise that the SM particles are typically rather strongly coupled (and that we assumed vanishing chemical potential), and thus we can assume that they never deviate too much from equilibrium, that is $Y_{\mathrm{SM}} = Y_{\mathrm{SM,eq}}$. In conclusion, we find the so-called Riccati equation

$$\frac{\mathrm{d}Y_{\mathrm{DM}}}{\mathrm{d}x} = \frac{\langle\sigma_{\mathrm{ann}} v\rangle s_{\mathrm{tot}}}{Hx}\left(Y_{\mathrm{DM,eq}}^2 - Y_{\mathrm{DM}}^2\right) \tag{4.21}$$

$$\Leftrightarrow \frac{x}{Y_{\mathrm{DM,eq}}}\frac{\mathrm{d}Y_{\mathrm{DM}}}{\mathrm{d}x} = \frac{\langle\sigma_{\mathrm{ann}} v\rangle n_{\mathrm{DM,eq}}}{H}\left(1 - \frac{Y_{\mathrm{DM}}^2}{Y_{\mathrm{DM,eq}}^2}\right) \,, \tag{4.22}$$

which makes it apparent that the interactions with the SM drive the DM yield generically towards its equilibrium density, i.e. vanishing RHS. This is an efficient process if the interaction rate is sufficiently fast, i.e. if the prefactor on the RHS is large enough. Let us therefore investigate this prefactor in more detail. The important factor driving the whole process is the dimensionless quantity $\langle\sigma_{\mathrm{ann,eq}} v\rangle n_{\mathrm{DM,eq}}/H \equiv \Gamma_{\mathrm{ann}}/H$. We immediately identify this as the ratio of the (would-be) equilibrium annihilation rate and the Hubble rate. We conclude that as soon as the reaction rate is less than the Hubble rate the process will drop out of equilibrium. Dropping out of equilibrium means that $Y_{\mathrm{DM,eq}}$ rapidly vanishes as the distribution suffers from Boltzmann suppression. In contrast, the actual yield will deviate from this behaviour. We will therefore consider the simplified equation where we can safely ignore the equilibrium yield in eq. (4.21)

$$\frac{\mathrm{d}Y_{\mathrm{DM}}}{\mathrm{d}x} = -\frac{\langle\sigma_{\mathrm{ann}} v\rangle s_{\mathrm{tot}}}{Hx} Y_{\mathrm{DM}}^2 \tag{4.23}$$

$$\Rightarrow \frac{\mathrm{d}Y_{\mathrm{DM}}}{\mathrm{d}x} = -\frac{\langle\sigma_{\mathrm{ann}} v\rangle s_{\mathrm{tot,f}} x_{\mathrm{f}}}{H_{\mathrm{f}} x^2} Y_{\mathrm{DM}}^2 \quad \text{with} \quad \frac{s_{\mathrm{tot}}}{H} = \frac{s_{\mathrm{tot,f}}}{H_{\mathrm{f}}}\left(\frac{x_{\mathrm{f}}}{x}\right) \tag{4.24}$$

$$\Rightarrow Y_{\mathrm{DM},\infty} \approx \frac{H_{\mathrm{f}}}{\langle\sigma_{\mathrm{ann}} v\rangle s_{\mathrm{tot,f}}} \,, \tag{4.25}$$

---

[18] As mentioned above, the Universe is dominated by the SM.

where we explicitly used the temperature dependence of s_{tot} and H and defined their values at freeze-out with subscript $_{\mathrm{f}}$. Furthermore, we assumed that a time-independent thermally averaged cross section is a reasonable approximation. We can immediately read off one of the most striking and maybe initially unintuitive results: the stronger the interaction, the less DM will be produced! Thinking about this phenomenon for a minute, it quickly becomes clear that the naive intuition ("more interactions = more DM") must be wrong. Stronger interactions keep up the equilibrium for longer and thus, less of the DM remains.

In the next step, we should determine x_{f}. For this, we effectively need to solve

$$\Gamma_{\mathrm{ann,f}} = \langle \sigma_{\mathrm{ann,eq}} v \rangle n_{\mathrm{DM,eq,f}} = H_{\mathrm{f}} \tag{4.26}$$

$$\Rightarrow \langle \sigma_{\mathrm{ann,eq}} v \rangle \left(\frac{m^2}{2\pi x_{\mathrm{f}}} \right)^{3/2} e^{-x_{\mathrm{f}}} = H_{\mathrm{f}} \,, \tag{4.27}$$

using the result from eq. (4.14a). We see that x_{f} scales mostly logarithmic with the other variables of the problem. Thus, determining it once will fix it for a broad parameter range. We will now make a rough estimate on purely dimensional grounds. Assuming that x_{f} does not vary too much from 1, we write $H_{\mathrm{f}} \sim m_{\mathrm{p}}^{-1}$ and $\langle \sigma_{\mathrm{ann,eq}} v \rangle \sim m^{-2}$. We thus find as the leading contribution $e^{-x_{\mathrm{f}}} \sim m/m_{\mathrm{p}}$ and therefore $x_{\mathrm{f}} \sim 30 - 40$ for DM masses around the GeV scale. In the literature, one may also find varying values like $10 - 20$ but this barely plays a role for our arguments here as the main purpose is a sketch of the mechanism.

Now that we have produced our DM candidate, we need to figure out how much DM we ended up with. We will continue using simple estimates and therefore, among other assumptions, we will neglect the SM effective degrees of freedom now and ignore $\mathcal{O}(1)$ prefactors, thus simply writing

$$\Omega_{\mathrm{CDM}} = \frac{\rho_{\mathrm{CDM}}}{\rho_{\mathrm{crit}}} = \frac{m n_{\mathrm{DM}}}{3 m_{\mathrm{p}}^2 H_0^2} \sim \frac{m Y_{\mathrm{DM},\infty} T_0^3}{3 m_{\mathrm{p}}^2 H_0^2} \sim 0.1 \frac{x_{\mathrm{f}}}{10} \frac{10^{-11}\,\mathrm{GeV}^{-2}}{\langle \sigma_{\mathrm{ann}} v \rangle} \,. \tag{4.28}$$

Note that we have explicitly defined the relative abundance of DM w.r.t. the complete energy density of the Universe from eq. (4.1a). This is labelled here as the critical energy density ρ_{crit}.

We have just witnessed the so-called WIMP miracle! For that, we realise that a weak-scale cross section will very roughly scale like $\sigma \sim \alpha^2/v_{\mathrm{EW}}^2 \sim 10^{-9}\,\mathrm{GeV}^{-2}$. Our result therefore shows that a particle with roughly this size of cross section can explain the correct DM relic abundance. Certainly, this extremely simplified picture might not be fully convincing but it captures the main essence. It should be emphasised here that this result is not just a product of the estimates we were taking as proper calculations yield the same result, too; see, e.g. Refs. [182, 276, 277]. This cosmological motivation, paired with theoretical expectations of supersymmetry (SUSY)[278] and the experimental feasibility of the discovery of such a particle at colliders [279], direct [6, 280] and indirect detection [281, 282] was the main driver for DM searches over a long time. The complete solution to the Riccati equation is visualised in fig. 4.3. We see that our analytical expectation is well-confirmed, i.e. the time of freeze-out is well-modelled by $x_{\mathrm{f}} = \mathcal{O}(10)$ and the final yield stays constant, whereas the equilibrium contribution vanishes quickly.

Before we now turn to the production of DPs in the early universe, we note that this process is very general and not only valid for DM. See also e.g. Ref. [182] for the freeze-out of neutrons, which is all-important for BBN, i.e. the production of light elements from the thermal plasma. Interestingly, neutrinos freeze-out as well but they are still relativistic at that time.

Furthermore, there are many variations of thermal production known in the literature which operate in different parts of parameter space like the freeze-in [283–286] which is

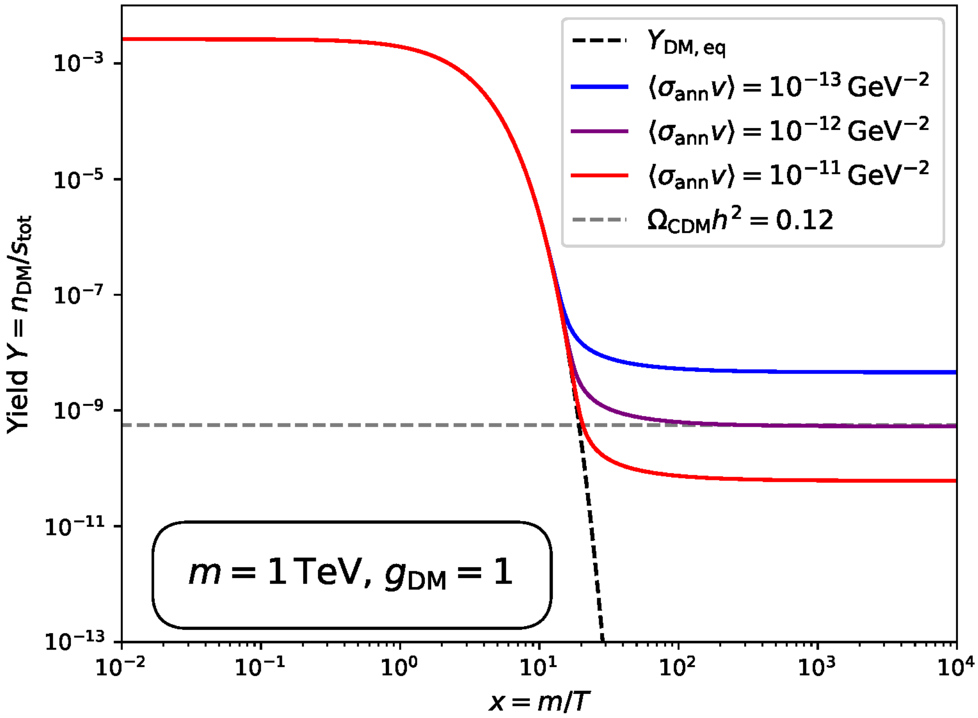

Figure 4.3: Solution to the Riccati equation (4.21) for a selection of cross section and a 1 TeV WIMP. The inverse proportionality of the final abundance to the cross section becomes clear. We further show the target abundance which yields the correct DM relic density.

relevant for particles with much weaker interactions. On top of this simple variation, there is a plethora of increasingly specific thermal mechanisms like forbidden DM [287, 288], Cannibal DM [289, 290], Coscattering DM [291–293], Zombie DM [294], Elder DM [295], Kinder DM [296], SIMP DM [297–299], and Pandemic DM [300, 301].

4.3 Dark Photon Dark Matter

In this section, we will delve deeper into the more specific production mechanism considered for DPDM. We will initially consider the case of DP production from the thermal plasma of the SM. We will quickly conclude that this mechanism is efficient only for comparatively heavy DPs around the electron mass threshold. Furthermore, the parameter space is robustly excluded, and thus we will consider the broad class of non-thermal production mechanisms.

4.3.1 Thermal Dark Photon Dark Matter

In the next step, we discuss the feasibility of thermal DPDM. Let us begin with rather heavy DPs, at least heavy enough to decay into electrons. Then for electrons alone, we have an inverse decay time [23] of

$$\tau_{e^+e^-}^{-1} = \frac{\epsilon^2 \alpha m}{3}\sqrt{1-\left(\frac{2m_e}{m}\right)^2}\left(1+\frac{2m_e^2}{m^2}\right)\,, \tag{4.29}$$

which of course increases if we take into account more decay channels that open up kinematically for higher masses.[19] We see that parametrically $\tau \lesssim \left(\epsilon^2 m\right)^{-1}$, which means, using $1\ \mathrm{eV}^{-1} \approx 7 \cdot 10^{-16}\,\mathrm{s}$, that the total lifetime is estimated as

$$\left(7 \cdot 10^{-25}\,\mathrm{s}\right) \epsilon^{-2} \left(\frac{\mathrm{GeV}}{m}\right) \gtrsim \tau_{\mathrm{tot}} \overset{!}{\gtrsim} 10^{25}\,\mathrm{s}\ , \tag{4.30}$$

where we have used that the lifetime of DM is constrained around $10^{25}\,\mathrm{s}$ (as discussed above) for heavy masses as an order of magnitude estimate. This makes it immediately clear that the DP must be extremely weakly coupled, in fact so weakly coupled that it cannot be produced thermally, at least not enough to be a viable DM candidate and especially not via freeze-out. However, there are interesting limits on the existence of DPs from thermal production and subsequent decays in specific islands of the parameter space, e.g. CMB bounds for MeV-scale masses and $\epsilon \sim 10^{-16}$ [303]. At this point, it is potentially interesting to point out that other models of spin-1 DM can fulfil the relic density while still being rather heavy [304, 305] but as the title of the first reference already suggests ("beyond the dark photon model"), these ideas are rather vaguely related to the minimal DP setup we are considering here. We will therefore now turn to a lighter regime.

The first detailed study about light DPDM from the thermal bath was performed in Ref. [306] which was refined that same year by Ref. [302]. In these seminal papers, the focus was on DPs below the electron mass threshold for DP decays but higher masses were also considered even though this will not lead to a stable DM candidate. In the latter work, it became clear that the parameter space for thermal DPDM is essentially ruled out, and additional work in the following years made this result even more robust with the inclusion of direct detection limits from absorption in the same style as discussed for the detection of solar DPs [119], see also chapter 3. Several direct detection experiments have thus been considered for DPDM exclusion and some of the best bounds are derived from there [120, 307–311].

Thermal DPDM production

Let us now sketch the production mechanism. We will focus on the slightly more detailed work in Ref. [302] which identified two very distinct regions. At the higher mass limit, the process of coalescence of an electron-positron pair is the dominant production mechanism. This at first seems unintuitive, since the on-shell condition requires that a given electron can only coalesce into a DP with a small subset of the phase space of positrons and vice versa. Nevertheless, this effect occurs at leading order in $\mathcal{O}(\alpha)$, while other interactions like Compton scattering or annihilations with DPs replacing photons are at higher order, i.e. $\mathcal{O}(\alpha^2)$, in the fine-structure constant even for resonant conversions which dominate the lower mass regime. All relevant processes are shown in fig. 4.4. We note in passing that pair annihilation can also produce two DPs at the same time, but this contribution is heavily suppressed by the small kinetic mixing. Furthermore, these production mechanisms only work if the DP never reaches thermal equilibrium, as otherwise, we would rather find a freeze-out-like behaviour. This cannot be in agreement with observations because light DPs would freeze-out late and therefore be hot and abundant during BBN or even the CMB decoupling which is heavily constrained.

The interesting observation is that the amount of DM produced only weakly depends on the DP mass and it is effectively independent of the exact processes producing the DPs

---

[19] We note a minimal typo in Ref. [302] which quotes the above result with a factor of 1/2 instead of 1/3, i.e. ignoring the longitudinal component of the DP.

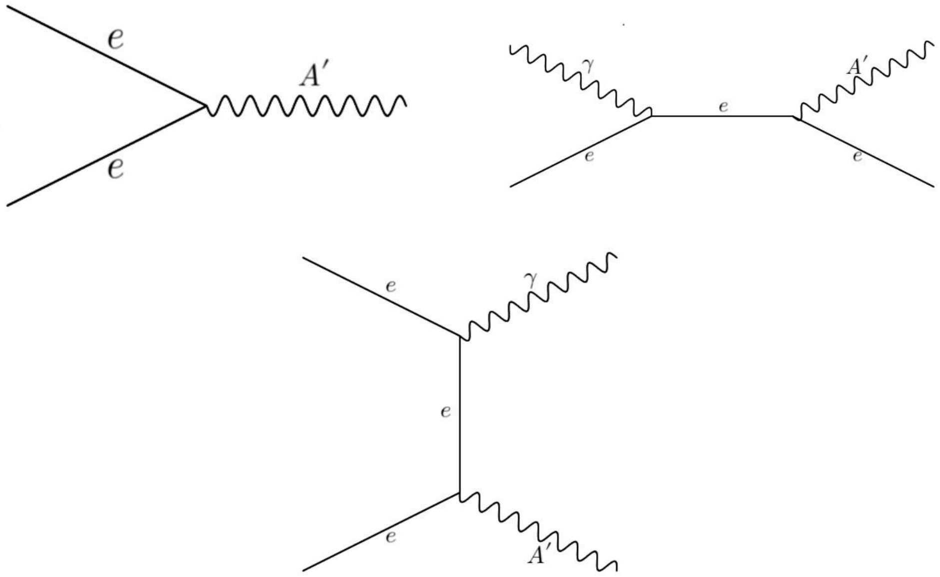

Figure 4.4: **Top left**: Coalescence/inverse decay of an electron and a positron into a DP. **Top right**: Sketch of the Compton contribution to DP production. **Bottom centre**: Sketch of the pair annihilation contribution to DP production.

which is due to the special behaviour at the resonance, an effect we already observed in chapter 3 where the solar DP production rate was independent of Γ, the production rate of photons. For a more detailed analytical and numerical treatment, we refer once again to Ref. [302]. The punchline here clearly is that while relatively light DPs (much lighter than the typical WIMP) can be produced from the thermal plasma, modern experiments and observations rule out this mechanism.

4.3.2 Non-thermal production for ultra-light Dark Photons

Now that we have realised that the presumably simplest production mechanism turns out to be in tension with experimental results let us turn to the class of non-thermal production mechanisms. There is a plethora of different mechanisms, all of which can produce the correct DM relic densities for light DPs without invoking interactions with the thermal plasma of SM particles.[20] We will keep the review of the vast literature concise, focussing only on a few outstanding examples.

Wave DM

However, before we begin with this discussion, let us spend some time explaining why we are interested in this light regime. The most obvious reason is that we have only a few hints at the mass of DM. As iterated before, DM essentially only needs to fulfil the criteria in section 4.1 which is feasible over a wide mass range, especially if DM is bosonic.[21] However, the same effect also drastically changes the behaviour of ultra-light DM. Whereas before, the typical DM search looks for direct particle-particle interactions,

---

[20] Of course, in the presence of kinetic mixing, there are additional constraints on DPs, independently of the production mechanism.

[21] The Pauli exclusion forces the mass of fermionic DM to be above $\sim 100\,\mathrm{eV}$, the so-called Tremaine-Gunn bound [312, 313] to explain DM bound to dwarf galaxies.

e.g. nuclear recoils, this becomes practically hopeless in this low mass regime since the non-relativistic particles carry only negligible kinetic energy. The only hope is therefore to detect the collective effects of the entire local density of DM. We will now see that this is in fact what happens to ultra-light DM. As DM is non-relativistic and confined to the galaxy, the particles can be localised down to their de Broglie wavelength $\lambda \approx 2\pi/(mv)$. For fermions, these regions clearly should not overlap resulting in the Tremaine-Gunn bound. For bosons, there is no problem in an overlapping wavefunction, and thus the particles can populate the same regions in phase space. To quantify this behaviour, let us determine the occupation number N_{dB} in a de Broglie volume from the local DM density

$$N_{\mathrm{dB}} \sim \frac{\rho_{\mathrm{DM}}}{m\lambda^3} \sim 1 \left(\frac{m}{10\,\mathrm{eV}}\right)^{-4} . \tag{4.31}$$

In conclusion, around the regime where fermionic DM becomes forbidden, we might expect new phenomena to emerge in bosonic DM models as well. Decreasing the mass further leads to a massive increase in the occupation number N_{dB} due to the scaling with the fourth power of m. Interestingly, as soon as the occupation number increases above 1 we observe that the DM particles start to behave differently: In this regime, the DM behaves more like a classical field than a collection of individual particles [96, 314]. The argument is that a quantum field ϕ can be decomposed according to [315]

$$\phi = \langle\phi\rangle + \delta\phi , \tag{4.32}$$

where $\langle\phi\rangle$ denotes the expectation value of the field and $\delta\phi$ stands for the quantum fluctuations. For a coherent state, the typical scaling is

$$\frac{\delta\phi}{\langle\phi\rangle} \sim \frac{1}{\sqrt{N_{\mathrm{dB}}}} , \tag{4.33}$$

i.e. the high occupation number derived above drives the field towards an almost ideal classical/wave-like state [316, 317]. See also the seminal paper on the quantum mechanical description of the EM field by Glauber [318].

Now we might wonder if this special regime comes with additional motivation and/or bounds. Let us therefore discuss the most extreme case first. The question is essentially, if DM could be arbitrarily light. The answer is a clear “no” since the uncertainty principle requires that, if DM is supposed to be bound to a system, e.g. a dwarf galaxy, it should be localised within this system. Therefore, the de Broglie wavelength should not exceed the size of dwarf galaxies.[22] This corresponds to bounds that require DM to be more massive than $\sim 10^{-21}\,\mathrm{eV}$, corresponding to kpc wavelengths, a number that follows quite consistently from the Lyman-α forest [320–322], density profiles [319, 323], Milky Way satellite masses [324], or from Milky Way satellite abundances [325].

DM in this extremely low mass regime is generally referred to as “fuzzy”. Intriguingly, there are also observational hints towards a preference for ultralight DM. One particular example would be the small-scale challenges of CDM which might be explained by fuzzy DM [326]. In particular, fuzzy DM reduces DM structure formation below its de Broglie wavelength and thus would deliver an explanation for the mismatch between simulated and observed DM core densities. This suppression of structure on smaller scales led to the initial introduction of this idea in Ref. [96]. However, since there are no clear hints towards the DM mass or even the approximate mass range there are parts of the community with a vivid interest in wave DM over all mass scales below $m \sim 10\,\mathrm{eV}$. The next chapter will discuss a particular sub-region around $10^{-17}\,\mathrm{eV}$.

---

[22] Ref. [319] refers to this as “folk wisdom”. Nevertheless, the estimates coming from this are in excellent agreement with a more rigorous treatment of this idea.

The misalignment mechanism

We will now return to the gravitational (i.e. non-thermal) production of DM in the ultra-light mass range. In this context, we will have a brief look at the first two papers [327, 328] that wanted to generalise the misalignment mechanism, a simple yet powerful method to produce (pseudo-)scalars from the expansion of the Universe and an initial misalignment in field space. (In-)Famously, these papers initially contained an error in the calculations, which seemed to imply that the misalignment mechanism can easily be transferred to vector particles as well. A more detailed look showed that only the transverse modes can be produced in this way if a non-minimal coupling to gravity is invoked [328].

We will now sketch the misalignment mechanism for a scalar field and then we will discover where the generalisation to vector fields breaks down. For this, we will begin with the action of a scalar on an FLRW background

$$\begin{aligned} S_{\text{scalar}} &= \int \mathrm{d}^4x\sqrt{-g}\left(\frac{1}{2}(\partial^\mu\phi)(\partial_\mu\phi) - \frac{m^2}{2}\phi^2 + \mathcal{L}_{\text{int}}\right) && (4.34)\\ &\xrightarrow{\text{EOM}} \partial_\mu\left(\sqrt{-g}\partial^\mu\phi\right) + \sqrt{-g}m^2\phi = 0 && (4.35)\\ &\xrightarrow{\partial_i\phi=0,\ \text{FLRW}} \ddot{\phi} + 3H\dot{\phi} + m^2\phi = 0\ . && (4.36)\end{aligned}$$

In the first step, we have derived the equations of motions from the action of the field, ignoring all interactions (including self-interactions) from $\mathcal{L}_{\text{int}}$. Early on, when the Hubble rate is much larger than the mass, this is the equation for an overdamped harmonic oscillator, albeit with a decreasing damping term. Nevertheless, this change of the damping does not play a major role as long as $H \gg m$, implying that the field value is frozen. Later on, once $H \ll m$, the field will oscillate rapidly while the overall amplitude, i.e. the envelope, slowly redshifts down. To clarify this, let us begin with an ansatz where we split ϕ into an oscillating and a slowly evolving part

$$\begin{aligned} &\phi = \phi_0(t)e^{imt} \quad \text{with} \quad |\dot{\phi}_0| \ll m|\phi_0| \quad \text{and} \quad |\ddot{\phi}_0| \ll m^2|\phi_0| && (4.37)\\ &\Rightarrow \ddot{\phi}_0 + (3H + 2im)\,\dot{\phi}_0 + 3imH\phi_0 = 0 && (4.38)\\ &\Rightarrow 2\dot{\phi}_0 = -3H\phi_0 + \mathcal{O}\left(\frac{H}{m}, \frac{\dot{\phi}_0}{m}, \frac{\ddot{\phi}_0}{m^2}\right) && (4.39)\\ &\Rightarrow \phi_0 \simeq \phi_{\text{ini}}\left(\frac{a_{\text{ini}}}{a}\right)^{3/2}\ , && (4.40)\end{aligned}$$

where we denote initial values with the subscript $_{\text{ini}}$.[23] In conclusion, the energy density[24] stored in ϕ, i.e. $\rho_\phi \propto \phi^2 \propto a^{-3}$, redshifts in a way that mimics the evolution of a non-relativistic matter component, i.e. CDM. We note in passing that this is the leading term in a WKB approximation that is a good match for late times but breaks down when $H \sim m$. For higher precision, one would need to introduce higher terms in the WKB expansion but if we consider the Hubble rate e.g. at BBN we already see that it is $H \sim T^2/m_{\text{p}} \sim (1\,\text{MeV})^2/10^{19}\,\text{GeV} \sim 10^{-16}\,\text{eV}$. We conclude that even during our earliest probe of cosmology, $m \gg H$ is a robust assumption in large parts of the generic DM parameter space.

---

[23] Note that we have used a time-independent mass for the scalar field. For the QCD axion, the mass is known to be explicitly temperature- and thus time-dependent [329].

[24] This can be derived from the stress-energy tensor of the field. For simplicity, we can read this off from the mass term in the Lagrangian. See also Ref. [328]. Furthermore, we average out the rapid oscillations.

The key difference for a vector boson lies in the Lorentz structure of the Lagrangian which modifies the equations of motion[25]

$$S_{\text{vector}} = \int \mathrm{d}^4x \sqrt{-g} \left(-\frac{1}{4} F_{\mu\nu} F^{\mu\nu} + \frac{m^2}{2} A_\mu A^\mu + \mathcal{L}_{\text{int}} \right) \tag{4.41}$$

$$\xrightarrow{\text{EOM}} -\partial_\mu \left(\sqrt{-g} F^{\mu\nu} \right) - \sqrt{-g} m^2 A^\nu = 0 \tag{4.42}$$

$$\xrightarrow{\partial_i A^\mu = 0,\ \text{FLRW}} \ddot{A}_j + H \dot{A}_j + m^2 A_j = 0 \ , \tag{4.43}$$

where in the first step we have once again written the EOM explicitly. Further simplifications then bring us to the third line. It is important to note that the equations of motion of a perfectly homogeneous field force the temporal component A^0 to vanish.[26] This equation was incorrectly derived in the original publications and thus, it was not realised that the DP behaves different free three independent scalars. Furthermore, we have to realise that $\rho_A \propto A^\mu A_\mu = g^{\mu\nu} A_\mu A_\nu = a^{-2} A_j^2 \equiv B_j^2$ (if we once again read this off from the mass term or consult Ref. [330]) and thus we should rather express our equations in terms of this quantity. This leads to a different equation of motion

$$\ddot{B}_j + 3H\dot{B}_j + \left(m^2 + \frac{\ddot{a}}{a} + H^2 \right) B_j = 0 \tag{4.44}$$

$$\Leftrightarrow \ddot{B}_j + 3H\dot{B}_j + \left(m^2 + \frac{R}{6} \right) B_j = 0 \ , \tag{4.45}$$

where we have explicitly defined the Ricci scalar R in the FLRW metric which was introduced earlier for the Einstein equations eq. (4.5). We see that the vector field cannot follow the same time evolution as the scalar, and thus we cannot use misalignment in the most naive formulation for the production of DPs. The trick is to introduce a non-minimal coupling to gravity

$$\mathcal{L}_{\text{grav}} = \frac{\kappa}{12} R A_\mu A^\mu \ , \tag{4.46}$$

with the conformal choice $\kappa = 1$ which will cancel the dangerous term and allow for the production of transversely polarised DPs. Unfortunately, this seems to cause unphysical behaviour in the longitudinal mode [331–335]. Focussing on the longitudinal mode instead, there is an alternative mechanism to misalignment which can produce longitudinally polarised DPs from quantum fluctuations during inflation, introduced in the seminal paper Ref. [330]. Since then, gravitational production has come under more scrutiny and this approach was explored in greater detail [336–338]. See also Ref. [339] for a recent review of gravitational particle production in cosmology including not just vector bosons.

Furthermore, there are additional mechanisms that qualify as non-thermal but require coupling to additional particles like the inflaton [340–343], a general spectator field [344–347], an axion [348, 349] or from cosmic strings [350].

The DP limit landscape

As a concluding remark, the detection (both direct and indirect), as well as the direct production, become increasingly tricky the further we go down the mass scale of the DPs.

---

[25] We note in passing that we should use the covariant derivative for the field strength $\partial_\mu \to \nabla_\mu$ but the antisymmetric structure of the tensor cancels the contributions from the Christoffel symbols. For the scalar, the covariant derivative in GR coincides with the one we are used to in Minkowski space. See e.g. Ref. [182] or any book on GR/cosmology for details on the covariant derivative.

[26] We will observe a similar effect in the following chapter 5 where we discuss the wave DM limit for DPs.

Plasma effects, or in general matter effects, play a major role in that context. As long as the DP has a non-negligible mass in a given setup, detection prospects are good. Now, the lighter the DP, the easier it is for usually irrelevant scales such as plasma frequencies to become larger than the actual DP mass. This generically induces decoupling, as we have realised in detail in the previous chapter 3. Therefore, in the next chapter, we will consider a modified version of the DP which enjoys the same non-thermal production mechanisms as the kinetically mixed DP but has experimental signatures which do not suffer so strongly from plasma effects.

However, before we move towards the next chapter, we should discuss the general landscape of kinetically mixed DPDM limits. In the previous chapter 3 we have already seen very strong limits on the sheer existence of DPs in the low mass regime. These included the solar/stellar limits [120] which start to become dominant below roughly the electron mass and peak around the keV scale. Their dominance is only broken by limits from cavity-based light-shining-through-the-wall experiments [351][27] at the μeV scale, especially DarkSRF [352]. Also, tests of the Coulomb law [43] can be very sensitive and are probably the strongest probe of the existence of DPs in a purely lab-based setup in this region. If we want to cover smaller masses, we need to check for cosmological observations [109, 110, 112] since resonant conversions of CMB photons into DPs can distort its black body spectrum which becomes relevant also at the μeV scale and stays the strongest bound down to around 10^{-15} eV. Interestingly, the limits for the existence of the DP at lowest masses are due to the magnetic field of Jupiter [76, 77] relevant at DP masses of around $10^{-16} - 10^{-17}$ eV. A good summary of all the limits can be found in fig. 4.5.

Finally, let us come to the DPDM limits, which are often stronger than the limits of the sheer existence of DPs.[28] Once again, there are limits from direct detection experiments such as XENON, now looking for the signal of DPDM [120] in the keV region. Toward lower masses, there is a plethora of dedicated[29] experiments, which penetrate deep into the parameter space around $10^{-4} - 10^{-7}$ eV. These experimental ideas have mostly been developed from theoretical proposals to real experiments in the last decade. These ideas can usually be categorised as broadband or resonant searches. Examples of the former are haloscopes [328], initially proposed for axion searches [115] and resonant, tunable LC circuits picking a DM-induced magnetic field [353] to name two important concepts. For the broadband case, a major example is the dish antenna setup [354] but as shown in Ref. [355], there is a transitional regime and quickly tunable setups can bridge the gap between resonant and broadband detection, as, e.g., in the case of dielectric layers (see the aforementioned paper and, e.g., [356]).

We will refrain from a complete collection of limits here and instead focus on the limits providing the deepest reach and/or the widest spread in DP mass. These are, among many others, ordered by mass range, WISPDMX [357], Dark E-Field [358], ADMX [359], BRASS-p [360], and DOSUE [361]. A quick look at the publication dates of these results shows that over the next few years, we can hope for a gradual coverage of the parameter space.

Until then, the gaps between these direct searches are dominated by cosmological limits on DPDM which are even stronger than the aforementioned CMB limits on the existence of DPs. At the highest masses where these limits become relevant, i.e. around the meV scale,

---

[27] It should be emphasised that this paper marked a new understanding of DPs in cavity setups and it enabled strong efforts in the experimental community.

[28] Only due to the Sun being so efficient at producing DPs, there is some parameter space where the DPDM limits do not dominate.

[29] These are typically experiments constructed mainly for ALP DM searches. Nevertheless, we have already realised in chapter 3 that these searches can often be reinterpreted in terms of DP bounds [102].

these come from the stringent constraints on the effective number of relativistic degrees of freedom at BBN and CMB (for more recent data see also [362] and [181], respectively for the data and [363] for DM-independent limits). Then analogously to the disappearance of CMB photons due to resonant conversions, a background of DPDM can resonantly oscillate into photons, thus potentially distorting the CMB black body spectrum. This effect dominates the limits from $\sim 10^{-4}\,\mathrm{eV}$ down to masses of neV. From here on downwards, there are even stronger limits, in fact globally among the deepest reach of the kinetic mixing parameter, derived from the heating of inhomogeneous structures as seen in the Ly-α forest [113] or from observations of the temperature of the intergalactic medium (IGM) during the time of HeII reionisation [110].[30]

Beyond these bounds from cosmology that reach $\sim 10^{-14}\,\mathrm{eV}$, the best limits come from astrophysical systems and the anomalous heating they receive from the presence of DPDM [133, 365, 366] which decouple comparatively slowly and thus stay dominant from here on until they vanish and/or become unreliable.[31] While these limits are indeed the strongest in the ultra-light regime, we should mention an idea brought forward for the direct detection of ultra-light DPDM, using the Earth itself as a cavity which generates an oscillating magnetic field which can be readily picked up [368, 369]. This intriguing idea is the strongest "lab-based" limit at an impressively small mass of $\sim 10^{-16}\,\mathrm{eV}$. With an analogous or at least similar concept, additional searches followed or have been proposed after the original publications [370–373].

Before we end this chapter, let us point out a final method for searching DPs which is almost completely independent of the kinetic mixing. The effect in question is called superradiance [374]. Simply put, rotating black holes can build up clouds of light bosons while simultaneously spinning down. The cloud build-up is only efficient for a DP Compton wavelength, i.e. the inverse mass, that roughly matches the horizon size of the black hole. The observation of spinning black holes with specific masses therefore limits the existence of DPs in a given mass range *without invoking kinetic mixing*. Therefore, this probe can be considered extremely powerful, excluding all parameter points with a given mass in the usual mass vs. kinetic mixing plot [375]. Interestingly, interactions with an extended dark sector or with the SM via kinetic mixing can inhibit the growth of the superradiant cloud and thus invalidate the limits in parts of the parameter space [114, 376].

Since the DP is an attractive model in general and an interesting candidate for DM, this field of research is constantly evolving, and new limits or proposals appear constantly. In this brief review, we have tried to focus primarily on peer-reviewed articles. However, there are numerous intriguing new ideas on the market. Let us explicitly mention Ref. [377] which utilised a satellite probe that was originally designed for a different purpose as a semi-direct detection search for DPDM.[32] Fundamentally, the idea is to use the Parker Solar Probe for the detection of monochromatic photons from the reflection of the interacting part of DPDM at the solar plasma [378].

---

[30] See also Ref. [364] for an earlier description of similar limits in that region of the parameter space.

[31] Note that some of the limits in [365] were later discovered to be invalid [367].

[32] This concept is very well aligned with the publications presented here in this thesis.

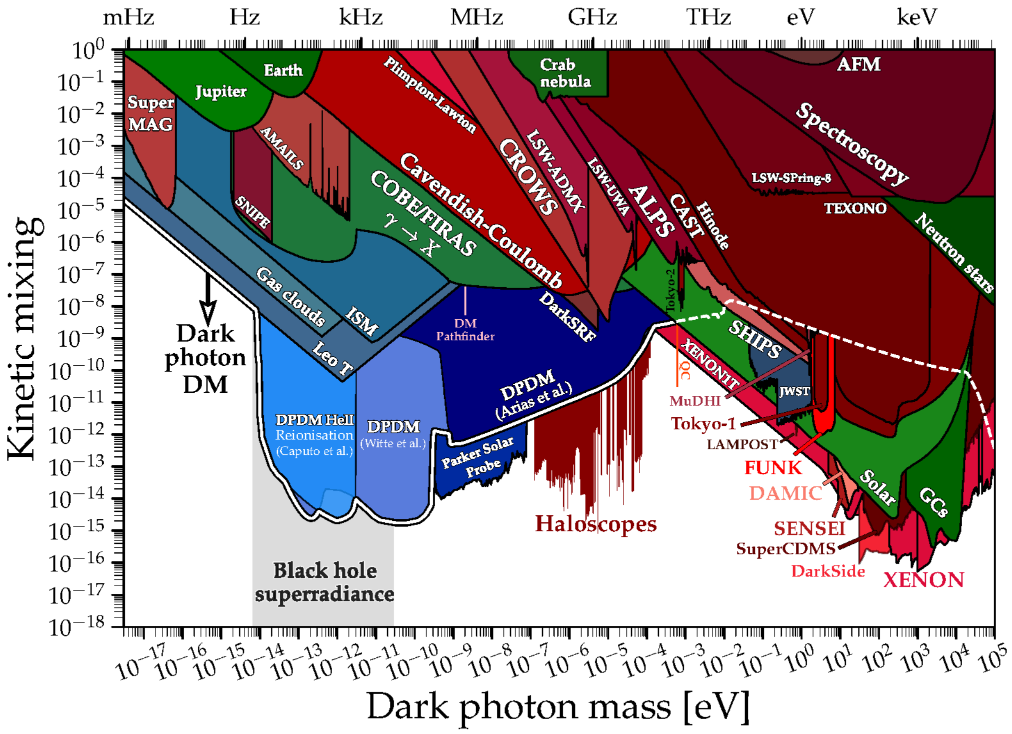

Figure 4.5: Exclusion limits of many DP(DM) searches [162]. Note that it is not immediately apparent from this plot which curves exclude the existence of DPs and which only bound the interactions of DPDM. We thus refer to our small review in this thesis, the GitHub repository itself, or Ref. [72] which covers a good explanation of many limits which however misses several recent developments.

5 Riding the Dark Matter Wave: General Dark Photon search with LISA Pathfinder

> Yes, there are two paths you can go by
> But in the long run
> There's still time to change the road you're on
>
> *Stairway to Heaven*
> LED ZEPPELIN

This chapter is based on the following publication:

[2] J. Frerick, J. Jaeckel, F. Kahlhoefer, and K. Schmidt-Hoberg, *Riding the dark matter wave: Novel limits on general dark photons from LISA Pathfinder*, *Phys. Lett. B* **848** (2024) 138328, [`arXiv:2310.06017`]

We further introduce the following improvements:

- More detailed discussion of the signal description and the signal-to-noise ratio
- Comment on criticism of the original work in Ref. [379]
- Further details on the exclusion of kinetic mixing from the analysis and clarification of the impact of plasma effects on general DPs
- Outlook on follow-up analysis

Having discussed the DM problem throughout this thesis and especially in chapter 4, we will now go ahead and perform a specific DM direct detection search. As discussed in the previous chapter, there is a case to be made for light and ultralight DPDM, which will be, with some features added, the focus of this chapter. These additional features are newly introduced vectorial couplings beyond the "vanilla" kinetic mixing. We will refer to this concept as generalised DP but for simplicity, we will call this particle just DP in this chapter. In practice, this simply means that the DP is gauged under a combination of baryon number (B) and lepton number (L), with a particular focus on the difference ($B - L$). For the later discussion of the vanilla/canonical DP in the same setup, we will therefore refer to it as the kinetically mixed DP (cf., e.g., [20, 22–25, 380]).

In this chapter, we will focus on the ultra-light mass regime of DM. Especially for small DP masses m, the Stückelberg [35, 36] mechanism is of great importance since the Higgs mechanism introduces a new, typically also ultra-light scalar into the particle spectrum which tends to dominate the phenomenology.

As introduced in the previous chapter, for $m \lesssim 10\,\mathrm{eV}$ the local DM halo behaves like a classical wave as the spacing between particles becomes smaller than the de Broglie wavelength [314]. Having discussed the plethora of production mechanisms, we will stay agnostic about the details of the mechanism as long as it is non-thermal.

Astrophysical objects like the Sun can efficiently produce light DPs even beyond the kinetic mixing paradigm, which, in turn, results in impressive limits on the existence of DPs without requiring them to be DM [1, 102, 104, 381, 382]. Additionally, lab experiments testing the equivalence principle are perfect setups to look for this kind of new physics that induces long-range forces beyond electromagnetism and gravity [383–386]. Planetary [387] and asteroidal [388, 389] orbits are also sensitive to new long-range forces. Finally, the gauge anomaly associated with baryon number leads to strong constraints from meson decays [25] for this specific gauge group.

If the DPs are also DM, new tests become available, e.g. with accelerometers as proposed in Ref. [390] and realised in [391]. A particularly interesting possibility is to search for these DM candidates directly at gravitational wave observatories. This idea was first pointed out in Ref. [392] for ultra-light scalar DM and later briefly discussed for DPDM in Ref. [390]. Independently, Ref. [393] focused especially on GW interferometry and performed a more detailed analysis for several instruments based on the small inhomogeneity of the field. We will use this work as a guideline for our analysis, as it also investigated new vector bosons gauged under B and $B-L$, and discussed both ground-based and space-based laser interferometers. However, it makes use of the differential acceleration between two equal test masses and is therefore limited by the small ratio of arm length to the scale of inhomogeneity. Here, we point out that the setup of LISA Pathfinder (LPF) also offers the possibility to use the differential acceleration between a test mass and the satellite carrying the interferometer itself. As we will argue this type of search is not limited by the arm length, significantly increasing the sensitivity in the relevant mass range compared to a previous analysis [394]. That said, we want to point out that the use of auxiliary channels was already proposed for KAGRA in Ref. [395] and applied by the LIGO/Virgo/KAGRA (LVK) collaboration directly [396].[1]

Before we discuss the detailed structure of this chapter, let us quickly point out that GW searches, in general, are also now considered as direct detection of DM-induced gravitational effects. See Refs. [397–404] for many different ideas and DM candidate searches with a variety of GW search setups.

We briefly discuss the signal prediction and analysis method in sec. 5.1 and point out the similarities and differences to previous DPDM interferometer limits. This is followed by an introduction to LPF including a discussion of the sensitivity in sec. 5.2. Finally, we estimate the sensitivity of this instrument to DPDM and discuss the necessary steps for a refined analysis in section 5.3 before we conclude in section 5.4.

5.1 Calculation of the signal

Our first step is to introduce a new Lagrangian for the general DP [20, 21, 51]

$$\mathcal{L} \supset -\frac{1}{4}F'_{\mu\nu}F'^{\mu\nu} - \frac{\epsilon_{\mathrm{KM}}}{2}F'_{\mu\nu}F^{\mu\nu} + \frac{m^2}{2}A'_{\mu}A'^{\mu} - \epsilon_g e A'_{\mu}J^{\mu}_{g}\ , \tag{5.1}$$

which contains the renormalisable interactions of the DP field A'_μ in full generality. To be specific, this model has both the (by now) well-known kinetic mixing ϵ_{KM} between the field strength tensors $F^{(\prime)}_{\mu\nu}$ of the SM photon and the dark photon, and an explicit direct coupling ϵ_g to a current J^{μ}_{g} associated with a new $U(1)$ gauge group g. Note that we have

---

[1] The LVK paper appeared only after the work this chapter is based on was published.

rescaled the gauge coupling g_g to the electromagnetic coupling e, i.e. $g_g = \epsilon_g e$. Adhering to our idea of a minimal setup, we will assume that the DP field constitutes all of DM.

5.1.1 Signatures of general Dark Photon Dark Matter

At this point, it should be pointed out that the interplay of an extended dark sector can be extremely rich, even if one introduces only a single new particle charged under this new gauge group. As mentioned in chapter 2, this setup is usually called (induced) millicharge and opens up a plethora of new effects and detection mechanisms. However, we will now transition from thinking about dark sectors[2] to new gauge groups in the visible sector. The existing global symmetries of the SM offer natural candidates for new gauge groups. However, as is well-known, there are certain consistency relations required for gauging symmetries to make a theory anomaly-free [25] which restricts our choices for gauging SM particles. This leaves us with a handful of global SM symmetries that can be gauged [20]. For most of this chapter, we focus on the explicit couplings with $g = B$ or $g = B - L$, i.e. gauging baryon and baryon-minus-lepton number, respectively, unless mentioned otherwise. In sec. 5.3 we will discuss how to generalise our analysis to arbitrary gauge groups and we will further give strong arguments for why we ignore the kinetic mixing in the following even though it was the main driver of the phenomenology in previous chapters. As we do not rely anymore on the interactions with the photon field, we will from now on drop the “ $'$ ” as long as there is no risk of confusion.

Under the choice of these two gauge groups, essentially any piece of baryonic matter is charged. To be more specific, let us focus on the atomic matter that makes up most of our surroundings, and thus also our experimental setups. For B, the situation is clear as the charge of an atom is just given by the number of nucleons, disregarding the electrons on the shell.[3] For $B - L$, the situation is slightly more complex. Basically, as atoms are charge neutral, we have $B - L = N_n + N_p - N_e = N_n$. The contribution from protons and electrons must cancel and thus $B - L$ is just given by the number of neutrons. In particular, this means that most hydrogen atoms, i.e. excluding deuterium and tritium, are neutral under this charge. Furthermore, ionisation impacts the total $B - L$ charge through missing or additional leptons in the form of electrons. Despite this complication, it is a good approximation to consider all the matter as not ionised and thus we can keep the simple rule $B - L = N_n$.

DP electrodynamics

As was discussed before, as soon as the DM mass drops below the eV mass scale, it can and should be described by a classical field as the quantum fluctuations become less and less relevant. As we have seen in the previous chapter, DM has to be cold (non-relativistic). Combining this with the classical description of a DP field with mass m yields

$$\mathbf{A}(t, \mathbf{x}) = \mathbf{A}_{\mathrm{DM}} e^{-i\omega t + \phi(\mathbf{x})}\,. \tag{5.2}$$

Here we have moved any spatial dependence into the phase $\phi(x) = i\,\mathbf{k}\cdot\mathbf{x} + \phi_0$ and we note $\omega = m(1 + \mathcal{O}(v^2))$ in our non-relativistic setup. To be specific, the typical DM velocity in our halo is given as $v \sim 10^{-3}$ [243]. Here we have focused explicitly on the 3-vector component of the field A_μ as we can always use the “Lorenz” condition to calculate the

---

[2] Note that most of the phenomenology still requires kinetic mixing to make contact with the SM.

[3] This further means that atoms and ions of arbitrary electric charge have the same B charge.

temporal component

$$\partial_\mu A^\mu = 0 \Rightarrow A^0(t) = -\frac{\mathbf{k} \cdot \mathbf{A}(t)}{\omega} \approx \mathbf{v} \cdot \mathbf{A}(t) \ll |\mathbf{A}(t)| \,, \tag{5.3}$$

which furthermore indicates that this component is velocity-suppressed compared to the 3-vector. We note that we have already made a similar observation in chapter 3, in eq. (3.22) to be specific. However, in that setup, it was not clear that the temporal component is small since the solar DPs can be relativistic. At this point, it needs to be emphasised again that this is dictated by the equation of motion (EOMs) for a massive vector boson in stark contrast to the massless case where this can be considered a gauge choice. For the detailed derivation, we refer to the aforementioned passage on plasma effects. Now that we have made sure that the temporal component is small, we can justifiably neglect it. Furthermore, we can see that in the case of a purely transversely polarised DP, the temporal component vanishes exactly since $\mathbf{k} \cdot \mathbf{A}_{\mathrm{DM}} = 0$. Whatever setup is present in a realistic scenario, we can thus safely ignore the temporal component.

DPDM properties: coherence & polarisation

Our above discussion is to some degree oversimplified. Instead of a slowly oscillating plane wave, we rather have several coherence patches neighbouring each other, which are however smoothly connected. Each of these patches has a different density [401, 405] and potentially also a different polarisation [379, 406]. We will neglect the aspect of the density here as it is difficult to handle in the analysis. We could be unlucky that the density during the mission time of LPF was anomalously low. On the other hand, even if we see a signal it might be that it slowly disappears as we are slowly moving towards a new coherence patch with a lower density such that potential follow-up experiments would not see anything. We will leave this issue aside for this thesis and always rely on the average value of the energy density. Indeed, the fluctuation of the energy density follows a Rayleigh distribution centred around the average density, indicating that we do not expect enormous or completely vanishing signals.

Let us now discuss the aspect of DP polarisation. In terms of DPDM polarisation, there are typically two classes of production mechanisms discussed in the literature, either polarised production over the entire Hubble patch or completely random polarisation (down to the coherence patch) [72].[4] On top of the different production mechanisms, there still is an ongoing debate about the gravitational infall into the potential well of galaxies. It is not clear yet whether it will break the polarisation down into coherence patches. The main argument for the breakdown of the polarisation comes from virialisation and the equipartition theorem [379]. On the other hand, there is a simple but robust argument presented in Ref. [72] based on the spin evolution in GR which may indicate that the non-relativistic infall will barely influence the alignment of the polarisation. This work also pointed out the need for simulations to settle this debate.

In general, this ongoing discussion motivates us to consider both scenarios in our setup to allow for truly robust and fundamentally conservative limits.[5] Even though the aspect of DPs having a polarisation in contrast to scalar ULDM seems like an additional complication, it also allows for novel signal discrimination opportunities. This effect will be

---

[4] This is *not* the case for thermal production which operates typically above the wave DM bound and so individual particles can have individual polarisations produced from a very homogeneous and isotropic SM plasma.

[5] We will discuss later that the polarisation can lead to blind spots in the worst-case scenario making naive limits potentially too optimistic.

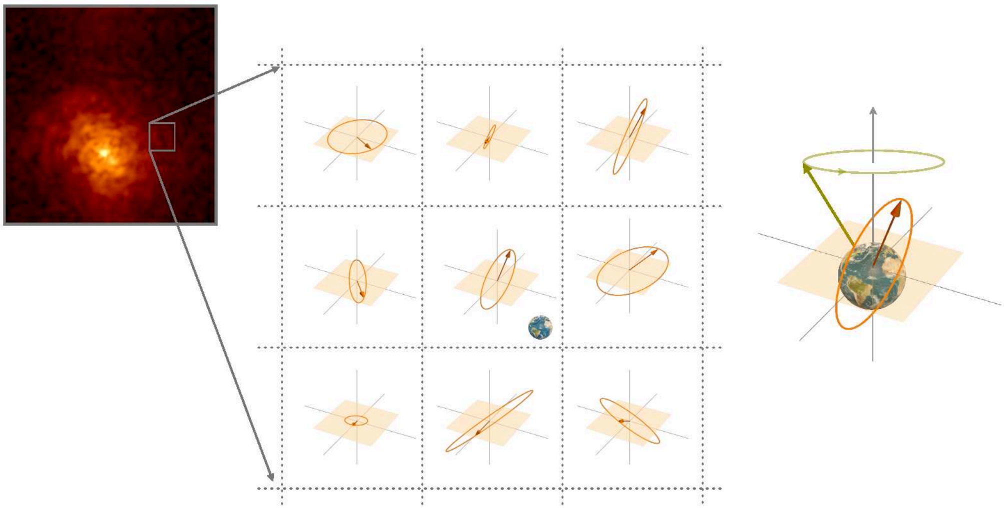

Figure 5.1: Visualisation of coherence patches taken from Ref. [379] with the left-most figure originating from Ref. [407]. We see the coherence patch structure of the DM halo and how we can imagine the coherence length as the size of these patches. The coherence time is then just the time it takes for an entire patch to pass by the position of the Earth.

discussed explicitly later in this chapter, even though certain aspects will already appear throughout the following paragraphs.

Now that we have discussed the polarisation in great detail, let us return to the coherence patches. These patches are found in simulations of vector DM, and by definition, within a coherence patch, the signal can be treated as being monochromatic. This derives from the narrow spread in velocities of the non-relativistic DM halo, i.e. the dispersion of the field is strongly suppressed. The typical size of these patches, i.e. the coherence length, is given by the wavelength $\lambda_c \simeq 2\pi/(mv)$.[6] By analogy, the coherence time is $t_c \simeq 2\pi/(mv^2)$. Simply speaking, the coherence time measures the amount of time it takes for a coherence patch to pass by a fixed position. The coherence length, on the other hand, measures the distance between two distinct patches. As a reminder of our earlier discussion, it is important to keep in mind that, on top of the monochromatic frequency, neither the amplitude nor the polarisation of the field changes (significantly) within a coherence patch. For a visualisation of this concept, we present fig. 5.1 taken from [379] which shows on the left a zoom-in of a simulation from Ref. [407]. We can clearly see the granular structure of the different patches. The graphic demonstrates the variation of density and polarisation in each patch.

As we shall see, the DPs will induce a signal that oscillates at a frequency given by the DP mass. LISA Pathfinder (LPF), as our improvised direct detection experiment, covers a frequency range from a few Hz down to around 10^{-5} Hz (see sec. 5.2). Especially for the lowest frequencies this implies an extremely long coherence time due to the non-relativistic velocities. Even for the highest frequencies in LPF's sensitivity range, the coherence time is more than a week. We conclude that even long-term searches for monochromatic signals suffer at most weakly from the decoherence of the signal, thus enhancing the limits

---

[6] Technically, the more relevant quantity would be the spread in velocities, Δv which is however of similar magnitude as v. This also explains the divergence in the $v \to 0$ limit as a field exactly at rest must oscillate perfectly at a frequency given by the DM mass and cannot have gradients since the momentum vanishes.

significantly without employing new technology. The decoherence should not be an enormous problem even in a dedicated search as, when looking for a DP with fixed mass, we already know the coherence time and we can bin the data accordingly as we should see a monochromatic line in every bin. Observing such a line over several coherence times will allow us to even probe the underlying velocity distribution. We refer to Refs. [408–411] for similar attempts in conventional direct detection.

Understanding the signal

For the sake of clarity, we will give a minimal description of LPF here and use it as an example of the main idea behind our analysis. A more detailed description will follow in sec. 5.2. We should emphasise that the following arguments are equally valid as a signal prediction for two generic objects. In LPF, two (almost) identical test masses (TMs) are enclosed separately in the spacecraft (SC), also referred to as the science module, and the relative motion between the TMs themselves and between TMs and the SC is tracked in the main and auxiliary channels, respectively. The dominant effect of the gauged DPDM on a charged object is analogous to the electric component of the Lorentz force. Conceptually, the following was discussed in Ref. [390] but several steps will be clarified and the result will be generalised. Before we can calculate any forces, we need to determine the "electric field" from the background DPDM

$$\mathbf{E}_g = -\partial_t \mathbf{A}(t, \mathbf{x}) = i\omega \mathbf{A}_{\mathrm{DM}} e^{-i\omega t + \phi(\mathbf{x})} \, . \tag{5.4}$$

For our purposes, we could completely ignore the phase of the field and set $\phi(\mathbf{x}) \approx 0$ and consider it spatially constant over the size of the experiment as already discussed in great detail. In the broader context of using GW interferometers as DPDM direct detection experiments, it is nevertheless very beneficial to keep this spatial dependence. In the case of LPF, it is however helpful to think about the field as oscillating at a single frequency as long as we consider only coherent time scales.

This field then exerts a force on all objects charged under the given gauge group. Therefore, we find the following acceleration

$$\mathbf{a}(t, \mathbf{x}) \simeq i\omega \epsilon_g e \frac{q}{M} \mathbf{A}_{\mathrm{DM}} e^{-i\omega t + \phi(\mathbf{x})} = i\epsilon_g e \frac{q}{M} \sqrt{2\rho_{\mathrm{DM}}}\, \hat{\mathbf{e}}_A \, e^{-i\omega t + \phi(\mathbf{x})} \, , \tag{5.5}$$

for an object of mass M and charge q (under g). The gradient of the temporal component contributes to the Lorentz force as well and so does the magnetic field, but these contributions are at least $\mathcal{O}(v^2)$ suppressed according to eq. (5.3). Therefore, we neglect these signatures in our deeply non-relativistic setup. Furthermore, we used the well-known relation between the average energy density and amplitude of wave-like DM

$$\rho_{\mathrm{DM}} = \frac{1}{2} \omega^2 |\mathbf{A}_{\mathrm{DM}}|^2 \, , \tag{5.6}$$

which is also correct up to quadratic terms in the velocity from the kinetic energy of the DPs. Finally, $\hat{\mathbf{e}}_A$ is the unit vector in the direction of the DPDM field within a coherence patch.

5.1.2 A brief introduction of the signal-to-noise ratio

For the exclusion of a given parameter point, we need to determine the signal prediction and compare it to the noise.[7] This is done via the signal-to-noise ratio (SNR). In the

---

[7] For our analysis, we will adhere to the use of simplified data from the calibration of the LPF auxiliary channels in the form of noise curves. Therefore, we will not be able to perform an actual search for

following, we will perform a simple derivation of this quantity based on Ref. [412] which can be consulted for a more extensive and pedagogical discussion.

Signal & Noise

On a general level, we can model the output of a generic detector s as

$$s(t) = h(t) + n(t) \ , \tag{5.7}$$

where h denotes the actual signal and n generically represents all noise.[8] In the next step, we will try to disentangle the noise from the signal. Initially, we will Fourier transform[9] these quantities

$$x(f) = \int \frac{\mathrm{d}t}{2\pi} x(t) e^{2\pi i f t} \ , \tag{5.8}$$

and assume that the noise is uncorrelated, i.e.

$$\langle n^*(f) n(f') \rangle = \delta(f - f') \frac{1}{2} S_n(f) \ . \tag{5.9}$$

We know that the noise is real, i.e. $n^*(t) = n(t)$ and thus $S_n(-f) = S_n^*(f)$. We will refer to this quantity as the power spectral density, and it has units of $[n]^2/\mathrm{Hz}$ where $[X]$ denotes the unit of the quantity X. Furthermore, we take

$$\langle n(t) \rangle = 0 \ . \tag{5.10}$$

We note that the δ-function in eq. (5.9) is an idealised result that derives from assuming that we can take an exact ensemble average on the LHS. Assuming ergodicity, we can approximate the ensemble average with several independent measurements over a time T. This procedure immediately introduces a frequency resolution $\Delta f = 1/T$. This finite resolution will soften the divergence of the δ distribution. Assuming a binning in Δf allows us to write the otherwise divergent function as

$$\delta(f - f) = \delta(0) \to \frac{1}{\Delta f} = T \ . \tag{5.11}$$

As a quick consistency check we see that for infinite resolution $\Delta f \to 0$, i.e. infinitely long measurements $T \to \infty$, the result is divergent as was the case for the exact ensemble average. We therefore conclude

$$\langle |n(f)|^2 \rangle = \frac{1}{2} S_n(f) T \ , \tag{5.12}$$

and we can determine the average of the quadratic noise in the time domain via

$$\langle n(t)^2 \rangle = \int \mathrm{d}f \, \mathrm{d}f' \, \langle n^*(f) n(f') \rangle = \int_0^\infty \mathrm{d}f \, S_n(f) \ . \tag{5.13}$$

We see therefore that the power spectral density is a very useful quantity for measuring properties of the noise. For a more intuitive handling of the noise, it is nevertheless helpful to define the amplitude spectral density (ASD) as $\sqrt{S_n(f)}$ which is what we will use later in our analysis.

---

monochromatic lines in the raw data. However, the noise curves are still sufficient to exclude parameter space.

[8] See the aforementioned [412] for more details on the origin and validity of this modelling, especially for the introduction of the transfer function. The notation h is usually used for GW detection, i.e. denoting the strain. We will be more interested in an acceleration, but we will continue to stick to this nomenclature so that the interested reader can more easily make contact with the existing literature.

[9] In the usual abuse of notation, we will not change the variable for the Fourier transformation and just write $x(t) \to x(f)$.

Matched filters

In the next step, we will have a brief look at matched filtering, an important step towards maximising the visibility of a known signal hidden in the noise. In other words, we define a new quantity

$$\hat{s} = \int_{-\infty}^{\infty} \mathrm{d}t\, s(t) K(t) \; , \tag{5.14}$$

where the detector output s is convoluted with a filter function K. We will now define the expectation value of $\hat{s}$ as

$$\begin{aligned} S &= \int_{-\infty}^{\infty} \mathrm{d}t\, \langle s(t) \rangle K(t) & \text{(5.15a)} \\ &= \int_{-\infty}^{\infty} \mathrm{d}t\, h(t) K(t) & \text{(5.15b)} \\ &= \int_{-\infty}^{\infty} \mathrm{d}f\, h(f) K^*(f) \; , & \text{(5.15c)} \end{aligned}$$

where we have used eq. (5.10) and Parseval's theorem to go from time to frequency space. We furthermore need the standard deviation of S, called N, in the absence of the signal

$$\begin{aligned} N^2 &= \left[\langle \hat{s}^2 \rangle - \langle \hat{s} \rangle^2 \right]_{h=0} & \text{(5.16a)} \\ &= \langle \hat{s}^2 \rangle_{h=0} & \text{(5.16b)} \\ &= \int \mathrm{d}t\, \mathrm{d}t'\, K(t) K(t') \langle n(t) n(t') \rangle & \text{(5.16c)} \\ &= \int \mathrm{d}t\, \mathrm{d}t'\, K(t) K(t') \int \mathrm{d}f\, \mathrm{d}f'\, \langle n^*(f) n(f') \rangle e^{2\pi i (ft - f't')} & \text{(5.16d)} \\ &= \frac{1}{2} \int_{-\infty}^{\infty} \mathrm{d}f\, S_n(f) |K(f)|^2 \; , & \text{(5.16e)} \end{aligned}$$

where we have again used eq. (5.10) and additionally eq. (5.9) in the last step. Now we can finally express the SNR for a general filter function as

$$\mathrm{SNR} = \frac{S}{N} = \frac{\int_{-\infty}^{\infty} \mathrm{d}f\, h(f) K^*(f)}{\sqrt{\frac{1}{2} \int_{-\infty}^{\infty} \mathrm{d}f\, S_n(f) |K(f)|^2}} \; . \tag{5.17}$$

The most urgent question now clearly is how to determine the ideal filter function. We will skip over the derivation for which we once again point towards the literature [412]. The result for the ideal matched filter is given by

$$K(f) = \frac{h(f)}{S_n(f)} \; , \tag{5.18}$$

up to an arbitrary rescaling constant. Plugging in this result yields an SNR of

$$\mathrm{SNR} = 2 \sqrt{\int_0^{\infty} \mathrm{d}f \frac{|h(f)|^2}{S_n(f)}} \; . \tag{5.19}$$

To use this knowledge, we now need to determine the Fourier transformation of the signal.

In our setup, we realise that $h(t) = a(t)$.[10] Since the signal is monochromatic, it is trivial to determine the Fourier transformation

$$a_i(f) = \frac{i}{2}\epsilon_g e \frac{q}{M}\sqrt{2\rho_{\rm DM}}\cos\theta_{A,i}\delta\left(f - \frac{m}{2\pi}\right) , \tag{5.20}$$

where $i = x, y, z$ denotes the axis and $\cos\theta_{A,i}$ denotes the angle between axis and polarisation and we needed to introduce a factor of 1/2 as we are working with one-sided ASDs. In passing we note that it becomes explicit in this expression that a one-dimensional setup or even a typical planar interferometer can, in principle, be insensitive to this effect if the polarisation is orthogonal to the plane of the experiment. LPF offers the advantage of having a full 3D sensitivity of the SC motion w.r.t. the TMs. We therefore find for the SNR of the *relative acceleration* between two test masses

$$\mathrm{SNR} = \frac{\frac{1}{2}\epsilon_g e\left(\Delta\frac{q}{M}\right)\sqrt{2\rho_{\rm DM}}\cos\theta_{A,i}}{\frac{1}{2}\sqrt{S_a}}\sqrt{\delta(f-f)} \equiv \frac{\Delta a_i}{\sqrt{S_n}}\sqrt{\delta(f-f)} \, . \tag{5.21}$$

This result could have been guessed given some intuition for the signal. Since it is monochromatic, we are sensitive to the amplitude Δa_i which corresponds to taking the real part of the signal and discarding the oscillatory component. Unfortunately, the expression will once again yield a divergent result. However, this is once again a relic of assuming infinite resolution, and we can replace the remaining delta function by the measurement time as done in eq. (5.11). We need to pay attention, though, since the signal is only monochromatic within a coherence time. For a complete treatment, we would require the stochasticity of the signal to be taken into account. However, we can still use a monochromatic description if we instead divide the measurement time into bins of coherence times. We therefore need to replace the δ-distribution by

$$\delta(0) \to T_{\rm eff} = \begin{cases} T_{\rm obs} \ , & T_{\rm obs} \leq t_c \\ \sqrt{T_{\rm obs} t_c} \ , & T_{\rm obs} > t_c \end{cases} , \tag{5.22}$$

as outlined e.g. in the appendix of Ref. [413] using both the observation time $T_{\rm obs}$ and coherence time t_c. The basic reasoning behind this result is that n different coherent patches are independent of each other and thus in eq. (5.19) we need to add n different $|h(f)|^2$ in quadrature, yielding a multiplicative factor $\sqrt{n}$. In the final result, this rescales t_c by $\sqrt{n}t_c = \sqrt{nt_c}\sqrt{t_c} = \sqrt{T_{\rm obs}t_c}$. Finally, we can write the full SNR as

$$\mathrm{SNR} = \frac{\Delta a_i}{\sqrt{S_n}}\sqrt{T_{\rm eff}} \, , \tag{5.23}$$

for which we know the theory prediction Δa_i and the time scale $T_{\rm eff}$. In the next section, we will discuss the ASDs $\sqrt{S_n}$ of LPF, thereby completing the set of relevant parameters.[11]

Let us end the computation of the signal prediction with another comment on the coherence patches. From our discussion of the coherence time, we conclude that in the ultra-low mass regime, we will not be able to tell the difference between the two polarisation models discussed before (barring higher order effects) as all experiments with realistic lifetimes will only observe a single coherence patch. At the higher end of the LPF frequency range

---

[10] On the scale of the experiment, it is well justified to disregard the spatial dependence of the signal, i.e. $\phi(\mathbf{x}) = 0$. We will later discuss higher-order effects, which are however negligible for the main analysis.

[11] Conventionally for most GW searches, results are quoted as ASDs for the relative displacement, also known as strain, instead of acceleration as used for this analysis. The translation from our ASD to this strain sensitivity is fairly simple as it only requires a rescaling factor of $\sim \omega^2/L$.

the situation might be more promising if we allow for an observation time of several years. This can get even better if the sensitivity can be extended to higher frequencies. In contrast, for larger masses, measuring at different times corresponds to measuring different polarisation of the DPs. Combining this with the fact that LPF has a non-trivial orbit and orientation will result in a very complex scheme required to perform a rigorous analysis. However, applying this information, which is known in principle, might provide additional constraining power as demonstrated in Ref. [72], following our discussion above. We will further comment on this issue in section 5.3. To conclude this discussion we emphasise that the position and orientation of the SC will not change significantly on the time scales of the used observations [414], i.e. a few days at a time per measurement series. Thus, a single measurement as we use it in this chapter will not have that additional constraining power, but it also does not require the complex scheme required for tracking LPF's orbit and relating it to a potential signal.

5.1.3 Alternative signals at gravitational wave interferometers

Before we begin our discussion of LPF in detail, we should still answer some remaining questions on the theory side. Now that we understand the relevant framework, let us quickly compare our result for the auxiliary channels between SC and TMs, to the case where $\Delta\frac{q}{M} = 0$. This corresponds to two bodies (i.e. TMs) made from the same material, which is the case for the main channel TMs in all existing and planned interferometric GW searches including LPF.[12] Additionally, any elemental impurities that could break this degeneracy are kept extremely small to improve the performance of the interferometer, even though in principle it might be worth investing as long as the impurity is larger than the suppression we get from higher order effects discussed in the following paragraphs.[13] In principle, according to the equivalence principle (EP) [417] the material will not make a difference in pure GR for the detection of GW waves and even potential violations for the EP are constrained to be so small that it would be completely negligible [386, 418]. While this seems to imply that any GW interferometer could be made more sensitive to DPDM by using different materials for the TMs without impacting the performance, this theorist's point of view is oversimplified as the technical aspects of the GW detectors make it much simpler to use the same material for all TMs. Especially in the case of ground-based detection like LIGO, Virgo or KAGRA, the mirrors[14] are the product of a long optimisation process after which the best material was chosen [419] such that the TMs are necessarily made from the same material.

Therefore, we have to look for subleading effects to detect the DPDM signal in equal TM setups like LIGO or the LPF main channel, e.g. from the phase in eq. (5.4) which however introduces both an arm-length and a velocity suppression. This is exactly the approach followed by Ref. [393]. Only later it was re-discovered that the finite light-travelling time of the laser [420] leads to an improvement if the length scale associated with the DP mass (i.e. $1/m$) coincides with the arm length of the interferometer L as already pointed

---

[12] LPF and LISA will use AuPT cubes while LIGO, Virgo and GEO600 use fused silica [396, 415]. KAGRA uses sapphire mirrors in the main channel, but as mentioned earlier, they have fused silica in their auxiliary channels [395, 396]. For the Einstein Telescope (ET), there will be two different sets of mirrors [416] but they are deployed in separate interferometers and it is unclear if there is a connecting channel between them which could be used for our analysis.

[13] Determining the composition of these impurities might, however, be difficult in itself but for this approach, such a determination would be crucial to interpret the data. Furthermore, in conventional GW interferometers, the suppression is substantially weaker than in LPF which makes this idea less attractive overall.

[14] We will use the term test mass and mirror interchangeably in this chapter.

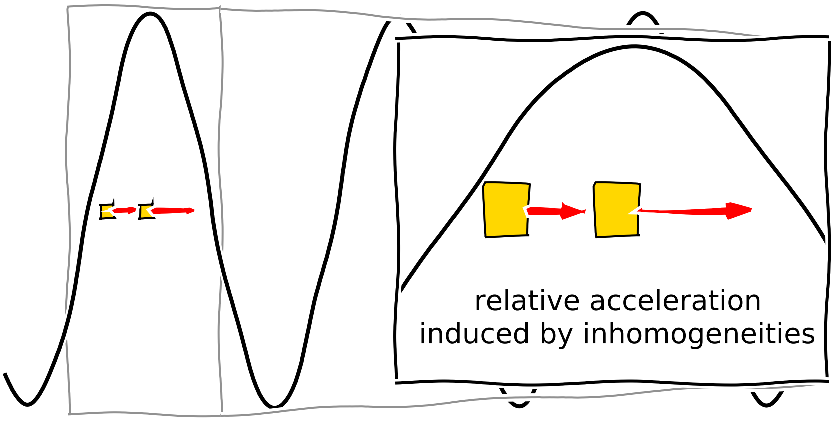

Figure 5.2: Sketch of the gradient/decoherence effect which represents a snapshot at a fixed time. The black lines indicate the background field where the inhomogeneity is strongly exaggerated. (Since the field is technically vectorial, this is just the projection of the field in the direction of the sensitive axis.) Furthermore, it is important to note that the field oscillates much faster in time than it does change with position. Since the two TMs experience different field values they are accelerated differently.

out in Refs. [390, 392].[15] This "new" analysis method and the decoherence effect from the small inhomogeneity of the field will give an observable relative acceleration even for strictly equal charge-to-mass ratios. However, the acceleration induced by these effects is suppressed by max $\left\{(\omega L)^2, v\omega L\right\}$. For full-scale interferometers where the arm length is on the scale of $1/m \sim 1/\omega$ by construction, this may not be big a problem. But for LPF with its very limited arm length of $\sim 40\,\text{cm}$, these effects will substantially suppress all limits derived following the standard methods in the literature, as shown in Ref. [394]. Therefore, looking for auxiliary channels between TMs and the SC that feature $\Delta\frac{q}{M} \neq 0$ is promising. Indeed for KAGRA and its auxiliary channels, this observation was already utilised in Ref. [395], which enhanced the limits in the low-frequency region significantly as pointed out above. The combined collaboration of LVK has followed up on this more conceptual work with a detailed analysis, which however performed significantly worse than expected from the original forecast due to high noise levels and short observation times [396]. Both the decoherence approach and the finite light-travelling time method are shown in fig. 5.2 and fig. 5.3, respectively. The scaling introduced above will now be derived in the following paragraphs based on the intuition gained from the two sketches.

The decoherence effect

Let us now quantify the behaviour of two identical TMs. For that, we will return to eq. (5.5) and specify a given axis x_i by introducing $\cos\theta_{A,i}$. Then, we can simply write for

---

[15] Thankfully, this interesting "historical anecdote" was pointed out by the anonymous referee of the original publication [2] this chapter is based on. This hint towards the historically correct version of how these limits were (re-)derived should be acknowledged here again to respect the original works on this topic. At this point, it should be emphasised that this analysis method was already applied directly to LIGO/VIRGO data [421, 422].

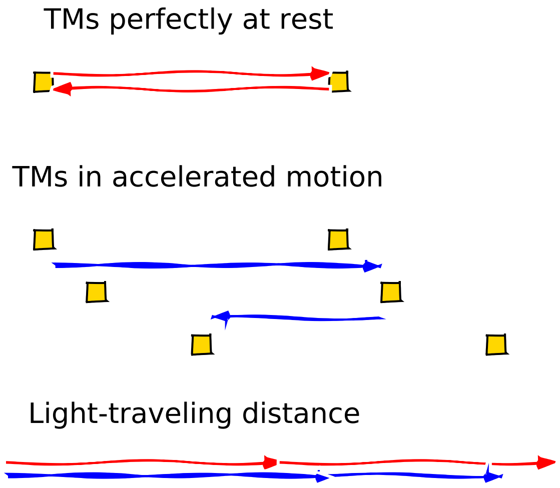

Figure 5.3: Sketch of the finite light-travelling distance effect active even for a perfectly homogeneous background. On top, we see the distance travelled by light in a setup at rest (or moving at constant velocity). The centre represents the change in the reflection for an accelerated motion for three snapshots in time which correspond to the time of emission of the light ray from the left TM, the time of reflection on the right TM, and the time of detection for the returning light ray, respectively. It is apparent from the lower sketch that even though the distance between the particles remains the same, the distance travelled by the light is still affected. This mimics a relative acceleration between the two TMs.

the relative acceleration between two objects with equal charge-to-mass ratio

$$\Delta a_i(t,\mathbf{x}) = i\epsilon_g e\frac{q}{M}\sqrt{2\rho_{\rm DM}}\cos\theta_{A,i}e^{-i\omega t}\left(1-e^{i\phi(\mathbf{x})}\right) \equiv a_i e^{-i\omega t}\left(1-e^{i\phi(\mathbf{x})}\right) \tag{5.24a}$$

$$= a_i e^{-i\omega t}\left(i\frac{\mathrm{d}\phi}{\mathrm{d}x_i}\Big|_{x=x_i}(x-x_i)+\mathcal{O}\left(\left(\frac{\mathrm{d}\phi}{\mathrm{d}x_i}|_{x=x_i}\right)^2(x-x_i)^2\right)\right) \tag{5.24b}$$

$$\approx i v_i x_i \omega a_i e^{-i\omega t}\,, \tag{5.24c}$$

where we have put the first object at $x_i = 0$ and assumed w.l.o.g. $\phi(0) = 0$. The definition of a_i reflects the previous definition of Δa_i in eq. (5.21) with $\Delta(q/M) \to q/M$. In the following step we have used that $\phi(\mathbf{x}) = \mathbf{x}\cdot\mathbf{k}$ and $\mathbf{k} \approx m\mathbf{v} \approx \omega\mathbf{v}$. It should be noted that in our calculation, there is only one axis of relevance. The usual two-arm interferometer however requires a more careful treatment as shown in the appendix of Ref. [393]. Plugging in that $x_i = L$, the distance between the two TMs, we have the well-known but rather discouraging gradient effect which says that small, equal TM interferometers suffer a massive suppression $\sim v\omega L$ which can be of the order of 10^{-15} or smaller for LPF. The fundamental idea is sketched (in a rather exaggerated way) in fig. 5.2. We note that this approximation breaks down for large excursions of the objects away from their initial position or large L. This decoherence effect is much more powerful in conventional GW detectors and is thus thoroughly discussed in the aforementioned literature.

The finite light-travelling time effect

The decoherence of the signal is not the only observable effect. The aforementioned finite light-travelling time effect is even at play when the field is perfectly homogeneous. We will therefore neglect the phase, i.e. the spatial dependence, once again. Interestingly, this is an "integrated" effect, and thus we need to work with positions instead of accelerations. For better visualisation, another sketch is provided in fig. 5.3. We will then derive the perceived acceleration in a second step. Assuming the same initial positions as before and vanishing initial velocities, we will now calculate the time it takes for a photon to propagate from one TM to the other and back again. We therefore define the positions as

$$x_{i,1}(t) = \frac{a_i}{\omega^2}\left(1 - e^{i\omega t}\right) \tag{5.25a}$$

$$x_{i,2}(t) = L + \frac{a_i}{\omega^2}\left(1 - e^{i\omega t}\right) \ , \tag{5.25b}$$

which ensures that the TMs start at the correct positions 0 and L. Furthermore, we have used a_i defined above in eq. (5.24a).

The trajectory described in the previous paragraph is the round-trip distance/time in conventional Fabry-Pérot interferometers where a light ray enters through one mirror and then returns after being reflected on the other. In LPF, this is not exactly what happens (c.f. fig. 5.5) but we will not focus on this since our auxiliary channel configuration is more sensitive anyway. Assuming a small armlength, i.e. a short travelling time w.r.t. the oscillation time (*not the wavelength!*) of the DP, we get for the distance travelled by the light

$$\begin{aligned}
\Delta x_i &\equiv \left(x_{i,2}(t+L) - x_{i,1}(t)\right) + \left(x_{i,2}(t+L) - x_{i,1}(t+2L)\right) - 2L && (5.26\text{a})\\
&= \left(L + \frac{a_i}{\omega^2}\left(e^{-i\omega(t+L)} - e^{-i\omega t}\right)\right) + \left(L + \frac{a_i}{\omega^2}\left(e^{-i\omega(t+L)} - e^{-i\omega(t+2L)}\right)\right) - 2L && (5.26\text{b})\\
&\approx \frac{a_i}{\omega^2}e^{-i\omega t}\left(2\left(1 - i\omega L - \frac{\omega^2 L^2}{2}\right) - 1 - \left(1 - 2i\omega L - 2\omega^2 L^2\right)\right) && (5.26\text{c})\\
&= \frac{a_i}{\omega^2}e^{-i\omega t}\omega^2 L^2 \ . && (5.26\text{d})
\end{aligned}$$

Also, here we needed to assume that to leading order the distance between the two objects stays at L, i.e. the arguments of $x_{i,1/2}$ have an $\mathcal{O}\left(a_i/\omega^2\right) \ll L$ correction, which we neglect. Furthermore, it needs to be emphasised that we can assume the light to propagate in vacuum and thus the travelling time is set by the travelling distance in natural units. From this apparent relative motion, we can extract a pseudo-relative acceleration

$$\Delta a_i(t) \equiv \omega^2 \Delta x_i \approx (\omega L)^2 a_i e^{-i\omega t} \ , \tag{5.27}$$

which we infer from the data although the distance between the TMs is L at every point in time. Therefore, this effect is based on the fact that the speed of light is finite and that the motion of the TMs is accelerated.[16] Nevertheless, the speed of light is very large, and thus this effect becomes massively suppressed, even more than the gradient scenario if $\omega L \ll v$ which is the case over the entire LPF parameter space. This observation also explains why Ref. [394] used only the gradient-induced acceleration, ignoring completely the pseudo-acceleration induced by the finite light-travelling time.

---

[16] It is important that the motion is accelerated since constant velocities would cancel each other in the above calculation.

5.2 LISA Pathfinder sensitivity

To begin this section, we will explain the experimental setup of LPF in more detail, now also taking into account technical considerations in contrast to the previous section where we have mostly taken a theorist's perspective.

LPF instrumentation

LPF [423] was a precursor mission to the planned space-borne gravitational wave interferometer LISA [424].[17] The mission's main objective was to demonstrate that the technology developed for LISA will be able to perform as predicted in a realistic space environment. For this purpose, a SC containing two TMs was sent to the first Lagrange point of the Sun-Earth system. These TMs are 2 kg Gold-Platinum alloy cubes with a side length of $\sim 5\,\mathrm{cm}$ which were placed in two separate electrode housings with an optical bench placed between them. The main aim was to keep the noise in the relative acceleration between the two (effectively) free-falling TMs at a level that would verify the applicability of this technology for LISA. In fact, the test was successful and performed even better than expected [425, 426]. Such a high-precision instrument requires more scrutiny than a single interferometer measuring the relative TM displacement. Therefore, LPF contained a radiation monitor [427], additional interferometers [428], and capacitive sensing [429]. Several of these auxiliary channels were used to avoid a collision between “TM1”, the reference test mass, and the SC. The choice of a preferred TM is required as two TMs on their respective geodesics within a single SC cannot coexist without a collision. Therefore, there are measures in place to correct the trajectory of the second TM w.r.t. the reference TM. In other words, the TM chosen to be the reference effectively guides the SC which moves around the TM to leave it unperturbed on its geodesic. As a result of these involved manoeuvres and due to the geodesic deviation[18] which generically induces a relative acceleration between two masses initially parallel to each other, the second test mass, i.e. TM2, has to be corrected on its orbit.

These two TMs are aligned on what the collaboration labelled the x-axis. On this axis, there is the so-called x_{12} interferometer which is the central instrument on-board as it is used to measure the relative acceleration between the TMs. For our purposes, we focus on another instrument, the x_1 interferometer, which controls the SC position w.r.t. TM1. This auxiliary interferometer will be the best channel for searching for DPDM over a large mass/frequency range. All interferometers use the optical bench placed between the TMs which is the heart of the mission [431].

LPF elemental composition

As we have pointed out in great detail in sec. 5.1 we require knowledge about the charge-to-mass ratio and therefore the elemental composition of both the TMs and the SC to calculate the signal correctly. Unfortunately, the SC itself is made up of a collection of different materials and components hard to determine from the literature. Nevertheless, on average they are expected to have much lower atomic numbers than Au or Pt for practical reasons. For example, it is highly preferable to have a light and cheap spacecraft and thus the science module will contain only negligible components with similarly heavy nuclei as the TMs. Thus, they will have different, or to be more specific for most cases even smaller,

---

[17] Earlier this year, the construction phase for LISA was officially confirmed by ESA.

[18] A derivation and discussion of the geodesic deviation equation can be found in most GR textbooks, e.g. in [430].

charge-to-mass ratios. This result is intuitive for $B-L$ as the total charge of an atom under this gauge group is given by the neutron number and the neutron-to-proton ratio tends to increase with atomic number for stable elements. This effect generates different charge-to-mass ratios for light and heavy elements.

This effect is more subtle for B. The difference mainly comes from the variation in binding energies and the small mass difference between proton and neutron, and it is not linearly increasing as clearly with the atomic number. For a first understanding, we can nevertheless find an estimate for the suppression of the charge-to-mass ratio w.r.t. the $B-L$ result: both the binding energies and the nucleon mass difference are of order MeV compared to the total nucleon masses which are at the GeV scale. Naively, this suggests a suppression factor $\sim 10^{-3}$ that turns out to be quite accurate, as we will see in section 5.3.

Let us now try to take a first step towards an estimate of the SC's elemental composition. The second most important contribution, after the technology package enclosing the TMs, arises from the base structure of the SC. This enclosing construction was built mainly from carbon and aluminium [432]. Unfortunately, the SC contains many different subcomponents beyond that, several of them with a similar mass. Furthermore, it is not unlikely that some of them will also contain elements with atomic numbers much larger than those of C or Al. A detailed analysis of the SC composition requires a deep dive into the development of LPF and might not be possible without intense discussion with the LPF collaboration itself. Thus, we will simply use a lower bound on the charge-to-mass ratio of the SC. To arrive at a conservative estimate, we will assume that all components are made from the same material as the TMs except for the SC structure which we assume to be entirely made from carbon. Using this approximation and table 1 from Ref. [432], we conclude that the 450 kg SC has an 83 kg C component and the remaining material will have a charge-to-mass ratio equal to that of gold.[19]

LPF data

To clarify the entire setup and especially for a better understanding of the geometry, we show an exploded view of LPF in fig. 5.4. For us, the propulsion module can be ignored as it was already detached during data taking. We can therefore focus on the remaining components. Let us now focus for a moment on the electrode housing. An important factor in the sensitivity analysis of the SC motion against the TMs will be that not just the x-axis but also the y- and z-axis are tracked where the z-axis points from the TMs to the solar array. The details are shown in fig. 5.5. These axes can not be measured with the optical bench and thus they are inferred via capacitive sensing which in general is less precise than the interferometers for most frequencies. Nevertheless, we have the advantage of being able to analyse the relative acceleration ASDs for all SC axes [433] and we show these results in fig. 5.6. They represent the simulated, data-backed sensitivities to the relative acceleration of the SC w.r.t. the TM(s) which is exactly what we are interested in for eq. (5.23).[20] These results were obtained from a 6.5-day noise-only run in April 2016 [425]. The curves explicitly account for all known noise on SC and TMs and therefore they present the best estimate for the stability of the SC w.r.t. the TM(s). To derive limits, we will set cuts at 1 Hz and 10^{-4} Hz since the noise model breaks down in these extreme regimes [433], therefore requiring further expertise on the instrument. However, a detailed analysis of

---

[19] The difference in the charge-to-mass ratio of gold and platinum is so small that we can safely neglect it here.

[20] In fact, the y- and z-directions are tracked w.r.t. the average of both TM coordinates while for the x-axis only the relative motion w.r.t. TM1 is measured via the additional interferometer. (See the discussion above for the reasoning behind this.)

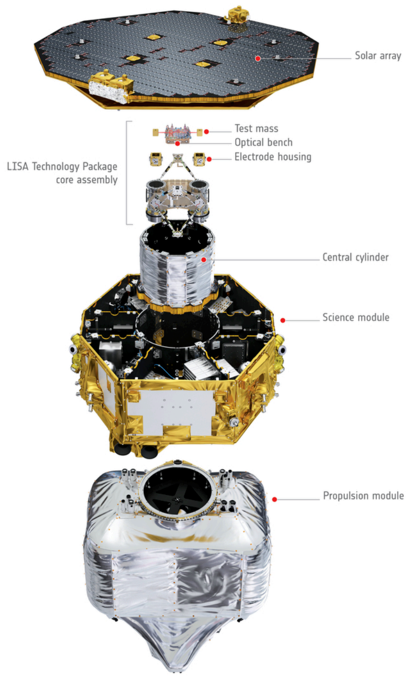

Figure 5.4: Exploded view of LPF showing the science module containing the test masses in its centre as well as the propulsion module. The technology package contains all of the experimental setup relevant to our analysis but since the entire mass of the SC goes into the calculation, we cannot completely ignore the structure or the solar panel. For simplicity, we will just perform a conservative estimate (see text). Image by ESA/ATG medialab (with permission).

the data will most likely lead to interesting constraints in these extremal regimes. We will briefly discuss a planned follow-up project in the concluding section 5.4 of this chapter which also takes into account that there is more data beyond the noise-only run from April 2016.

Before we calculate the limits from the ASDs derived from this data set, let us briefly discuss the frequency dependence and the distinct features in the curves in fig. 5.6. For higher frequencies down to $\sim 10^{-3}$ Hz, the sensitivity is limited mostly by the so-called out-of-loop noise which describes several external influences on the SC. This is where the ASDs are the weakest compared to the main channel, which is shielded from these influences by the SC arranging itself around the TM. The bump at the low frequency part of the spectrum is due to the star-tracker noise which comes from imperfections in the determination of the position of the SC. Ref. [433] argues that this low-frequency noise will most likely be mitigated in the LISA mission, pointing out an interesting avenue for future investigations of gauged DPDM. We will discuss this in more detail in sec. 5.3. In the extremely low frequency region, we observe an additional loss in sensitivity from the capacitive actuation noise experienced by the TMs. In this regime, the simulation also predicts a significantly better sensitivity than the data as shown in Ref. [433] further justifying the cuts introduced above. At peak sensitivity, the x-axis almost reaches the TM1-TM2 result, cf. the dashed

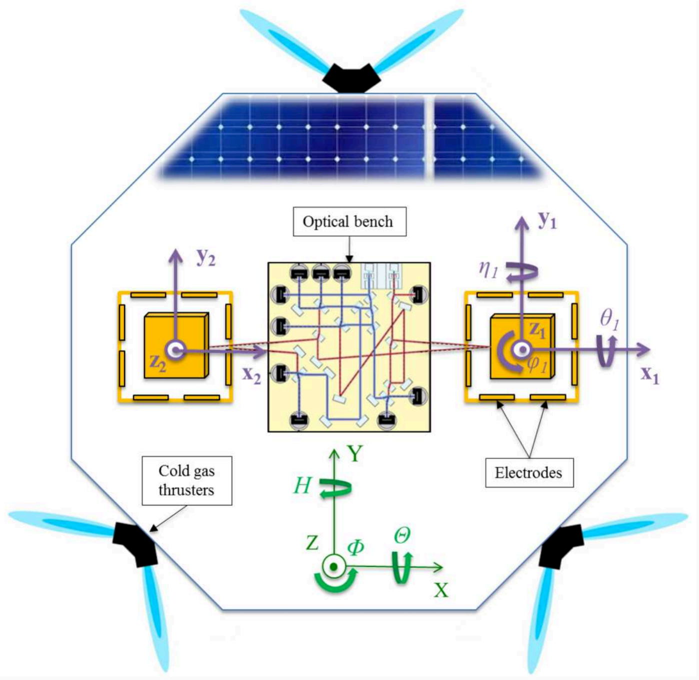

Figure 5.5: Sketch of the science module with the degrees of freedom tracked during the LPF mission. These are x_{12}, x_1, as well as the y and z direction and rotations of the test masses. Furthermore, the same is done for the SC. The optical bench in the centre is responsible for the most precise tracking on the x axis. The electrodes inside the housing track the movement in the other directions and the SC is itself controlled by the thrusters. Image taken from Ref. [433].

black line in fig. 5.6 taken from Ref. [425] which is based on the same data sample.[21] At this point of best sensitivity the other axes perform comparably worse as the capacitive sensing cannot compete with the interferometer on the x-axis.

5.3 Results

Now let us piece together our detailed knowledge of the LPF sensitivity with our signal prediction. Table 5.1 shows the elemental charge-to-mass ratios for carbon and gold [434]. As argued above, we ignore the Pt contribution to the TMs as its charge-to-mass ratio is close to the one of Au. We can derive the simple relation for the SC-TM difference of charge-to-mass ratio under the conservative assumptions about the SC composition of sec. 5.2

$$\left(\frac{q}{M}\right)_{\mathrm{TM}} = \left(\frac{q}{M}\right)_{\mathrm{Au}} \tag{5.28a}$$

$$\left(\frac{q}{M}\right)_{\mathrm{SC}} \approx f_{\mathrm{C}}\left(\frac{q}{M}\right)_{\mathrm{C}} + (1-f_{\mathrm{C}})\left(\frac{q}{M}\right)_{\mathrm{Au}} \tag{5.28b}$$

$$\left|\Delta\left(\frac{q}{M}\right)\right| = \left|\left(\frac{q}{M}\right)_{\mathrm{TM}} - \left(\frac{q}{M}\right)_{\mathrm{SC}}\right| \approx f_{\mathrm{C}}\left|\left(\frac{q}{M}\right)_{\mathrm{Au}} - \left(\frac{q}{M}\right)_{\mathrm{C}}\right| \tag{5.28c}$$

with $f_{\mathrm{C}} \approx 83\,\mathrm{kg}/450\,\mathrm{kg} \approx 0.18$. The last column of Table 5.1 shows the corresponding absolute value of this difference. It is an unfortunate coincidence that the baryon charge-to-mass ratio is so similar for Au and C. Taking into account the true composition of the

---

[21] Unfortunately, the full frequency range is not shown in that work.

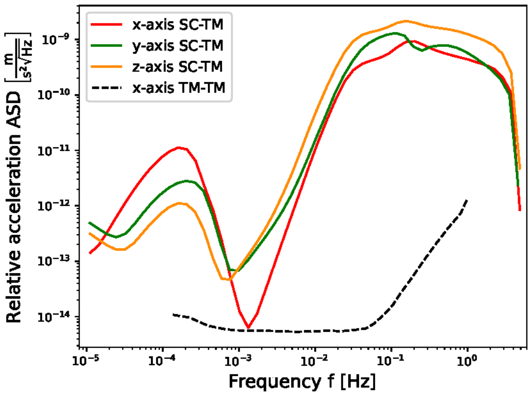

Figure 5.6: Sensitivity of the LPF SC acceleration w.r.t. the TM(s). Red shows the interferometer sensitivity, focussing only on TM1, while green and orange are found from the capacitive sensors in the housing averaged over both TMs; data from [433]. The dashed black line shows the maximum sensitivity of the LPF TM-TM measurement based on the same data set; taken from [425]

.

Material	Au	C	SC-TM
$\left(\frac{q}{M}\right)_{B-L}$ in GeV^{-1}	0.64	0.54	0.018
$\left(\frac{q}{M}\right)_{B}$ in GeV^{-1}	1.0736	1.0737	$1.8 \cdot 10^{-5}$

Table 5.1: Charge-to-mass ratios for Au, C, and the difference between these two elements rescaled to our estimate for the SC composition.

SC will alleviate this suppression. At this point, it should be emphasised that these are very conservative limits in both cases and that we rather expect the suppression in both cases to be about an order of magnitude weaker once the full SC is taken into account, i.e. introducing f_X for all existing elements and their corresponding contribution to the total mass. In the end, of course, we need to have $\sum_X f_X = 1$ and since the typical charge-to-mass ratio of light elements is similar to the one of C, especially for $B-L$, this will alleviate the suppression. Finally, we observe that our initial estimate of the suppression in the B charge-to-mass ratio to be about 10^{-3} is in good agreement with the actual calculation.

Combining the different axes

Demanding that the SNR in eq. (5.23) is at most unity we get a good estimate for the LPF sensitivity on the coupling strength of the DP to the chosen gauge group. For the DM density, we assume $\rho_{\text{DM}} \simeq 0.4\,\text{GeV}/\text{cm}^3$ [435].[22]

As noted earlier, there is a rigorous way to combine the different axes but it requires taking into account a proper convolution of SC position and orientation with all possible

---

[22] We note in passing that unfortunately, for the otherwise outstanding repository of limits in Ref. [162], the DM density varies between different sources which leads to somewhat limited comparability. However, as most DPDM limits scale only with $\sqrt{\rho_{\text{DM}}}$ and the values considered in the literature usually vary only between $0.3 - 0.45\,\text{GeV}/\text{cm}^3$, the actual effect is expected to be rather small in practice.

DP polarisations. Although this procedure necessitates knowledge of the exact orbit of LPF, it will provide even stronger limits if one follows the detailed guide provided in Ref. [72]. LPF offers the advantageous feature that it is in principle sensitive in all three spatial dimensions[23] which means that our results cannot suffer from "blindness" due to an unfortunate orientation of the polarisation. We can always set a conservative estimate by taking the least sensitive axis for every frequency according to fig. 5.6.

$B - L$ sensitivity

In fig. 5.7, we show our main result for $B-L$ as solid lines for the individual axes following the colour-coding of fig. 5.6. Here we assume for each axis separately that the polarisation is exactly aligned with the given axis, i.e. setting $\cos\theta_{A,i} = 1$ in eq. (5.20). We see that we get rather similar constraints from all axes, except for the better peak sensitivity of the x-axis. Following the above argument by taking the upper envelope, that is, just considering the weakest limit for every mass, we can obtain a conservative combination of the limits. At this point, we should comment on the criticism brought forward in Ref. [379] which rightfully points out that the polarisation might not be linear as assumed throughout the publication this chapter is based on. While this certainly changes the signal, our search is effectively independent of the polarisation being linear or elliptical, as we have solely focused on the projection to some axis which will still just give a sinusoidal signal. Our setup is effectively sensitive on all axes and thus with sufficient statistics, in case of a signal, it might even be possible to extract the exact polarisation by combining results from all channels.

Keeping this in mind, we will opt for a more optimistic way to simplify the visualisation of additional forecasts and later the results for B. Following Ref. [393] we perform an average over all possible velocities and polarisations. While this is technically not the most conservative assumption for these long coherence times, we adopt this approach to facilitate comparison with previous LPF limits [394] and LISA projections [393, 420].[24] As our limits are independent of the velocity of the DPs as a direct result of not having to rely on the gradient, the resulting "geometry factor" is $1/\sqrt{3}$ as compared to the usual result of $1/3$. Then, instead of taking the upper envelope, we will use the lower envelope, i.e. the strongest limit for every mass, multiplied by this suppression factor. We will refer to this as the envelope simplification.[25]

Using this approach, we also include an estimate of the improved reach of LPF as a dashed blue line taking into account the entire data set and using the improved understanding of the detector noise and the reduction of Brownian noise in the later stages of the mission [426].[26] We demonstrate the impact of the observation time by also including the blue dotted line, which assumes the same sensitivity as the solid lines, but we set the observation time to the coherence time for each frequency. This explains why the high frequency sensitivity is similar to the "fixed observation time" scenario: For the highest frequencies available, i.e. around 1 Hz, the coherence time is about 10^6 s, which is roughly

---

[23] We note that it would be preferable though to rely only on the interferometer for the analysis. While this is a good option for taking into account the entire data, our analysis is limited to an "instantaneous" measurement, i.e. the SC attitude barely changes throughout the 6.5 days. Therefore, electrostatic measurements are important to avoid complete blindness. We thank Luis Mendes for this hint.

[24] We refer appendix A of Ref. [436] or all of Ref. [437] for a thorough discussion of this issue.

[25] Most of the limits we show with this method are more optimistic projections anyway. Only for the solid blue line of the B limits in fig. 5.8 and the blue region in fig. 5.9 we should keep the shape of all three axes in mind.

[26] For this we set the observation time to 1 month and assume an improvement in noise-reduction by a factor 3.

on the time scale of a week, coinciding with the real observation time used to model the sensitivity curve. On the low frequency end of the spectrum, the coherence times approach millennia scales making the dashed line much stronger than the other limits. Although people have considered the possibility of ultra-long time observations [438], we will refrain from considering this as a realistic forecast. However, this sensitivity scaling with time is an interesting aspect of ultralight DM in general. In this regime, the time evolution of the signal is effectively completely deterministic once we have measured it since the coherence time is far beyond the realistic plannability of future missions and thus the signal looks monochromatic with fixed polarisation for the lifespan of any observation.

To demonstrate the power of our approach we compare it to three major results from the literature. We see that our analysis can cover new parameter space beyond the otherwise dominant limits set by the fifth-force search interpretation of the MICROSCOPE experiment [386]. Furthermore, it is immediately clear that our analysis can easily outperform previous LPF limits [394] just because there is no need to rely on the decoherence of the field which is the dominant effect if one only considers the two test masses. The improvement of our limits over the naive results that can be obtained from the decoherence method evaluated around our peak sensitivity at $\sim 5 \cdot 10^{-18}$ eV is given by

$$\frac{\epsilon_{B-L,\mathrm{sat}}}{\epsilon_{B-L,\mathrm{dec}}} \sim \frac{\Delta\frac{q}{m}}{\frac{q}{M}} (mvL)^{-1} \sim 3 \cdot 10^{12} , \tag{5.29}$$

ignoring the small difference in sensitivity between the x_{12} and the x_1 sensitivity at this mass. The first factor takes into account that our method suffers from a mild charge-to-mass ratio suppression w.r.t. the decoherence method, while the second factor comes from the smallness of the decoherence on a length scale of 40 cm. If we go beyond the peak sensitivity, we, of course, receive a penalty from the decline in sensitivity of the auxiliary channels. We note that the limits found in Ref. [394] are better than naively expected from our analysis method, presumably because of their more sophisticated statistical analysis. This observation gives us confidence in the potential reach of our approach for future analyses using all available data. The third literature result is a LISA forecast using the conventional analysis method [420].

B sensitivity

Before turning to the LISA projections, let us discuss the results for B shown in fig. 5.8. We lose around 3 orders of magnitude in sensitivity which can be explained by the stronger charge-to-mass ratio suppression in eq. (5.29) for B. This becomes immediately clear in the comparison of our results to the decoherence limits from LPF which do not suffer from this issue as they scale with the total charge-to-mass ratio. Nevertheless, the decrease in sensitivity of the Equivalence Principle limits due to the same effect still allows to probe a small region of new parameter space and makes an extended study of LPF (and LISA) auxiliary channels very attractive as it will cover a significant amount of new parameter space. Additionally, we added limits from the baryon number anomaly [25] which are non-existent for $B - L$. It is fascinating that our limits can be stronger than this line even though it grows with decreasing mass. This demonstrates the exquisite sensitivity of instruments such as LPF or MICROSCOPE.

LISA forecast

The limits shown as solid lines are rather robust and include conservative estimates on several different levels. Now we will take a more optimistic point of view and focus especially

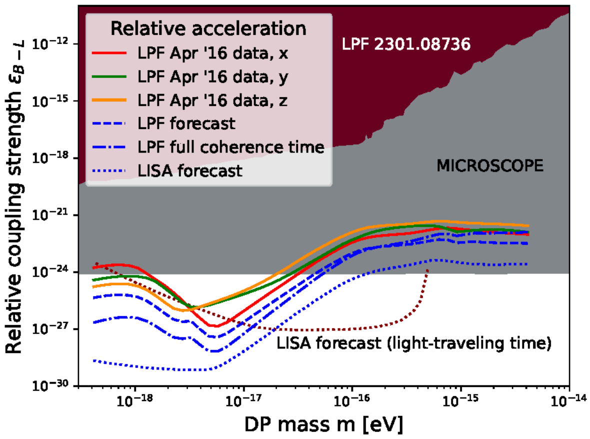

Figure 5.7: Limits on the rescaled coupling to $B-L$, ϵ_{B-L}, of DPDM. In grey, we show the DM-independent limits from searches for violation of the Equivalence Principle [386] and the dark red filled region shows the LPF limits derived from decoherence in Ref. [394]. The dark red dotted line shows the forecast from LISA [420]. In red, green and orange we show the main result of this paper. Forecasts for similar analyses are shown in blue using the envelope simplification explained in the text.

on the future LISA mission. As noted earlier in eqs. (5.22) & (5.23), longer observation times up to one coherence time are extremely efficient to enhance the limits. With the peak sensitivity of LPF lying at around 10^{-3} Hz, it would be ideal to have data for around 30 years, which of course is far beyond the actual lifetime of the mission. Nevertheless, the LISA mission may take data for up to 10 years [424] which means that it naively maximises the efficiency for frequencies around $\sim 3 \cdot 10^{-3}$ Hz. Together with a general decrease in the noise, this will allow for probing the ultra-low frequency parameter space complementary to the previous LISA forecasts.[27]

Previous projections using the planned arm length of around $2.5 \cdot 10^6$ km significantly cut into unexplored parameter space as shown in figs. 5.7 & 5.8. These limits are based on looking for TM-TM displacements using the light-travelling time method and they are strongest around masses of 10^{-16} eV. However, reducing the mass by just one order of magnitude already introduces a decline of the limits by a factor of at least 100. In contrast to that, our method is well-suited for the lowest frequencies available because eq. (5.23) does not depend on the arm length at all. Thus, there is no suppression of the constraints for low frequencies, i.e. large coherence lengths, except for the intrinsic sensitivity loss of the instrument. Indeed, the enhanced reach of our limits at small masses agrees very well with the findings of Ref. [395] using the KAGRA auxiliary channels. Even though these auxiliary channels are at best as sensitive as the main interferometer, they outperform the conventional limits in the low mass region. In conclusion, the LISA mission will provide us with a very powerful tool to constrain the interactions of DPDM when combining the main channel analysis with the auxiliary channel analysis. These limits, spanning several orders of magnitude in mass, will reach deep into the unprobed parameter space.

---

[27] Optimistically, we will assume a factor 10 improvement from the LPF sensitivity in 2016 and mitigation of the star tracker noise for our projections.

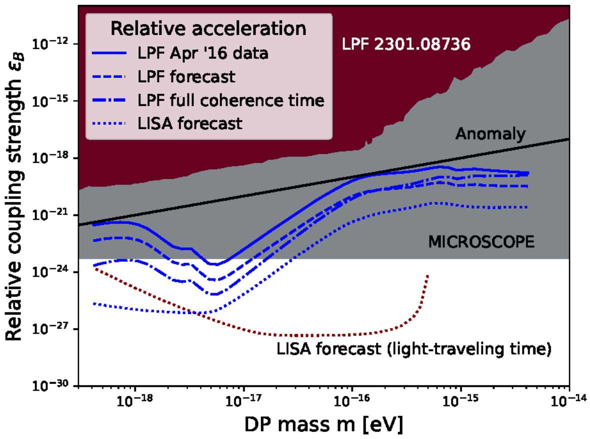

Figure 5.8: Limits on the rescaled coupling to B, ϵ_B, of DPDM. While most of the limits in fig. 5.7 are quite similar for baryon number, there are additional limits from the anomalous nature of this gauge group [25] shown as a solid black line.

Generalisation to different couplings

As mentioned in section 5.1 our approach is not limited to $B-L$ and B. There are a number of additional gauge groups g that will have very similar limits. These limits require just a proper rescaling procedure depending on the type of coupling. As noted earlier, there are essentially two types of couplings in our problem when it comes to analysing observations involving different elements. The first one ("$B-L$-like") is essentially sensitive to different neutron-to-proton ratios of the different elements while the second one ("B-like") relies on the smaller differences in binding energies for different nuclei. Limits that instead depend on the total charge-to-mass ratio do not suffer from this "binding energy suppression" as can be seen from the small changes between the LISA projections and the previous LPF limits in fig. 5.7 to fig. 5.8. For arbitrary gauge groups with a given combination of baryon and lepton number $\alpha B-\beta L$ we find that the charge-to-mass ratio can change from element to element.[28] Therefore, ignoring different isotopes and changing to nuclear physics notation we find for an element with atomic number $Z = L$ and mass number $A = B$

$$\left(\frac{q}{M}\right)_{\alpha B-\beta L} \simeq \frac{\alpha A-\beta Z}{A m_p} = \alpha\frac{1}{m_p} - \beta\frac{Z/A}{m_p}\,, \tag{5.30}$$

where m_p denotes the proton mass.

If instead, we are interested in the difference between two elements we find

$$\Delta\left(\frac{q}{M}\right)_{\alpha B-\beta L} = \begin{cases} \alpha\Delta\left(\frac{q}{M}\right)_B\,, & \beta = 0 \\ \beta\Delta\left(\frac{q}{M}\right)_{B-L}\,, & \text{else} \end{cases}\,, \tag{5.31}$$

using our results for the total charge-to-mass ratios from before. This makes the distinction between "$B-L$-like" and "B-like" immediately clear. Only a gauge group without coupling to the electron number will suffer from the binding energy suppression. The interesting observation is that the calculation for $\beta \neq 0$ is already enough to rescale our limits to all possible gauge groups that meet this criterion. We present a selection of groups in table 5.2. The second column shows the rescaling for the relative charge-to-mass ratio, and the third column shows the rescaling for the total charge-to-mass ratio. We note that

---

[28] For simplicity, we take $L = L_e$ here as L_μ and L_τ will give no contribution.

Limits	Type of coupling	Relative Acceleration	Decoherence/Light-travelling time (Au)
$L_e - L_\mu$	$B - L$	1	$79/(197-79) \approx 0.67$
$L_e - L_\tau$	$B - L$	1	$79/(197-79) \approx 0.67$
$B - 3L_e$	$B - L$	3	$(3 \cdot 79 - 197)/(197-79) \approx 0.34$
$B - 3L_\mu$	B	1	1
$B - 3L_\tau$	B	1	1

Table 5.2: Recipe to rescale the limits for more gauge groups. We give the type of coupling and the corresponding rescaling factor.

the decoherence/light-travelling limit rescalings are technically only valid for Au and the $\beta = 0$ are only valid for Au-C systems. Nevertheless, the rescalings for these cases will still give solid approximations for the true rescaling factor to arbitrary elements.

A rigorous discussion of kinetic mixing

In section 5.1 we neglected any contribution from kinetic mixing. Let us discuss the reasons why this is well justified although the limits on the kinetic mixing parameter ϵ_{KM} are much weaker in this mass range (c.f. fig. 4.5). First, both TMs and SC are essentially electrically neutral [439], immensely suppressing the charge-to-mass ratio compared to $B - L$ or B. One way to circumvent this problem is by instead investigating higher order effects like the radiation pressure on the TMs.[29] Even this higher order effect will be shielded from the TMs by the SC which acts effectively like a Faraday cage for the TMs since the background field is effectively static. Furthermore, the enormous wavelength of the DPs has another effect: the reflection of the DPs on the SC is massively suppressed. Since the SC is extremely small compared to the wavelength of the DP, the DPs will essentially undergo Rayleigh scattering with the SC, i.e. the long wavelength limit of the scattering of EM waves on small objects. Thus, the reflection and with it the radiation pressure is suppressed by $\sim (L_{\mathrm{SC}}/\lambda_c)^4$, where L_{SC} denotes the scale of the SC. All the tools necessary for a simplified calculation can be found in Ref. [440] which is straightforwardly generalised to DP-modified electrodynamics.[30]

Finally, there is another effect suppressing the radiation pressure of DPs. As we have already realised in chapter 3, in-medium effects lead to the effective suppression of the kinetic mixing if the plasma mass $\omega_p = \sqrt{4\pi\alpha n/m_e}$ is larger than the DP mass [102], i.e. $\epsilon_{\mathrm{KM,eff}} \propto m^2/\omega_p^2$. m_e denotes the electron mass and $n \sim 5e^-/\mathrm{cm}^3$ denotes the electron density in the interplanetary medium close to Earth [441] implying a plasma mass of $\sim 10^{-10}\,\mathrm{eV}$ which is much larger than our mass range of interest. For a more thorough treatment, we refer to chapter 3. Of course, the plasma will also interact with the gauged DPs and we will now improve the treatment of the original publication [2] using the results from [442]. Although this work focused on the relativistic plasma in the early Universe, the results can also be applied to the non-relativistic plasma of the interplanetary medium which is dominated by electrons. To be precise, the only relevant contribution to the plasma mass comes from electrons since they are the lightest charged particles in the plasma. We

---

[29] This effect is complementary to looking for the reflected interacting component in a dish antenna setup [354]. Instead of the power focused on the receiver antenna, one would look for the pressure applied on the mirror by the same process.

[30] The idea is to follow the spherical cow approach and make the crude approximation of a spherical satellite. Then the DP and the photonic field can be expanded in vector spherical harmonics (Mie scattering), and the reflection coefficient can be derived for large wavelengths compared to the scale of the satellite.

Particle f	q_f	$q_{f,B-L}$	$q_{f,B}$	$q_{f,\alpha B-\beta L}$	$\tilde{q}_f$	$\tilde{q}_{f,B-L}$	$\tilde{q}_{f,B}$	$\tilde{q}_{f,\alpha B-\beta L}$
Electron	-1	-1	0	$-\beta$	0	0	0	0
Proton	$+1$	$+1$	$+1$	$+\alpha$	0	0	$+1$	$\alpha-\beta$
Neutron	0	$+1$	$+1$	$+\alpha$	0	$+1$	$+1$	α

Table 5.3: Impact of the plasma effects on the constituents of atomic matter.

can then have a quick look at the expression for the effective charge $\tilde{q}_{f,g}$ of a fermion f with $\mathcal{L} \supset \epsilon e \tilde{q}_{f,g} \bar{f} \not{A}' f$ resulting from the plasma mixing effects on general DPs via eq. (9) of Ref. [442][31]

$$\tilde{q}_{f,g} = \left(q_{f,g} - \frac{q_{e,g}}{q_e} q_f \right) \tag{5.32}$$

where we denote with the subscript g the gauge group, e.g. $B-L$, and with the subscript e the electron. We will evaluate this in table 5.3. We can see, that the components similar to photon couplings get eliminated in this framework, a statement that explicitly holds for kinetic mixing which just couples proportional to EM and thus gets projected out completely. For the sum of charges in an atom, it is now simple to conclude that the total charge under a given group is not modified at all. This is easiest to see for $B-L$ where before electron and proton contributions cancelled and now in a plasma environment, they effectively do not carry any charge. The result in both cases is that the total $B-L$ charge of an atom is its neutron number.

In conclusion, all these effects modifying the kinetic mixing sensitivity cannot be compensated by weaker limits on ϵ_{KM} and thus, especially the shielding and plasma effects make it virtually impossible to directly detect kinetically mixed DPs at extremely low masses.

Finally, let us put the constraints derived in this chapter into a larger context for gauged $B-L$ using once again the excellent collection of limits from Ref. [162] shown in fig. 5.9.[32] Note that the y-axis shows the gauge coupling $g_{B-L} = \epsilon_{B-L} e$. In addition to the limits shown above, one can also consider conventional equivalence principle violation searches as direct detection experiments in a similar mass range [391]. These limits are quite similar to our work as they also search for a monochromatic DPDM signal on a "$B-L$-dipole" test mass. Several additional projections are shown in this figure that come from asteroids [436], atomic interferometry [443], space-based quantum sensors [444], and future torsion balance experiments [390]. We see that neither LPF nor LISA are expected to have the best sensitivity in the long run but as LPF already has available data, this makes it the leading limit over almost two orders of magnitude in mass and at peak sensitivity, it outperforms the current limits by more than two orders of magnitude in the gauge coupling. Furthermore, we have outlined why and how a detailed analysis of the LPF data can push the sensitivity providing excellent motivation for further work.

5.4 Discussion

In this chapter, we drew from our knowledge of DPs and DM to constrain ultralight DPDM. We demonstrated how to improve existing DP limits based on the LPF data. The

---

[31] We will slightly modify the nomenclature from this work, i.e. define the EM charges with q_f and the ones of the additional $U(1)_g$ by $q_{f,g}$.

[32] The result derived in this work was later added to this repository. For consistency, we will nevertheless use the plot which was part of the original publication.

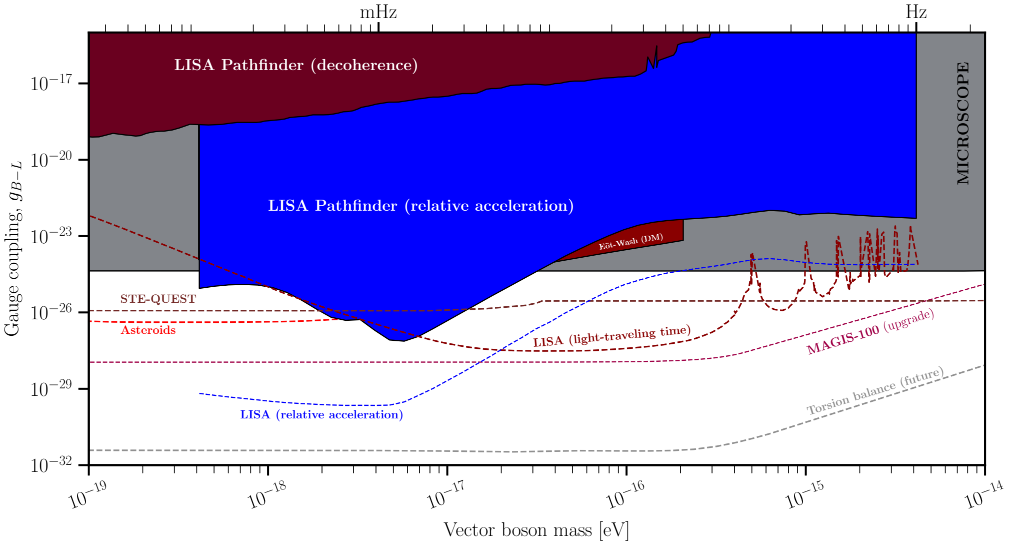

Figure 5.9: Limits on the gauge coupling of $B-L$ DPDM. These now include additional projections and limits as presented in [162].

novel idea is that there is the option to use auxiliary measurements for the acceleration between the SC and the TMs to constrain the coupling strength of gauged $B-L$ and B DPDM in analogy to the use of auxiliary arms in KAGRA [420]. The main advantage is the different atomic compositions of the test masses and the spacecraft leading to a relative acceleration. Relying only on the measurement between the two TMs will lead to extremely suppressed limits as the TMs react identically to the DPDM field. The existing literature focused on decoherence and light-travelling time effects which weakly break this degeneracy at the cost of a massive suppression for low frequencies where the arm length is much smaller than the wavelength. While our new limits are also moderately suppressed by the similar charge-to-mass ratios they are free from any arm length suppression and can therefore rely on the auxiliary channels working at almost full sensitivity. For LPF, the auxiliary channels are not significantly more noisy than the main (x_{12}) channel at their peak frequency which is an important advantage for our work. Furthermore, we can cover all three spatial dimensions with the auxiliary channels, which will prevent a potential blindness toward specific DP polarisations.

We showed that even conservative estimates of the LPF results are already able to probe much new parameter space in the $B-L$ case and at least a small region for B considering masses around $5 \cdot 10^{-18}$ eV. Our approach offers an improvement of up to about 12 orders of magnitude over the most naive analysis of $B-L$. It is therefore likely that a detailed analysis of the whole data set of LPF will set even better and thus world-leading limits over a considerable mass range. Additionally, this work motivates a rigorous analysis of the reach of LISA using auxiliary channels as our approach might be highly complementary to the previous forecasts.

6 Conclusions

> Sounds of laughter shades of life are ringing
> Through my open ears inciting and inviting me
> Limitless undying love which shines around me like a million suns
> It calls me on and on across the universe
>
> *Across the Universe*
> THE BEATLES

This chapter marks the end of this thesis and will thus provide concluding remarks on the results collected in the previous chapters. In general, this thesis investigated two aspects of the DP model in great detail: the angular distribution of the potential solar DP flux and the direct detection of general DPDM using gravitational wave interferometry.

Initially, we discussed the general impact of a DP on the electroweak sector in chapter 2. We drew the important conclusion that in the low-energy limit, the DP behaves very similarly to an EM photon, an aspect we have heavily relied on in later chapters. Furthermore, we have clarified the decoupling of the dark photon from general high-energy phenomena in the extremely low mass limit. This result was a reoccurring theme in this thesis, where we often saw that beyond a scale dictated by SM physics, the effect of kinetic mixing drops out. Beyond these general results for the rest of the thesis, we have also presented a toy analysis of the impact of the DP on EW precision observables as shown in fig. 2.1. We conclude that some interesting aspects of the generalised mixing parameters might require further scrutiny than what we have shown here and point towards potential future work. Finally, we introduced the concept of millicharge in this chapter, discussing some literature results.

Chaper 3 was dedicated to a detailed description of the angular dependence of the solar DP flux, improving upon existing literature predictions. The main result is summarised in fig. 3.2 which demonstrates the main points worked out in this work. Furthermore, we have included a more rigorous discussion of plasma effects than in the original publication. We have then introduced an analysis framework for an “impovised helioscope”, Hinode XRT, in great detail which, in increasing complexity, showed how the additional angular and spectral information can be incorporated. The emphasis in this analysis, as shown in figure 3.9, was placed on the relative improvement of the limits due to the enriched information available by exploiting the theory prediction as much as possible. However, fig. 3.14 demonstrates that the limits are also strong in a global context, especially if we keep in mind that Hinode XRT was not designed as a helioscope. Furthermore, we pointed out that future helioscopes might be able to use this formalism for stronger constraints and discrimination power in case of detecting a signal.

After having concluded the discussion of solar DP production, we began to focus on DPDM in chapter 4. This required a concise summary of the history and observations of DM that are at our disposal. As is self-evident, we need any viable DM candidate to agree with the observations, both the gravitational effects (positive observations) and the lack of direct signals (negative observations). The first main task was then to discuss the production of DPDM. Motivated by our previous discussion of DP production from the solar plasma, we investigated briefly the production of DPs from the primordial SM plasma. We argued that this simple mechanism is in tension with other observations, and thus we briefly introduced gravitational, or in general non-thermal, DPDM production. We then reviewed the state of DPDM bounds from the rich set of existing literature.

Finally, our last full-blown chapter 5 investigated the concept of general DPDM in the ultralight regime with greater scrutiny. With increasing coverage of the standard DPDM parameter space, this extended class of DPs is an interesting alternative. Furthermore, the kinetically mixed DP in the ultralight regime is notoriously hard to detect because of the by now often-discussed plasma effects which we quickly reviewed towards the end of this chapter. The focus therefore lay on B and $B-L$ gauged DPs and their direct detection via GW interferometers, specifically using LPF data. We summarised the conventional approach using the finite light-travelling time and the decoherence effect and pointed out the advantages of having a non-vanishing difference of charge-to-mass ratios available, even if it was only in the auxiliary channels. We applied this idea to pre-analysed LISA Pathfinder data, which allowed us to set world-leading limits in fig. 5.7 and fig. 5.8. We then set these limits in a global picture in fig. 5.9 and emphasised the need for a thorough analysis of the LPF data.

Let us now end this thesis with a conclusion on its overarching theme. Generically, new $U(1)$ symmetries are considered in many BSM scenarios, thus providing enormous motivation to study the DP. Especially in string theory, we even expect the existence of many new $U(1)$s. The importance of the DP in BSM physics is further emphasised by the simplicity of the kinetic mixing term. We have seen that the DP can be just a small part of a larger dark sector, but we emphasised here that with a DP alone, there is a rich phenomenology in particle physics, astrophysics and cosmology. Although all searches conducted so far, including the ones presented in this thesis, could not find a definite signal, the search will continue because of the strong evidence for DM. Extending the scope of the searches from WIMPy to light or ultralight DM seems like the logical next step. Also, with the advent of GW detection, multi-messenger observations will only increase in scope and precision which offers us an increasingly complete picture of our Universe. As discussed, many experiments will be conducted in the next years and we can only look forward to new results and hope for a discovery, be it in direct detection, in astrophysical/cosmological observations or in lab experiments.

Bibliography

[1] J. Frerick, F. Kahlhoefer, and K. Schmidt-Hoberg, *A' view of the sunrise: boosting helioscopes with angular information*, *JCAP* **03** (2023) 001, [`arXiv:2211.00022`].

[2] J. Frerick, J. Jaeckel, F. Kahlhoefer, and K. Schmidt-Hoberg, *Riding the dark matter wave: Novel limits on general dark photons from LISA Pathfinder*, *Phys. Lett. B* **848** (2024) 138328, [`arXiv:2310.06017`].

[3] T. Emken, J. Frerick, S. Heeba, and F. Kahlhoefer, *Electron recoils from terrestrial upscattering of inelastic dark matter*, *Phys. Rev. D* **105** (2022), no. 5 055023, [`arXiv:2112.06930`].

[4] G. Bertone and D. Hooper, *History of dark matter*, *Rev. Mod. Phys.* **90** (2018), no. 4 045002, [`arXiv:1605.04909`].

[5] B. Carr, F. Kuhnel, and M. Sandstad, *Primordial Black Holes as Dark Matter*, *Phys. Rev. D* **94** (2016), no. 8 083504, [`arXiv:1607.06077`].

[6] T. Lin, *Dark matter models and direct detection*, *PoS* **333** (2019) 009, [`arXiv:1904.07915`].

[7] DAMA Collaboration, R. Bernabei et al., *First results from DAMA/LIBRA and the combined results with DAMA/NaI*, *Eur. Phys. J. C* **56** (2008) 333–355, [`arXiv:0804.2741`].

[8] XENON Collaboration, E. Aprile et al., *Excess electronic recoil events in XENON1T*, *Phys. Rev. D* **102** (2020), no. 7 072004, [`arXiv:2006.09721`].

[9] R. D. Peccei and H. R. Quinn, *CP Conservation in the Presence of Instantons*, *Phys. Rev. Lett.* **38** (1977) 1440–1443.

[10] F. Wilczek, *Problem of Strong P and T Invariance in the Presence of Instantons*, *Phys. Rev. Lett.* **40** (1978) 279–282.

[11] S. Weinberg, *A New Light Boson?*, *Phys. Rev. Lett.* **40** (1978) 223–226.

[12] M. Cirelli, A. Strumia, and J. Zupan, *Dark matter*, 2024.

[13] G. Alonso-Álvarez, F. Ertas, J. Jaeckel, F. Kahlhoefer, and L. J. Thormaehlen, *Hidden Photon Dark Matter in the Light of XENON1T and Stellar Cooling*, *JCAP* **11** (2020) 029, [`arXiv:2006.11243`].

[14] P. Athron et al., *Global fits of axion-like particles to XENON1T and astrophysical data*, *JHEP* **05** (2021) 159, [`arXiv:2007.05517`].

[15] I. M. Bloch, A. Caputo, R. Essig, D. Redigolo, M. Sholapurkar, and T. Volansky, *Exploring new physics with O(keV) electron recoils in direct detection experiments*, *JHEP* **01** (2021) 178, [`arXiv:2006.14521`].

[16] K. Kannike, M. Raidal, H. Veermäe, A. Strumia, and D. Teresi, *Dark Matter and the XENON1T electron recoil excess*, *Phys. Rev. D* **102** (2020), no. 9 095002, [`arXiv:2006.10735`].

[17] B. Fornal, P. Sandick, J. Shu, M. Su, and Y. Zhao, *Boosted Dark Matter Interpretation of the XENON1T Excess*, *Phys. Rev. Lett.* **125** (2020), no. 16 161804, [`arXiv:2006.11264`].

[18] M. Baryakhtar, A. Berlin, H. Liu, and N. Weiner, *Electromagnetic signals of inelastic dark matter scattering*, *JHEP* **06** (2022) 047, [`arXiv:2006.13918`].

[19] L. B. Okun, *LIMITS OF ELECTRODYNAMICS: PARAPHOTONS?*, *Sov. Phys. JETP* **56** (1982) 502.

[20] M. Bauer, P. Foldenauer, and J. Jaeckel, *Hunting All the Hidden Photons*, *JHEP* **07** (2018) 094, [`arXiv:1803.05466`].

[21] B. Holdom, *Two U(1)'s and Epsilon Charge Shifts*, *Phys. Lett. B* **166** (1986) 196–198.

[22] J. Jaeckel, *A force beyond the Standard Model - Status of the quest for hidden photons*, *Frascati Phys. Ser.* **56** (2012) 172–192, [`arXiv:1303.1821`].

[23] M. Fabbrichesi, E. Gabrielli, and G. Lanfranchi, *The Dark Photon*, [`arXiv:2005.01515`].

[24] P. Fayet, *On the Search for a New Spin 1 Boson*, *Nucl. Phys. B* **187** (1981) 184–204.

[25] J. A. Dror, R. Lasenby, and M. Pospelov, *New constraints on light vectors coupled to anomalous currents*, *Phys. Rev. Lett.* **119** (2017), no. 14 141803, [`arXiv:1705.06726`].

[26] K. R. Dienes, C. F. Kolda, and J. March-Russell, *Kinetic mixing and the supersymmetric gauge hierarchy*, *Nucl. Phys. B* **492** (1997) 104–118, [`hep-ph/9610479`].

[27] S. A. Abel, M. D. Goodsell, J. Jaeckel, V. V. Khoze, and A. Ringwald, *Kinetic Mixing of the Photon with Hidden U(1)s in String Phenomenology*, *JHEP* **07** (2008) 124, [`arXiv:0803.1449`].

[28] A. Hebecker, J. Jaeckel, and R. Kuespert, *Small Kinetic Mixing in String Theory*, [`arXiv:2311.10817`].

[29] S. Davidson, S. Hannestad, and G. Raffelt, *Updated bounds on millicharged particles*, *JHEP* **05** (2000) 003, [`hep-ph/0001179`].

[30] W.-Z. Feng, Z.-H. Zhang, and K.-Y. Zhang, *Sub-GeV millicharge dark matter from the $U(1)_X$ hidden sector*, [`arXiv:2312.03837`].

[31] I. Y. Kobzarev, L. B. Okun, and I. Y. Pomeranchuk, *On the possibility of experimental observation of mirror particles*, *Sov. J. Nucl. Phys.* **3** (1966), no. 6 837–841.

[32] H. M. Hodges, *Mirror baryons as the dark matter*, *Phys. Rev. D* **47** (1993) 456–459.

[33] C.-W. Chiang, T. Nomura, and J. Tandean, *Nonabelian Dark Matter with Resonant Annihilation*, *JHEP* **01** (2014) 183, [`arXiv:1306.0882`].

[34] G. Alonso-Álvarez, R. Cao, J. M. Cline, K. Moorthy, and T. Xiao, *Nonabelian kinetic mixing in a confining phase: a framework for composite dark photons*, *JHEP* **02** (2024) 017, [`arXiv:2309.13105`].

[35] E. C. G. Stueckelberg, *Die wechselwirkungskräfte in der elektrodynamik und in der feldtheorie der kernkräfte. teil ii und iii*, *Helvetica Physica Acta* **11** (1938), no. IV 299.

[36] H. Ruegg and M. Ruiz-Altaba, *The Stueckelberg field*, *Int. J. Mod. Phys. A* **19** (2004) 3265–3348, [`hep-th/0304245`].

[37] P. W. Higgs, *Broken Symmetries and the Masses of Gauge Bosons*, *Phys. Rev. Lett.* **13** (1964) 508–509.

[38] M. Ahlers, J. Jaeckel, J. Redondo, and A. Ringwald, *Probing Hidden Sector Photons through the Higgs Window*, *Phys. Rev. D* **78** (2008) 075005, [`arXiv:0807.4143`].

[39] M. Redi and A. Tesi, *Dark photon Dark Matter without Stueckelberg mass*, *JHEP* **10** (2022) 167, [`arXiv:2204.14274`].

[40] D. Cyncynates and Z. J. Weiner, *Detectable, defect-free dark photon dark matter*, [`arXiv:2310.18397`].

[41] V. E. Lyubovitskij, A. S. Zhevlakov, A. Kachanovich, and S. Kuleshov, *Dark $SU(2)$ Stueckelberg portal*, *Phys. Rev. D* **107** (2023), no. 5 055006, [`arXiv:2210.05555`].

[42] A. S. Goldhaber and M. M. Nieto, *Terrestrial and extra-terrestrial limits on the photon mass*, *Rev. Mod. Phys.* **43** (1971) 277–296.

[43] E. R. Williams, J. E. Faller, and H. A. Hill, *New experimental test of Coulomb's law: A Laboratory upper limit on the photon rest mass*, *Phys. Rev. Lett.* **26** (1971) 721–724.

[44] L.-C. Tu, J. Luo, and G. T. Gillies, *The mass of the photon*, *Rept. Prog. Phys.* **68** (2005) 77–130.

[45] A. S. Goldhaber and M. M. Nieto, *Photon and Graviton Mass Limits*, *Rev. Mod. Phys.* **82** (2010) 939–979, [`arXiv:0809.1003`].

[46] Particle Data Group Collaboration, R. L. Workman et al., *Review of Particle Physics*, *PTEP* **2022** (2022) 083C01.

[47] S. V. Kuzmin and D. G. C. McKeon, *Stueckelberg mass in the Glashow-Weinberg-Salam model*, *Mod. Phys. Lett. A* **16** (2001) 747–753.

[48] B. Kors and P. Nath, *A Stueckelberg extension of the standard model*, *Phys. Lett. B* **586** (2004) 366–372, [`hep-ph/0402047`].

[49] B. Kors and P. Nath, *Aspects of the Stueckelberg extension*, *JHEP* **07** (2005) 069, [`hep-ph/0503208`].

[50] D. Feldman, Z. Liu, and P. Nath, *The Stueckelberg Z-prime Extension with Kinetic Mixing and Milli-Charged Dark Matter From the Hidden Sector*, *Phys. Rev. D* **75** (2007) 115001, [`hep-ph/0702123`].

[51] K. S. Babu, C. F. Kolda, and J. March-Russell, *Implications of generalized Z - Z-prime mixing*, *Phys. Rev. D* **57** (1998) 6788–6792, [`hep-ph/9710441`].

[52] M. E. Peskin and T. Takeuchi, *A New constraint on a strongly interacting Higgs sector*, *Phys. Rev. Lett.* **65** (1990) 964–967.

[53] M. E. Peskin and T. Takeuchi, *Estimation of oblique electroweak corrections*, *Phys. Rev. D* **46** (1992) 381–409.

[54] B. Holdom, *Oblique electroweak corrections and an extra gauge boson*, *Phys. Lett. B* **259** (1991) 329–334.

[55] C. P. Burgess, S. Godfrey, H. Konig, D. London, and I. Maksymyk, *Model independent global constraints on new physics*, *Phys. Rev. D* **49** (1994) 6115–6147, [`hep-ph/9312291`].

[56] CDF Collaboration, T. Aaltonen et al., *High-precision measurement of the W boson mass with the CDF II detector*, *Science* **376** (2022), no. 6589 170–176.

[57] J. de Blas, M. Pierini, L. Reina, and L. Silvestrini, *Impact of the Recent Measurements of the Top-Quark and W-Boson Masses on Electroweak Precision Fits*, *Phys. Rev. Lett.* **129** (2022), no. 27 271801, [`arXiv:2204.04204`].

[58] C.-T. Lu, L. Wu, Y. Wu, and B. Zhu, *Electroweak precision fit and new physics in light of the W boson mass*, *Phys. Rev. D* **106** (2022), no. 3 035034, [`arXiv:2204.03796`].

[59] A. Strumia, *Interpreting electroweak precision data including the W-mass CDF anomaly*, *JHEP* **08** (2022) 248, [`arXiv:2204.04191`].

[60] Y. Cheng, X.-G. He, F. Huang, J. Sun, and Z.-P. Xing, *Dark photon kinetic mixing effects for the CDF W-mass measurement*, *Phys. Rev. D* **106** (2022), no. 5 055011, [`arXiv:2204.10156`].

[61] K. Harigaya, E. Petrosky, and A. Pierce, *Precision Electroweak Tensions and a Dark Photon*, [`arXiv:2307.13045`].

[62] ATLAS Collaboration, G. Aad et al., *Measurement of the W-boson mass and width with the ATLAS detector using proton-proton collisions at $\sqrt{s} = 7$ TeV*, [`arXiv:2403.15085`].

[63] J. Haller, A. Hoecker, R. Kogler, K. Mönig, T. Peiffer, and J. Stelzer, *Update of the global electroweak fit and constraints on two-Higgs-doublet models*, *Eur. Phys. J. C* **78** (2018), no. 8 675, [`arXiv:1803.01853`].

[64] F. Steininger, T. Mieling, and P. T. Chruściel, *No Proca photons*, *Phys. Rev. D* **107** (2023), no. 5 056013, [`arXiv:2212.12408`].

[65] D. Hanneke, S. Fogwell, and G. Gabrielse, *New Measurement of the Electron Magnetic Moment and the Fine Structure Constant*, *Phys. Rev. Lett.* **100** (2008) 120801, [`arXiv:0801.1134`].

[66] X. Fan, T. G. Myers, B. A. D. Sukra, and G. Gabrielse, *Measurement of the Electron Magnetic Moment*, *Phys. Rev. Lett.* **130** (2023), no. 7 071801, [`arXiv:2209.13084`].

[67] L. Morel, Z. Yao, P. Cladé, and S. Guellati-Khélifa, *Determination of the fine-structure constant with an accuracy of 81 parts per trillion*, *Nature* **588** (2020), no. 7836 61–65.

[68] T. Aoyama, T. Kinoshita, and M. Nio, *Theory of the Anomalous Magnetic Moment of the Electron*, *Atoms* **7** (2019), no. 1 28.

[69] BESIII Collaboration, M. Ablikim et al., *Design and Construction of the BESIII Detector*, *Nucl. Instrum. Meth. A* **614** (2010) 345–399, [`arXiv:0911.4960`].

[70] BELLE-II Collaboration, W. Altmannshofer et al., *The Belle II Physics Book*, *PTEP* **2019** (2019), no. 12 123C01, [`arXiv:1808.10567`]. [Erratum: PTEP 2020, 029201 (2020)].

[71] NA62 Collaboration, E. Cortina Gil et al., *The Beam and detector of the NA62 experiment at CERN*, *JINST* **12** (2017), no. 05 P05025, [`arXiv:1703.08501`].

[72] A. Caputo, A. J. Millar, C. A. J. O'Hare, and E. Vitagliano, *Dark photon limits: A handbook*, *Phys. Rev. D* **104** (2021), no. 9 095029, [`arXiv:2105.04565`].

[73] S. J. Plimpton and W. E. Lawton, *A Very Accurate Test of Coulomb's Law of Force Between Charges*, *Phys. Rev.* **50** (1936), no. 11 1066.

[74] D. F. Bartlett and S. Loegl, *LIMITS ON AN ELECTROMAGNETIC FIFTH FORCE*, *Phys. Rev. Lett.* **61** (1988) 2285–2287.

[75] D. Kroff and P. C. Malta, *Constraining hidden photons via atomic force microscope measurements and the Plimpton-Lawton experiment*, *Phys. Rev. D* **102** (2020), no. 9 095015, [`arXiv:2008.02209`].

[76] L. Davis, Jr., A. S. Goldhaber, and M. M. Nieto, *Limit on the photon mass deduced from Pioneer-10 observations of Jupiter's magnetic field*, *Phys. Rev. Lett.* **35** (1975) 1402–1405.

[77] G. Marocco, *Dark photon limits from magnetic fields and astrophysical plasmas*, [`arXiv:2110.02875`].

[78] J. Jaeckel and S. Roy, *Spectroscopy as a test of Coulomb's law: A Probe of the hidden sector*, *Phys. Rev. D* **82** (2010) 125020, [`arXiv:1008.3536`].

[79] M. Pospelov, *Secluded U(1) below the weak scale*, *Phys. Rev. D* **80** (2009) 095002, [`arXiv:0811.1030`].

[80] S. N. Gninenko and N. V. Krasnikov, *Probing the muon g_μ - 2 anomaly, $L_\mu - L_\tau$ gauge boson and Dark Matter in dark photon experiments*, *Phys. Lett. B* **783** (2018) 24–28, [`arXiv:1801.10448`].

[81] NA64 Collaboration, Y. M. Andreev et al., *Constraints on New Physics in Electron $g-2$ from a Search for Invisible Decays of a Scalar, Pseudoscalar, Vector, and Axial Vector*, *Phys. Rev. Lett.* **126** (2021), no. 21 211802, [`arXiv:2102.01885`].

[82] C. Cosme, M. Dutra, S. Godfrey, and T. R. Gray, *Testing freeze-in with axial and vector Z' bosons*, *JHEP* **09** (2021) 056, [`arXiv:2104.13937`].

[83] P. Anastasopoulos, K. Kaneta, E. Kiritsis, and Y. Mambrini, *Anomalous and axial Z' contributions to g–2*, *JHEP* **02** (2023) 051, [`arXiv:2209.12947`].

[84] R. Foot, H. Lew, and R. R. Volkas, *Electric charge quantization*, *J. Phys. G* **19** (1993) 361–372, [`hep-ph/9209259`]. [Erratum: J.Phys.G 19, 1067 (1993)].

[85] S. D. McDermott, H.-B. Yu, and K. M. Zurek, *Turning off the Lights: How Dark is Dark Matter?*, *Phys. Rev. D* **83** (2011) 063509, [`arXiv:1011.2907`].

[86] A. D. Dolgov, S. L. Dubovsky, G. I. Rubtsov, and I. I. Tkachev, *Constraints on millicharged particles from Planck data*, *Phys. Rev. D* **88** (2013), no. 11 117701, [`arXiv:1310.2376`].

[87] G. Magill, R. Plestid, M. Pospelov, and Y.-D. Tsai, *Millicharged particles in neutrino experiments*, *Phys. Rev. Lett.* **122** (2019), no. 7 071801, [`arXiv:1806.03310`].

[88] H. Liu, N. J. Outmezguine, D. Redigolo, and T. Volansky, *Reviving Millicharged Dark Matter for 21-cm Cosmology*, *Phys. Rev. D* **100** (2019), no. 12 123011, [`arXiv:1908.06986`].

[89] A. Haas, C. S. Hill, E. Izaguirre, and I. Yavin, *Looking for milli-charged particles with a new experiment at the LHC*, *Phys. Lett. B* **746** (2015) 117–120, [`arXiv:1410.6816`].

[90] A. Fung, S. Heeba, Q. Liu, V. Muralidharan, K. Schutz, and A. C. Vincent, *New bounds on light millicharged particles from the tip of the red-giant branch*, *Phys. Rev. D* **109** (2024), no. 8 083011, [`arXiv:2309.06465`].

[91] Z. Bogorad and N. Toro, *Ultralight millicharged dark matter via misalignment*, *JHEP* **07** (2022) 035, [`arXiv:2112.11476`].

[92] A. Berlin, J. A. Dror, X. Gan, and J. T. Ruderman, *Millicharged relics reveal massless dark photons*, *JHEP* **05** (2023) 046, [`arXiv:2211.05139`].

[93] A. Berlin, R. Tito D'Agnolo, S. A. R. Ellis, and J. I. Radkovski, *Signals of millicharged dark matter in light-shining-through-wall experiments*, *JHEP* **08** (2023) 017, [`arXiv:2305.05684`].

[94] T. Ferber, C. Garcia-Cely, and K. Schmidt-Hoberg, *Belle II sensitivity to long-lived dark photons*, [`arXiv:2202.03452`].

[95] M. Graham, C. Hearty, and M. Williams, *Searches for Dark Photons at Accelerators*, *Ann. Rev. Nucl. Part. Sci.* **71** (2021) 37–58, [`arXiv:2104.10280`].

[96] W. Hu, R. Barkana, and A. Gruzinov, *Cold and fuzzy dark matter*, *Phys. Rev. Lett.* **85** (2000) 1158–1161, [`astro-ph/0003365`].

[97] E. D. Kovetz, I. Cholis, and D. E. Kaplan, *Bounds on ultralight hidden-photon dark matter from observation of the 21 cm signal at cosmic dawn*, *Phys. Rev. D* **99** (2019), no. 12 123511, [`arXiv:1809.01139`].

[98] J. Suzuki, T. Horie, Y. Inoue, and M. Minowa, *Experimental Search for Hidden Photon CDM in the eV mass range with a Dish Antenna*, *JCAP* **09** (2015) 042, [`arXiv:1504.00118`].

[99] M. Baryakhtar, J. Huang, and R. Lasenby, *Axion and hidden photon dark matter detection with multilayer optical haloscopes*, *Phys. Rev. D* **98** (2018), no. 3 035006, [`arXiv:1803.11455`].

[100] H. An, S. Ge, W.-Q. Guo, X. Huang, J. Liu, and Z. Lu, *Direct detection of dark photon dark matter using radio telescopes*, [`arXiv:2207.05767`].

[101] R. Cervantes, C. Braggio, B. Giaccone, D. Frolov, A. Grasselino, R. Harnik, O. Melnychuk, R. Pilipenko, S. Posen, and A. Romanenko, *Deepest Sensitivity to Wavelike Dark Photon Dark Matter with SRF Cavities*, [`arXiv:2208.03183`].

[102] J. Redondo, *Helioscope Bounds on Hidden Sector Photons*, *JCAP* **07** (2008) 008, [`arXiv:0801.1527`].

[103] J. Redondo, *Atlas of solar hidden photon emission*, *JCAP* **07** (2015) 024, [`arXiv:1501.07292`].

[104] H. An, M. Pospelov, and J. Pradler, *New stellar constraints on dark photons*, *Phys. Lett. B* **725** (2013) 190–195, [`arXiv:1302.3884`].

[105] H. An, M. Pospelov, and J. Pradler, *Dark Matter Detectors as Dark Photon Helioscopes*, *Phys. Rev. Lett.* **111** (2013) 041302, [`arXiv:1304.3461`].

[106] J. Redondo and G. Raffelt, *Solar constraints on hidden photons re-visited*, *JCAP* **08** (2013) 034, [`arXiv:1305.2920`].

[107] D. K. Hong, C. S. Shin, and S. Yun, *Cooling of young neutron stars and dark gauge bosons*, *Phys. Rev. D* **103** (2021), no. 12 123031, [`arXiv:2012.05427`].

[108] A. Caputo, H. Liu, S. Mishra-Sharma, and J. T. Ruderman, *Modeling Dark Photon Oscillations in Our Inhomogeneous Universe*, *Phys. Rev. D* **102** (2020), no. 10 103533, [`arXiv:2004.06733`].

[109] A. Mirizzi, J. Redondo, and G. Sigl, *Microwave Background Constraints on Mixing of Photons with Hidden Photons*, *JCAP* **03** (2009) 026, [`arXiv:0901.0014`].

[110] A. Caputo, H. Liu, S. Mishra-Sharma, and J. T. Ruderman, *Dark Photon Oscillations in Our Inhomogeneous Universe*, *Phys. Rev. Lett.* **125** (2020), no. 22 221303, [`arXiv:2002.05165`].

[111] K. Bondarenko, J. Pradler, and A. Sokolenko, *Constraining dark photons and their connection to 21 cm cosmology with CMB data*, *Phys. Lett. B* **805** (2020) 135420, [`arXiv:2002.08942`].

[112] A. A. Garcia, K. Bondarenko, S. Ploeckinger, J. Pradler, and A. Sokolenko, *Effective photon mass and (dark) photon conversion in the inhomogeneous Universe*, *JCAP* **10** (2020) 011, [`arXiv:2003.10465`].

[113] S. J. Witte, S. Rosauro-Alcaraz, S. D. McDermott, and V. Poulin, *Dark photon dark matter in the presence of inhomogeneous structure*, *JHEP* **06** (2020) 132, [`arXiv:2003.13698`].

[114] A. Caputo, S. J. Witte, D. Blas, and P. Pani, *Electromagnetic signatures of dark photon superradiance*, *Phys. Rev. D* **104** (2021), no. 4 043006, [`arXiv:2102.11280`].

[115] P. Sikivie, *Experimental Tests of the Invisible Axion*, *Phys. Rev. Lett.* **51** (1983) 1415–1417. [Erratum: Phys.Rev.Lett. 52, 695 (1984)].

[116] K. van Bibber, G. G. Raffelt, D. M. Moltz, F. R. Huson, J. T. White, P. M. McIntyre, R. N. Boyd, and H. N. Nelson, "Construction and operation of an axion helioscope." FERMILAB-PROPOSAL-0794, 1988.

[117] CAST Collaboration, I. G. Irastorza et al., *The CERN Axion Solar Telescope (CAST): Status and prospects*, in *4th International Workshop on the Identification of Dark Matter*, 11, 2002. [`astro-ph/0211606`].

[118] M. Schwarz, E.-A. Knabbe, A. Lindner, J. Redondo, A. Ringwald, M. Schneide, J. Susol, and G. Wiedemann, *Results from the Solar Hidden Photon Search (SHIPS)*, *JCAP* **08** (2015) 011, [`arXiv:1502.04490`].

[119] H. An, M. Pospelov, J. Pradler, and A. Ritz, *New limits on dark photons from solar emission and keV scale dark matter*, *Phys. Rev. D* **102** (2020) 115022, [`arXiv:2006.13929`].

[120] XENON Collaboration, E. Aprile et al., *Emission of single and few electrons in XENON1T and limits on light dark matter*, *Phys. Rev. D* **106** (2022), no. 2 022001, [`arXiv:2112.12116`].

[121] CAST Collaboration, V. Anastassopoulos et al., *New CAST Limit on the Axion-Photon Interaction*, *Nature Phys.* **13** (2017) 584–590, [`arXiv:1705.02290`].

[122] L. Golub, E. Deluca, G. Austin, J. Bookbinder, D. Caldwell, P. Cheimets, J. Cirtain, M. Cosmo, P. Reid, A. Sette, M. Weber, T. Sakao, R. Kano, K. Shibasaki, H. Hara, S. Tsuneta, K. Kumagai, T. Tamura, M. Shimojo, J. McCracken, J. Carpenter, H. Haight, R. Siler, E. Wright, J. Tucker, H. Rutledge, M. Barbera, G. Peres, and S. Varisco, *The X-Ray Telescope (XRT) for the Hinode Mission*, *Solar Physics* **243** (June, 2007) 63–86.

[123] A. A. Anselm, *Experimental Test for Arion $\leftrightarrow$ Photon Oscillations in a Homogeneous Constant Magnetic Field*, *Phys. Rev. D* **37** (1988) 2001.

[124] K. Van Bibber, N. R. Dagdeviren, S. E. Koonin, A. Kerman, and H. N. Nelson, *Proposed experiment to produce and detect light pseudoscalars*, *Phys. Rev. Lett.* **59** (1987) 759–762.

[125] L. Acton, M. Bruner, J. Lemen, S. Tsuneta, Y. Ogawara, J. Nishimura, R. Bentley, L. Culhane, R. Canfield, H. Hudson, et al., *The yohkoh mission for high-energy solar physics*, *Science* **258** (1992), no. 5082 618–625.

[126] S. Hill, V. Pizzo, C. Balch, D. Biesecker, P. Bornmann, E. Hildner, L. Lewis, R. Grubb, M. Husler, K. Prendergast, et al., *The noaa goes-12 solar x-ray imager (sxi) 1. instrument, operations, and data*, *Solar Physics* **226** (2005) 255–281.

[127] L. Smaldone and G. Vitiello, *Neutrino Mixing and Oscillations in Quantum Field Theory: A Comprehensive Introduction*, *Universe* **7** (2021), no. 12 504, [`arXiv:2111.11809`].

[128] L. Wolfenstein, *Neutrino Oscillations in Matter*, *Phys. Rev. D* **17** (1978) 2369–2374.

[129] S. Knapen, T. Lin, and K. M. Zurek, *Light Dark Matter: Models and Constraints*, *Phys. Rev. D* **96** (2017), no. 11 115021, [`arXiv:1709.07882`].

[130] V. Popov and O. Vasil'Ev, *Deviations from electrodynamics: sun and laser*, *Europhysics Letters* **15** (1991), no. 1 7.

[131] J. von Neumann and E. P. Wigner, *Über merkwürdige diskrete eigenwerte*, *The Collected Works of Eugene Paul Wigner: Part A: The Scientific Papers* (1993) 291–293.

[132] G. Raffelt and L. Stodolsky, *Mixing of the Photon with Low Mass Particles*, *Phys. Rev. D* **37** (1988) 1237.

[133] S. Dubovsky and G. Hernández-Chifflet, *Heating up the Galaxy with Hidden Photons*, *JCAP* **12** (2015) 054, [`arXiv:1509.00039`].

[134] F. F. Chen et al., *Introduction to plasma physics and controlled fusion*, vol. 1. Springer, 1984.

[135] P. Drude, *Zur elektronentheorie der metalle*, *Annalen der Physik* **312** (1902), no. 3 687–692.

[136] H. A. Weldon, *Simple Rules for Discontinuities in Finite Temperature Field Theory*, *Phys. Rev. D* **28** (1983) 2007.

[137] J. N. Bahcall, A. M. Serenelli, and S. Basu, *New solar opacities, abundances, helioseismology, and neutrino fluxes*, *Astrophys. J. Lett.* **621** (2005) L85–L88, [`astro-ph/0412440`].

[138] E. Caffau, H.-G. Ludwig, M. Steffen, B. Freytag, and P. Bonifacio, *Solar Chemical Abundances Determined with a CO5BOLD 3D Model Atmosphere*, *Solar Phys.* **268** (2011) 255, [`arXiv:1003.1190`].

[139] E. Magg et al., *Observational constraints on the origin of the elements - IV. Standard composition of the Sun*, *Astron. Astrophys.* **661** (2022) A140, [`arXiv:2203.02255`].

[140] C. J. Copi, J. Heo, and L. M. Krauss, *Directional sensitivity, WIMP detection, and the galactic halo*, *Phys. Lett. B* **461** (1999) 43–48, [`hep-ph/9904499`].

[141] B. Morgan, A. M. Green, and N. J. C. Spooner, *Directional statistics for WIMP direct detection*, *Phys. Rev. D* **71** (2005) 103507, [`astro-ph/0408047`].

[142] F. Mayet et al., *A review of the discovery reach of directional Dark Matter detection*, *Phys. Rept.* **627** (2016) 1–49, [`arXiv:1602.03781`].

[143] Y. Hochberg, Y. Kahn, M. Lisanti, C. G. Tully, and K. M. Zurek, *Directional detection of dark matter with two-dimensional targets*, *Phys. Lett. B* **772** (2017) 239–246, [`arXiv:1606.08849`].

[144] C. A. J. O'Hare, *New Definition of the Neutrino Floor for Direct Dark Matter Searches*, *Phys. Rev. Lett.* **127** (2021), no. 25 251802, [`arXiv:2109.03116`].

[145] K. C. Y. Ng, J. F. Beacom, A. H. G. Peter, and C. Rott, *Solar Atmospheric Neutrinos: A New Neutrino Floor for Dark Matter Searches*, *Phys. Rev. D* **96** (2017), no. 10 103006, [`arXiv:1703.10280`].

[146] C. A. J. O'Hare, *Dark matter astrophysical uncertainties and the neutrino floor*, *Phys. Rev. D* **94** (2016), no. 6 063527, [`arXiv:1604.03858`].

[147] E. Churazov, S. Sazonov, R. Sunyaev, and M. Revnivtsev, *Earth X-ray albedo for CXB radiation in the 1-1000 keV band*, [`astro-ph/0608252`].

[148] T. Kosugi, K. Matsuzaki, T. Sakao, T. Shimizu, Y. Sone, S. Tachikawa, T. Hashimoto, K. Minesugi, A. Ohnishi, T. Yamada, et al., *The hinode (solar-b) mission: an overview*, *The Hinode Mission* (2008) 5–19.

[149] R. Kano, T. Sakao, H. Hara, S. Tsuneta, K. Matsuzaki, K. Kumagai, M. Shimojo, K. Minesugi, K. Shibasaki, E. E. DeLuca, L. Golub, J. Bookbinder, D. Caldwell, P. Cheimets, J. Cirtain, E. Dennis, T. Kent, and M. Weber, *The Hinode X-Ray Telescope (XRT): Camera Design, Performance and Operations*, *Solar Physics* **249** (June, 2008) 263–279.

[150] N. Narukage et al., *Coronal Temperature Diagnostic Capability of the Hinode/X-Ray Telescope Based on Self-Consistent Calibration*, *Solar Phys.* **269** (2011) 169, [`arXiv:1011.2867`].

[151] N. Narukage, T. Sakao, R. Kano, M. Shimojo, A. Winebarger, M. Weber, and K. K. Reeves, *Coronal-Temperature-Diagnostic Capability of the Hinode/X-Ray Telescope Based on Self-Consistent Calibration. II. Calibration with on-Orbit Data*, *Solar Phys.* **289** (2014) 1029, [`arXiv:1307.4489`].

[152] K. Matsuzaki, M. Shimojo, T. Tarbell, L. Harra, and E. Deluca, *Data archive of the hinode mission*, *The Hinode Mission* (2008) 21–26.

[153] A. R. Kobelski, S. H. Saar, M. A. Weber, D. E. McKenzie, and K. K. Reeves, *Calibrating Data from the Hinode/X-Ray Telescope and Associated Uncertainties*, *Solar Physics* **289** (July, 2014) 2781–2802, [`arXiv:1312.4850`].

[154] S. Freeland and B. Handy, *Data analysis with the solarsoft system*, *Solar Physics* **182** (1998) 497–500.

[155] XMM Collaboration, F. Jansen et al., *XMM-Newton observatory. I. The spacecraft and operations.*, *Astron. Astrophys.* **365** (2001) L1–L6.

[156] M. C. Weisskopf, H. D. Tananbaum, L. P. van Speybroeck, and S. L. O'Dell, *Chandra x-ray observatory (cxo):overview*, *Proc. SPIE Int. Soc. Opt. Eng.* **4012** (2000) 2, [`astro-ph/0004127`].

[157] H. S. Hudson, L. W. Acton, E. DeLuca, I. G. Hannah, K. Reardon, and K. Van Bibber, *X-Ray Searches for Solar Axions*, *ASP Conf. Ser.* **455** (2012) 25, [`arXiv:1201.4607`].

[158] H. Chernoff, *On the Distribution of the Likelihood Ratio*, *Ann. Math. Stat.* **25** (1954) 573–578.

[159] J. Conrad, *Statistical Issues in Astrophysical Searches for Particle Dark Matter*, *Astropart. Phys.* **62** (2015) 165–177, [`arXiv:1407.6617`].

[160] M. Afshari, G. Peres, P. Jibben, A. Petralia, F. Reale, and M. Weber, *X-raying the dark side of venus—scatter from venus'magnetotail?*, *The Astronomical Journal* **152** (2016), no. 4 107.

[161] B. J. Wargelin, M. Markevitch, M. Juda, V. Kharchenko, R. J. Edgar, and A. Dalgarno, *Chandra observations of the 'dark' moon and geocoronal solar - wind charge transfer*, *Astrophys. J.* **607** (2004) 596–610, [`astro-ph/0402247`].

[162] C. O'Hare, "cajohare/axionlimits: Axionlimits." `https://cajohare.github.io/AxionLimits/`, July, 2020.

[163] K. Ehret et al., *New ALPS Results on Hidden-Sector Lightweights*, *Phys. Lett. B* **689** (2010) 149–155, [`arXiv:1004.1313`].

[164] ALPS Collaboration, A. Spector, *ALPSII Status Report*, in *14th Patras Workshop on Axions, WIMPs and WISPs*, 6, 2019. [`arXiv:1906.09011`].

[165] N. Vinyoles, A. Serenelli, F. L. Villante, S. Basu, J. Redondo, and J. Isern, *New axion and hidden photon constraints from a solar data global fit*, *JCAP* **10** (2015) 015, [`arXiv:1501.01639`].

[166] S. Balaji, P. S. B. Dev, J. Silk, and Y. Zhang, *Improved stellar limits on a light CP-even scalar*, [`arXiv:2205.01669`].

[167] IAXO Collaboration, A. Abeln et al., *Conceptual design of BabyIAXO, the intermediate stage towards the International Axion Observatory*, *JHEP* **05** (2021) 137, [`arXiv:2010.12076`].

[168] IAXO Collaboration, B. Lakić, *International Axion Observatory (IAXO) status and prospects*, *J. Phys. Conf. Ser.* **1342** (2020), no. 1 012070.

[169] S. Turck-Chièze, *The Standard Solar Model and beyond*, *J. Phys. Conf. Ser.* **665** (2016), no. 1 012078.

[170] N. Vinyoles, A. M. Serenelli, F. L. Villante, S. Basu, J. Bergström, M. C. Gonzalez-Garcia, M. Maltoni, C. Peña Garay, and N. Song, *A new Generation of Standard Solar Models*, *Astrophys. J.* **835** (2017), no. 2 202, [`arXiv:1611.09867`].

[171] S. Fabiani, I. Baffo, S. Bonomo, G. Contini, E. Costa, G. Cucinella, G. De Cesare, E. Del Monte, A. Del Re, S. Di Cosimo, et al., *Cusp: a two cubesats constellation for space weather and solar flares x-ray polarimetry*, .

[172] S. Profumo, *An Introduction to Particle Dark Matter*. World Scientific, 2017.

[173] S. Weinberg, *The Cosmological Constant Problem*, *Rev. Mod. Phys.* **61** (1989) 1–23.

[174] P. J. E. Peebles and B. Ratra, *The Cosmological Constant and Dark Energy*, *Rev. Mod. Phys.* **75** (2003) 559–606, [`astro-ph/0207347`].

[175] T. Padmanabhan, *Cosmological constant: The Weight of the vacuum*, *Phys. Rept.* **380** (2003) 235–320, [`hep-th/0212290`].

[176] I. Zlatev, L.-M. Wang, and P. J. Steinhardt, *Quintessence, cosmic coincidence, and the cosmological constant*, *Phys. Rev. Lett.* **82** (1999) 896–899, [`astro-ph/9807002`].

[177] S. M. Carroll, *The Cosmological constant*, *Living Rev. Rel.* **4** (2001) 1, [`astro-ph/0004075`].

[178] J. Martin, *Everything You Always Wanted To Know About The Cosmological Constant Problem (But Were Afraid To Ask)*, *Comptes Rendus Physique* **13** (2012) 566–665, [`arXiv:1205.3365`].

[179] P. Bull et al., *Beyond ΛCDM: Problems, solutions, and the road ahead*, *Phys. Dark Univ.* **12** (2016) 56–99, [`arXiv:1512.05356`].

[180] J. Sola, *Cosmological constant and vacuum energy: old and new ideas*, *J. Phys. Conf. Ser.* **453** (2013) 012015, [`arXiv:1306.1527`].

[181] Planck Collaboration, N. Aghanim et al., *Planck 2018 results. VI. Cosmological parameters*, *Astron. Astrophys.* **641** (2020) A6, [`arXiv:1807.06209`]. [Erratum: Astron.Astrophys. 652, C4 (2021)].

[182] D. Baumann, *Cosmology.* Cambridge University Press, 7, 2022.

[183] A. D. Sakharov, *Violation of CP Invariance, C asymmetry, and baryon asymmetry of the universe*, *Pisma Zh. Eksp. Teor. Fiz.* **5** (1967) 32–35.

[184] A. G. Cohen, D. B. Kaplan, and A. E. Nelson, *Progress in electroweak baryogenesis*, *Ann. Rev. Nucl. Part. Sci.* **43** (1993) 27–70, [`hep-ph/9302210`].

[185] H. Georgi, *A MODEST PROPOSAL FOR ELIMINATING THE GAUGE HIERARCHY PROBLEM IN UNIFIED THEORIES*, *Hadronic J.* **2** (1979) 568.

[186] L. Susskind, *THE GAUGE HIERARCHY PROBLEM, TECHNICOLOR, SUPERSYMMETRY, AND ALL THAT.*, *Phys. Rept.* **104** (1984) 181–193.

[187] M. Carena and H. E. Haber, *Higgs Boson Theory and Phenomenology*, *Prog. Part. Nucl. Phys.* **50** (2003) 63–152, [`hep-ph/0208209`].

[188] J. R. Ellis and M. K. Gaillard, *Strong and Weak CP Violation*, *Nucl. Phys. B* **150** (1979) 141–162.

[189] M. Dine, W. Fischler, and M. Srednicki, *A Simple Solution to the Strong CP Problem with a Harmless Axion*, *Phys. Lett. B* **104** (1981) 199–202.

[190] H.-Y. Cheng, *The Strong CP Problem Revisited*, *Phys. Rept.* **158** (1988) 1.

[191] W.-Y. Ai, J. S. Cruz, B. Garbrecht, and C. Tamarit, *Consequences of the order of the limit of infinite spacetime volume and the sum over topological sectors for CP violation in the strong interactions*, *Phys. Lett. B* **822** (2021) 136616, [`arXiv:2001.07152`].

[192] W.-Y. Ai, B. Garbrecht, and C. Tamarit, *CP conservation in the strong interactions*, [`arXiv:2404.16026`].

[193] D. Albandea, G. Catumba, and A. Ramos, *The Strong CP Problem in the Quantum Rotor*, [`arXiv:2402.17518`].

[194] E. Di Valentino et al., *Snowmass2021 - Letter of interest cosmology intertwined II: The hubble constant tension*, *Astropart. Phys.* **131** (2021) 102605, [`arXiv:2008.11284`].

[195] E. Di Valentino, O. Mena, S. Pan, L. Visinelli, W. Yang, A. Melchiorri, D. F. Mota, A. G. Riess, and J. Silk, *In the realm of the Hubble tension—a review of solutions*, *Class. Quant. Grav.* **38** (2021), no. 15 153001, [`arXiv:2103.01183`].

[196] N. Schöneberg, G. Franco Abellán, A. Pérez Sánchez, S. J. Witte, V. Poulin, and J. Lesgourgues, *The H0 Olympics: A fair ranking of proposed models*, *Phys. Rept.* **984** (2022) 1–55, [`arXiv:2107.10291`].

[197] A. Addazi et al., *Quantum gravity phenomenology at the dawn of the multi-messenger era—A review*, *Prog. Part. Nucl. Phys.* **125** (2022) 103948, [`arXiv:2111.05659`].

[198] A. Ashtekar and E. Bianchi, *A short review of loop quantum gravity*, *Rept. Prog. Phys.* **84** (2021), no. 4 042001, [`arXiv:2104.04394`].

[199] F. Zwicky, *Die Rotverschiebung von extragalaktischen Nebeln*, *Helv. Phys. Acta* **6** (1933) 110–127.

[200] V. C. Rubin and W. K. Ford, Jr., *Rotation of the Andromeda Nebula from a Spectroscopic Survey of Emission Regions*, *Astrophys. J.* **159** (1970) 379–403.

[201] J. I. Read, *The Local Dark Matter Density*, *J. Phys. G* **41** (2014) 063101, [`arXiv:1404.1938`].

[202] A. A. Penzias and R. W. Wilson, *A Measurement of excess antenna temperature at 4080-Mc/s*, *Astrophys. J.* **142** (1965) 419–421.

[203] COBE Collaboration, G. F. Smoot et al., *Structure in the COBE differential microwave radiometer first year maps*, *Astrophys. J. Lett.* **396** (1992) L1–L5.

[204] D. J. Fixsen, E. S. Cheng, J. M. Gales, J. C. Mather, R. A. Shafer, and E. L. Wright, *The Cosmic Microwave Background spectrum from the full COBE FIRAS data set*, *Astrophys. J.* **473** (1996) 576, [`astro-ph/9605054`].

[205] WMAP Collaboration, D. N. Spergel et al., *First year Wilkinson Microwave Anisotropy Probe (WMAP) observations: Determination of cosmological parameters*, *Astrophys. J. Suppl.* **148** (2003) 175–194, [`astro-ph/0302209`].

[206] D. J. Hegyi and K. A. Olive, *Can Galactic Halos Be Made of Baryons?*, *Phys. Lett. B* **126** (1983) 28.

[207] M. Fukugita, C. J. Hogan, and P. J. E. Peebles, *The Cosmic baryon budget*, *Astrophys. J.* **503** (1998) 518, [`astro-ph/9712020`].

[208] EROS Collaboration, T. Lasserre, *Not enough stellar mass machos in the galactic halo*, *Astron. Astrophys.* **355** (2000) L39–L42, [`astro-ph/0002253`].

[209] S. D. M. White, C. S. Frenk, and M. Davis, *Clustering in a Neutrino Dominated Universe*, *Astrophys. J. Lett.* **274** (1983) L1–L5.

[210] P. J. E. Peebles, *PRIMEVAL ADIABATIC PERTURBATIONS: EFFECT OF MASSIVE NEUTRINOS*, *Astrophys. J.* **258** (1982) 415–424.

[211] D. Clowe, M. Bradac, A. H. Gonzalez, M. Markevitch, S. W. Randall, C. Jones, and D. Zaritsky, *A direct empirical proof of the existence of dark matter*, *Astrophys. J. Lett.* **648** (2006) L109–L113, [`astro-ph/0608407`].

[212] D. N. Spergel and P. J. Steinhardt, *Observational evidence for selfinteracting cold dark matter*, *Phys. Rev. Lett.* **84** (2000) 3760–3763, [`astro-ph/9909386`].

[213] M. Rocha, A. H. G. Peter, J. S. Bullock, M. Kaplinghat, S. Garrison-Kimmel, J. Onorbe, and L. A. Moustakas, *Cosmological Simulations with Self-Interacting Dark Matter I: Constant Density Cores and Substructure*, *Mon. Not. Roy. Astron. Soc.* **430** (2013) 81–104, [`arXiv:1208.3025`].

[214] V. M. Sabarish, M. Brüggen, K. Schmidt-Hoberg, M. S. Fischer, and F. Kahlhoefer, *Simulations of galaxy cluster mergers with velocity-dependent, rare, and frequent self-interactions*, *Mon. Not. Roy. Astron. Soc.* **529** (2024), no. 3 2032–2046, [`arXiv:2310.07769`].

[215] M. S. Fischer, L. Kasselmann, M. Brüggen, K. Dolag, F. Kahlhoefer, A. Ragagnin, A. Robertson, and K. Schmidt-Hoberg, *Cosmological and idealized simulations of dark matter haloes with velocity-dependent, rare and frequent self-interactions*, *Mon. Not. Roy. Astron. Soc.* **529** (2024), no. 3 2327–2348, [`arXiv:2310.07750`].

[216] S. Adhikari et al., *Astrophysical Tests of Dark Matter Self-Interactions*, [`arXiv:2207.10638`].

[217] A. H. G. Peter, M. Rocha, J. S. Bullock, and M. Kaplinghat, *Cosmological Simulations with Self-Interacting Dark Matter II: Halo Shapes vs. Observations*, *Mon. Not. Roy. Astron. Soc.* **430** (2013) 105, [`arXiv:1208.3026`].

[218] S. Tulin and H.-B. Yu, *Dark Matter Self-interactions and Small Scale Structure*, *Phys. Rept.* **730** (2018) 1–57, [`arXiv:1705.02358`].

[219] J. A. Sellwood and A. Kosowsky, *Does dark matter exist?*, *ASP Conf. Ser.* **240** (2001) 311, [`astro-ph/0009074`].

[220] E. D'Onghia and G. Lake, *Cold Dark Matter's small scale crisis grows up*, *Astrophys. J.* **612** (2004) 628–632, [`astro-ph/0309735`].

[221] M. G. Baring, T. Ghosh, F. S. Queiroz, and K. Sinha, *New Limits on the Dark Matter Lifetime from Dwarf Spheroidal Galaxies using Fermi-LAT*, *Phys. Rev. D* **93** (2016), no. 10 103009, [`arXiv:1510.00389`].

[222] R. Hajjar, *Multi-messenger lifetime constraints on heavy decaying dark matter*, *J. Phys. Conf. Ser.* **2156** (2021), no. 1 012047.

[223] HAWC Collaboration, S. Hernández Cadena, J. S. Franco, R. Alfaro Molina, V. Gammaldi, E. Karukes, and P. Salucci, *Constraints on cross-section and lifetime of dark matter with HAWC Observations of dwarf Irregular galaxies*, *PoS* **ICRC2019** (2021) 520, [`arXiv:1908.08884`].

[224] H. Yuksel and M. D. Kistler, *Circumscribing late dark matter decays model independently*, *Phys. Rev. D* **78** (2008) 023502, [`arXiv:0711.2906`].

[225] S. D. McDermott, H. H. Patel, and H. Ramani, *Dark Photon Decay Beyond The Euler-Heisenberg Limit*, *Phys. Rev. D* **97** (2018), no. 7 073005, [`arXiv:1705.00619`].

[226] M.-Y. Wang, R. A. C. Croft, A. H. G. Peter, A. R. Zentner, and C. W. Purcell, *Lyman-α forest constraints on decaying dark matter*, *Phys. Rev. D* **88** (2013), no. 12 123515, [`arXiv:1309.7354`].

[227] L. Fuß and M. Garny, *Decaying Dark Matter and Lyman-α forest constraints*, *JCAP* **10** (2023) 020, [`arXiv:2210.06117`].

[228] S. Aoyama, T. Sekiguchi, K. Ichiki, and N. Sugiyama, *Evolution of perturbations and cosmological constraints in decaying dark matter models with arbitrary decay mass products*, *JCAP* **07** (2014) 021, [`arXiv:1402.2972`].

[229] B. Audren, J. Lesgourgues, G. Mangano, P. D. Serpico, and T. Tram, *Strongest model-independent bound on the lifetime of Dark Matter*, *JCAP* **12** (2014) 028, [`arXiv:1407.2418`].

[230] F. K. D. Kahlhoefer, *Complementarity of Searches for Dark Matter.* PhD thesis, Oxford U., 2014.

[231] C. Blanco, B. Elshimy, R. F. Lang, and R. Orlando, *Models of ultraheavy dark matter visible to macroscopic mechanical sensing arrays*, *Phys. Rev. D* **105** (2022), no. 11 115031, [`arXiv:2112.14784`].

[232] D. Carney, S. Ghosh, G. Krnjaic, and J. M. Taylor, *Proposal for gravitational direct detection of dark matter*, *Phys. Rev. D* **102** (2020), no. 7 072003, [`arXiv:1903.00492`].

[233] WINDCHIME Collaboration, A. Attanasio et al., *Snowmass 2021 White Paper: The Windchime Project*, in *Snowmass 2021*, 3, 2022. [`arXiv:2203.07242`].

[234] M. W. Goodman and E. Witten, *Detectability of Certain Dark Matter Candidates*, *Phys. Rev. D* **31** (1985) 3059.

[235] XENON Collaboration, E. Aprile et al., *First Dark Matter Search with Nuclear Recoils from the XENONnT Experiment*, *Phys. Rev. Lett.* **131** (2023), no. 4 041003, [`arXiv:2303.14729`].

[236] LZ Collaboration, J. Aalbers et al., *First Dark Matter Search Results from the LUX-ZEPLIN (LZ) Experiment*, *Phys. Rev. Lett.* **131** (2023), no. 4 041002, [`arXiv:2207.03764`].

[237] LZ Collaboration, J. Aalbers et al., *Constraints On Covariant WIMP-Nucleon Effective Field Theory Interactions from the First Science Run of the LUX-ZEPLIN Experiment*, [`arXiv:2404.17666`].

[238] PANDAX Collaboration, A. Abdukerim et al., *PandaX-xT: a Multi-ten-tonne Liquid Xenon Observatory at the China Jinping Underground Laboratory*, [`arXiv:2402.03596`].

[239] D. Carney et al., *Snowmass2021 cosmic frontier white paper: Ultraheavy particle dark matter*, *SciPost Phys. Core* **6** (2023) 075, [`arXiv:2203.06508`].

[240] XENON Collaboration, E. Aprile et al., *Searching for Heavy Dark Matter near the Planck Mass with XENON1T*, *Phys. Rev. Lett.* **130** (2023), no. 26 261002, [`arXiv:2304.10931`].

[241] J. Billard, L. Strigari, and E. Figueroa-Feliciano, *Implication of neutrino backgrounds on the reach of next generation dark matter direct detection experiments*, *Phys. Rev. D* **89** (2014), no. 2 023524, [`arXiv:1307.5458`].

[242] K. Miuchi, *Challenges for the Directional Dark Matter Direct Detection*, *JAIS* **2024** (2024) 473, [`arXiv:2309.13923`].

[243] N. W. Evans, C. A. J. O'Hare, and C. McCabe, *Refinement of the standard halo model for dark matter searches in light of the Gaia Sausage*, *Phys. Rev. D* **99** (2019), no. 2 023012, [`arXiv:1810.11468`].

[244] F. Gao, "First measurement of coherent elastic neutrino nucleus scattering of solar 8b neutrinos in xenonnt." `https://agenda.infn.it/event/39713/contributions/237829/attachments/123564/181262/xenonnt-cevns-newresults-idm-2024.pdf`, July, 2024. IDM2024.

[245] E. Aprile et al., *First measurement of solar ^8b neutrinos via coherent elastic neutrino-nucleus scattering with xenonnt*, [`arXiv:2408.02877`].

[246] PandaX Collaboration, Z. Bo et al., *First Measurement of Solar ^8B Neutrino Flux through Coherent Elastic Neutrino-Nucleus Scattering in PandaX-4T*, [`arXiv:2407.10892`].

[247] D. Tucker-Smith and N. Weiner, *Inelastic dark matter*, *Phys. Rev. D* **64** (2001) 043502, [`hep-ph/0101138`].

[248] G. D. V. Garcia, F. Kahlhoefer, M. Ovchynnikov, and T. Schwetz, *Not-so-inelastic Dark Matter*, [`arXiv:2405.08081`].

[249] M. Ibe, W. Nakano, Y. Shoji, and K. Suzuki, *Migdal Effect in Dark Matter Direct Detection Experiments*, *JHEP* **03** (2018) 194, [`arXiv:1707.07258`].

[250] XENON Collaboration, E. Aprile et al., *Search for Light Dark Matter Interactions Enhanced by the Migdal Effect or Bremsstrahlung in XENON1T*, *Phys. Rev. Lett.* **123** (2019), no. 24 241803, [`arXiv:1907.12771`].

[251] J. Xu et al., *Search for the Migdal effect in liquid xenon with keV-level nuclear recoils*, *Phys. Rev. D* **109** (2024), no. 5 L051101, [`arXiv:2307.12952`].

[252] R. Essig, J. Mardon, and T. Volansky, *Direct Detection of Sub-GeV Dark Matter*, *Phys. Rev. D* **85** (2012) 076007, [`arXiv:1108.5383`].

[253] R. Essig, T. Volansky, and T.-T. Yu, *New Constraints and Prospects for sub-GeV Dark Matter Scattering off Electrons in Xenon*, *Phys. Rev. D* **96** (2017), no. 4 043017, [`arXiv:1703.00910`].

[254] R. Catena, T. Emken, N. A. Spaldin, and W. Tarantino, *Atomic responses to general dark matter-electron interactions*, *Phys. Rev. Res.* **2** (2020), no. 3 033195, [`arXiv:1912.08204`].

[255] R. Essig, *Some progress & challenges for the direct-detection of sub-GeV dark matter*, *Nucl. Phys. B* **1003** (2024) 116484.

[256] S. Balan et al., *Resonant or asymmetric: The status of sub-GeV dark matter*, [`arXiv:2405.17548`].

[257] J. I. Collar and F. T. Avignone, III, *The Effect of elastic scattering in the Earth on cold dark matter experiments*, *Phys. Rev. D* **47** (1993) 5238–5246.

[258] T. Emken, R. Essig, C. Kouvaris, and M. Sholapurkar, *Direct Detection of Strongly Interacting Sub-GeV Dark Matter via Electron Recoils*, *JCAP* **09** (2019) 070, [`arXiv:1905.06348`].

[259] Y. Hochberg, *SIMP Dark Matter*, *SciPost Phys. Lect. Notes* **59** (2022) 1.

[260] E. Bernreuther, F. Kahlhoefer, M. Krämer, and P. Tunney, *Strongly interacting dark sectors in the early Universe and at the LHC through a simplified portal*, *JHEP* **01** (2020) 162, [`arXiv:1907.04346`].

[261] C. A. J. O'Hare, *Cosmology of axion dark matter*, *PoS* **COSMICWISPers** (2024) 040, [`arXiv:2403.17697`].

[262] R. Catena and P. Ullio, *A novel determination of the local dark matter density*, *JCAP* **08** (2010) 004, [`arXiv:0907.0018`].

[263] M. Pato, O. Agertz, G. Bertone, B. Moore, and R. Teyssier, *Systematic uncertainties in the determination of the local dark matter density*, *Phys. Rev. D* **82** (2010) 023531, [`arXiv:1006.1322`].

[264] J. Bovy and S. Tremaine, *On the local dark matter density*, *Astrophys. J.* **756** (2012) 89, [`arXiv:1205.4033`].

[265] P. G. Staudt, J. S. Bullock, M. Boylan-Kolchin, A. Wetzel, and X. Ou, *Sliding into DM: Determining the local dark matter density and speed distribution using only the local circular speed of the Galaxy*, [`arXiv:2403.04122`].

[266] D. Baumann, *Primordial Cosmology*, *PoS* **TASI2017** (2018) 009, [`arXiv:1807.03098`].

[267] K. J. Ludwick, *The viability of phantom dark energy: A review*, *Mod. Phys. Lett. A* **32** (2017), no. 28 1730025, [`arXiv:1708.06981`].

[268] DESI Collaboration, A. G. Adame et al., *DESI 2024 VI: Cosmological Constraints from the Measurements of Baryon Acoustic Oscillations*, [`arXiv:2404.03002`].

[269] K. V. Berghaus, J. A. Kable, and V. Miranda, *Quantifying Scalar Field Dynamics with DESI 2024 Y1 BAO measurements*, [`arXiv:2404.14341`].

[270] G. Baym and L. P. Kadanoff, *Conservation Laws and Correlation Functions*, *Phys. Rev.* **124** (1961) 287–299.

[271] M. Hufnagel, *Primordial Nucleosynthesis in the Presence of MeV-scale Dark Sectors.* PhD thesis, Hamburg U., Hamburg, 2020.

[272] P. F. Depta, *Dark Sector Cosmologies: Evolution and Constraints.* PhD thesis, Hamburg U., Hamburg, 2021.

[273] J. Chluba and R. A. Sunyaev, *The evolution of CMB spectral distortions in the early Universe*, *Mon. Not. Roy. Astron. Soc.* **419** (2012) 1294–1314, [`arXiv:1109.6552`].

[274] L. C. Thomas, T. Dezen, E. B. Grohs, and C. T. Kishimoto, *Electron-Positron Annihilation Freeze-Out in the Early Universe*, *Phys. Rev. D* **101** (2020), no. 6 063507, [`arXiv:1910.14050`].

[275] M. Drees, F. Hajkarim, and E. R. Schmitz, *The Effects of QCD Equation of State on the Relic Density of WIMP Dark Matter*, *JCAP* **06** (2015) 025, [`arXiv:1503.03513`].

[276] E. W. Kolb and M. S. Turner, *The Early Universe*, vol. 69. 1990.

[277] S. Dodelson, *Modern Cosmology.* Academic Press, Amsterdam, 2003.

[278] P. J. Fox, *TASI Lectures on WIMPs and Supersymmetry*, *PoS* **TASI2018** (2019) 005.

[279] P. J. Fox, R. Harnik, J. Kopp, and Y. Tsai, *Missing Energy Signatures of Dark Matter at the LHC*, *Phys. Rev. D* **85** (2012) 056011, [`arXiv:1109.4398`].

[280] J. L. Feng, *The WIMP paradigm: Theme and variations*, *SciPost Phys. Lect. Notes* **71** (2023) 1, [`arXiv:2212.02479`].

[281] D. Hooper, *TASI Lectures on Indirect Searches For Dark Matter*, *PoS* **TASI2018** (2019) 010, [`arXiv:1812.02029`].

[282] Fermi-LAT Collaboration, M. Ackermann et al., *The Fermi Galactic Center GeV Excess and Implications for Dark Matter*, *Astrophys. J.* **840** (2017), no. 1 43, [`arXiv:1704.03910`].

[283] L. J. Hall, K. Jedamzik, J. March-Russell, and S. M. West, *Freeze-In Production of FIMP Dark Matter*, *JHEP* **03** (2010) 080, [`arXiv:0911.1120`].

[284] X. Chu, T. Hambye, and M. H. G. Tytgat, *The Four Basic Ways of Creating Dark Matter Through a Portal*, *JCAP* **05** (2012) 034, [`arXiv:1112.0493`].

[285] R. T. Co, F. D'Eramo, L. J. Hall, and D. Pappadopulo, *Freeze-In Dark Matter with Displaced Signatures at Colliders*, *JCAP* **12** (2015) 024, [`arXiv:1506.07532`].

[286] T. Bringmann, S. Heeba, F. Kahlhoefer, and K. Vangsnes, *Freezing-in a hot bath: resonances, medium effects and phase transitions*, *JHEP* **02** (2022) 110, [`arXiv:2111.14871`].

[287] R. T. D'Agnolo and J. T. Ruderman, *Light Dark Matter from Forbidden Channels*, *Phys. Rev. Lett.* **115** (2015), no. 6 061301, [`arXiv:1505.07107`].

[288] R. T. D'Agnolo, D. Liu, J. T. Ruderman, and P.-J. Wang, *Forbidden dark matter annihilations into Standard Model particles*, *JHEP* **06** (2021) 103, [`arXiv:2012.11766`].

[289] D. Pappadopulo, J. T. Ruderman, and G. Trevisan, *Dark matter freeze-out in a nonrelativistic sector*, *Phys. Rev. D* **94** (2016), no. 3 035005, [`arXiv:1602.04219`].

[290] M. Farina, D. Pappadopulo, J. T. Ruderman, and G. Trevisan, *Phases of Cannibal Dark Matter*, *JHEP* **12** (2016) 039, [`arXiv:1607.03108`].

[291] R. T. D'Agnolo, D. Pappadopulo, and J. T. Ruderman, *Fourth Exception in the Calculation of Relic Abundances*, *Phys. Rev. Lett.* **119** (2017), no. 6 061102, [`arXiv:1705.08450`].

[292] M. Garny, J. Heisig, B. Lülf, and S. Vogl, *Coannihilation without chemical equilibrium*, *Phys. Rev. D* **96** (2017), no. 10 103521, [`arXiv:1705.09292`].

[293] R. T. D'Agnolo, D. Pappadopulo, J. T. Ruderman, and P.-J. Wang, *Thermal Relic Targets with Exponentially Small Couplings*, *Phys. Rev. Lett.* **124** (2020), no. 15 151801, [`arXiv:1906.09269`].

[294] E. D. Kramer, E. Kuflik, N. Levi, N. J. Outmezguine, and J. T. Ruderman, *Heavy Thermal Dark Matter from a New Collision Mechanism*, *Phys. Rev. Lett.* **126** (2021), no. 8 081802, [`arXiv:2003.04900`].

[295] E. Kuflik, M. Perelstein, N. R.-L. Lorier, and Y.-D. Tsai, *Elastically Decoupling Dark Matter*, *Phys. Rev. Lett.* **116** (2016), no. 22 221302, [`arXiv:1512.04545`].

[296] P. J. Fitzpatrick, H. Liu, T. R. Slatyer, and Y.-D. Tsai, *New pathways to the relic abundance of vector-portal dark matter*, *Phys. Rev. D* **106** (2022), no. 8 083517, [`arXiv:2011.01240`].

[297] E. D. Carlson, M. E. Machacek, and L. J. Hall, *Self-interacting dark matter*, *Astrophys. J.* **398** (1992) 43–52.

[298] Y. Hochberg, E. Kuflik, T. Volansky, and J. G. Wacker, *Mechanism for Thermal Relic Dark Matter of Strongly Interacting Massive Particles*, *Phys. Rev. Lett.* **113** (2014) 171301, [`arXiv:1402.5143`].

[299] J. Smirnov and J. F. Beacom, *New Freezeout Mechanism for Strongly Interacting Dark Matter*, *Phys. Rev. Lett.* **125** (2020), no. 13 131301, [`arXiv:2002.04038`].

[300] T. Bringmann, P. F. Depta, M. Hufnagel, J. T. Ruderman, and K. Schmidt-Hoberg, *Dark Matter from Exponential Growth*, *Phys. Rev. Lett.* **127** (2021), no. 19 191802, [`arXiv:2103.16572`].

[301] T. Bringmann, P. F. Depta, M. Hufnagel, J. Kersten, J. T. Ruderman, and K. Schmidt-Hoberg, *Minimal sterile neutrino dark matter*, *Phys. Rev. D* **107** (2023), no. 7 L071702, [`arXiv:2206.10630`].

[302] J. Redondo and M. Postma, *Massive hidden photons as lukewarm dark matter*, *JCAP* **02** (2009) 005, [`arXiv:0811.0326`].

[303] A. Fradette, M. Pospelov, J. Pradler, and A. Ritz, *Cosmological Constraints on Very Dark Photons*, *Phys. Rev. D* **90** (2014), no. 3 035022, [`arXiv:1407.0993`].

[304] R. Catena, D. Cole, T. Emken, M. Matas, N. Spaldin, W. Tarantino, and E. Urdshals, *Dark matter-electron interactions in materials beyond the dark photon model*, *JCAP* **03** (2023) 052, [`arXiv:2210.07305`].

[305] R. Catena and T. R. Gray, *Spin-1 thermal targets for dark matter searches at beam dump and fixed target experiments*, *JCAP* **11** (2023) 058, [`arXiv:2307.02207`].

[306] M. Pospelov, A. Ritz, and M. B. Voloshin, *Bosonic super-WIMPs as keV-scale dark matter*, *Phys. Rev. D* **78** (2008) 115012, [`arXiv:0807.3279`].

[307] SENSEI Collaboration, P. Adari et al., *SENSEI: First Direct-Detection Results on sub-GeV Dark Matter from SENSEI at SNOLAB*, [`arXiv:2312.13342`].

[308] SuperCDMS Collaboration, T. Aralis et al., *Constraints on dark photons and axionlike particles from the SuperCDMS Soudan experiment*, *Phys. Rev. D* **101** (2020), no. 5 052008, [`arXiv:1911.11905`]. [Erratum: Phys.Rev.D 103, 039901 (2021)].

[309] DAMIC Collaboration, A. Aguilar-Arevalo et al., *Constraints on Light Dark Matter Particles Interacting with Electrons from DAMIC at SNOLAB*, *Phys. Rev. Lett.* **123** (2019), no. 18 181802, [`arXiv:1907.12628`].

[310] DarkSide Collaboration, P. Agnes et al., *Search for Dark Matter Particle Interactions with Electron Final States with DarkSide-50*, *Phys. Rev. Lett.* **130** (2023), no. 10 101002, [`arXiv:2207.11968`].

[311] I. M. Bloch, R. Essig, K. Tobioka, T. Volansky, and T.-T. Yu, *Searching for Dark Absorption with Direct Detection Experiments*, *JHEP* **06** (2017) 087, [`arXiv:1608.02123`].

[312] S. Tremaine and J. E. Gunn, *Dynamical Role of Light Neutral Leptons in Cosmology*, *Phys. Rev. Lett.* **42** (1979) 407–410.

[313] L. Boubekeur and S. Profumo, *Tremaine-Gunn limit with mass-varying particles*, *Phys. Rev. D* **107** (2023), no. 10 103535, [`arXiv:2302.10246`].

[314] L. Hui, *Wave Dark Matter*, *Ann. Rev. Astron. Astrophys.* **59** (2021) 247–289, [`arXiv:2101.11735`].

[315] A. H. Guth, M. P. Hertzberg, and C. Prescod-Weinstein, *Do Dark Matter Axions Form a Condensate with Long-Range Correlation?*, *Phys. Rev. D* **92** (2015), no. 10 103513, [`arXiv:1412.5930`].

[316] G. Dvali and S. Zell, *Classicality and Quantum Break-Time for Cosmic Axions*, *JCAP* **07** (2018) 064, [`arXiv:1710.00835`].

[317] A. Eberhardt, A. Zamora, M. Kopp, and T. Abel, *Classical field approximation of ultralight dark matter: Quantum break times, corrections, and decoherence*, *Phys. Rev. D* **109** (2024), no. 8 083527, [`arXiv:2310.07119`].

[318] R. J. Glauber, *Coherent and incoherent states of the radiation field*, *Phys. Rev.* **131** (1963) 2766–2788.

[319] T. Zimmermann, J. Alvey, D. J. E. Marsh, M. Fairbairn, and J. I. Read, *Dwarf galaxies imply dark matter is heavier than* $\mathbf{2.2 \times 10^{-21}\,eV}$, [`arXiv:2405.20374`].

[320] V. Iršič, M. Viel, M. G. Haehnelt, J. S. Bolton, and G. D. Becker, *First constraints on fuzzy dark matter from Lyman-α forest data and hydrodynamical simulations*, *Phys. Rev. Lett.* **119** (2017), no. 3 031302, [`arXiv:1703.04683`].

[321] T. Kobayashi, R. Murgia, A. De Simone, V. Iršič, and M. Viel, *Lyman-α constraints on ultralight scalar dark matter: Implications for the early and late universe*, *Phys. Rev. D* **96** (2017), no. 12 123514, [`arXiv:1708.00015`].

[322] E. Armengaud, N. Palanque-Delabrouille, C. Yèche, D. J. E. Marsh, and J. Baur, *Constraining the mass of light bosonic dark matter using SDSS Lyman-α forest*, *Mon. Not. Roy. Astron. Soc.* **471** (2017), no. 4 4606–4614, [`arXiv:1703.09126`].

[323] N. Bar, D. Blas, K. Blum, and S. Sibiryakov, *Galactic rotation curves versus ultralight dark matter: Implications of the soliton-host halo relation*, *Phys. Rev. D* **98** (2018), no. 8 083027, [`arXiv:1805.00122`].

[324] M. Safarzadeh and D. N. Spergel, *Ultra-light Dark Matter is Incompatible with the Milky Way's Dwarf Satellites*, [`arXiv:1906.11848`].

[325] DES Collaboration, E. O. Nadler et al., *Milky Way Satellite Census. III. Constraints on Dark Matter Properties from Observations of Milky Way Satellite Galaxies*, *Phys. Rev. Lett.* **126** (2021) 091101, [`arXiv:2008.00022`].

[326] E. G. M. Ferreira, *Ultra-light dark matter*, *Astron. Astrophys. Rev.* **29** (2021), no. 1 7, [`arXiv:2005.03254`].

[327] A. E. Nelson and J. Scholtz, *Dark Light, Dark Matter and the Misalignment Mechanism*, *Phys. Rev. D* **84** (2011) 103501, [`arXiv:1105.2812`].

[328] P. Arias, D. Cadamuro, M. Goodsell, J. Jaeckel, J. Redondo, and A. Ringwald, *WISPy Cold Dark Matter*, *JCAP* **06** (2012) 013, [`arXiv:1201.5902`].

[329] D. J. E. Marsh, *Axion Cosmology*, *Phys. Rept.* **643** (2016) 1–79, [`arXiv:1510.07633`].

[330] P. W. Graham, J. Mardon, and S. Rajendran, *Vector Dark Matter from Inflationary Fluctuations*, *Phys. Rev. D* **93** (2016), no. 10 103520, [`arXiv:1504.02102`].

[331] B. Himmetoglu, C. R. Contaldi, and M. Peloso, *Instability of anisotropic cosmological solutions supported by vector fields*, *Phys. Rev. Lett.* **102** (2009) 111301, [`arXiv:0809.2779`].

[332] B. Himmetoglu, C. R. Contaldi, and M. Peloso, *Ghost instabilities of cosmological models with vector fields nonminimally coupled to the curvature*, *Phys. Rev. D* **80** (2009) 123530, [`arXiv:0909.3524`].

[333] M. Karciauskas and D. H. Lyth, *On the health of a vector field with (R A^2)/6 coupling to gravity*, *JCAP* **11** (2010) 023, [`arXiv:1007.1426`].

[334] C. Capanelli, L. Jenks, E. W. Kolb, and E. McDonough, *Runaway Gravitational Production of Dark Photons*, [`arXiv:2403.15536`].

[335] A. Hell, *Unveiling the inconsistency of the Proca theory with non-minimal coupling to gravity*, [`arXiv:2403.18673`].

[336] Y. Ema, K. Nakayama, and Y. Tang, *Production of purely gravitational dark matter: the case of fermion and vector boson*, *JHEP* **07** (2019) 060, [`arXiv:1903.10973`].

[337] E. W. Kolb and A. J. Long, *Completely dark photons from gravitational particle production during the inflationary era*, *JHEP* **03** (2021) 283, [`arXiv:2009.03828`].

[338] A. Ahmed, B. Grzadkowski, and A. Socha, *Gravitational production of vector dark matter*, *JHEP* **08** (2020) 059, [`arXiv:2005.01766`].

[339] E. W. Kolb and A. J. Long, *Cosmological gravitational particle production and its implications for cosmological relics*, [`arXiv:2312.09042`].

[340] M. Bastero-Gil, J. Santiago, L. Ubaldi, and R. Vega-Morales, *Vector dark matter production at the end of inflation*, *JCAP* **04** (2019) 015, [`arXiv:1810.07208`].

[341] Y. Nakai, R. Namba, and Z. Wang, *Light Dark Photon Dark Matter from Inflation*, *JHEP* **12** (2020) 170, [`arXiv:2004.10743`].

[342] H. Firouzjahi, M. A. Gorji, S. Mukohyama, and B. Salehian, *Dark photon dark matter from charged inflaton*, *JHEP* **06** (2021) 050, [`arXiv:2011.06324`].

[343] N. Kitajima and K. Nakayama, *Viable vector coherent oscillation dark matter*, *JCAP* **07** (2023) 014, [`arXiv:2303.04287`].

[344] Y. Nakai, R. Namba, and I. Obata, *Peaky production of light dark photon dark matter*, *JCAP* **08** (2023) 032, [`arXiv:2212.11516`].

[345] J. A. Dror, K. Harigaya, and V. Narayan, *Parametric Resonance Production of Ultralight Vector Dark Matter*, *Phys. Rev. D* **99** (2019), no. 3 035036, [`arXiv:1810.07195`].

[346] K. Nakayama, *Vector Coherent Oscillation Dark Matter*, *JCAP* **10** (2019) 019, [`arXiv:1907.06243`].

[347] B. Salehian, M. A. Gorji, H. Firouzjahi, and S. Mukohyama, *Vector dark matter production from inflation with symmetry breaking*, *Phys. Rev. D* **103** (2021), no. 6 063526, [`arXiv:2010.04491`].

[348] P. Agrawal, N. Kitajima, M. Reece, T. Sekiguchi, and F. Takahashi, *Relic Abundance of Dark Photon Dark Matter*, *Phys. Lett. B* **801** (2020) 135136, [`arXiv:1810.07188`].

[349] R. T. Co, A. Pierce, Z. Zhang, and Y. Zhao, *Dark Photon Dark Matter Produced by Axion Oscillations*, *Phys. Rev. D* **99** (2019), no. 7 075002, [`arXiv:1810.07196`].

[350] A. J. Long and L.-T. Wang, *Dark Photon Dark Matter from a Network of Cosmic Strings*, *Phys. Rev. D* **99** (2019), no. 6 063529, [`arXiv:1901.03312`].

[351] P. W. Graham, J. Mardon, S. Rajendran, and Y. Zhao, *Parametrically enhanced hidden photon search*, *Phys. Rev. D* **90** (2014), no. 7 075017, [`arXiv:1407.4806`].

[352] A. Romanenko et al., *Search for Dark Photons with Superconducting Radio Frequency Cavities*, *Phys. Rev. Lett.* **130** (2023), no. 26 261801, [`arXiv:2301.11512`].

[353] S. Chaudhuri, P. W. Graham, K. Irwin, J. Mardon, S. Rajendran, and Y. Zhao, *Radio for hidden-photon dark matter detection*, *Phys. Rev. D* **92** (2015), no. 7 075012, [`arXiv:1411.7382`].

[354] D. Horns, J. Jaeckel, A. Lindner, A. Lobanov, J. Redondo, and A. Ringwald, *Searching for WISPy Cold Dark Matter with a Dish Antenna*, *JCAP* **04** (2013) 016, [`arXiv:1212.2970`].

[355] J. Jaeckel and J. Redondo, *Resonant to broadband searches for cold dark matter consisting of weakly interacting slim particles*, *Phys. Rev. D* **88** (2013), no. 11 115002, [`arXiv:1308.1103`].

[356] MADMAX Working Group Collaboration, B. Majorovits and J. Redondo, *MADMAX: A new Dark Matter Axion Search using a Dielectric Haloscope*, in *12th Patras Workshop on Axions, WIMPs and WISPs*, pp. 94–97, 2017. [`arXiv:1611.04549`].

[357] L. H. Nguyen, A. Lobanov, and D. Horns, *First results from the WISPDMX radio frequency cavity searches for hidden photon dark matter*, *JCAP* **10** (2019) 014, [`arXiv:1907.12449`].

[358] B. Godfrey et al., *Search for dark photon dark matter: Dark E field radio pilot experiment*, *Phys. Rev. D* **104** (2021), no. 1 012013, [`arXiv:2101.02805`].

[359] I. Stern, *ADMX Status*, *PoS* **ICHEP2016** (2016) 198, [`arXiv:1612.08296`].

[360] F. Bajjali et al., *First results from BRASS-p broadband searches for hidden photon dark matter*, *JCAP* **08** (2023) 077, [`arXiv:2306.05934`].

[361] DOSUE-RR Collaboration, S. Adachi, R. Fujinaka, S. Honda, Y. Muto, H. Nakata, Y. Sueno, T. Sumida, J. Suzuki, O. Tajima, and H. Takeuchi, *Search for dark photon dark matter in the mass range 41–74 μeV using millimeter-wave receiver and radioshielding box*, *Phys. Rev. D* **109** (2024), no. 1 012008, [`arXiv:2308.14656`].

[362] B. D. Fields, K. A. Olive, T.-H. Yeh, and C. Young, *Big-Bang Nucleosynthesis after Planck*, *JCAP* **03** (2020) 010, [`arXiv:1912.01132`]. [Erratum: JCAP 11, E02 (2020)].

[363] J. Jaeckel, J. Redondo, and A. Ringwald, *Signatures of a hidden cosmic microwave background*, *Phys. Rev. Lett.* **101** (2008) 131801, [`arXiv:0804.4157`].

[364] S. D. McDermott and S. J. Witte, *Cosmological evolution of light dark photon dark matter*, *Phys. Rev. D* **101** (2020), no. 6 063030, [`arXiv:1911.05086`].

[365] A. Bhoonah, J. Bramante, F. Elahi, and S. Schon, *Galactic Center gas clouds and novel bounds on ultralight dark photon, vector portal, strongly interacting, composite, and super-heavy dark matter*, *Phys. Rev. D* **100** (2019), no. 2 023001, [`arXiv:1812.10919`].

[366] D. Wadekar and G. R. Farrar, *Gas-rich dwarf galaxies as a new probe of dark matter interactions with ordinary matter*, *Phys. Rev. D* **103** (2021), no. 12 123028, [`arXiv:1903.12190`].

[367] G. R. Farrar, F. J. Lockman, N. M. McClure-Griffiths, and D. Wadekar, *Comment on the paper "Calorimetric Dark Matter Detection with Galactic Center Gas Clouds"*, *Phys. Rev. Lett.* **124** (2020), no. 2 029001, [`arXiv:1903.12191`].

[368] M. A. Fedderke, P. W. Graham, D. F. J. Kimball, and S. Kalia, *Earth as a transducer for dark-photon dark-matter detection*, *Phys. Rev. D* **104** (2021), no. 7 075023, [`arXiv:2106.00022`].

[369] M. A. Fedderke, P. W. Graham, D. F. Jackson Kimball, and S. Kalia, *Search for dark-photon dark matter in the SuperMAG geomagnetic field dataset*, *Phys. Rev. D* **104** (2021), no. 9 095032, [`arXiv:2108.08852`].

[370] I. A. Sulai et al., *Hunt for magnetic signatures of hidden-photon and axion dark matter in the wilderness*, *Phys. Rev. D* **108** (2023), no. 9 096026, [`arXiv:2306.11575`].

[371] M. Jiang, T. Hong, D. Hu, Y. Chen, F. Yang, T. Hu, X. Yang, J. Shu, Y. Zhao, and X. Peng, *Search for dark photons with synchronized quantum sensor network*, [`arXiv:2305.00890`].

[372] I. M. Bloch and S. Kalia, *Curl up with a good B: detecting ultralight dark matter with differential magnetometry*, *JHEP* **2024** (2024), no. 1 178, [`arXiv:2308.10931`].

[373] C. Beadle, A. Caputo, and S. A. R. Ellis, *Resonant Conversion of Wave Dark Matter in the Ionosphere*, [`arXiv:2405.13882`].

[374] R. Brito, V. Cardoso, and P. Pani, *Superradiance: New Frontiers in Black Hole Physics*, *Lect. Notes Phys.* **906** (2015) pp.1–237, [`arXiv:1501.06570`].

[375] V. Cardoso, O. J. C. Dias, G. S. Hartnett, M. Middleton, P. Pani, and J. E. Santos, *Constraining the mass of dark photons and axion-like particles through black-hole superradiance*, *JCAP* **03** (2018) 043, [`arXiv:1801.01420`].

[376] E. Cannizzaro, L. Sberna, A. Caputo, and P. Pani, *Dark photon superradiance quenched by dark matter*, *Phys. Rev. D* **106** (2022), no. 8 083019, [`arXiv:2206.12367`].

[377] H. An, S. Ge, J. Liu, and M. Liu, *In-situ Measurements of Dark Photon Dark Matter using Parker Solar Probe: Going beyond the Radio Window*, [`arXiv:2405.12285`].

[378] H. An, F. P. Huang, J. Liu, and W. Xue, *Radio-frequency Dark Photon Dark Matter across the Sun*, *Phys. Rev. Lett.* **126** (2021), no. 18 181102, [`arXiv:2010.15836`].

[379] D. W. P. Amaral, M. Jain, M. A. Amin, and C. Tunnell, *Vector Wave Dark Matter and Terrestrial Quantum Sensors*, [`arXiv:2403.02381`].

[380] P. Fayet, *Extra U(1)'s and New Forces*, *Nucl. Phys. B* **347** (1990) 743–768.

[381] E. Hardy and R. Lasenby, *Stellar cooling bounds on new light particles: plasma mixing effects*, *JHEP* **02** (2017) 033, [`arXiv:1611.05852`].

[382] S.-P. Li and X.-J. Xu, *Production rates of dark photons and Z' in the Sun and stellar cooling bounds*, [`arXiv:2304.12907`].

[383] T. A. Wagner, S. Schlamminger, J. H. Gundlach, and E. G. Adelberger, *Torsion-balance tests of the weak equivalence principle*, *Class. Quant. Grav.* **29** (2012) 184002, [`arXiv:1207.2442`].

[384] P. Fayet, *MICROSCOPE limits for new long-range forces and implications for unified theories*, *Phys. Rev. D* **97** (2018), no. 5 055039, [`arXiv:1712.00856`].

[385] P. Fayet, *MICROSCOPE limits on the strength of a new force, with comparisons to gravity and electromagnetism*, *Phys. Rev. D* **99** (2019), no. 5 055043, [`arXiv:1809.04991`].

[386] MICROSCOPE Collaboration, P. Touboul et al., *MICROSCOPE Mission: Final Results of the Test of the Equivalence Principle*, *Phys. Rev. Lett.* **129** (2022), no. 12 121102, [`arXiv:2209.15487`].

[387] T. Kumar Poddar, S. Mohanty, and S. Jana, *Constraints on long range force from perihelion precession of planets in a gauged $L_e - L_{\mu,\tau}$ scenario*, *Eur. Phys. J. C* **81** (2021), no. 4 286, [`arXiv:2002.02935`].

[388] Y.-D. Tsai, Y. Wu, S. Vagnozzi, and L. Visinelli, *Novel constraints on fifth forces and ultralight dark sector with asteroidal data*, *JCAP* **04** (2023) 031, [`arXiv:2107.04038`].

[389] Y.-D. Tsai, D. Farnocchia, M. Micheli, S. Vagnozzi, and L. Visinelli, *Constraints on fifth forces and ultralight dark matter from OSIRIS-REx target asteroid Bennu*, [`arXiv:2309.13106`].

[390] P. W. Graham, D. E. Kaplan, J. Mardon, S. Rajendran, and W. A. Terrano, *Dark Matter Direct Detection with Accelerometers*, *Phys. Rev. D* **93** (2016), no. 7 075029, [`arXiv:1512.06165`].

[391] E. A. Shaw, M. P. Ross, C. A. Hagedorn, E. G. Adelberger, and J. H. Gundlach, *Torsion-balance search for ultralow-mass bosonic dark matter*, *Phys. Rev. D* **105** (2022), no. 4 042007, [`arXiv:2109.08822`].

[392] A. Arvanitaki, J. Huang, and K. Van Tilburg, *Searching for dilaton dark matter with atomic clocks*, *Phys. Rev. D* **91** (2015), no. 1 015015, [`arXiv:1405.2925`].

[393] A. Pierce, K. Riles, and Y. Zhao, *Searching for Dark Photon Dark Matter with Gravitational Wave Detectors*, *Phys. Rev. Lett.* **121** (2018), no. 6 061102, [`arXiv:1801.10161`].

[394] A. L. Miller and L. Mendes, *First search for ultralight dark matter with a space-based gravitational-wave antenna: LISA Pathfinder*, *Phys. Rev. D* **107** (2023), no. 6 063015, [`arXiv:2301.08736`].

[395] Y. Michimura, T. Fujita, S. Morisaki, H. Nakatsuka, and I. Obata, *Ultralight vector dark matter search with auxiliary length channels of gravitational wave detectors*, *Phys. Rev. D* **102** (2020), no. 10 102001, [`arXiv:2008.02482`].

[396] LIGO Scientific, VIRGO, KAGRA Collaboration, A. G. Abac et al., *Ultralight vector dark matter search using data from the KAGRA O3GK run*, [`arXiv:2403.03004`].

[397] N. Seto and A. Cooray, *Search for small-mass black hole dark matter with space-based gravitational wave detectors*, *Phys. Rev. D* **70** (2004) 063512, [`astro-ph/0405216`].

[398] A. Khmelnitsky and V. Rubakov, *Pulsar timing signal from ultralight scalar dark matter*, *JCAP* **02** (2014) 019, [`arXiv:1309.5888`].

[399] J. Jaeckel, S. Schenk, and M. Spannowsky, *Probing dark matter clumps, strings and domain walls with gravitational wave detectors*, *Eur. Phys. J. C* **81** (2021), no. 9 828, [`arXiv:2004.13724`].

[400] S. Baum, M. A. Fedderke, and P. W. Graham, *Searching for dark clumps with gravitational-wave detectors*, *Phys. Rev. D* **106** (2022), no. 6 063015, [`arXiv:2206.14832`].

[401] H. Kim, *Gravitational interaction of ultralight dark matter with interferometers*, *JCAP* **12** (2023) 018, [`arXiv:2306.13348`].

[402] H. Kim and A. Mitridate, *Stochastic ultralight dark matter fluctuations in pulsar timing arrays*, *Phys. Rev. D* **109** (2024), no. 5 055017, [`arXiv:2312.12225`].

[403] H. Kim, *Astrometric Search for Ultralight Dark Matter*, [`arXiv:2406.03539`].

[404] J. A. Dror and S. Verner, *Astrometric Detection of Ultralight Dark Matter*, [`arXiv:2406.03526`].

[405] H.-Y. Schive, T. Chiueh, and T. Broadhurst, *Cosmic Structure as the Quantum Interference of a Coherent Dark Wave*, *Nature Phys.* **10** (2014) 496–499, [`arXiv:1406.6586`].

[406] H. Nakatsuka, S. Morisaki, T. Fujita, J. Kume, Y. Michimura, K. Nagano, and I. Obata, *Stochastic effects on observation of ultralight bosonic dark matter*, *Phys. Rev. D* **108** (2023), no. 9 092010, [`arXiv:2205.02960`].

[407] M. A. Amin, M. Jain, R. Karur, and P. Mocz, *Small-scale structure in vector dark matter*, *JCAP* **08** (2022), no. 08 014, [`arXiv:2203.11935`].

[408] P. J. Fox, G. D. Kribs, and T. M. P. Tait, *Interpreting Dark Matter Direct Detection Independently of the Local Velocity and Density Distribution*, *Phys. Rev. D* **83** (2011) 034007, [`arXiv:1011.1910`].

[409] P. J. Fox, J. Liu, and N. Weiner, *Integrating Out Astrophysical Uncertainties*, *Phys. Rev. D* **83** (2011) 103514, [`arXiv:1011.1915`].

[410] B. Feldstein and F. Kahlhoefer, *A new halo-independent approach to dark matter direct detection analysis*, *JCAP* **08** (2014) 065, [`arXiv:1403.4606`].

[411] E. Bernreuther, P. J. Fox, B. Lillard, A.-M. Taki, and T.-T. Yu, *Extracting halo independent information from dark matter electron scattering data*, *JCAP* **03** (2024) 047, [`arXiv:2311.04957`].

[412] M. Maggiore, *Gravitational Waves. Vol. 1: Theory and Experiments.* Oxford University Press, 2007.

[413] D. Budker, P. W. Graham, M. Ledbetter, S. Rajendran, and A. Sushkov, *Proposal for a Cosmic Axion Spin Precession Experiment (CASPEr)*, *Phys. Rev. X* **4** (2014), no. 2 021030, [`arXiv:1306.6089`].

[414] L. Giulicchi, S.-F. Wu, and T. Fenal, *Attitude and orbit control systems for the lisa pathfinder mission*, *Aerospace Science and Technology* **24** (2013), no. 1 283–294. VFE-2.

[415] J. R. Smith, G. Cagnoli, D. R. Crooks, M. M. Fejer, S. Goßler, H. Lück, S. Rowan, J. Hough, and K. Danzmann, *Mechanical quality factor measurements of monolithically suspended fused silica test masses of the GEO 600 gravitational wave detector*, *Class. Quant. Grav.* **21** (2004) S1091–S1098.

[416] Einstein Telescope Collaboration, E. Coccia, *The Einstein Telescope*, *PoS* **ICRC2023** (2024) 1591.

[417] A. Einstein, *On the relativity principle and the conclusions drawn from it*, *Jahrb Radioaktivitat Elektronik* **4** (1907) 411–462.

[418] S. Schlamminger, K. Y. Choi, T. A. Wagner, J. H. Gundlach, and E. G. Adelberger, *Test of the equivalence principle using a rotating torsion balance*, *Phys. Rev. Lett.* **100** (2008) 041101, [`arXiv:0712.0607`].

[419] L. Pinard, C. Michel, B. Sassolas, L. Balzarini, J. Degallaix, V. Dolique, R. Flaminio, D. Forest, M. Granata, B. Lagrange, et al., *Mirrors used in the ligo interferometers for first detection of gravitational waves*, *Applied optics* **56** (2017), no. 4 C11–C15.

[420] S. Morisaki, T. Fujita, Y. Michimura, H. Nakatsuka, and I. Obata, *Improved sensitivity of interferometric gravitational wave detectors to ultralight vector dark matter from the finite light-traveling time*, *Phys. Rev. D* **103** (2021), no. 5 L051702, [`arXiv:2011.03589`].

[421] H.-K. Guo, K. Riles, F.-W. Yang, and Y. Zhao, *Searching for Dark Photon Dark Matter in LIGO O1 Data*, *Commun. Phys.* **2** (2019) 155, [`arXiv:1905.04316`].

[422] LIGO Scientific, KAGRA, Virgo Collaboration, R. Abbott et al., *Constraints on dark photon dark matter using data from LIGO's and Virgo's third observing run*, *Phys. Rev. D* **105** (2022), no. 6 063030, [`arXiv:2105.13085`].

[423] LISA Pathfinder Collaboration, L. P. collaboration, *LISA Pathfinder: First steps to observing gravitational waves from space*, *J. Phys. Conf. Ser.* **840** (2017), no. 1 012001.

[424] LISA Collaboration, P. Amaro-Seoane et al., *Laser Interferometer Space Antenna*, [`arXiv:1702.00786`].

[425] M. Armano et al., *Sub-Femto- g Free Fall for Space-Based Gravitational Wave Observatories: LISA Pathfinder Results*, *Phys. Rev. Lett.* **116** (2016), no. 23 231101.

[426] M. Armano et al., *Beyond the Required LISA Free-Fall Performance: New LISA Pathfinder Results down to 20 μHz*, *Phys. Rev. Lett.* **120** (2018), no. 6 061101.

[427] M. Armano et al., *Measuring the Galactic Cosmic Ray Flux with the LISA Pathfinder Radiation Monitor*, *Astropart. Phys.* **98** (2018) 28–37, [`arXiv:1711.07427`].

[428] LISA Pathfinder Collaboration, H. E. Audley, *LISA Pathfinder: Optical Metrology System monitoring during operations*, *J. Phys. Conf. Ser.* **840** (2017), no. 1 012034.

[429] LISA Pathfinder Collaboration, M. Armano et al., *Capacitive sensing of test mass motion with nanometer precision over millimeter-wide sensing gaps for space-borne gravitational reference sensors*, *Phys. Rev. D* **96** (2017), no. 6 062004.

[430] L. D. Landau, *TEXTBOOK ON THEORETICAL PHYSICS. VOL. 2: CLASSICAL FIELD THEORY. (IN GERMAN).* 1987.

[431] LISA Pathfinder Collaboration, K. Danzmann et al., *LISA Pathfinder: Einstein's Geodesic Explorer: The Science Case for LISA Pathfinder*, .

[432] G. D. Racca and P. W. McNamara, *The LISA Pathfinder mission: Tracing Einstein's geodesics in space*, *Space Sci. Rev.* **151** (2010) 159–181.

[433] LISA Pathfinder Collaboration, M. Armano et al., *LISA Pathfinder Platform Stability and Drag-free Performance*, *Phys. Rev. D* **99** (2019), no. 8 082001, [`arXiv:1812.05491`].

[434] `https://www.nist.gov/pml/atomic-weights-and-isotopic-compositions-relative-atomic-mas`

[435] P. F. de Salas, K. Malhan, K. Freese, K. Hattori, and M. Valluri, *On the estimation of the Local Dark Matter Density using the rotation curve of the Milky Way*, *JCAP* **10** (2019) 037, [`arXiv:1906.06133`].

[436] M. A. Fedderke and A. Mathur, *Asteroids for ultralight dark-photon dark-matter detection*, *Phys. Rev. D* **107** (2023), no. 4 043004, [`arXiv:2210.09324`].

[437] S. Morisaki and T. Suyama, *Detectability of ultralight scalar field dark matter with gravitational-wave detectors*, *Phys. Rev. D* **100** (2019), no. 12 123512, [`arXiv:1811.05003`].

[438] R. J. Scherrer and A. Loeb, *Ultra long-term cosmology and astrophysics*, *New Astron.* **99** (2023) 101940, [`arXiv:2209.06572`].

[439] LISA Pathfinder Collaboration, M. Armano et al., *Charging of free-falling test masses in orbit due to cosmic rays: Results from LISA Pathfinder*, *Phys. Rev. D* **107** (2023), no. 6 062007, [`arXiv:2211.09309`].

[440] C. Bohren and D. Huffman, *Absorption and Scattering of Light by Small Particles.* Wiley Science Series. Wiley, 2008.

[441] K. Issautier, C. Perche, S. Hoang, C. Lacombe, M. Maksimovic, J.-L. Bougeret, and C. Salem, *Solar wind electron density and temperature over solar cycle 23: Thermal noise measurements on wind*, *Advances in Space Research* **35** (2005), no. 12 2141–2146. The Dynamic Heliosphere.

[442] S. Heeba and F. Kahlhoefer, *Probing the freeze-in mechanism in dark matter models with U(1)' gauge extensions*, *Phys. Rev. D* **101** (2020), no. 3 035043, [`arXiv:1908.09834`].

[443] MAGIS-100 Collaboration, M. Abe et al., *Matter-wave Atomic Gradiometer Interferometric Sensor (MAGIS-100)*, *Quantum Sci. Technol.* **6** (2021), no. 4 044003, [`arXiv:2104.02835`].

[444] STE-QUEST Collaboration, P. Wolf et al., *STE-QUEST: Space Time Explorer and QUantum Equivalence principle Space Test*, [`arXiv:2211.15412`].

Acknowledgements

It will not come to anyone's surprise that my first and foremost gratitude goes towards my supervisor Kai. From the day he hired he was always available for me, be it for organisational questions, science discussions or just a ~~coffee~~ tea break. (Furthermore, he introduced me to the DESY theory football). But above all, I am grateful for his style of supervision. He understands perfectly, how to motivate his students to become independent researchers, interfering only when strictly necessary and giving advice instead of explicitly explaining what to do next. In addition, his physics intuition was always a helpful guide for me, especially when approaching new topics. A special "thank you" goes out to you for making my US trip possible. Without you there is no way I could have gotten such a promising postdoc position, thank you so much!

Furthermore, I thank my PhD defence committee, namely Dieter Horns (chair), Marcus Brüggen, Hyungjin Kim, and Kostas Nikolopoulos for agreeing to take on this task. Special thanks go to Marcus as my co-supervisor and Hyungjin for many interesting physics discussions throughout my PhD.

Of course, I am also immensely grateful to all my collaborators! I want to specifically point out Felix Kahlhöfer (my inofficial co-supervisor) who is as responsible as Kai is for my academic journey. Thanks for transforming a naive bachelor student into an "experienced" (but still naive) researcher. I really appreciate that you have been around for the projects that form the basis of this thesis. Further thanks go to Joerg Jaeckel for the incredible expertise that he provided for our project and also in the subsequent discussion with the LPF experts. Another big "thank you" goes to Marco Hufnagel and Frederik Depta[1] not only for our collaboration on the BBN project but also for your advice when I started here in Hamburg, and all the physics discussions we had over the years (like pandemic DPs), as well as your advice on thesis (including Frederik's template). All the best for your life outside physics, you will be missed!

Also, the rest of Kai's group deserves my deepest gratitude. Thank you Mathias for many interesting discussions and useful input when I was stuck. Thank you Sara for the many, many spontaneous meetings we had and your energy (both negative and positive :D) that really makes our collaboration so nice and (and hopefully also) productive. And finally, a huge thank you to Carlo, my PhD twin, for making (office) life much more enjoyable. Be it our time at Fermilab, the office parties or just a good evening at Headcrash, my life would have been much lamer without all of this. Furthermore, all of you (and Kai!) deserve another "thank you" for helpful feedback on the thesis and the good physics discussions.

Now we come to the part of the acknowledgements which I was always afraid of. There were so many people who enriched my time here. I will therefore refrain from excessive name-dropping but I hope that the following list will include you in one way or another. Let's start with my office mates, thanks for making 2a/301 the undisputedly best office in the theory group! I also want to thank the PhD students and Postdocs of the Strings group back in the day when I arrived here for making me feel at home in the early stages of my PhD. Furthermore, I thank the DESY Higgsers as well as the board games group for many great hours during lunch, coffee breaks and game nights. Finally, many people in the cosmo

---

[1] The order of names does not reflect any preferences :D

group deserve another thank you, for good physics discussion, sitting through $\mathcal{O}(100)$ DP paper discussions in the JC, or going running with me. In addition, dear cookie masters, thank you so much for this amazing service! The people at DESY know me for maybe three defining character traits: Eating sweets, DPs, and football. Therefore, here is another big, big "thank you" for all people who have ever joined our theory football (especially those who attend(ed) regularly). I also want to thank the theory group at Fermilab for being so welcoming in a lab that tries hard to not be welcoming and all the people I met throughout these three years, at conferences, schools, etc. Finally, one man deserves special treatment: thank you Guilherme for being a genius (at googling LaTeXstuff).

Going beyond DESY, there are many more people I need to thank! First of all, I must say thank you to Flo for making the 5 years in Aachen so memorable and successful. Without our shared suffering, I don't know if I would have even made it through the first semester. Staying in Aachen, I want to thank the "Haribo" group for an amazing time. And finally, going back all the way: Thanks to the "Europapokal" group and to the "Augenkommando" for giving me mental support throughout my Bachelor, Master, and PhD (probably without realising it). Finally, I also thank my friends from Rhade, i.e. the infamous "Thomas Müller" group. Special thanks go out to Lars for being around for so, so many years... thanks for everything!

Das Beste kommt zum Schluss: Mama und Papa, danke für alles!!! Ohne euch hätte ich es nicht ansatzweise bis hier hin geschafft. Danke, dass ihr mich bei meinen Entscheidungen unterstützt habt. Als ich damals nach Aachen gezogen bin, hätte ich es niemals für möglich gehalten, irgendwann mal an einem renommierten Institut wie DESY meine Doktorarbeit zu schreiben. Danke für alles, was ihr vor und nach meinem Auszug für mich geleistet habt! Desweiteren danke ich allen, die mich von klein auf geprägt haben und mich bis jetzt immer unterstützt haben. Das sind vor allem Marco, Karin, Opa Jupp, Oma Luzie und Oma Anneliese, aber noch viele mehr. Danke für all die schönen Momente über die vielen Jahre und dafür, dass ihr zumindest meistens ein bisschen Interesse gezeigt habt, wenn ich über Physik geredet habe.

Eidesstattliche Versicherung/Declaration on oath

Hiermit versichere ich an Eides statt, die vorliegende Dissertationsschrift selbst verfasst und keine anderen als die angegebenen Hilfsmittel und Quellen benutzt zu haben.

Sofern im Zuge der Erstellung der vorliegenden Dissertationsschrift generative Künstliche Intelligenz (gKI) basierte elektronische Hilfsmittel verwendet wurden, versichere ich, dass meine eigene Leistung im Vordergrund stand und dass eine vollständige Dokumentation aller verwendeten Hilfsmittel gemäß der Guten wissenschaftlichen Praxis vorliegt. Ich trage die Verantwortung für eventuell durch die gKI generierte fehlerhafte oder verzerrte Inhalte, fehlerhafte Referenzen, Verstöße gegen das Datenschutz- und Urheberrecht oder Plagiate.

I hereby declare and affirm that this doctoral dissertation is my own work and that I have not used any aids and sources other than those indicated.

If electronic resources based on generative artificial intelligence (gAI) were used in the course of writing this dissertation, I confirm that my own work was the main and value-adding contribution and that complete documentation of all resources used is available in accordance with good scientific practice. I am responsible for any erroneous or distorted content, incorrect references, violations of data protection and copyright law or plagiarism that may have been generated by the gAI.

Ort & Datum/Place & Date	Unterschrift/Signature Jonas Frerick